ACS OMEGA

Article

Cite This: ACS Omega 2019, 4, 3409−3419

http://pubs.acs.org/journal/acsodf

Highlighting the Influence of Thermodynamic Coupling on Kinetic Separations with Microporous Crystalline Materials

Rajamani Krishna*

Van 't Hoff Institute for Molecular Sciences, University of Amsterdam, Science Park 904, 1098 XH Amsterdam, The Netherlands

Supporting Information

ABSTRACT: The main focus of this article is on mixture separations that are driven by differences in intracrystalline diffusivities of guest molecules in microporous crystalline adsorbent materials. Such "kinetic" separations serve to over-ride, and reverse, the selectivities dictated by mixture adsorption equilibrium. The Maxwell−Stefan formulation for the description of intracrystalline fluxes shows that the flux of each species is coupled with that of the partner species. For n-component mixtures, the coupling is quantified by a $n \times n$ dimensional matrix of thermodynamic correction factors with elements Γ_{ij}; these elements can be determined from the model used to describe the mixture adsorption equilibrium. If the thermodynamic coupling effects are essentially ignored, i.e., the Γ_{ij} is assumed to be equal to δ_{ij}, the Kronecker delta, the Maxwell−Stefan formulation degenerates to yield uncoupled flux relations. The significance of thermodynamic coupling is highlighted by detailed analysis of separations of five different mixtures: N_2/CH_4, CO_2/C_2H_6, O_2/N_2, C_3H_6/C_3H_8, and hexane isomers. In all cases, the productivity of the purified raffinate, containing the tardier species, is found to be significantly larger than that anticipated if the simplification $\Gamma_{ij} = \delta_{ij}$ is assumed. The reason for the strong influence of Γ_{ij} on transient breakthroughs is traceable to the phenomenon of uphill intracrystalline diffusion of more mobile species. The major conclusion to emerge from this study is that modeling of kinetic separations needs to properly account for the thermodynamic coupling effects.

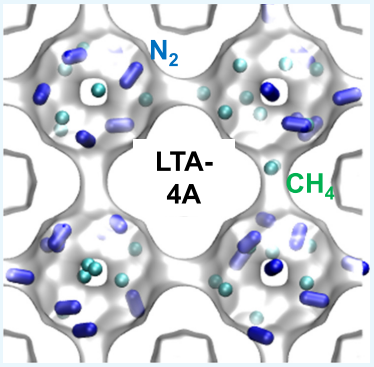

1. INTRODUCTION

Most commonly, the driver for mixture separations in fixed-bed adsorbers is the selectivity based on mixture adsorption equilibrium. Industrially important examples of such equilibrium-based separations include H_2 purification, production of purified oxygen, and separation of xylene isomers.[1−8] However, there are practical instances of kinetic separations in which diffusional effects over-ride the influence of mixture adsorption equilibrium and are the prime driver for separations;[9] examples include production of N_2 from air and removal of N_2 from natural gas.[2−4]

In recent years, there has been substantial progress in the development of novel materials for industrially important separations[10] that are primarily driven by diffusion selectivities and size exclusion. For industrially important separation of C_2H_4/C_2H_6 mixtures, the pore dimensions of UTSA-280, an ultra-microporous molecular sieve $[Ca(C_4O_4)(H_2O)]$, are tuned to only allow C_2H_4 to enter the channels, resulting in almost total exclusion of the saturated alkane.[11] Pimentel and Lively[12] demonstrate the potential of ZIF-8/cellulose acetate fiber sorbents for the kinetic separation of C_3H_6/C_3H_8 mixtures. Several other examples of kinetic separations are discussed in the review by Wang and Zhao.[13]

For the design and development of pressure swing adsorption (PSA) technologies exploiting diffusion-selective separations, it is of vital importance to use mathematical models for transient uptakes and breakthroughs in fixed adsorbers that properly describe both mixture adsorption equilibrium and the intracrystalline diffusion characteristics.[14] Commonly, the ideal adsorbed solution theory (IAST)[15] is the appropriate model to describe mixture adsorption equilibrium.[9] In the simple case of single-site Langmuir isotherms, with equal saturation capacities of guest species, the IAST degenerates to yield the mixed-gas Langmuir model

$$\frac{q_i}{q_{sat}} = \frac{b_i p_i}{1 + \sum_{j=1}^{n} b_j p_j}; \quad i = 1, 2, \ldots n \tag{1}$$

In eq 1, p_i are the component partial pressures, q_i are the component loadings defined in terms of moles per kg of framework, $q_{i,sat}$ are the saturation capacities, and b_i are Langmuir binding constants, with units of Pa^{-1}.

The most practical approach to modeling n-component diffusion in porous materials is the Maxwell−Stefan (M−S) formulation that has its basis in irreversible thermodynamics. The M−S formulation relates the intracrystalline molar fluxes N_i to the chemical potential gradients[16−20]

$$-\rho \frac{q_i}{RT} \frac{\partial \mu_i}{\partial r} = \sum_{\substack{j=1 \\ j \neq i}}^{n} \frac{x_j N_i - x_i N_j}{Đ_{ij}} + \frac{N_i}{Đ_i}; \quad i = 1, 2, \ldots n \tag{2}$$

Received: December 12, 2018
Accepted: January 31, 2019
Published: February 15, 2019

DOI: 10.1021/acsomega.8b03480
ACS Omega 2019, 4, 3409−3419

In eq 2, R is the gas constant, T is the temperature, ρ represents the framework density of the microporous crystalline material, r is the radial distance coordinate, and the component loadings q_i are defined in terms of moles per kg of framework. The x_i in eq 2 are the component mole fractions of the adsorbed phase within the micropores

$$x_i = q_i/q_t;\ \ q_t = q_1 + q_2 + \ldots q_n;\ \ i = 1, 2, \ldots n \tag{3}$$

$Đ_i$ characterize and quantify the interaction between species i and pore walls. The advantage of using eq 2 is that the M−S diffusivity $Đ_i$ equals the corresponding diffusivity for a unary system, determined at the same pore occupancy.[19] Furthermore, the M−S diffusivity $Đ_i$ for any species i in a mixture remains invariant to the choice of the partner(s) species.[19]

$Đ_{ij}$, defined in the first right member of eq 2, reflect how the facility for transport of species i correlates with that of species j. The Onsager reciprocal relations demand the symmetry constraint

$$Đ_{ij} = Đ_{ji} \tag{4}$$

The magnitude of $Đ_i$ relative to that of $Đ_{ij}$ determines the extent to which the flux of species i is influenced by the driving force of species j. The degree of correlations, defined by $Đ_i/Đ_{ij}$, is governed by a wide variety of factors such as pore size, channel topology, and connectivity.[21,22] Generally speaking, the tardier-more-strongly-adsorbed species will have the effect of slowing down the more-mobile-less-strongly-adsorbed partner in the mixture.[21] In other words, the presence of the first term on the right of eq 2 serves to reduce the differences in the effective mobilities of the constituent species within the pores. Therefore, correlation effects are undesirable for kinetic separations that seek to exploit the differences in the mobilities. In practice, we aim to select materials for which $Đ_i/Đ_{ij} \to \infty$ is a good approximation and the first right member of eq 2 can be ignored, resulting in

$$N_i = -\rho Đ_i \frac{q_i}{RT}\frac{\partial \mu_i}{\partial r};\ \ i = 1, 2, \ldots n \tag{5}$$

Examples of materials for which the flux expression 5 provides a good description of intracrystalline fluxes are cage-type structures such as CHA, DDR, ERI, LTA, and ZIF-8 that have narrow windows in the 3−4.2 Å size range.[23] In such structures, the windows allow the intercage hopping of only one molecule at a time; consequently, the jumps are practically uncorrelated.[24]

The chemical potential gradients $\partial \mu_i/\partial r$ can be related to the gradients of the molar loadings, q_i, by defining the thermodynamic correction factors Γ_{ij}

$$\frac{q_i}{RT}\frac{\partial \mu_i}{\partial r} = \sum_{j=1}^{n} \Gamma_{ij}\frac{\partial q_j}{\partial r};\ \Gamma_{ij} = \frac{q_i}{p_i}\frac{\partial p_i}{\partial q_j};\ i, j = 1, \ldots n \tag{6}$$

The thermodynamic correction factors Γ_{ij} can be calculated by differenting the model describing the mixture adsorption equilibrium,[25] such as eq 1. Combining eqs 5 and 6, we get

$$N_i = -\rho Đ_i \sum_{j=1}^{n} \Gamma_{ij}\frac{\partial q_j}{\partial r};\ \ i = 1, 2, \ldots n \tag{7}$$

Finite magnitudes of the off-diagonal elements Γ_{ij} $(i \neq j)$ cause the flux of species i to be also influenced by the gradient of the molar loading of species j.[26] To appreciate the significance of such thermodynamic "coupling", Figure 1 presents the calculations of the thermodynamic correction factors Γ_{ij} for

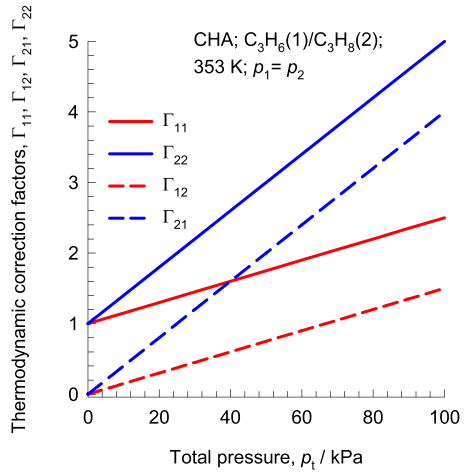

Figure 1. Calculations of the matrix of thermodynamic factors for 50:50 $C_3H_6(1)/C_3H_8(2)$ mixture adsorption within the crystals of all-silica CHA at 353 K. Further details and input data are provided in Chapter 9 of the Supporting Information.

50:50 $C_3H_6(1)/C_3H_8(2)$ mixture adsorption within the crystals of all-silica CHA zeolite at 353 K. We note that at a total pressure of 100 kPa, the cross-coefficients are about 60−80% of the magnitudes of the diagonal elements, indicating that thermodynamic coupling effects are extremely significant.

In the Henry regime of adsorption, at low pore occupancies, $\Gamma_{ij} \to \delta_{ij}$, the Kronecker delta, and eq 7 degenerates to yield a set of n uncoupled flux expressions[27]

$$N_i = -\rho Đ_i \frac{\partial q_i}{\partial r};\ \ i = 1, 2, \ldots n \tag{8}$$

Even though eq 8 is strictly valid at low pore occupancies, a large number of implementations of intracrystalline diffusion in models for fixed-bed adsorbers ignore the contribution of Γ_{ij}; see the comprehensive review of Shafeeyan et al.[28] The primary objective of this article is to investigate and highlight the strong influence of thermodynamic coupling effects, engendered by Γ_{ij} $(i \neq j)$, on the effectiveness of kinetic separations. We aim to show that the use of the simpler uncoupled flux expression 8 often leads to significant errors in the prediction of recoveries and productivities of the purified raffinate during the adsorption cycle of PSA operations. To meet our objective, we investigate the kinetically driven separation of five different mixtures N_2/CH_4, CO_2/C_2H_6, O_2/N_2, C_3H_6/C_3H_8, and hexane isomers. In each case, we compare the separation effectiveness predicted by breakthrough simulations incorporating eqs 7 and 8.

The Supporting Information accompanying this publication provides (a) details of the methodology used for modeling of the transient breakthroughs in fixed-bed adsorbers, with incorporation of the IAST and the Maxwell−Stefan diffusion formulations, (b) input data on unary isotherms, and M−S diffusivities, for each of the five cases studies investigated, and (c) structural details of the zeolites and metal−organic frameworks (MOFs).

DOI: 10.1021/acsomega.8b03480
ACS Omega 2019, 4, 3409−3419

2. MODELING TRANSIENT UPTAKES AND BREAKTHROUGHS

For an n-component gas mixture flowing through a fixed-bed adsorber maintained under isothermal, isobaric conditions, the molar concentrations in the gas phase at any position and instance of time are obtained by solving the following set of partial differential equations for each of the species i in the gas mixture[4,18,26]

$$-D_{ax}\frac{\partial^2 c_i(t,z)}{\partial z^2}+\frac{\partial c_i(t,z)}{\partial t}+\frac{\partial(v(t,z)c_i(t,z))}{\partial z}+\frac{(1-\varepsilon)}{\varepsilon}\rho\frac{\partial \overline{q}_i(t,z)}{\partial t}=0;\ \ i=1,2,\ldots n \tag{9}$$

In eq 9, t is the time, z is the distance along the adsorber, ε is the bed voidage, D_{ax} is the axial dispersion coefficient, v is the interstitial gas velocity, and $\overline{q}_i(t,z)$ is the spatially averaged molar loading within the crystallites of radius r_c, monitored at position z and at time t.[18] Ruthven et al.[4] state, "when mass transfer resistance is significantly greater than axial dispersion, one may neglect the axial dispersion term and assume plug flow". The assumption of plug flow is appropriate for kinetically controlled separations and is invoked in all the simulation results presented in this article.

The radial distribution of molar loadings, q_i, is obtained from a solution of a set of differential equations describing the transient uptake within a spherical crystallite of radius r_c

$$\rho\frac{\partial q_i(r,t)}{\partial t}=-\frac{1}{r^2}\frac{\partial}{\partial r}(r^2N_i) \tag{10}$$

The intracrystalline fluxes N_i, in turn, are related to the radial gradients in the molar loadings by eq 7. At any time t, the component loadings at the surface of the particle $q_i(r_c,t)=q_i^*$ is in equilibrium with the bulk phase gas mixture.[29] The loadings q_i^* are determined by the IAST or mixed-gas Langmuir model, as appropriate.[30]

At any time t, during the transient approach to thermodynamic equilibrium, the spatial-averaged component loading within the crystallites of radius r_c is calculated using

$$\overline{q}_i(t)=\frac{3}{r_c^3}\int_0^{r_c}q_i(r,t)r^2\,dr \tag{11}$$

In all of the simulations reported in this article, the entire bed of crystalline particles is considered to be devoid of adsorbates at time $t=0$, i.e., we have the initial condition

$$t=0;\ \ q_i(0,z)=0 \tag{12}$$

At time, $t=0$, the inlet to the adsorber, $z=0$, is subject to a step input of the feed gas mixture, with inlet partial pressures p_{i0}, and this step input is maintained till the end of the adsorption cycle when steady-state conditions are reached.

$$t\geq 0;\ \ p_i(0,t)=p_{i0};\ \ c_i(0,t)=c_{i0} \tag{13}$$

Combination of the discretized partial differential equations along with the algebraic equations describing mixture adsorption equilibrium (IAST or mixed-gas Langmuir model) results in a set of differential−algebraic equations, which are solved using a sparse matrix solver based on the semi-implicit Runge−Kutta method;[30] further numerical details are provided in the Supporting Information.

Validation of the simulation methodology for transient uptakes and breakthroughs by comparison with published experimental works is available in earlier works.[9,18,29,31−34] As an illustration, Figure 2 presents the experimental data of

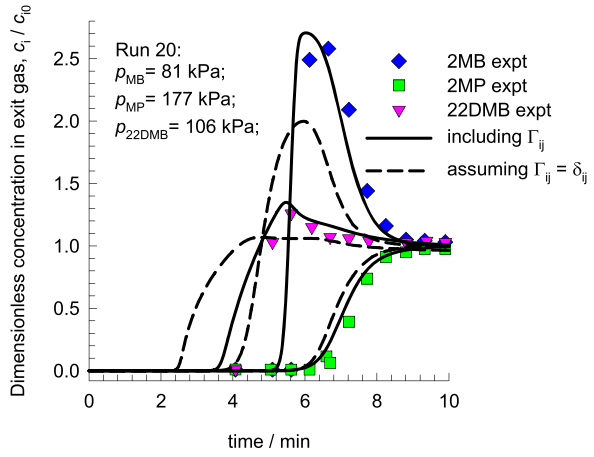

Figure 2. Transient breakthrough experiments of run 20 of Jolimaître et al.[35] for 2MB/2MP/22DMB ternary mixtures at 473 K.[18] The continuous solid lines are simulations based on eq 7. The dashed lines are the simulations based on eq 8. Further details and input data are provided in Chapter 10 of the Supporting Information, which also contains the rationale for ignoring correlation effects.

Jolimaître et al.[35] for transient breakthrough of a ternary mixture of 2-methylbutane (2MB), 2-methylpentane (2MP), and 2,2-dimethylbutane (22DMB) at 473 K in a fixed bed packed with MFI zeolite that has a topology consisting of a set of intersecting straight channels and zig-zag channels approximately 5.5 Å in size.[8] Branched alkanes are located preferentially at the channel intersections. The hierarchy of adsorption strengths is 2MP > 22DMB > 2MB, whereas the diffusion hierarchy is 2MB > 2MP ≫ 22DMB. Due to the diffusional penalty, 22DMB breaks through earlier than the more mobile 2MB. The experimental breakthroughs are quantitatively captured by simulations that adopt the flux expressions including Γ_{ij}.[18] If the assumption $\Gamma_{ij}=\delta_{ij}$ is invoked, the agreement is significantly worse.[18] Similar good agreement of the breakthrough simulations based on eq 7 is obtained for the complete set of seven experimental runs, with different entering feed mixture compositions, using the same set of isotherm and diffusivity parameters;[18] details are provided in Chapter 10 of the Supporting Information.

3. RESULTS AND DISCUSSIONS ON FIVE MIXTURE SEPARATIONS

3.1. Separation of N_2/CH_4 Mixtures. Many natural gas reserves contain nitrogen in concentrations ranging to about 20%.[36] To meet pipeline specifications, the nitrogen level must be reduced to below 4%.[37] A large majority of nitrogen removal facilities use cryogenic distillation, but such units are economical only for large-capacity wells. For smaller reserves, PSA technology has economic benefits, especially because the feed mixtures are available at high pressures.[36−38] It is desirable to use adsorbents in PSA units that are selective to N_2. For most known adsorbents, the selectivity for the separation of N_2/CH_4 mixtures is in favor of CH_4 due to its higher polarizability.[18]

DOI: 10.1021/acsomega.8b03480
ACS Omega 2019, 4, 3409−3419

In a classic paper published in 1958, Habgood[39] reported experimental data on transient uptake of $N_2(1)/CH_4(2)$ mixtures in crystallites of LTA-4A zeolite at 194 K. The data measured with partial pressures (a) p_1 = 50.9 kPa, p_2 = 49.1 kPa and (b) p_1 = 10 kPa, p_2 = 90 kPa are shown in Figure 3a,b.[40] The nitrogen molecule has a "pencil-like" shape with dimensions of 4.4 Å × 3.3 Å; it can hop length-wise across the narrow 4.1 Å × 4.5 Å 8-ring windows of LTA-4A.[41] The methane molecule is spherical with dimensions of 3.7 Å; it is much more severely constrained and has a diffusivity that is 22 times lower than that of N_2.[29,42] The adsorption strength of CH_4 is higher than that of N_2 by a factor 2.2. During the early stages of the transient uptake process, the pores of LTA-4A are significantly richer in the more mobile N_2. With increasing time, the nitrogen contained within the pores is progressively displaced by the more strongly adsorbed, tardier CH_4 molecules.[18] The net result is an overshoot in the N_2 uptake in both experimental uptake campaigns. The continuous solid lines in Figure 3a,b are uptake simulations based on eq 7; these simulations successfully capture the overshoot in the uptake of the more mobile N_2. The dashed lines are the simulations based on eq 8, ignoring thermodynamic coupling, i.e., $\Gamma_{ij} = \delta_{ij}$; in this scenario, no N_2 overshoot is experienced. The attainment of supraequilibrium loadings of N_2 during the early transience signals the phenomena of uphill diffusion, which can be exploited to achieve kinetic separations in fixed-bed adsorption devices.[7,20,29]

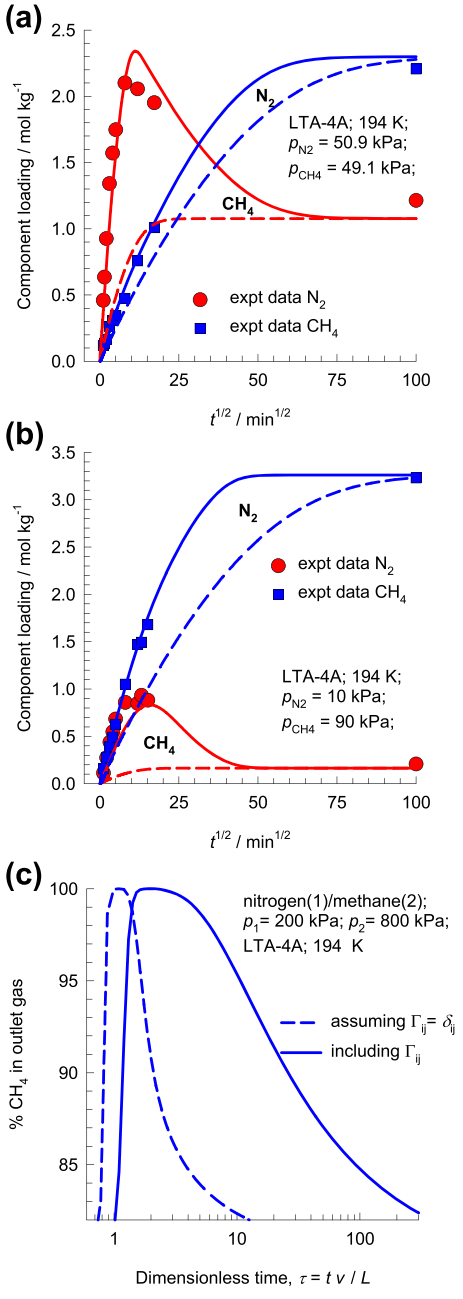

Figure 3. (a, b) Experimental data of Habgood[39] on transient uptake of $N_2(1)/CH_4(2)$ mixture within LTA-4A crystals exposed to binary gas mixtures at partial pressures (a) p_1 = 50.9 kPa, p_2 = 49.1 kPa and (b) p_1 = 10 kPa, p_2 = 90 kPa at 194 K.[18] (c) Transient breakthrough of 20:80 $N_2(1)/CH_4(2)$ mixture in a fixed-bed adsorber packed with LTA-4A crystals operating at 194 K and total pressure p_t = 100 kPa. The continuous solid lines are simulations based on eq 7. The dashed lines are simulations based on eq 8. Further details and input data are provided in Chapter 6 of the Supporting Information.

Figure 3c shows the transient breakthrough simulations for 20:80 N_2/CH_4 mixtures through fixed-bed adsorber packed with LTA-4A crystals operating at 194 K and total pressure p_t = 100 kPa.[29] The x-axis is the dimensionless time, $\tau = tv/L$, obtained by dividing the actual time, t, by the characteristic time, L/v, where L is the length of the adsorber.[5,6,30] The continuous solid lines are simulations based on eq 7; the dashed lines are simulations based on eq 8. For the target purity of CH_4 is 96%, corresponding to prescribed pipeline specification, we can determine the moles of 96% + pure CH_4 produced. Expressed per kg of LTA-4A zeolite in the packed bed, the respective productivities are 0.09 and 0.002 mol kg^{-1}. Ignoring the thermodynamic coupling effects severely underestimates the separation performance by a factor of about 50.

N_2/CH_4 separations with LTA-4A zeolite are effective only at low temperatures, and other materials such as Ba-ETS-4 and clinoptilolites are more suitable for kinetic separations at ambient conditions.[3,36−38] The experimental data of Majumdar et al.[43] on transient uptake of N_2/CH_4 mixtures in Ba-ETS-4 show overshoots in N_2 loading, confirming the manifestation of uphill diffusion and thermodynamic coupling effects.[18,29]

3.2. Separation of CO_2/C_2H_6 Mixtures. The separation of CO_2/C_2H_6 mixtures is relevant in the context of natural gas processing. Current technologies for CO_2/C_2H_6 separations use extractive distillation because of CO_2/C_2H_6 azeotrope formation.[44] Another alternative is to combine distillation technology with membrane separations; for this purpose, cross-linked poly(ethylene oxide) membranes have demonstrated to have good separation potential.[45−47]

Figure 4a−c shows the experimental data of Binder et al.[48] and Lauerer et al.[49] for spatial-averaged transient uptake of (a) 1:1, (b) 2:1, and (c) 3:1 CO_2/C_2H_6 gas mixtures within the crystals of DDR zeolite at 298 K.[9] The DDR zeolite consists of cages of 277.8 $Å^3$ volume separated by 3.65 Å × 4.37 Å 8-ring windows.[41,50] Both guest molecules, CO_2 and C_2H_6, jump length-wise across the 8-ring windows of the DDR zeolite.[51] The cross-sectional dimension of CO_2 is smaller than that of C_2H_6,[5] and therefore, the intracrystalline M−S diffusivity of CO_2 is significantly higher than that of C_2H_6 by about 2−3 orders of magnitude; for further details, see Chapter 7 of the Supporting Information.

The Maxwell−Stefan flux expression including thermodynamic coupling quantitatively captures the overshoots in CO_2 loadings with good accuracy for all three experiments.[29] If

DOI: 10.1021/acsomega.8b03480
ACS Omega 2019, 4, 3409−3419

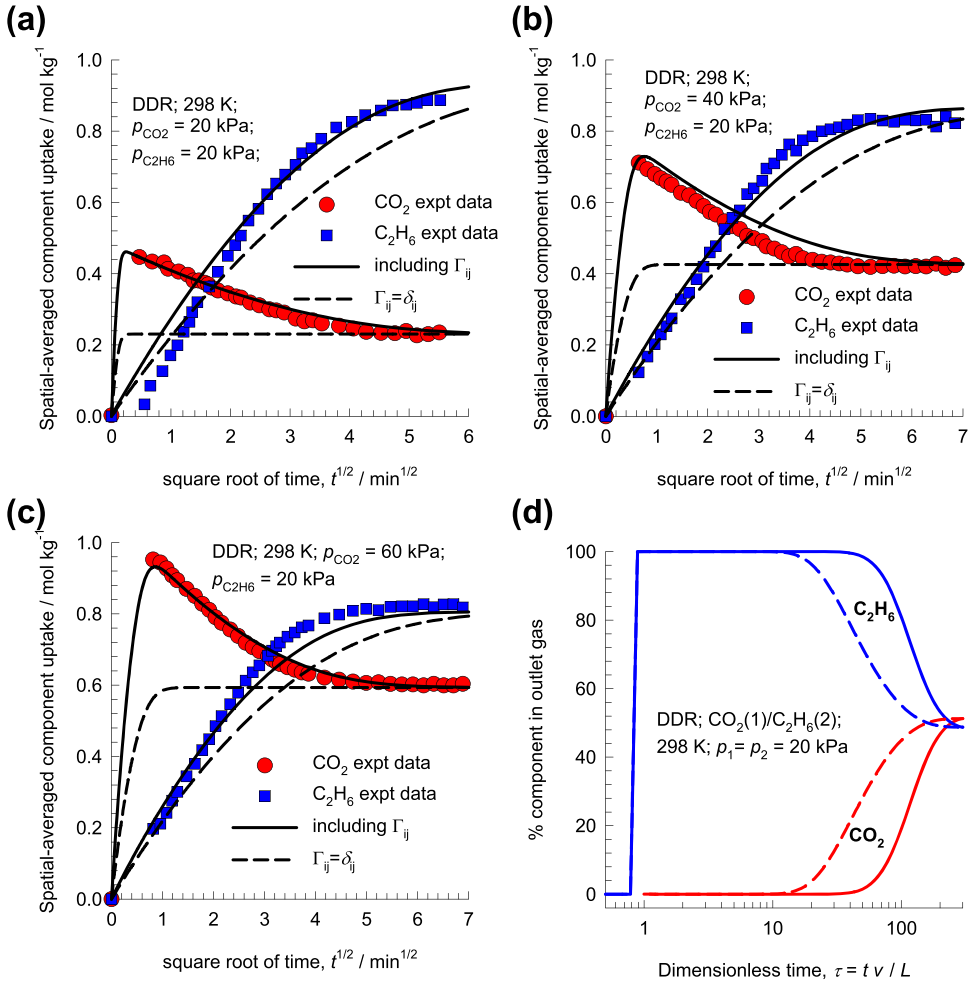

Figure 4. (a–c) Experimental data of Binder et al.[48] and Lauerer et al.[49] (indicated by symbols) for spatial-averaged transient uptake of (a) 1:1, (b) 2:1, and (c) 3:1 $CO_2(1)/C_2H_6(2)$ gas mixtures within the crystals of DDR zeolite at 298 K.[9,29] (b) Transient breakthrough of 1:1 CO_2/C_2H_6 mixtures through fixed-bed adsorber packed with DDR crystals operating at 298 K and total pressure p_t = 40 kPa. The continuous solid lines in are simulations based on eq 7. The dashed lines are simulations based on eq 8. Further details and input data are provided in Chapter 7 of the Supporting Information.

thermodynamic coupling effects are ignored and the assumption $\Gamma_{ij} = \delta_{ij}$ is invoked, no overshoots in CO_2 uptake are experienced, and the simulations show poor agreement with experiments during the early transience.[29]

Figure 4d shows the transient breakthrough simulations for 1:1 CO_2/C_2H_6 mixtures through fixed-bed adsorber packed with DDR crystals operating at 298 K and total pressure p_t = 40 kPa.[29] Assuming that target purity of C_2H_6 is 90%, we can determine the moles of more than 90% pure C_2H_6 produced. The productivities of more than 90% pure C_2H_6 are 0.18 and 0.054 mol kg^{-1}, respectively, for the two scenarios in which thermodynamic coupling is accounted for, or ignored. Ignoring the thermodynamic coupling effects underestimates the separation performance by a factor of about three.

3.3. Separation of O_2/N_2 Mixtures. For the production of purified N_2 from air, it is desirable to have an adsorbent that is selective to O_2, which constitutes 21% of the feed mixture; purified N_2 can be recovered as a raffinate during the initial transience of the adsorption cycle.[4,18,52] However, for most adsorbents, the mixture adsorption equilibrium is in favor of N_2, which has a higher quadrupole moment compared to O_2. Oxygen-selective separations are achieved with LTA-4A zeolite and carbon molecular sieve (CMS); in these materials, O_2 has higher diffusivity due to its smaller size.[3,53−56]

Simulations of transient uptake of O_2/N_2 mixture in LTA-4A zeolite at 298 K and total pressure of 600 kPa, display an overshoot in the O_2 uptake (see Figure 5a). The overshoot in the O_2 loading disappears with the simplification $\Gamma_{ij} = \delta_{ij}$. The experimental data of Chen et al.[55] for transient O_2/N_2 uptake in CMS also show an overshoot in the O_2 uptake, confirming the occurrence of uphill diffusion and attainment of supra-equilibrium O_2 loadings for a short time span.[20,29]

Figure 5b presents transient breakthrough simulations for a fixed-bed operating at 298 K and total pressure of 600 kPa. For an assumed target purity of more than 95% N_2, we can determine the moles of more than 95% pure N_2 produced; expressed per kg of LTA-4A zeolite in the packed bed, the productivities are 0.066 and 0.036 mol kg^{-1} for the respective models including and ignoring thermodynamic coupling influences. Ignoring thermodynamic coupling effects underestimates the separation performance by a factor of 50%.

3.4. Separation of C_3H_6/C_3H_8 Mixtures. Cryogenic distillation of C_3H_6/C_3H_8 mixtures is the currently used technology for making polymer-grade propene with more than 99.5% purity. Propane of more than 90% purity is used for

DOI: 10.1021/acsomega.8b03480
ACS Omega 2019, 4, 3409−3419

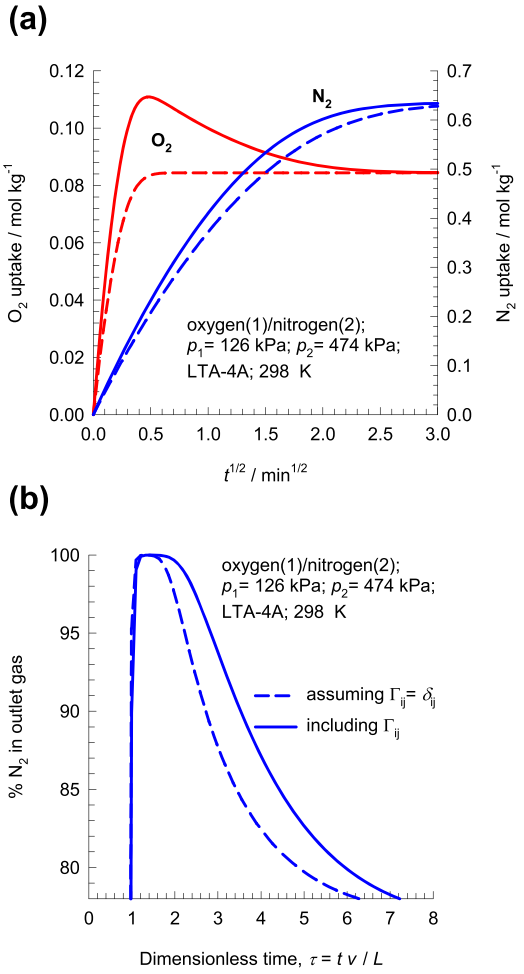

Figure 5. (a) Transient uptake of $O_2(1)/N_2(2)$ mixture in LTA-4A zeolite at 298 K and total pressure of 600 kPa. The partial pressures of the components in the bulk gas phase are p_1 = 126 kPa and p_2 = 474 kPa. (b) Transient breakthrough characteristics of $O_2(1)/N_2(2)$ mixture in a fixed-bed adsorber packed with LTA-4A operating at a total pressure of 600 kPa and 298 K. The partial pressures of the components in the bulk gas phase at the inlet are p_1 = 126 kPa and p_2 = 474 kPa. The continuous solid lines are simulations based on eq 7. The dashed lines are simulations based on eq 8. Further details and input data are provided in Chapter 8 of the Supporting Information.

various purposes such as fuel for engines, oxy-gas torches, and barbecues; this can be obtained as the bottoms product of the cryogenic distillation column.[57] The boiling points are close to each other: propene (226 K) and propane (231.3 K). Consequently, the distillation columns are some of the largest and tallest distillation columns used in the petrochemical industries with about 150−200 trays and operate at reflux ratios of about 15.[58] A PSA process can be an attractive alternative for C_3H_6/C_3H_8 separations because of its expected low energy demand. A variety of adsorbents have been investigated for this separation task.[57,59−61] Promising good potential for alkene/alkane separations are MOFs with coordinatively unsaturated metal centers that may be created by evacuation of frameworks that have metal-bound solvent molecules. This strategy has been employed to expose M^{2+} cation sites in M_2(dobdc) [M = Mg, Mn, Co, Ni, Zn, Fe; $dobdc^{4-}$ = 2,5-dioxido-1,4-benzenedicarboxylate].[62] Unsaturated alkynes and alkenes such as C_2H_2, C_2H_4, and C_3H_6 can bind with M^{2+} of M_2(dobdc), with side-on attachment and π-coordination.[5,63,64] The potential of M_2(dobdc) for the technologically important separations of C_2H_2/C_2H_4, C_2H_4/C_2H_6, and C_3H_6/C_3H_8 mixtures has been established in laboratory studies.[32,63−65] Other adsorbents that also exhibit adsorption selectivity in favor of the unsaturated propene include CuBTC,[66] LTA-4A zeolite,[59,60] and NaX (=13X) zeolite.[59,61] An important disadvantage of the C_3H_6/C_3H_8 separations with the adsorbents listed above is that the desired alkene product, required for the production of polymer-grade feedstock, can only be recovered in the desorption phase. It becomes necessary to operate PSA units with multiple beds, involving five different steps; the C_3H_6 product of desired purity is recovered in the final step by counter-current vacuum blowdown.[34,60,61,67]

The recovery of high-purity C_3H_6 product in the final vacuum blowdown step is expected to be enhanced if C_3H_8 is (almost) excluded from the pores during the high-pressure adsorption cycle. Near-total exclusion of C_3H_8 is achievable by kinetically based separations using cage-type zeolites with 8-ring windows.[51] Due to the smaller cross section of the propene molecule (the dimensions are provided by Chng et al.[68]), kinetic separations selective to propene are possible using all-silica CHA zeolite that consists of cages of volume 316 Å^3 and separated by 3.8 Å × 4.2 Å 8-ring windows.[8,57,69−71]

Using the input data on isotherms and diffusivities provided by Khalighi et al.,[57] we first examine the influence of thermodynamic coupling on transient uptake within a single spherical crystallite of CHA zeolite, initially devoid of guest molecules, exposed to a bulk 50:50 C_3H_6/C_3H_8 mixture at 100 kPa and T = 353 K. For the uptake simulations using eq 7, the more mobile C_3H_6 exhibits a pronounced overshoot in its approach to thermodynamic equilibrium (see Figure 6a).[20,29] If thermodynamic coupling is ignored, no C_3H_6 overshoot is detected.

We should expect the transient overshoot phenomena, and uphill diffusion, to have a beneficial effect on the transient breakthrough characteristics in fixed beds.[29] Figure 6b shows the simulations for transient breakthrough of 50:50 C_3H_6/C_3H_8 mixtures in a fixed bed adsorber packed with crystals of all-silica CHA at 353 K and operating at a total pressure of 100 kPa. The simulations clearly show that more than 90% pure C_3H_8 can be collected during the earlier stages of transience. If thermodynamic coupling effects are ignored and simplified eq 8 are invoked, the time interval during which more than 90% pure C_3H_8 can be recovered is reduced by about an order of magnitude. Expressed per kg of CHA zeolite in the packed bed, the respective productivities of more than 90% pure C_3H_8 are 0.62 and 0.06 mol kg^{-1}, a reduction by a factor of about 10 due to neglect of thermodynamic coupling.

It must be remarked that the model used by Khalighi et al.[57] takes due account of thermodynamic coupling effects, whereas more simplified approach using the linear driving force approximation is adopted by Da Silva and Rodrigues[61] for modeling kinetic separations of C_3H_6/C_3H_8 mixtures using LTA-4A zeolite.

Cadiau et al.[72] report the synthesis of NbOFFIVE-1-Ni (also named KAUST-7), a customized MOF for C_3H_6/C_3H_8 separations that belongs to the class of SIFSIX materials,[73] using pyrazine as the organic linker. The $(SiF_6)^{2-}$ pillars in the cage are replaced with somewhat bulkier $(NbOF_5)^{2-}$ pillars. This causes tilting of the pyrazine molecule on the linker, effectively reducing the aperture opening from 0.50 nm [with

DOI: 10.1021/acsomega.8b03480
ACS Omega 2019, 4, 3409−3419

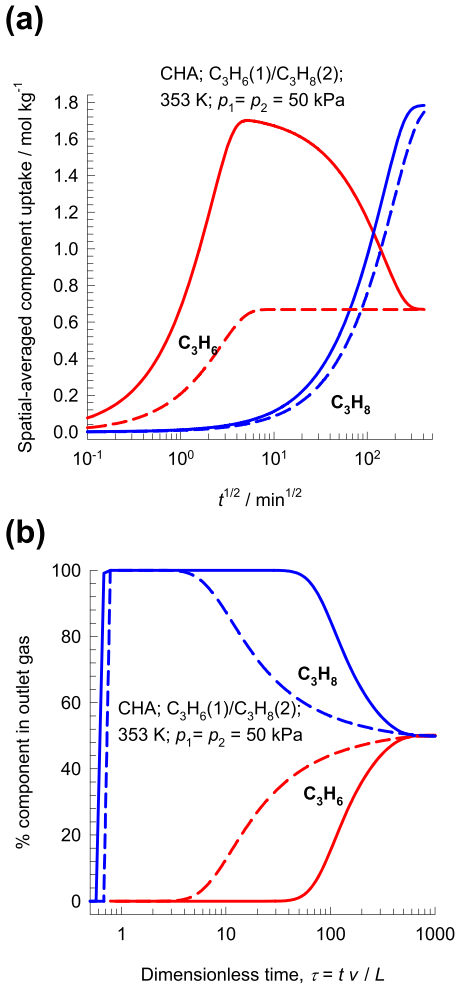

Figure 6. (a) Simulations of transient uptake of 50:50 $C_3H_6(1)/C_3H_8(2)$ mixtures within crystals of all-silica CHA at 353 K. (b) Simulations of transient breakthrough of 50:50 $C_3H_6(1)/C_3H_8(2)$ mixtures in a fixed-bed adsorber packed with crystals of all-silica CHA at 353 K and operating at a total pressure of 100 kPa. The continuous solid lines are simulations based on eq 7. The dashed lines are simulations based on eq 8. Further details and input data are provided in Chapter 9 of the Supporting Information.

$(SiF_6)^{2-}$ pillars] to 0.30 nm. The small aperture permits ingress of the smaller C_3H_6 molecules but practically excludes C_3H_8 on the basis of subtle differences in bond lengths, bond angles, and molecular conformations.[5] Figure 7 presents a comparison of the percentage C_3H_8 in the outlet gas leaving fixed-bed adsorbers packed with KAUST-7 and CHA zeolite. Both of these adsorbents appear to be equally effective in near-total exclusion of C_3H_8. Further investigation and detailed PSA simulations such as that presented by Khalighi et al.[67] are required to determine whether KAUST-7 offers significant improvements over CHA zeolite for the production of more than 99.5% pure C_3H_6. It is worth mentioning that in Figure S12 of Cadiau et al.,[72] breakthroughs of KAUST-7 are compared with data on LTA-4A and LTA-5A zeolites but not with all-silica CHA.

3.5. Separation of Mixtures of Hexane Isomers. An important step in the production of high-octane gasoline is the separation of hexane isomers, *n*-hexane (*n*C6), 2-methylpentane (2MP), 3-methylpentane (3MP), 2,2-dimethylbutane (22DMB), and 2,3-dimethylbutane (23DMB). The values of

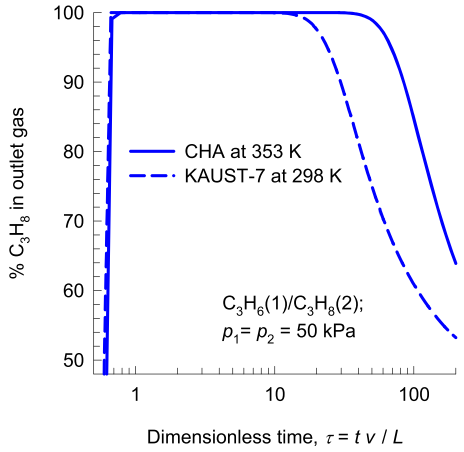

Figure 7. Comparison of the percentage C_3H_8 in the outlet gas leaving fixed-bed adsorbers packed with KAUST-7 and CHA zeolite. Both simulations are based on eq 7. Further details and input data are provided in Chapter 9 of the Supporting Information.

the Research Octane Number (RON) increases with the degree of branching: *n*C6 = 30, 2MP = 74.5, 3MP = 75.5, 22DMB = 94, and 23DMB = 105. Due to their higher RON values, di-branched isomers are preferred products for inclusion in the high-octane gasoline pool.[18,74,75] There are a number of adsorbents that have potential use in the separation of hexane isomers.[18,76] Separations using MFI zeolite[18] have some unique characteristics; these features arise from the preferential location of the mono- and di-branched isomers at the channel intersections, whereas the linear *n*C6 can locate anywhere within the channel network.[6,77,78] As a consequence, the hierarchy of adsorption strengths, dictated by configurational entropy considerations,[6,79,80] is *n*C6 > 2MP ≈ 3MP > 22DMB ≈ 23DMB. The hierarchy of the magnitudes of intracrystalline diffusivities is *n*C6 ≫ 2MP ≈ 3MP ≫ 22DMB ≈ 23DMB.[58] Consequently, both adsorption and diffusion act synergistically.[18,81]

The transient uptake of *n*C6/2MP mixtures in MFI crystals, exposed to an equimolar gas-phase mixture at constant total pressure (=2.6 Pa) have been reported by Titze et al.[29,81] (see Figure 8a). The transient equilibration of *n*C6 displays a pronounced overshoot, achieving supraequilibrium loadings during transient equilibration. The origin of the *n*C6 overshoot is traceable to the contribution of finite off-diagonal elements of Γ_{ij}; if the assumption $\Gamma_{ij} = \delta_{ij}$ is invoked, the overshoot disappears.

Uphill diffusion of *n*C6 is beneficial to the hexane isomer separations in fixed beds because the desired raffinate phase will be richer in the branched isomers that have high octane numbers. To confirm this expectation, transient breakthrough simulations were performed for a 5-component *n*C6/2MP/3MP/22DMB/23DMB mixture. The transient variations of the RON values of the gas mixture exiting the adsorber are plotted in Figure 8b.[7,18,29] Assuming that the target RON value of the raffinate is 92+ RON, we can determine the number of moles of 92+ RON product that can be recovered during the initial transience. The 92+ RON productivity is 0.36 mol kg^{-1} for the scenario in which thermodynamic coupling is included. The 92+ RON productivity is lowered to a value of 0.28 mol kg^{-1} for invoking the simplification $\Gamma_{ij} = \delta_{ij}$.

DOI: 10.1021/acsomega.8b03480
ACS Omega 2019, 4, 3409−3419

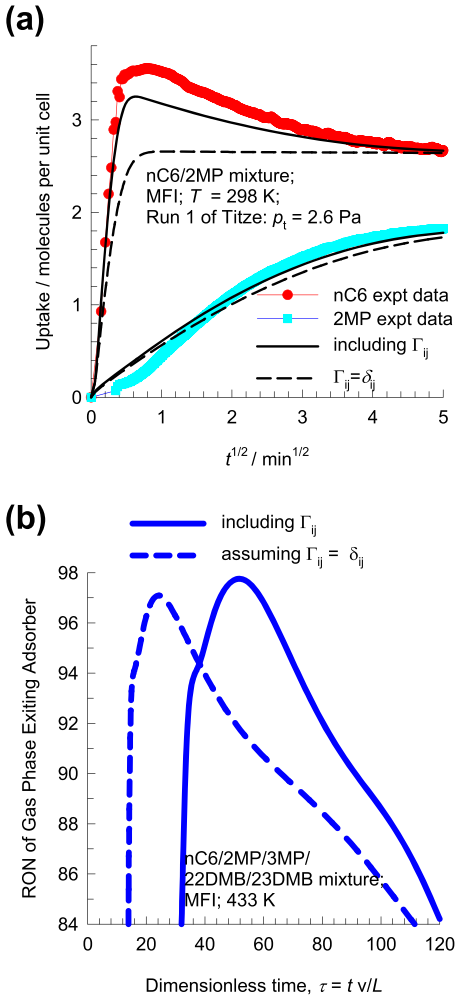

Figure 8. (a) Experimental data of Titze et al.[81] for the transient uptake of *n*C6/2MP mixtures in MFI zeolite at 298 K.[29] (b) RON of product gas mixture leaving fixed-bed adsorber packed with MFI operating at a total pressure of 100 kPa and 433 K; the feed is a 5-component *n*C6/2MP/3MP/22DMB/23DMB mixture with partial pressure of 20 kPa for each component. The continuous solid lines are simulations based on eq 7. The dashed lines are simulations based on eq 8. Further details and input data are provided in Chapter 10 of the Supporting Information, which also contains the rationale for ignoring correlation effects.

4. CONCLUSIONS

The major conclusion that emerges from our investigation of kinetic separations of five different mixtures is the need for proper modeling of the intracrystalline diffusion, which takes proper account of thermodynamic coupling influences.[51] The off-diagonal elements Γ_{ij} $(i \neq j)$ engender overshoots in the loading of the more mobile partner species during transient uptakes within a microporous particle. Such overshoots, signifying uphill diffusion, are beneficial, resulting in increasing productivity of the tardier component that is recovered in purified form as raffinate during the high-pressure adsorption cycle of PSA operations.

Although the inclusion of thermodynamic coupling influences for kinetic separations in adsorbers is properly recognized by Ruthven, Farooq, and others,[4,37,43,52,54,57,67] there are several other published works that adopt much simpler approaches employing eq 8;[28] the simulations presented in this article demonstrate that such simplified approaches may lead to severely pessimistic estimates of the effectiveness of kinetic separations.

Thermodynamic coupling effects should also be expected to have strong influences on the selectivity and conversion of diffusion-limited zeolite-catalyzed reactions carried in fixed-bed reactors;[78] this aspect deserves further investigation.

■ ASSOCIATED CONTENT

Supporting Information

The Supporting Information is available free of charge on the ACS Publications website at DOI: 10.1021/acsomega.8b03480.

Calculation procedure for mixture adsorption equilibrium, along with derivations of the mixed-gas Langmuir model, summary of the Maxwell−Stefan theory of diffusion in microporous materials, methodology adopted for numerical solutions to transient uptake within single crystalline particle, methodology used for transient breakthroughs in fixed-bed adsorbers, and simulation details and input data on unary isotherms, and Maxwell−Stefan diffusivities are provided for each of the five case studies (PDF)

■ AUTHOR INFORMATION

Corresponding Author

*E-mail: r.krishna@contact.uva.nl.

ORCID

Rajamani Krishna: 0000-0002-4784-8530

Notes

The author declares no competing financial interest.

■ ACKNOWLEDGMENTS

The simulation code for transient breakthroughs was developed by Dr Richard Baur and Dr Jasper van Baten; their assistance and help is gratefully acknowledged.

■ NOMENCLATURE

Latin Alphabet

b_i, Langmuir binding constant, Pa^{-1}
c_i, molar concentration of species i, mol m^{-3}
c_{i0}, molar concentration of species i in fluid mixture at inlet, mol m^{-3}
D_{ax}, axial dispersion coefficient, m^2 s^{-1}
$Đ_i$, Maxwell−Stefan diffusivity for molecule−wall interaction, m^2 s^{-1}
$Đ_{ij}$, M−S exchange coefficient for n-component mixture, m^2 s^{-1}
n, number of species in the mixture, dimensionless
L, length of packed-bed adsorber, m
N_i, molar flux of species i with respect to framework, mol m^{-2} s^{-1}
p_i, partial pressure of species i in mixture, Pa
p_t, total system pressure, Pa
q_i, component molar loading of species i, mol kg^{-1}
$q_{i,sat}$, molar loading of species i at saturation, mol kg^{-1}
q_t, total molar loading in mixture, mol kg^{-1}
$\overline{q}_i(t)$, spatial-averaged component uptake of species i, mol kg^{-1}
r, radial direction coordinate, m
r_c, radius of crystallite, m
R, gas constant, 8.314 J mol^{-1} K^{-1}

DOI: 10.1021/acsomega.8b03480
ACS Omega 2019, 4, 3409−3419

t,time, s
T,absolute temperature, K
v,interstitial gas velocity in packed bed, m s^{-1}
x_i,mole fraction of species i in adsorbed phase, dimensionless
z,distance along the adsorber, m

Greek Alphabet

Γ_{ij},thermodynamic factors, dimensionless
δ_{ij},Kronecker delta, dimensionless
ε,voidage of packed bed, dimensionless
μ_i,molar chemical potential, J mol^{-1}
ρ,framework density, kg m^{-3}
τ,time, dimensionless

REFERENCES

(1) Ruthven, D. M. *Principles of Adsorption and Adsorption Processes*; John Wiley: NY, 1984.
(2) Yang, R. T. *Gas Separation by Adsorption Processes*; Butterworth: Boston, 1987.
(3) Yang, R. T. *Adsorbents: Fundamentals and Applications*; John Wiley & Sons, Inc.: Hoboken, NJ, 2003.
(4) Ruthven, D. M.; Farooq, S.; Knaebel, K. S. *Pressure Swing Adsorption*; VCH Publishers: NY, 1994.
(5) Krishna, R. Methodologies for Screening and Selection of Crystalline Microporous Materials in Mixture Separations. *Sep. Purif. Technol.* **2018**, *194*, 281−300.
(6) Krishna, R. Screening Metal-Organic Frameworks for Mixture Separations in Fixed-Bed Adsorbers using a Combined Selectivity/Capacity Metric. *RSC Adv.* **2017**, *7*, 35724−35737.
(7) Krishna, R. Methodologies for Evaluation of Metal-Organic Frameworks in Separation Applications. *RSC Adv.* **2015**, *5*, 52269−52295.
(8) Krishna, R. Elucidation and Characterization of Entropy Effects in Mixture Separations with Micro-porous Crystalline Adsorbents. *Sep. Purif. Technol.* **2019**, *215*, 227−241.
(9) Krishna, R. A Maxwell-Stefan-Glueckauf Description of Transient Mixture Uptake in Microporous Adsorbents. *Sep. Purif. Technol.* **2018**, *191*, 392−399.
(10) Krishna, R.; van Baten, J. M. Investigating the potential of MgMOF-74 membranes for CO_2 capture. *J. Membr. Sci.* **2011**, *377*, 249−260.
(11) Lin, R.-B.; Li, L.; Zhou, H.-L.; Wu, H.; He, C.; Li, S.; Krishna, R.; Li, J.; Zhou, W.; Chen, B. Molecular Sieving of Ethylene from Ethane using a Rigid Metal-Organic Framework. *Nat. Mater.* **2018**, *17*, 1128−1133.
(12) Pimentel, B. R.; Lively, R. P. Propylene Enrichment via Kinetic Vacuum Pressure Swing Adsorption Using ZIF-8 Fiber Sorbents. *ACS Appl. Mater. Interfaces* **2018**, *10*, 36323−36331.
(13) Wang, Y.; Zhao, D. Beyond Equilibrium: Metal−Organic Frameworks for Molecular Sieving and Kinetic Gas Separation. *Cryst. Growth Des.* **2017**, *17*, 2291−2308.
(14) Sircar, S. Basic research needs for design of adsorptive gas separation processes. *Ind. Eng. Chem. Res.* **2006**, *45*, 5435−5448.
(15) Myers, A. L.; Prausnitz, J. M. Thermodynamics of Mixed Gas Adsorption. *AIChE J.* **1965**, *11*, 121−130.
(16) Krishna, R. Describing the Diffusion of Guest Molecules inside Porous Structures. *J. Phys. Chem. C* **2009**, *113*, 19756−19781.
(17) Krishna, R. Diffusion in Porous Crystalline Materials. *Chem. Soc. Rev.* **2012**, *41*, 3099−3118.
(18) Krishna, R. The Maxwell-Stefan Description of Mixture Diffusion in Nanoporous Crystalline Materials. *Microporous Mesoporous Mater.* **2014**, *185*, 30−50.
(19) Krishna, R. Occupancy Dependency of Maxwell−Stefan Diffusivities in Ordered Crystalline Microporous Materials. *ACS Omega* **2018**, *3*, 15743−15753.
(20) Krishna, R. Diffusing Uphill with James Clerk Maxwell and Josef Stefan. *Chem. Eng. Sci.* **2019**, *195*, 851−880.
(21) Krishna, R.; van Baten, J. M. Maxwell−Stefan modeling of slowing-down effects in mixed gas permeation across porous membranes. *J. Membr. Sci.* **2011**, *383*, 289−300.
(22) Krishna, R.; van Baten, J. M. Influence of Adsorption on the Diffusion Selectivity for Mixture Permeation across Mesoporous Membranes. *J. Membr. Sci.* **2011**, *369*, 545−549.
(23) Krishna, R.; van Baten, J. M. A molecular dynamics investigation of the diffusion characteristics of cavity-type zeolites with 8-ring windows. *Microporous Mesoporous Mater.* **2011**, *137*, 83−91.
(24) Krishna, R.; van Baten, J. M. Investigating the Influence of Diffusional Coupling on Mixture Permeation across Porous Membranes. *J. Membr. Sci.* **2013**, *430*, 113−128.
(25) Krishna, R. The Maxwell-Stefan Description of Mixture Permeation across Nanoporous Graphene Membranes. *Chem. Eng. Res. Des.* **2018**, *133*, 316−325.
(26) Krishna, R.; Baur, R. Modelling Issues in Zeolite Based Separation Processes. *Sep. Purif. Technol.* **2003**, *33*, 213−254.
(27) Krishna, R.; Li, S.; van Baten, J. M.; Falconer, J. L.; Noble, R. D. Investigation of slowing-down and speeding-up effects in binary mixture permeation across SAPO-34 and MFI membranes. *Sep. Purif. Technol.* **2008**, *60*, 230−236.
(28) Shafeeyan, M. S.; Daud, W. M. A. W.; Shamiri, A. A Review of Mathematical Modeling of Fixed-Bed Columns for Carbon dioxide Adsorption. *Chem. Eng. Res. Des.* **2014**, *92*, 961−988.
(29) Krishna, R. Tracing the Origins of Transient Overshoots for Binary Mixture Diffusion in Microporous Crystalline Materials. *Phys. Chem. Chem. Phys.* **2016**, *18*, 15482−15495.
(30) Krishna, R.; Long, J. R. Screening metal-organic frameworks by analysis of transient breakthrough of gas mixtures in a fixed bed adsorber. *J. Phys. Chem. C* **2011**, *115*, 12941−12950.
(31) Krishna, R. Uphill Diffusion in Multicomponent Mixtures. *Chem. Soc. Rev.* **2015**, *44*, 2812−2836.
(32) Chen, D.-L.; Shang, H.; Zhu, W.; Krishna, R. Transient Breakthroughs of CO_2/CH_4 and C_3H_6/C_3H_8 Mixtures in Fixed Beds packed with Ni-MOF-74. *Chem. Eng. Sci.* **2014**, *117*, 407−415.
(33) Chen, D.-L.; Wang, N.; Wang, F.-F.; Xie, J.; Zhong, Y.; Zhu, W.; Johnson, J. K.; Krishna, R. Utilizing Gate-Opening Mechanism in ZIF-7 for Adsorption Discrimination between N_2O and CO_2. *J. Phys. Chem. C* **2014**, *118*, 17831−17838.
(34) Chen, D.-L.; Wang, N.; Xu, C.; Tu, G.; Zhu, W.; Krishna, R. A combined theoretical and experimental analysis on transient breakthroughs of C2H6/C2H4 in fixed beds packed with ZIF-7. *Microporous Mesoporous Mater.* **2015**, *208*, 55−65.
(35) Jolimaître, E.; Ragil, K.; Tayakout-Fayolle, M.; Jallut, C. Separation of Mono- and Dibranched Hydrocarbons on Silicalite. *AIChE J.* **2002**, *48*, 1927−1937.
(36) Tagliabue, M.; Farrusseng, D.; Valencia, S.; Aguado, S.; Ravon, U.; Rizzo, C.; Corma, A.; Mirodatos, C. Natural gas treating by selective adsorption: Material science and chemical engineering interplay. *Chem. Eng. J.* **2009**, *155*, 553−566.
(37) Bhadra, S. J.; Farooq, S. Separation of Methane Nitrogen Mixture by Pressure Swing Adsorption for Natural Gas Upgrading. *Ind. Eng. Chem. Res.* **2011**, *50*, 14030−14045.
(38) Jayaraman, A.; Hernandez-Maldonado, A. J.; Yang, R. T.; Chinn, D.; Munson, C. L.; Mohr, D. H. Clinoptilolites for Nitrogen/Methane Separation. *Chem. Eng. Sci.* **2004**, *59*, 2407−2417.
(39) Habgood, H. W. The Kinetics of Molecular Sieve Action. Sorption of Nitrogen-Methane Mixtures by Linde Molecular Sieve 4A. *Can. J. Chem.* **1958**, *36*, 1384−1397.
(40) Krishna, R. Diffusing Uphill with James Clerk Maxwell and Josef Stefan. *Curr. Opin. Chem. Eng.* **2016**, *12*, 106−119.
(41) Krishna, R.; Van Baten, J. M. Investigating the Non-idealities in Adsorption of CO_2-bearing Mixtures in Cation-exchanged Zeolites. *Sep. Purif. Technol.* **2018**, *206*, 208−217.
(42) Krishna, R.; van Baten, J. M. Using Molecular Dynamics Simulations for Elucidation of Molecular Traffic in Ordered Crystalline Microporous Materials. *Microporous Mesoporous Mater.* **2018**, *258*, 151−169.

DOI: 10.1021/acsomega.8b03480
ACS Omega 2019, 4, 3409−3419

(43) Majumdar, B.; Bhadra, S. J.; Marathe, R. P.; Farooq, S. Adsorption and Diffusion of Methane and Nitrogen in Barium Exchanged ETS-4. *Ind. Eng. Chem. Res.* **2011**, *50*, 3021−3034.
(44) Lastari, F.; Pareek, V.; Trebble, M.; Tade, M. O.; Chinn, D.; Tsai, N. C.; Chan, K. I. Extractive Distillation for CO_2−Ethane Azeotrope Separation. *Chem. Eng. Process.* **2012**, *52*, 155−161.
(45) Ribeiro, C. P.; Freeman, B. D.; Paul, D. R. Pure- and Mixed-Gas Carbon Dioxide/Ethane Permeability and Diffusivity in a Cross-linked Poly(ethylene oxide) Copolymer. *J. Membr. Sci.* **2011**, *377*, 110−123.
(46) Krishna, R. Describing Mixture Permeation across Polymeric Membranes by a Combination of Maxwell-Stefan and Flory-Huggins Models. *Polymer* **2016**, *103*, 124−131.
(47) Krishna, R. Using the Maxwell-Stefan formulation for Highlighting the Influence of Interspecies (1−2) Friction on Binary Mixture Permeation across Microporous and Polymeric Membranes. *J. Membr. Sci.* **2017**, *540*, 261−276.
(48) Binder, T.; Lauerer, A.; Chmelik, C.; Haase, J.; Kärger, J.; Ruthven, D. M. Micro-imaging of transient intracrystalline concentration profiles during 2-component uptake of light hydrocarbon - carbon dioxide mixtures by DDR-type zeolites. *Ind. Eng. Chem. Res.* **2015**, *54*, 8997−9004.
(49) Lauerer, A.; Binder, T.; Chmelik, C.; Miersemann, E.; Haase, J.; Ruthven, D. M.; Kärger, J. Uphill Diffusion and Overshooting in the Adsorption of Binary Mixtures in Nanoporous Solids. *Nat. Commun.* **2015**, *6*, No. 7697.
(50) Krishna, R.; van Baten, J. M.; Baur, R. Highlighting the Origins and Consequences of Thermodynamic Nonidealities in Mixture Separations using Zeolites and Metal-Organic Frameworks. *Microporous Mesoporous Mater.* **2018**, *267*, 274−292.
(51) Krishna, R.; van Baten, J. M. Influence of Adsorption Thermodynamics on Guest Diffusivities in Nanoporous Crystalline Materials. *Phys. Chem. Chem. Phys.* **2013**, *15*, 7994−8016.
(52) Ruthven, D. M.; Farooq, S. Air Separation by Pressure Swing Adsorption. *Gas Sep. Purif.* **1990**, *4*, 141−148.
(53) Farooq, S.; Rathor, M. N.; Hidajat, K. A Predictive Model for a Kinetically Controlled Pressure Swing Adsorption Separation Process. *Chem. Eng. Sci.* **1993**, *48*, 4129−4141.
(54) Farooq, S. Sorption and Diffusion of Oxygen and Nitrogen in Molecular- Sieve RS-10. *Gas Sep. Purif.* **1995**, *9*, 205−212.
(55) Chen, Y. D.; Yang, R. T.; Uawithya, P. Diffusion of oxygen, nitrogen and their mixtures in Carbon Molecular-Sieve. *AIChE J.* **1994**, *40*, 577−585.
(56) Sircar, S.; Myers, A. L. Gas Separation by Zeolites. In *Handbook of Zeolite Science and Technology*; Auerbach, S. M., Carrado, K. A., Dutta, P. K., Eds.; Marcel Dekker: NY, 2003; Chapter 22.
(57) Khalighi, M.; Chen, Y. F.; Farooq, S.; Karimi, I. A.; Jiang, J. W. Propylene/Propane Separation Using SiCHA. *Ind. Eng. Chem. Res.* **2013**, *52*, 3877−3892.
(58) Krishna, R. A Smörgåsbord of Separation Strategies using Microporous Crystalline Materials. *Indian Chem. Eng.* **2014**, *56*, 147−174.
(59) Da Silva, F. A.; Rodrigues, A. E. Vacuum swing adsorption for propylene/propane separation with 4A zeolite. *Ind. Eng. Chem. Res.* **2001**, *40*, 5758−5774.
(60) Grande, C. A.; Poplow, F.; Rodrigues, A. E. Vacuum pressure swing adsorption to produce polymer-grade polypropylene. *Sep. Sci. Technol.* **2010**, *45*, 1252−1259.
(61) Da Silva, F. A.; Rodrigues, A. E. Propylene Propane Separation by Vacuum Swing Adsorption Using 13X Zeolite. *AIChE J.* **2001**, *47*, 341−357.
(62) Bloch, E. D.; Murray, L.; Queen, W. L.; Chavan, S. M.; Maximoff, S. N.; Bigi, J. P.; Krishna, R.; Peterson, V. K.; Grandjean, F.; Long, G. J.; Smit, B.; Bordiga, S.; Brown, C. M.; Long, J. R. Selective Binding of O_2 over N_2 in a Redox-Active Metal-Organic Framework with Open Iron(II) Coordination Sites. *J. Am. Chem. Soc.* **2011**, *133*, 14814−14822.
(63) Bloch, E. D.; Queen, W. L.; Krishna, R.; Zadrozny, J. M.; Brown, C. M.; Long, J. R. Hydrocarbon Separations in a Metal-Organic Framework with Open Iron(II) Coordination Sites. *Science* **2012**, *335*, 1606−1610.
(64) Geier, S. J.; Mason, J. A.; Bloch, E. D.; Queen, W. L.; Hudson, M. R.; Brown, C. M.; Long, J. R. Selective adsorption of ethylene over ethane and propylene over propane in the metal−organic frameworks M_2(dobdc) (M = Mg, Mn, Fe, Co, Ni, Zn). *Chem. Sci.* **2013**, *4*, 2054−2061.
(65) Böhme, U.; Barth, B.; Paula, C.; Kuhnt, A.; Schwieger, W.; Mundstock, A.; Caro, J.; Hartmann, M. Ethene/Ethane and Propene/Propane Separation via the Olefin and Paraffin Selective Metal−Organic Framework Adsorbents CPO-27 and ZIF-8. *Langmuir* **2013**, *29*, 8592−8600.
(66) Yoon, J. W.; Jang, I. T.; Lee, K.-Y.; Hwang, Y. K.; Chang, J.-S. Adsorptive Separation of Propylene and Propane on a Porous Metal-Organic Framework, Copper Trimesate. *Bull. Korean Chem. Soc.* **2010**, *31*, 220−223.
(67) Khalighi, M.; Karimi, I. A.; Farooq, S. Comparing SiCHA and 4A Zeolite for Propylene/Propane Separation using a Surrogate-Based Simulation/Optimization Approach. *Ind. Eng. Chem. Res.* **2014**, *53*, 16973−16983.
(68) Chng, M. L.; Xiao, Y.; Chung, T.-S.; Toriida, M.; Tamai, S. Enhanced propylene/propane separation by carbonaceous membrane derived from poly (aryl ether ketone)/2,6-bis(4-azidobenzylidene)-4-methyl-cyclohexanone interpenetrating network. *Carbon* **2009**, *47*, 1857−1866.
(69) Olson, D. H.; Camblor, M. A.; Vallaescusa, L. A.; Kuehl, G. H. Light hydrocarbon sorption properties of pure silica Si-CHA and ITQ-3 and high silica ZSM-58. *Microporous Mesoporous Mater.* **2004**, *67*, 27−33.
(70) Hedin, N.; DeMartin, G. J.; Roth, W. J.; Strohmaier, K. G.; Reyes, S. C. PFG NMR self-diffusion of small hydrocarbons in high silica DDR, CHA and LTA structures. *Microporous Mesoporous Mater.* **2008**, *109*, 327−334.
(71) Ruthven, D. M.; Reyes, S. C. Adsorptive separation of light olefins from paraffins. *Microporous Mesoporous Mater.* **2007**, *104*, 59−66.
(72) Cadiau, A.; Adil, K.; Bhatt, P. M.; Belmabkhout, Y.; Eddaoudi, M. A Metal-Organic Framework−Based Splitter for Separating Propylene from Propane. *Science* **2016**, *353*, 137−140.
(73) Cui, X.; Chen, K.; Xing, H.; Yang, Q.; Krishna, R.; Bao, Z.; Wu, H.; Zhou, W.; Dong, X.; Han, Y.; Li, B.; Ren, Q.; Zaworotko, M. J.; Chen, B. Pore Chemistry and Size Control in Hybrid Porous Materials for Acetylene Capture from Ethylene. *Science* **2016**, *353*, 141−144.
(74) Krishna, R.; van Baten, J. M. Screening of zeolite adsorbents for separation of hexane isomers: A molecular simulation study. *Sep. Purif. Technol.* **2007**, *55*, 246−255.
(75) Dubbeldam, D.; Krishna, R.; Calero, S.; Yazaydın, A. Ö. Computer-Assisted Screening of Ordered Crystalline Nanoporous Adsorbents for Separation of Alkane Isomers. *Angew. Chem., Int. Ed.* **2012**, *51*, 11867−11871.
(76) Herm, Z. R.; Wiers, B. M.; Van Baten, J. M.; Hudson, M. R.; Zajdel, P.; Brown, C. M.; Maschiocchi, N.; Krishna, R.; Long, J. R.; et al. Separation of Hexane Isomers in a Metal-Organic Framework with Triangular Channels. *Science* **2013**, *340*, 960−964.
(77) Krishna, R.; Smit, B.; Vlugt, T. J. H. Sorption-induced Diffusion-selective Separation of Hydrocarbon Isomers Using Silicalite. *J. Phys. Chem. A* **1998**, *102*, 7727−7730.
(78) Krishna, R.; Baur, R.; Van Baten, J. M. Highlighting Diffusional Coupling Effects in Zeolite Catalyzed Reactions by Combining the Maxwell-Stefan and Langmuir-Hinshelwood Formulations. *React. Chem. Eng.* **2017**, *2*, 324−336.
(79) Krishna, R.; van Baten, J. M. Commensurate-Incommensurate Adsorption and Diffusion in Ordered Crystalline Microporous Materials. *Phys. Chem. Chem. Phys.* **2017**, *19*, 20320−20337.
(80) Vlugt, T. J. H.; Krishna, R.; Smit, B. Molecular Simulations of Adsorption Isotherms for Linear and Branched Alkanes and Their Mixtures in Silicalite. *J. Phys. Chem. B* **1999**, *103*, 1102−1118.

DOI: 10.1021/acsomega.8b03480
ACS Omega 2019, 4, 3409−3419

(81) Titze, T.; Chmelik, C.; Kärger, J.; van Baten, J. M.; Krishna, R. Uncommon Synergy Between Adsorption and Diffusion of Hexane Isomer Mixtures in MFI Zeolite Induced by Configurational Entropy Effects. *J. Phys. Chem. C* **2014**, *118*, 2660−2665.

DOI: 10.1021/acsomega.8b03480
ACS Omega 2019, 4, 3409−3419

Highlighting the Influence of Thermodynamic Coupling on Kinetic Separations with Microporous Crystalline Materials

Rajamani Krishna

Van 't Hoff Institute for Molecular Sciences

University of Amsterdam

Science Park 904

1098 XH Amsterdam, The Netherlands

email: r.krishna@contact.uva.nl

Table of Contents

1 Preamble

This Supporting Information accompanying the article *Highlighting the Influence of Thermodynamic Coupling on Kinetic Separations with Microporous Crystalline MaterialsAdsorbers* provides:

(a) Brief review of adsorption fundamentals

(b) Brief summary of the Ideal Adsorbed Solution theory for calculation of mixture adsorption equilibrium, along with derivations of the mixed-gas Langmuir model

(c) Brief summary of the Maxwell-Stefan theory of diffusion in microporous materials

(d) Methodology adopted for numerical solutions to transient uptake within single crystalline particle

(e) Methodology used for transient breakthroughs in fixed bed adsorbers, incorporating the Maxwell-Stefan description of intra-particle diffusion

(f) Five different case studies illustrating kinetic separations of CO_2/C_2H_6, N_2/CH_4, O_2/N_2, C_3H_6/C_3H_8, and hexane isomer mixtures. Simulation details and input data on pure component isotherms, and Maxwell-Stefan diffusivities are provided for each of the five case studies.

For ease of reading, the Supplementary Material is written as a stand-alone document.

2 “Equilibrium” vs “Kinetic” Separations

Separation technologies such as distillation, absorption, and extraction are energy intensive because of vapor/liquid phase transformations in condensers, reboilers and solvent recovery sections. The energy consumption for distillation accounts for about 50% of the total energy consumption for all separations.[1] The largest opportunities for energy reduction are offered by replacing distillation with (a) low-energy demanding separation systems such as adsorption or membranes, or (b) hybrid systems that combine distillation with adsorption or membranes.[1] In many cases, the hybrid processing option is easier to implement technically because adsorption and membrane separations often cannot produce products with the purity levels that are achievable with distillation. The success of such replacement strategies is crucially dependent on development of suitable porous materials that can be used in fixed bed adsorption devices or as thin layers in membrane permeation units.

Basically, there are two broad strategies for separations in fixed bed adsorption devices and membrane units:

(a) “Equilibrium Separations” that rely on selectivities dictated by mixture adsorption equilibrium, and

(b) “Kinetic Separations” that are rely on differences in the rates of diffusion of guest molecules within the framework of the microporous materials.

Even for “Equilibrium Separations”, diffusional influences may alter the separation performance, often leading to diminished separation effectiveness. For “Kinetic Separations”, the mixture adsorption equilibrium often lowers the separation performance. For the proper understanding, and modelling of separations in fixed bed adsorption devices and membrane units it is important to have an understanding of both mixture adsorption equilibrium and intra-particle diffusion.

We first summarize the various factors that govern the adsorption strength of a guest molecule; the treatment essentially follows that of Yang,[2] and Ruthven.[3]

2.1 Potential energies for adsorption

The total potential between the adsorbate molecules and the adsorbent is the sum of the adsorbate-adsorbate and adsorbate-adsorbent interaction potentials. Let us focus on the factors that govern the adsorbate-adsorbent interaction potential, ϕ. If we ignore π-complexation and chemical bonding,[2] the two contributions to the adsorbate-adsorbent interaction potential, ϕ, are dispersion interactions and electrostatic interactions. The adsorbate-adsorbent interaction potential, ϕ, is the sum of various contributions

$$\phi = \phi_D + \phi_R + \phi_{Ind} + \phi_{F\mu} + \phi_{\dot{F}Q} \tag{S-1}$$

In Equation (S-1):

$\phi_D = -\frac{A}{r^6}$ = dispersion energy

$\phi_R = \frac{B}{r^{12}}$ = close-range repulsion energy

where r is the distance between the centres of the interacting pairs of atoms/molecules

ϕ_{Ind} = induction energy (interaction between electric field and an induced dipole)

$\phi_{F\mu}$ = interaction between an electric field F and a permanent dipole μ

$\phi_{\dot{F}Q}$ = interaction between an electric field gradient $\dot{F}$ and a quadrupole (with quadrupole moment Q)

The dispersion and repulsion interactions form the Lennard-Jones potential

$$\phi_D + \phi_R = 4\varepsilon\left(\left(\frac{\sigma}{r}\right)^{12} - \left(\frac{\sigma}{r}\right)^{6}\right) \tag{S-2}$$

At the equilibrium distance r_0 we have $\phi_D + \phi_R = 0$; $\frac{d\phi}{dr} = 0$ and $B = -\frac{Ar_0^6}{2}$.

The most commonly used expression for calculating A is the Kirkwood-Müller formula for interaction between atoms and molecules (denoted by subscripts i and j)

$$A = \frac{6mc^2\alpha_i\alpha_j}{\frac{\alpha_i}{\chi_i}+\frac{\alpha_j}{\chi_j}} \tag{S-3}$$

The potential for interaction between electric field and an induced dipole is

$$\phi_{Ind} = -\frac{1}{2}\alpha F^2 = -\frac{1}{2}\alpha\frac{q^2}{r^4(4\pi\varepsilon_0)^2} \tag{S-4}$$

The potential for interaction between electric field F (of an ion) and point dipole is

$$\phi_{F\mu} = -\mu F\cos\theta = -\mu\frac{q}{r^2(4\pi\varepsilon_0)}\cos\theta \tag{S-5}$$

The potential for interaction between electric field gradient $\dot{F}$ and linear point quadrupole is

$$\phi_{\dot{F}Q} = \frac{1}{2}Q\dot{F} = -\frac{1}{2}Q\frac{q}{2r^3(4\pi\varepsilon_0)}(3\cos^2\theta - 1) \tag{S-6}$$

where

m = mass of electron

c = speed of light

α = polarizability

χ = magnetic susceptibility

α = polarizability

F = electric field

q = electronic charge of ion on surface

ε_0 = permittivity of a vacuum

μ = permanent dipole moment

θ = angle between the direction of the field or field gradient and the axis of the dipole or linear quadrupole

Q = linear quadrupole moment (+ or -)

r = distance between the centers of the interacting pairs

For a given sorbent, the sorbate-sorbent interaction potential depends on the properties of the sorbate. Among the five different types of interactions, the first two contributions $\phi_D + \phi_R$ are non-specific, which are operative in all sorbate-sorbent systems; the non-specific interactions $\phi_D + \phi_R$ are nonelectrostatic. The London – van der Waals dispersion interaction energies are largely dictated by the polarizabilities of the guest molecules and surfaces atoms of the adsorbent materials; see schematics in Figure S-16, and Figure S-2. The polarizabilities of a wide variety of guest molecules are tabulated by Sircar and Myers.[4] Broadly speaking, the polarizabilites of molecules increase with increasing molar masses, as illustrated for noble gases He, Ne, Ar, Kr, and Xe in Figure S-2, and for homologous series of hydrocarbons in Figure S-3(a,b). The value of α generally increases with the molecular weight because more electrons are available for polarization.

The last three contributions $\phi_{Ind} + \phi_{F\mu} + \phi_{FQ}$ arise from charges (which create electric fields) on the solid surface. For activated carbon, the non-specific interactions dominate. On a surface without charges, such as graphite, ϕ_{Ind} = 0. For metal oxides, zeolites, and ionic solids, the electrostatic interactions often dominate, depending on the adsorbate. For adsorbate with a quadrupole, the net interaction between a uniform field and the quadrupole is zero. However, the quadrupole interacts strongly with the field gradient, thus the term ϕ_{FQ}.

Figure S-4(a,b) compare the polarizabilities, dipole moments, and quadrupole moments of H_2, Ar, O_2, N_2, CO, CH_4, and CO_2. Of these sorbates, only CO has a permanent dipole moment. The four guest sorbates O_2, N_2, CO, and CO_2 all possess finite quadrupole moments, with the hierarchy of magnitudes $O_2 < N_2 < CO < CO_2$. Interestingly, the polarizability of CH_4 is higher than that of CO, but does not possess either dipole or significant quadrupole moments. Therefore, in a non-charged adsorbent such as

activated the adsorption strength of CH_4 is higher than that of CO. However, in cation-exchanged zeolites, CO may have a higher adsorption strength than CH_4.

We also note that each of the three electrostatic contributions $\phi_{Ind}, \phi_{F\mu}, \phi_{FQ}$ are proportion to the ionic charges of the sorbent, q: $\phi_{Ind} \propto \alpha \frac{q^2}{r^4}$; $\phi_{F\mu} \propto \mu \frac{q}{r^2}$; $\phi_{FQ} \propto Q \frac{q}{r^3}$ Therefore Ca^{++} should be yield stronger interaction potential that Na^+, with say CO_2, on the basis of this consideration; note that these two cations have nearly the same ionic radius; see Figure S-5. The electrostatic contributions are also inversely proportional to a power of the distance between the centers of the interacting pairs: $\phi_{Ind} \propto \alpha \frac{q^2}{r^4}$; $\phi_{F\mu} \propto \mu \frac{q}{r^2}$; $\phi_{FQ} \propto Q \frac{q}{r^3}$, we should expect the interaction potentials to be larger for Li^+ than for Na^+, because of the significantly smaller ionic radius of Li^+. This explains, albeit qualitatively, why LiLSX is the favored sorbent for selective adsorption of N_2 for O_2/N_2 mixtures.[2]

2.2 H_2 purification using Activated Carbon and LTA-5A zeolite

As illustration of the various contributions to the sorbate-sorbent interaction potential, let us consider the technologically important problem of production of purified H_2 from a feed containing $H_2/N_2/CO/CH_4/CO_2$ mixtures. In industrial practice, the production of purified H_2 is carried out using the Skarstrom, or modified Skarstrom PSA cycle. There are multiple steps, or stages, involved in the operation of each of the beds in the Skarstrom cycle; see schematic in Figure S-6.[2, 3, 5]

In the simplest case, the four steps in the sequence are as follows. [2, 3, 5]

(a) Pressurization (with feed or raffinate product)

(b) High pressure adsorption separation with feed, with withdrawal of purified raffinate

(c) Depressurization, or "blowdown", co-current or counter-current to the feed

(d) Desorption at the lower operating pressure. This is accomplished by evacuation or purging the bed with (a portion) of the purified raffinate product

In the following, we consider step (b) of the above scheme using two different adsorbent materials, Activated Carbon and LTA-5A zeolite.

"Equilibrium" vs "Kinetic" Separations

Figure S-7(a) presents data on the polarizabilities of variety of gaseous molecules, such as H_2, N_2, CO, CH_4, and CO_2, encountered in hydrogen purification processes. The unary isotherm data of these guest molecules in activated carbon (AC) are shown in Figure S-7(b). The binding strengths of these guest molecules follow the hierarchy $H_2 < N_2 < CO < CH_4 < CO_2$. Since the activated carbon has no surface functionalities or surface charges, the hierarchy of binding strengths should be dictated by the corresponding polarizabilities. This is indeed the case, as evidenced by the comparison of Figure S-7(a,b).

Figure S-8 shows the transient breakthrough of 73/4/3/4/16 $H_2/N_2/CO/CH_4/CO_2$ mixture, typical of steam methane reformer off-gas, in fixed bed adsorber packed with activated carbon, operating at 2 MPa total pressure and $T = 313$ K. The hierarchy of breakthrough times $H_2 < N_2 < CO < CH_4 < CO_2$ follows the hierarchy of binding strengths. If the production of say 99.95% pure H_2 is desired, then the productivity of 99.95%+ pure H_2 will be dictated by the difference of the breakthrough times of H_2 and N_2. Choosing an adsorbent with stronger binding of N_2 would result in a higher productivity of 99.95%+ pure H_2.

One strategy to increase the binding strength of N_2 with respect to that of H_2 is to use say LTA-5A zeolite (also called 5A or NaCaA zeolite; contains 96Si, 96 Al, 32 Na^+, 32 Ca^{++} per unit cell; Si/Al=1) as adsorbent; the structural details are provided in Figure S-9. The extra-framework cations Na^+, and Ca^{++} cause electrostatic interactions with the guest molecules, enhancing the binding strengths significantly over that dictated by London – van der Waals interactions. The strength of these electro-static interactions depend on the dipole moments and quadrupole moments of the guest molecules.

Figure S-10(a) shows the unary adsorption isotherms of H_2, N_2, CO, CH_4, and CO_2 in LTA-5A at 313 K. The binding strengths of these guest molecules follow the hierarchy $H_2 < N_2 < CH_4 < CO < CO_2$. In comparison with activated carbon (cf. Figure S-7(b)) it is noteworthy that CO has a stronger binding strength than CH_4 in LTA-5A. The polarizability of CH_4 is higher than that of CO, but does not possess either dipole or significant quadrupole moments. Therefore, in a non-charged adsorbent such as

activated the adsorption strength of CH_4 is higher than that of CO. However, in LTA-5A, CO has a higher adsorption strength than CH_4 due to the significant contribution of $\phi_{F\mu} \propto \mu \frac{q}{r^2}$.

Figure S-10(b) shows the transient breakthrough of 73/4/3/4/16 $H_2/N_2/CO/CH_4/CO_2$ mixture in fixed bed adsorber packed with LTA-5A, operating at 2 MPa total pressure and T = 313 K. The hierarchy of breakthrough times $H_2 < N_2 < CH_4 < CO < CO_2$ follows the hierarchy of binding strengths.

The unary isotherms of N_2 in activated carbon and LTA-5A zeolite are compared in Figure S-11(a). The stronger binding of N_2 in LTA-5A caused due to the contribution of the quadrupole moment of N_2: $\phi_{FQ} \propto Q \frac{q}{r^3}$. Consequently, the breakthrough of N_2 occurs significantly later with LTA-5A, as compared to activated carbon; compare Figure S-8 and Figure S-10(b). Due to the later breakthrough of N_2 in LTA-5A, the productivity of pure H_2 in a fixed bed adsorber (containing the same volume of activated carbon or LTA-5A) is higher with LTA-5A; see the comparison of H_2 breakthroughs in Figure S-11(b).

Due to the large quadrupole moment of CO_2, the significantly large contribution of $\phi_{FQ} \propto Q \frac{q}{r^3}$ causes the loading of CO_2 in LTA-5A to be significantly higher than that of activated carbon; see Figure S-12. . The strong binding of CO_2 in LTA-5A is disadvantageous because deep vacuum will be required to reduce the CO_2 loading to the desired level during the purge step (d) in Figure S-6. Consequently, despite the superior separation performance of LTA-5A, resulting in higher productivity of pure H_2 per L of adsorbent, LTA-5A is not used on its own in the PSA schemes. Industrial practice is to use multi-layered beds (see Figure S-12), consisting of:

(a) activated alumina, or silica gel, to remove water from the feed mixtures

(b) activated carbon layer, that has the function of adsorbing most of the CO_2 present in the feed mixture

(c) LTA-5A layer, whose function is to remove the remainder of the impurities N_2, CO, CH_4 in order to meet with the desired H_2 product purity, typically 99.95%+.

2.3 O_2/N_2 separations

Equilibrium separations, such as illustrated above for H_2 purification, are particularly successful because the desired purified product is recovered as raffinate during the adsorption step (b) of the scheme in Figure S-6. The same PSA scheme may be applied to production of purified O_2 by selective adsorption of N_2 for O_2/N_2 mixtures using LiX, or LiLSX as adsorbent.[2] Due to the larger quadrupole moment of N_2, its interaction potential with cation-exchanged zeolites is stronger than for O_2. For production of purified N_2, required in a variety of applications,[5, 6] a practical and viable approach to producing purified N_2 as raffinate is to resort to "kinetic separations", as explained in detail in Chapter 8. A further advantage of selective adsorption of O_2, rather than N_2, is that only 21% of feed mixture needs to be adsorbed, rather than 79%; this results in energy savings in the desorption step.

2.4 N_2/CH_4 separations

Natural gas reserves may contain up to 20% N_2, that needs to be reduced to below 4% to meet pipeline specifications. It is desirable to choose adsorbents in pressure swing adsorption (PSA) units that are selective to N_2 so that CH_4 can be recovered in 96%+ purity from the raffinate phase leaving the adsorption phase of the PSA cycle. For most known adsorbents, the adsorption selectivity for separation of N_2/CH_4 mixtures is in favor of CH_4 due to its higher polarizability; see Figure S-4(a,b). The notable exception is MIL-100(Cr), activated at 523 K, that shows adsorption selectivity in favor of N_2,[7] due to the interaction of the field gradients in MIL-100(Cr) and the quadrupole moment of N_2. However, as we shall show in Chapter 6, the N_2/CH_4 selectivity of MIL-100(Cr) is low, and a significant amount of CH_4 is adsorbed. Consequently, the recovery of purified CH_4 is expected to be unacceptably low.

The practical solution to the problem of N_2/CH_4 mixture separations is to exploit kinetic selectivities, as will be discussed in Chapter 6.

2.5 C_2H_4/C_2H_6 and C_3H_6/C_3H_8 separations

Ethene is an important chemical used as feedstock in manufacture of polymers such as polyethene, polyvinyl chloride, polyester, polystyrene as well as other organic chemicals. Propene is an important

chemical used as feedstock in manufacture of polymers such as polypropene. Key processing steps in preparing feedstocks for polymer production are the separations of ethene/ethane, and propene/propane mixtures. The boiling points are below ambient temperatures: ethane (184.5 K), ethene (169.4 K), propane (231.3 K), propene (226 K). Due to the small differences in the boiling points, the separations of ethene/ethane, and propene/propane mixtures have low relative volatilities, in the range of 1.1 – 1.2. These separations are traditionally carried out by distillation columns that operate at high pressures and low temperatures. The purity requirement of the alkenes as feedstocks to polymerization reactors is 99.95%, and consequently the distillation columns are some of the largest and tallest distillation columns used in the petrochemical industries with about 150 - 200 trays, and operating at reflux ratios of about 15. Distillation is energy intensive, and adsorptive separations offer an attractive, energy-efficient, alternative.

Figure S-13(a,b,c) presents data on the polarizabilities, dipole moments, and quadrupole moments of C_2H_4, C_2H_6, C_3H_6, and C_3H_8. C_3H_8 has a significantly large dipole moment. Each of the unsaturated alkenes C_2H_4, and C_3H_8 possesses a pi-bond (see Figure S-14 and Figure S-15), and the preferential adsorption of the alkene from the corresponding alkane with the same number of C atoms can be achieved by choosing zeolitic adsorbents with extra-framework cations, or MOFs with unsaturated "open" metal sites.[8] All of the atoms of C_2H_4 lie on the same plane (see Figure S-14), and its dipole moment is zero; however it does possess a quadrupole moment.

Several nmicroporous crystalline materials have potential for separation of ethene/ethane and propene/propane mixtures.[8, 9] Most of these adsorb the unsaturated alkene preferentially due to the strong electrostatic interactions with extra-framework cations in zeolites and unsaturated metal atoms in MOFs. Therefore, the purified alkene can only be recovered as extract during vacuum desorption.

The subtle differences in the molecular dimensions, bond lengths, and bond angles (see Figure S-14 and Figure S-15) can be exploited to device kinetic separations; these are discussed in Chapter 9.

2.6 List of Figures for “Equilibrium” vs “Kinetic” Separations

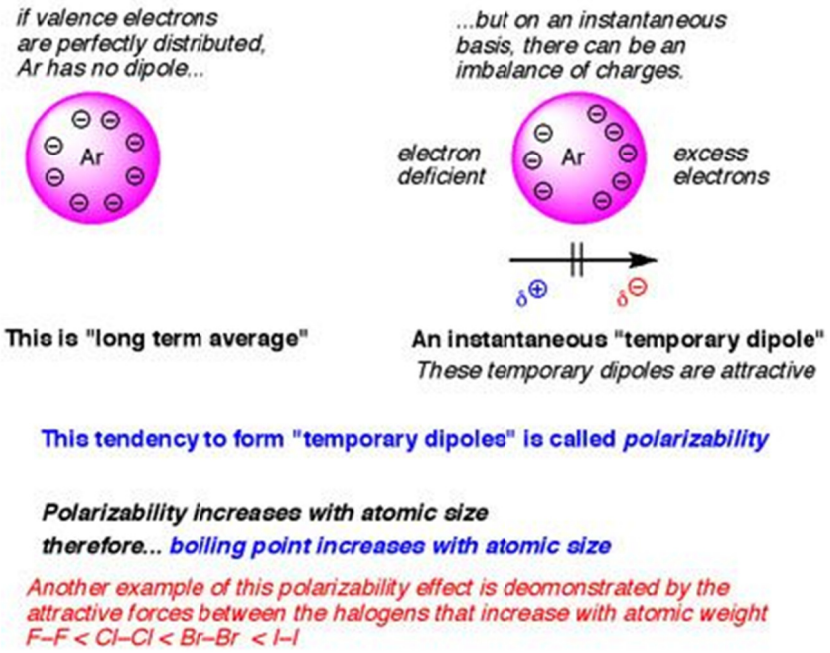

Figure S-1. Schematic of London – van der Waals dispersion interactions.

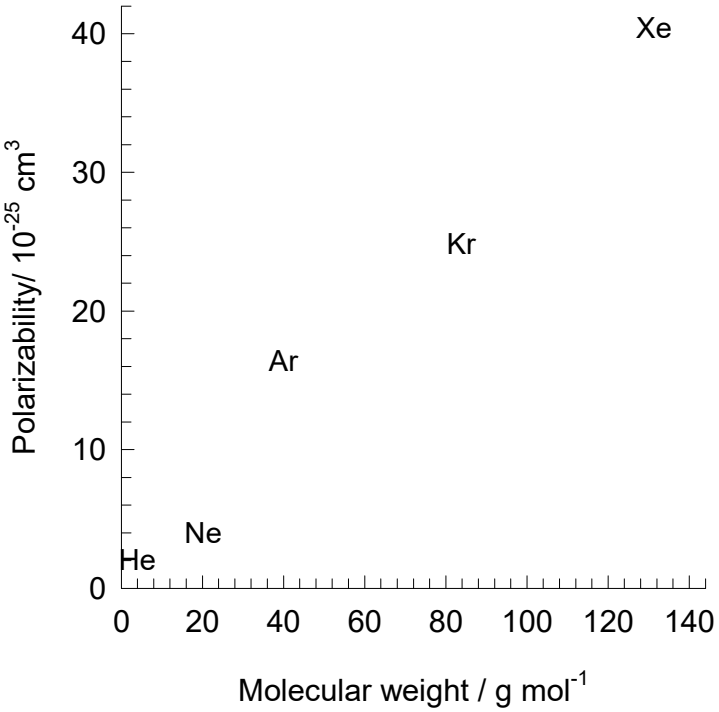

Figure S-2. Polarizabilities of noble gases. The data on polarizabilities are taken from Sircar and Myers.[4]

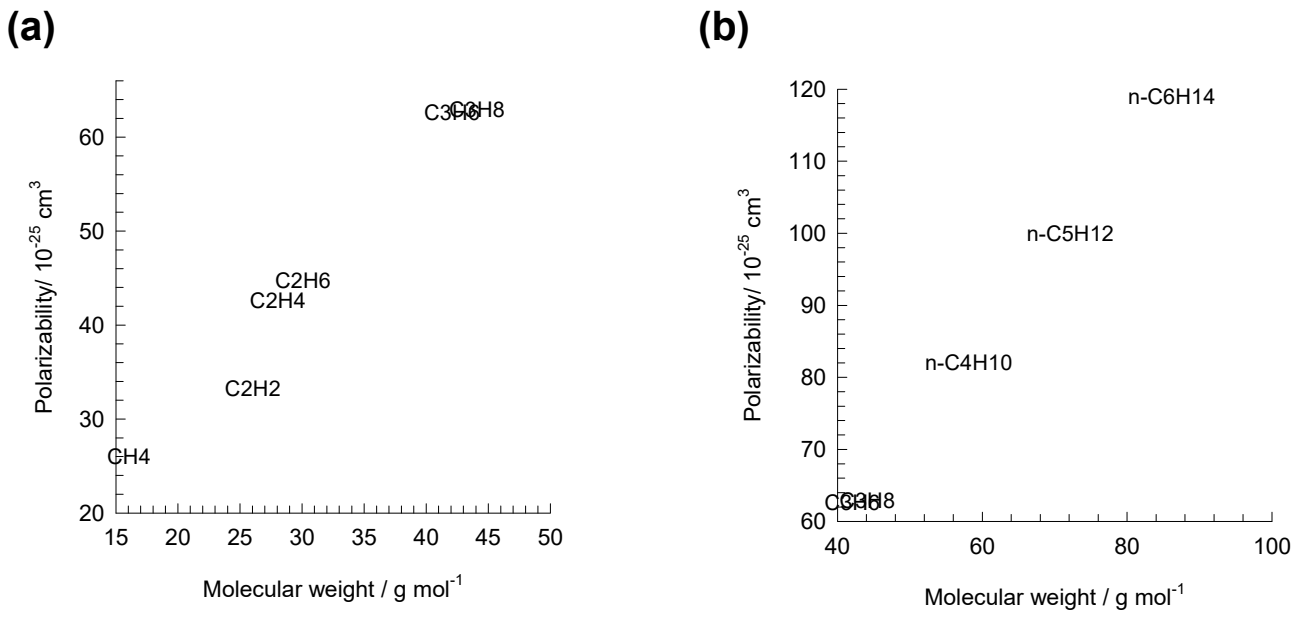

Figure S-3. Polarizabilities of hydrocarbons, The data on polarizabilities are taken from Sircar and Myers.[4]

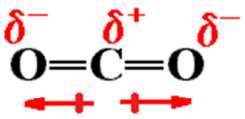

No net dipole moment; strong quadrupole

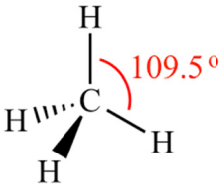

No dipole moment; negligible quadrupole

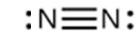

One σ bond
Two π bonds

No net dipole moment; finite quadrupole

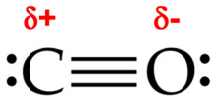

net dipole moment; finite quadrupole, lower than for CO_2

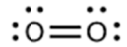

One σ bond
One π bond

No net dipole moment; finite quadrupole, smaller than for N_2

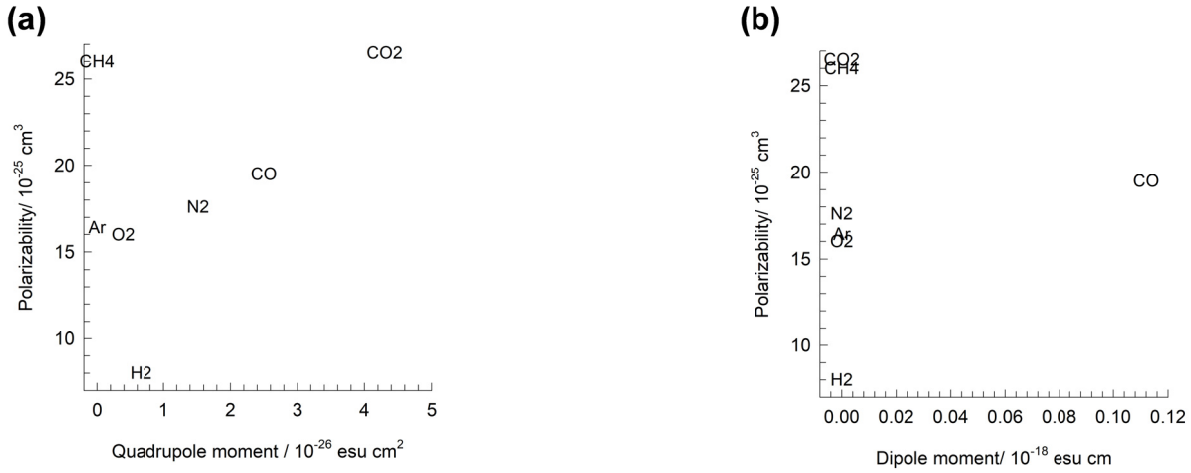

Figure S-4. (a, b) Polarizabilities, dipole moments, and quadrupole moments of H_2, Ar, N_2, O_2, CO, CH_4, and CO_2. The data are taken from Sircar and Myers.[4]

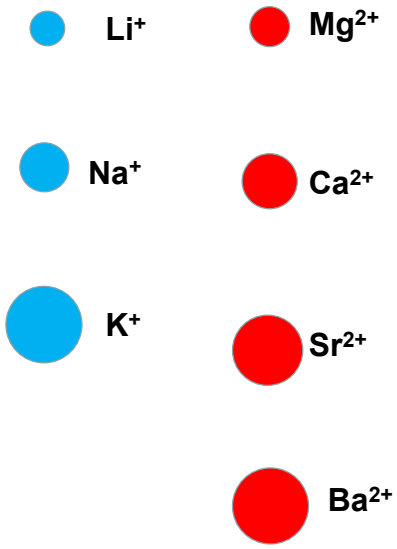

Figure S-5. Relative sizes of cations.

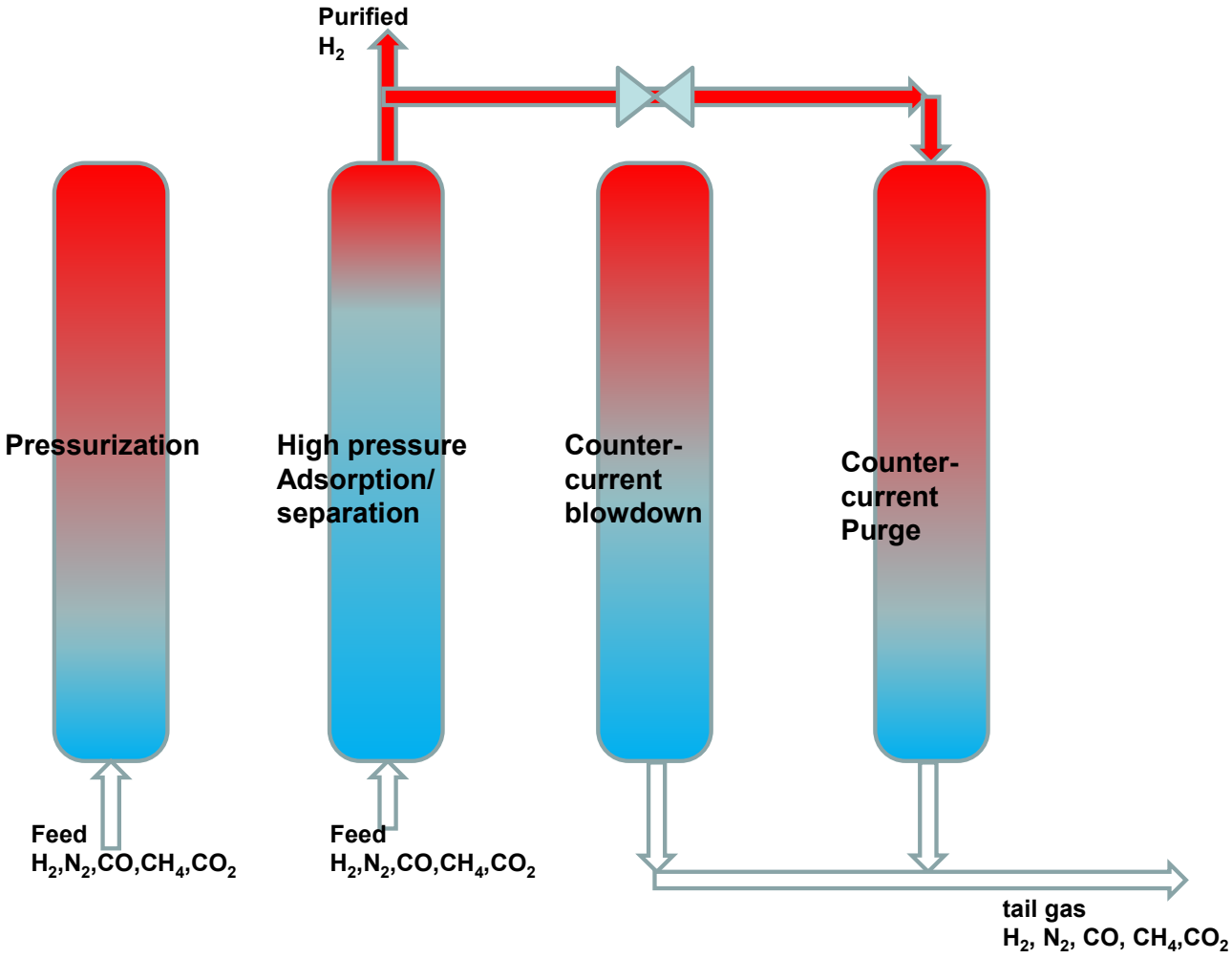

Figure S-6. Sequential steps in the operation of a single bed in the Skarstrom cycle for H_2 purification.

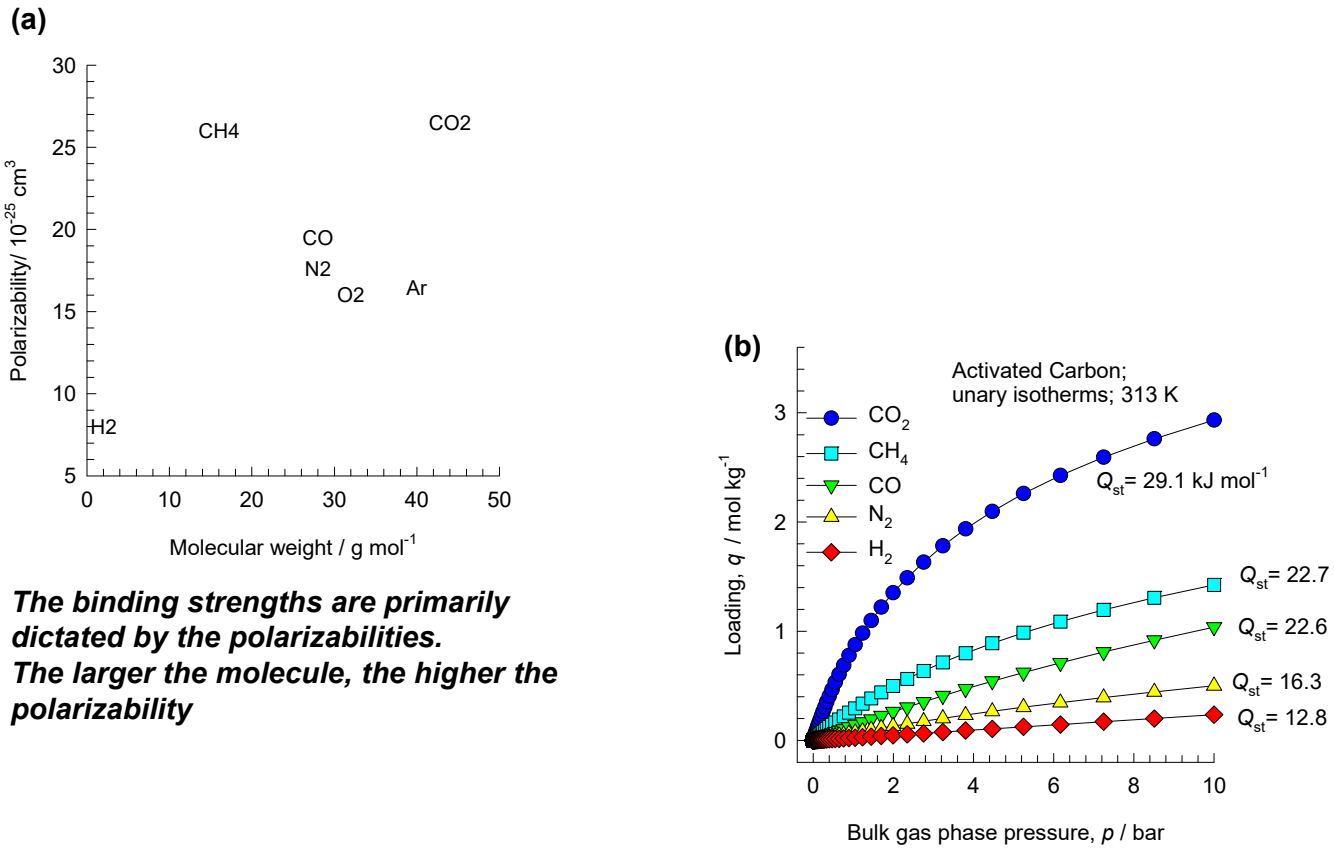

Figure S-7. (a) Polarizabilities of variety of gaseous molecules encountered in hydrogen purification processes. The data on polarizabilities are taken from Sircar and Myers.[4] (b) Unary isotherms at 313 K in activated carbon. The multi-site Langmuir parameters are listed in Table 4 of Ribeiro et al;[10] These parameters were used to refit the isotherms using dual-site Langmuir model; these unary isotherms at 313 K are plotted in (b). Also indicated in (b) are the isosteric heats of adsorption, Q_{st}, as listed in Table 4 of Ribeiro et al.[10]

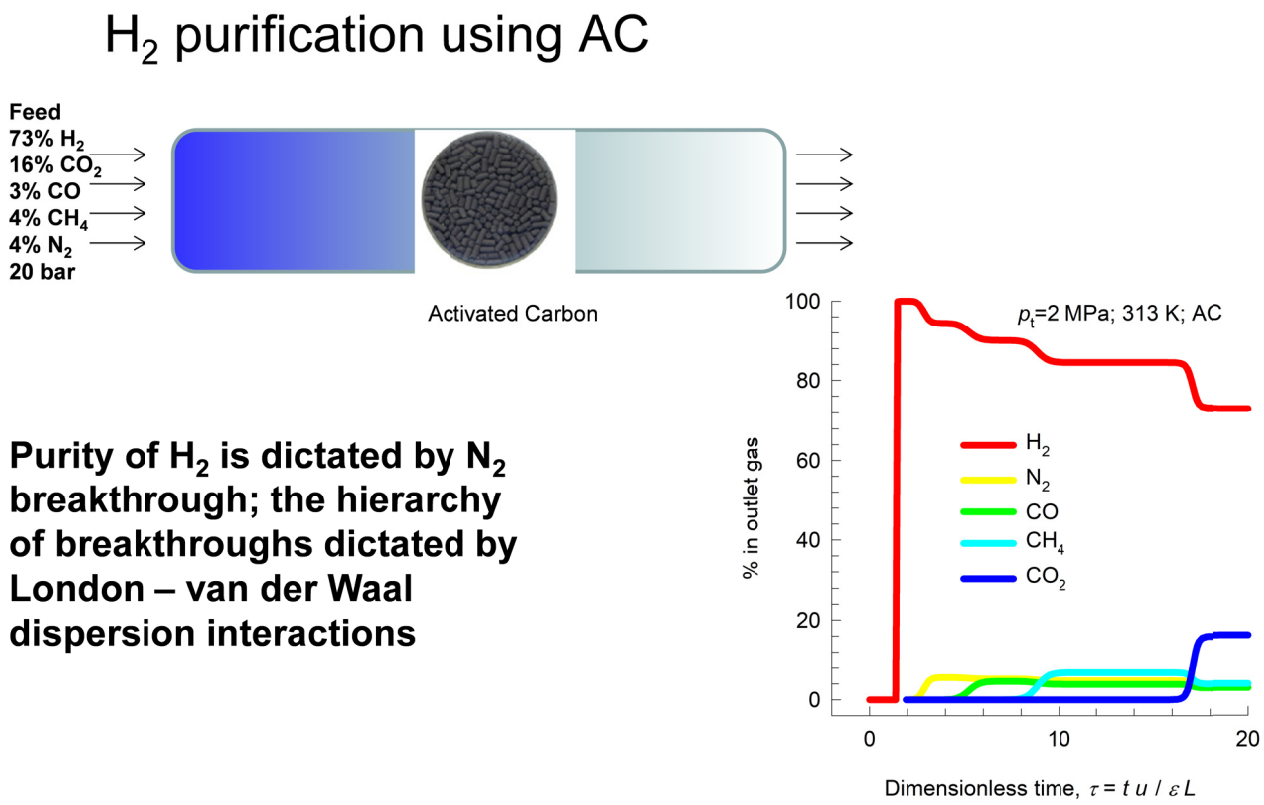

Figure S-8. Transient breakthrough of 73/4/3/4/16 $H_2/N_2/CO/CH_4/CO_2$ mixture in fixed bed adsorber packed with activated carbon operating at a total pressure of 2 MPa, and T = 313 K. The transient breakthrough simulation methodology is described in Chapter 5. These breakthroughs are performed assuming negligible axial dispersion, and negligible diffusional influences. The unary isotherm data are from Ribeiro et al.,[10] after re-fitting using the dual-site Langmuir model. In the breakthrough simulations, the mixture adsorption equilibrium was determined using the IAST.

LTA-5A

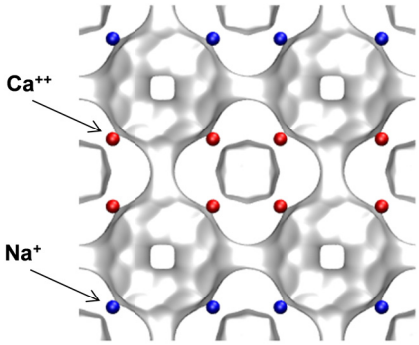

LTA-5A (32 Na^+, 32 Ca^{++})

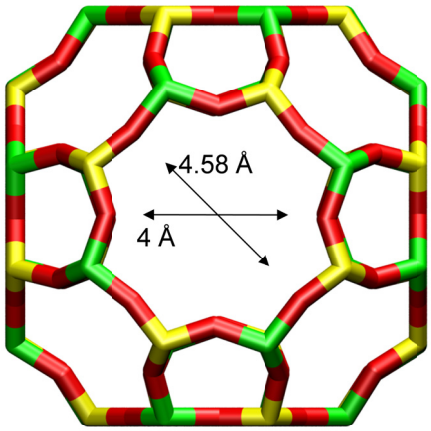

LTA-5A

The window dimension calculated using the van der Waals diameter of framework atoms = 2.7 Å is indicated above by the arrow.

	LTA-5A
a /Å	24.555
b /Å	24.555
c /Å	24.555
Cell volume / Å^3	14805.39
conversion factor for [molec/uc] to [mol per kg Framework]	0.0744
conversion factor for [molec/uc] to [kmol/m^3]	0.2955
ρ [kg/m3] (with cations)	1508.376
MW unit cell [g/mol framework+cations)]	13448.48
ϕ, fractional pore volume	0.380
open space / Å^3/uc	5620.4
Pore volume / cm^3/g	0.252
Surface area /m^2/g	
DeLaunay diameter /Å	4.00

Figure S-9. Structural details of LTA-5A zeolite.

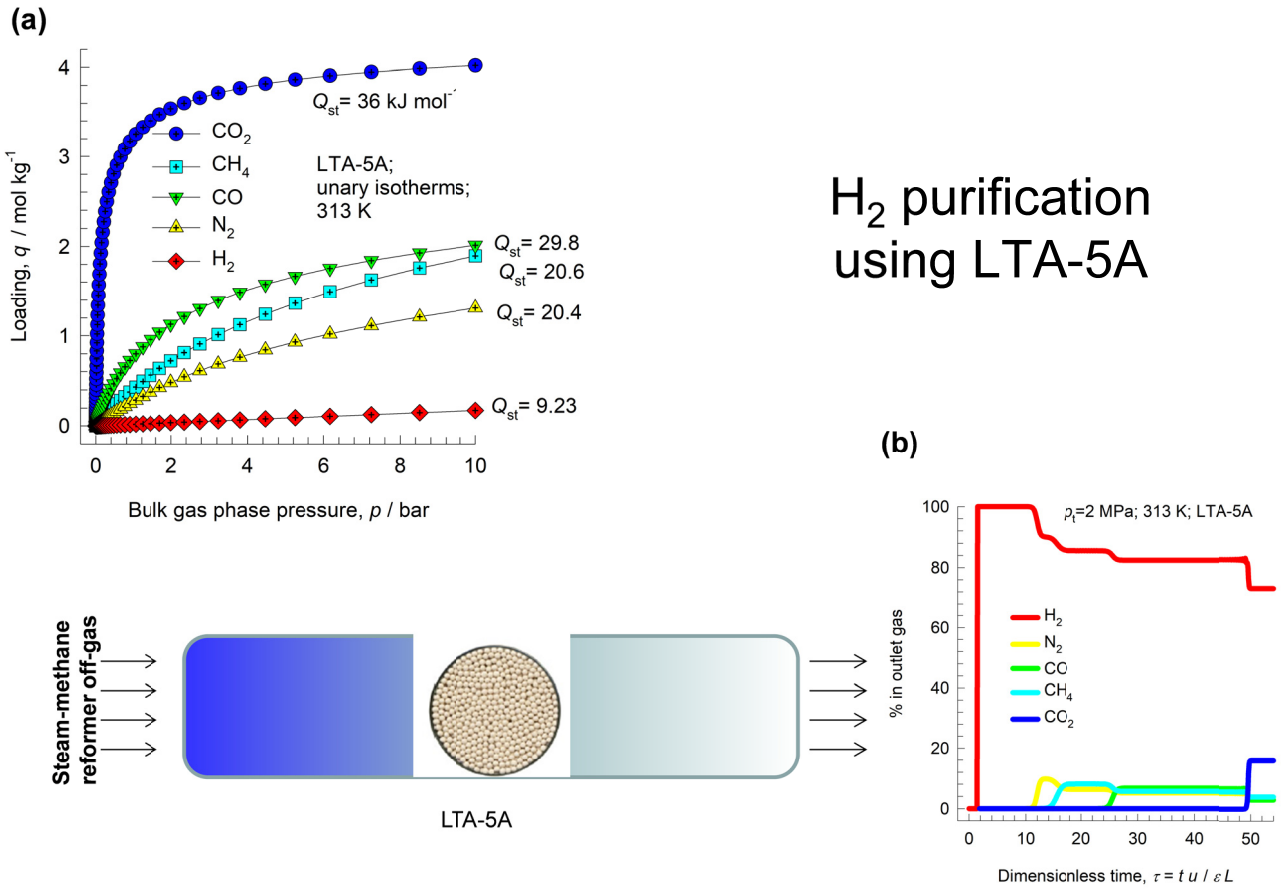

Figure S-10. (a) Unary isotherms of H_2, N_2, CO, CH_4, and CO_2 at 313 K in LTA-5A. The multi-site Langmuir parameters are listed in Table 4 of Ribeiro et al;[10] These parameters were used to refit the isotherms using dual-site Langmuir model; these unary isotherms at 313 K are plotted in (a). Also indicated in (a) are the isosteric heats of adsorption, Q_{st}, as listed in Table 4 of Ribeiro et al.[10] (b) Transient breakthrough of 73/4/3/4/16 $H_2/N_2/CO/CH_4/CO_2$ mixture in fixed bed adsorber packed with LTA-5A operating at a total pressure of 2 MPa, and T = 313 K. The transient breakthrough simulation methodology is described in Chapter 5. These breakthroughs are performed assuming negligible axial dispersion, and negligible diffusional influences.

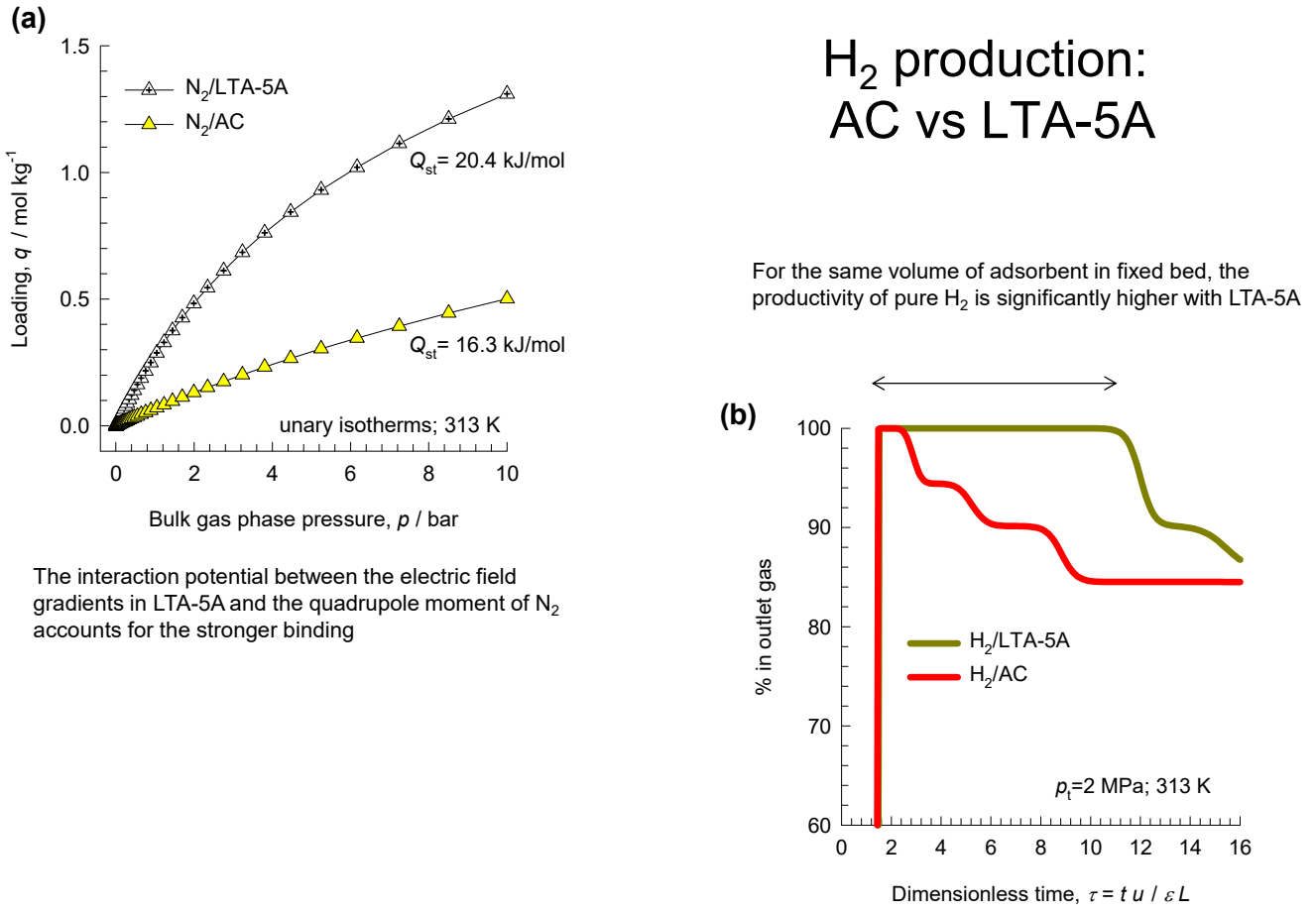

Figure S-11. (a) Comparison of the unary isotherms of N_2 in activated carbon and LTA-5A at 313 K. (b) Comparison of the breakthroughs of H_2 in fixed beds packed with activated carbon and LTA-5A, operating at 2 MPa at 313 K.

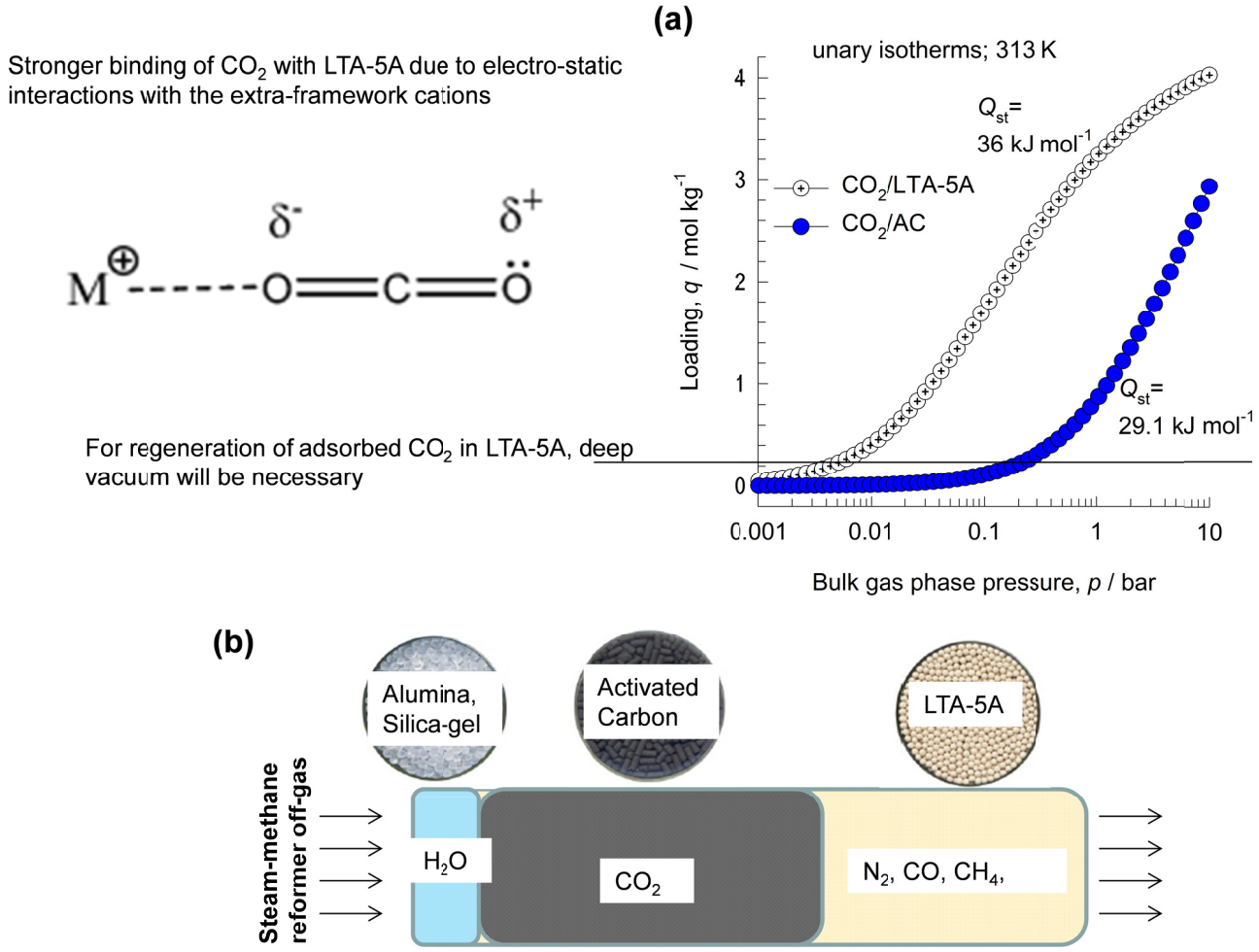

Figure S-12. (a) Comparison of the unary isotherms of CO_2 in activated carbon and LTA-5A at 313 K. (b) Schematic of multi-layered bed for H_2 purification.

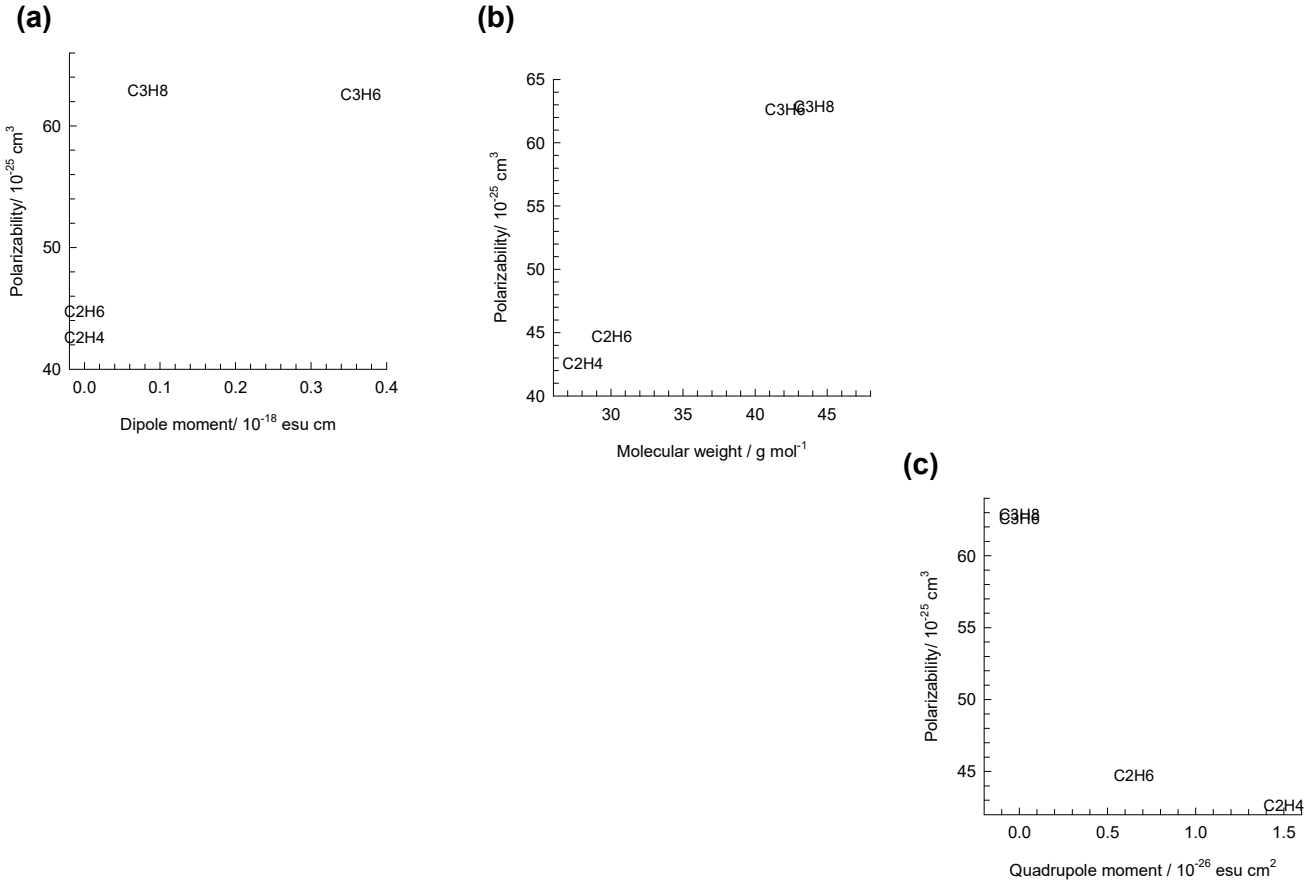

Figure S-13. (a, b, c) Polarizabilities, dipole moments, and quadrupole moments of C_2H_4, C_2H_6, C_3H_6, and C_3H_8. The data are taken from Sircar and Myers.[4]

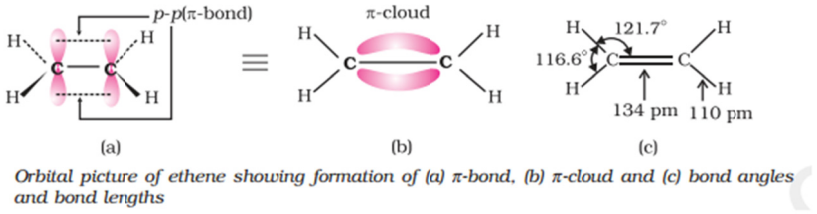

Orbital picture of ethene showing formation of (a) π-bond, (b) π-cloud and (c) bond angles and bond lengths

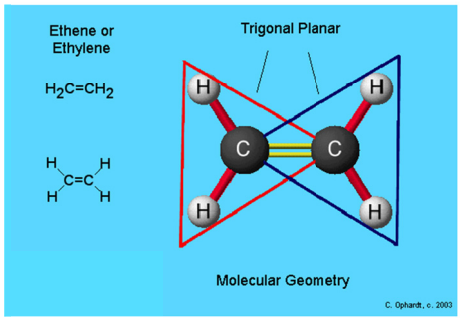

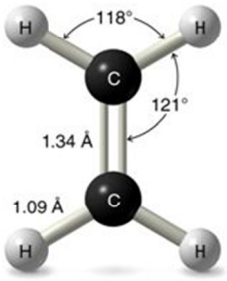

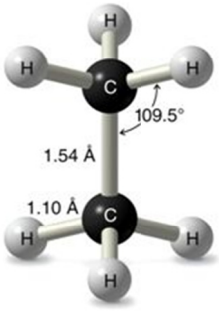

all atoms lie in the same plane

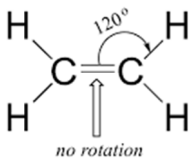

ethene

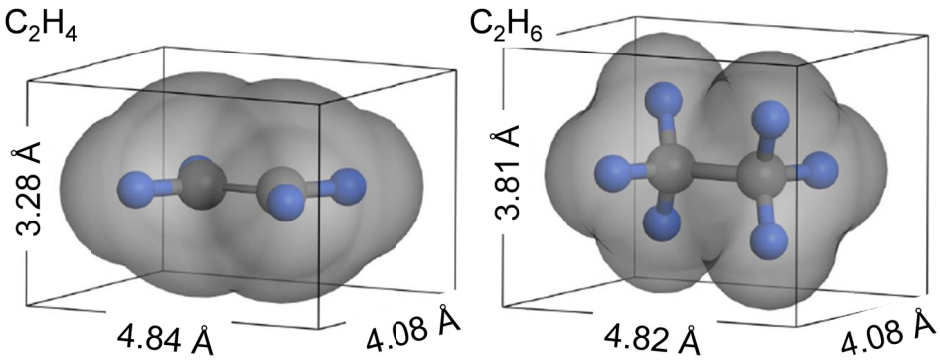

Figure S-14. Bond lengths and bond angles for C_2H_4, and C_2H_6.

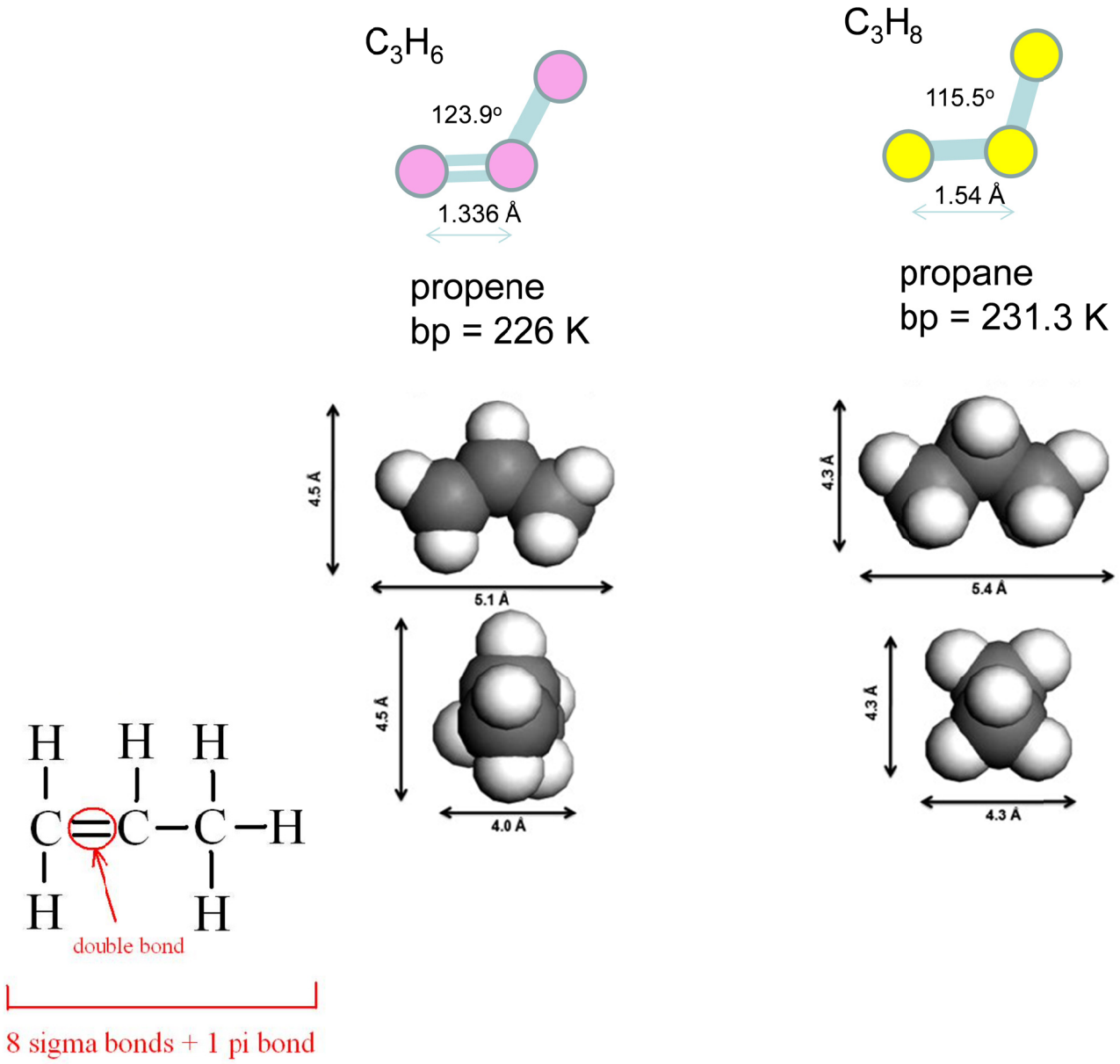

Figure S-15. Bond lengths and bond angles for C_3H_6, and C_3H_8.

3 The Ideal Adsorbed Solution Theory (IAST)

A brief summary of the IAST theory is provided in order to facilitate comparisons with the statistical thermodynamics based models to be discussed later in this article.

3.1 Brief outline of theory

Within microporous crystalline materials, the guest molecules exist in the adsorbed phase. The Gibbs adsorption equation[3] in differential form is

$$Ad\pi = \sum_{i=1}^{n} q_i d\mu_i \tag{S-7}$$

The quantity A is the surface area per kg of framework, with units of m^2 per kg of the framework of the crystalline material; q_i is the molar loading of component i in the adsorbed phase with units moles per kg of framework; μ_i is the molar chemical potential of component i. The spreading pressure π has the same units as surface tension, i.e. N m^{-1}.

The chemical potential of any component in the adsorbed phase, μ_i, equals that in the bulk fluid phase. If the partial fugacities in the bulk fluid phase are f_i, we have

$$d\mu_i = RTd \ln f_i \tag{S-8}$$

where R is the gas constant (= 8.314 J mol^{-1} K^{-1}).

Briefly, the basic equation of Ideal Adsorbed Solution Theory (IAST) theory of Myers and Prausnitz[11] is the analogue of Raoult's law for vapor-liquid equilibrium, i.e.

$$f_i = P_i^0 x_i; \quad i = 1,2,...n \tag{S-9}$$

where x_i is the mole fraction in the adsorbed phase

$$x_i = \frac{q_i}{q_1 + q_2 + ...q_n} \tag{S-10}$$

and P_i^0 is the pressure for sorption of every component *i*, which yields the same spreading pressure, π for each of the pure components, as that for the mixture:

$$\frac{\pi A}{RT} = \int_0^{P_1^0} \frac{q_1^0(f)}{f} df = \int_0^{P_2^0} \frac{q_2^0(f)}{f} df = \int_0^{P_3^0} \frac{q_3^0(f)}{f} df = ... \tag{S-11}$$

where $q_i^0(f)$ is the *pure* component adsorption isotherm. The units of $\frac{\pi A}{RT}$, also called the adsorption potential,[12] are mol kg^{-1}.

The unary isotherm may be described by say the 1-site Langmuir isotherm

$$q^0(f) = q_{sat} \frac{bf}{1+bf}; \quad \theta = \frac{bf}{1+bf} \tag{S-12}$$

where we define the fractional *occupancy* of the adsorbate molecules, $\theta = q^0(f)/q_{sat}$. The superscript 0 is used to emphasize that $q^0(f)$ relates the *pure component* loading to the bulk fluid fugacity. More generally, the unary isotherms may need to be described by, say, the dual-Langmuir-Freundlich model

$$q^0(f) = q_{A,sat} \frac{b_A f^{\nu A}}{1+b_A f^{\nu A}} + q_{B,sat} \frac{b_B f^{\nu B}}{1+b_B f^{\nu B}} \tag{S-13}$$

or the 3-site Langmuir-Freundlich model:

$$q^0 = q_{A,sat} \frac{b_A f^{\nu_A}}{1+b_A f^{\nu_A}} + q_{B,sat} \frac{b_B f^{\nu_B}}{1+b_B f^{\nu_B}} + q_{C,sat} \frac{b_C f^{\nu_C}}{1+b_C f^{\nu_C}} \tag{S-14}$$

Each of the integrals in Equation (S-11) can be evaluated analytically. For the 3-site Langmuir-Freundlich isotherm, for example, the integration yields for component *i*,

$$\begin{aligned} \int_{f=0}^{P_i^0} \frac{q^0(f)}{f} df &= \frac{q_{A,sat}}{\nu_A} \ln\left(1+b_A\left(P_i^0\right)^{\nu_A}\right) + \frac{q_{B,sat}}{\nu_B} \ln\left(1+b_B\left(P_i^0\right)^{\nu_B}\right) + \frac{q_{C,sat}}{\nu_C} \ln\left(1+b_C\left(P_i^0\right)^{\nu_C}\right) \\ \int_{f=0}^{P_i^0} \frac{q^0(f)}{f} df &= \frac{q_{A,sat}}{\nu_A} \ln\left(1+b_A\left(\frac{f_i}{x_i}\right)^{\nu_A}\right) + \frac{q_{B,sat}}{\nu_B} \ln\left(1+b_B\left(\frac{f_i}{x_i}\right)^{\nu_B}\right) + \frac{q_{C,sat}}{\nu_C} \ln\left(1+b_C\left(\frac{f_i}{x_i}\right)^{\nu_C}\right) \end{aligned} \tag{S-15}$$

The right hand side of equation (S-15) is a function of P_i^0. For multicomponent mixture adsorption, each of the equalities on the right hand side of Equation (S-11) must be satisfied. These constraints may

be solved using a suitable equation solver, to yield the set of values of P_1^0, P_2^0, P_3^0,.. P_n^0, all of which satisfy Equation (S-11). The corresponding values of the integrals using these as upper limits of integration must yield the same value of $\frac{\pi A}{RT}$ for each component; this ensures that the obtained solution is the correct one.

The adsorbed phase mole fractions x_i are then determined from

$$x_i = \frac{f_i}{P_i^0}; \quad i = 1,2,...n \tag{S-16}$$

A key assumption of the IAST is that the enthalpies and surface areas of the adsorbed molecules do not change upon mixing. If the total mixture loading is q_t, the area covered by the adsorbed mixture is $\frac{A}{q_t}$ with units of m^2 (mol mixture)$^{-1}$. Therefore, the assumption of no surface area change due to mixture adsorption translates as $\frac{A}{q_t} = \frac{Ax_1}{q_1^0\left(P_1^0\right)} + \frac{Ax_2}{q_2^0\left(P_2^0\right)} + \cdots \frac{Ax_n}{q_n^0\left(P_n^0\right)}$; the total mixture loading is q_t is calculated from

$$q_t = q_1 + q_2 ... + q_n = \frac{1}{\frac{x_1}{q_1^0(P_1^0)} + \frac{x_2}{q_2^0(P_2^0)} + ... + \frac{x_n}{q_n^0(P_n^0)}} \tag{S-17}$$

in which $q_1^0(P_1^0)$, $q_2^0(P_2^0)$,… $q_n^0(P_n^0)$ are determined from the unary isotherm fits, using the sorption pressures for each component P_1^0, P_2^0, P_3^0,.. P_n^0 that are available from the solutions to equations Equations (S-11), and (S-15).

The entire set of equations (S-9) to (S-17) need to be solved numerically to obtain the loadings, q_i of the individual components in the mixture.

3.2 IAST model: 1-site Langmuir isotherms

The IAST procedure for will be explained in a step-by-step manner for binary mixture adsorption in which the unary isotherms are described by the 1-site Langmuir model. The objective is to determine the molar loadings, q_1, and q_2, in the adsorbed phase.

Performing the integration of Equation (S-11) results in an expression relating the sorption pressures P_i^0 of the two species

$$\begin{aligned}&\frac{\pi A}{RT} = q_{1,sat}\ln\left(1+b_1P_1^0\right) = q_{2,sat}\ln\left(1+b_2P_2^0\right)\\ &b_1P_1^0 = \exp\left(\frac{\pi A}{q_{1,sat}RT}\right)-1; \quad b_2P_2^0 = \exp\left(\frac{\pi A}{q_{2,sat}RT}\right)-1\end{aligned} \tag{S-18}$$

The adsorbed phase mole fractions of component 1, and component 2 are given by equation (S-16)

$$x_1 = \frac{f_1}{P_1^0}; \quad x_2 = 1-x_1 = \frac{f_2}{P_2^0} \tag{S-19}$$

Since the mole fractions add to unity, we may combine equations (S-18), and (S-19) to obtain a relation in just *one* unknown, x_1:

$$\frac{\pi A}{RT} = q_{1,sat}\ln\left(1+b_1\frac{f_1}{x_1}\right) = q_{2,sat}\ln\left(1+b_2\frac{f_2}{1-x_1}\right) \tag{S-20}$$

Equation (S-20) is a non-linear equation

$$q_{1,sat}\ln\left(1+b_1\frac{f_1}{x_1}\right) - q_{2,sat}\ln\left(1+b_2\frac{f_2}{1-x_1}\right) = 0 \tag{S-21}$$

The partial fugacities of the two components in the bulk gas phase are known, and equation (S-21) needs to be solved using a root finder to solve for the unknown, x_1. Once x_1, and $x_2 = 1-x_1$ are determined, the sorption pressures can be calculated:

$$P_1^0 = \frac{f_1}{x_1}; \quad P_2^0 = \frac{f_2}{x_2} = \frac{f_2}{1-x_1} \tag{S-22}$$

The total amount adsorbed, $q_t = q_1 + q_2$ can be calculated from

$$q_t = q_1 + q_2 = \frac{1}{\dfrac{x_1}{q_1^0(P_1^0)} + \dfrac{x_2}{q_2^0(P_2^0)}} \tag{S-23}$$

in which $q_1^0(P_1^0)$, and $q_2^0(P_2^0)$ are determined from the Langmuir parameters along with the sorption pressures, determined from equation (S-22). The component loadings, q_1, and q_2 are then determined from $q_1 = q_t x_1; \quad q_2 = q_t(1 - x_1)$.

3.3 Langmuir isotherms with equal saturation capacities

For the special case of binary mixture adsorption with equal saturation capacities, $q_{1,sat} = q_{2,sat} = q_{sat}$, the component loadings can be determined explicitly. Equation (S-21) can be solved explicitly to obtain the adsorbed phase mole fractions

$$\frac{x_1}{x_2} = \frac{q_1}{q_2} = \frac{b_1 f_1}{b_2 f_2}; \quad x_1 = \frac{q_1}{q_t} = \frac{b_1 f_1}{b_1 f_1 + b_2 f_2}; \quad x_2 = \frac{q_2}{q_t} = \frac{b_2 f_2}{b_1 f_1 + b_2 f_2} \tag{S-24}$$

Equation (S-18) simplifies to yield

$$\begin{aligned} &\frac{\pi A}{RT} = q_{sat} \ln\left(1 + b_1 P_1^0\right) = q_{sat} \ln\left(1 + b_2 P_2^0\right) \\ &b_1 P_1^0 = b_2 P_2^0 = \exp\left(\frac{\pi A}{q_{sat} RT}\right) - 1 = \exp\left(\frac{\pi A}{q_{sat} RT}\right) - 1 \end{aligned} \tag{S-25}$$

From equation (S-22) we get

$$\begin{aligned} &b_i P_1^0 = \frac{b_1 f_1}{x_1} = b_2 P_2^0 = \frac{b_2 f_2}{x_2} = b_1 f_1 + b_2 f_2 \\ &1 + b_i P_1^0 = 1 + b_2 P_2^0 = 1 + b_1 f_1 + b_2 f_2 \end{aligned} \tag{S-26}$$

Equations (S-23), (S-24), (S-25), and (S-26) yield

$$\begin{aligned} &\frac{q_{sat}}{q_t} = \frac{x_1}{b_1 P_1^0}\left(1 + b_1 P_1^0\right) + \frac{x_2}{b_2 P_2^0}\left(1 + b_2 P_2^0\right) = \frac{1 + b_1 f_1 + b_2 f_2}{b_1 f_1 + b_2 f_2} \\ &q_t = q_{sat} \frac{b_1 f_1 + b_2 f_2}{1 + b_1 f_1 + b_2 f_{22}} \end{aligned} \tag{S-27}$$

Combining equations (S-24), and (S-27) we obtain the following explicit expressions for the component loadings, and fractional occupancies

$$\theta_1 = \frac{q_1}{q_{sat}} = \frac{b_1 f_1}{1 + b_1 f_1 + b_2 f_2}; \quad \theta_2 = \frac{q_2}{q_{sat}} = \frac{b_2 f_2}{1 + b_1 f_1 + b_2 f_2} \tag{S-28}$$

Equation (S-28) is commonly referred to as the mixed-gas Langmuir model, or extended Langmuir model. Rao and Sircar[13] show that the mixed-gas Langmuir model described by Equation (S-28) passes the thermodynamic consistency test only when the saturation capacities equal each other, i.e. $q_{1,sat} = q_{2,sat}$.

From Equation (S-28), it also follows that the adsorbed phase mole fraction is

$$x_1 = \frac{1}{1 + \frac{b_2 f_2}{b_1 f_1}} \tag{S-29}$$

4 Diffusion in Microporous Crystalline Materials

4.1 The Maxwell-Stefan (M-S) description of diffusion

Within micro-porous crystalline materials, such as zeolites, metal-organic frameworks (MOFs), and zeolitic imidazolate frameworks (ZIFs), the guest molecules exist in the adsorbed phase. The Maxwell-Stefan (M-S) equations for *n*-component diffusion in porous materials is applied in the following manner[14-21]

$$\begin{aligned}
-\frac{\partial \mu_1}{\partial r} &= \frac{RT}{Đ_{12}} x_2 \left(u_1 - u_2\right) + \frac{RT}{Đ_{13}} x_3 \left(u_1 - u_3\right) + \ldots + \frac{RT}{Đ_1}\left(u_1\right) \\
-\frac{\partial \mu_2}{\partial r} &= \frac{RT}{Đ_{21}} x_1 \left(u_2 - u_1\right) + \frac{RT}{Đ_{23}} x_3 \left(u_2 - u_3\right) + \ldots + \frac{RT}{Đ_2}\left(u_2\right) \\
&\cdots\cdots \\
-\frac{\partial \mu_n}{\partial r} &= \frac{RT}{Đ_{n1}} x_1 \left(u_n - u_1\right) + \frac{RT}{Đ_{n2}} x_2 \left(u_n - u_3\right) + \ldots + \frac{RT}{Đ_n}\left(u_n\right)
\end{aligned} \tag{S-30}$$

The left members of equation (S-30) are the negative of the gradients of the chemical potentials, with the units N mol^{-1}; it represents the driving force acting per mole of species 1, 2, 3,..*n*. The u_i represents the velocity of motion of the adsorbate, defined in a reference frame with respect to the framework material. The crystalline framework is considered to be stationary. The term $RT/Đ_i$ is interpreted as the drag or friction coefficient between the guest species *i* and the pore wall. The term $RT/Đ_{ij}$ is interpreted as the friction coefficient for the *i-j* pair of guest molecules. The multiplier $x_i = q_i / q_t$ where q_i is the molar loading of adsorbate, and q_t is the *total* mixture loading $q_t = \sum_{i=1}^{n} q_i$. We expect the friction to be dependent on the number of molecules of *j* relative to that of component *i*.

An important, persuasive, argument for the use of the M-S formulation for mixture diffusion is that the M-S diffusivity $Đ_i$ in mixtures can be estimated using information on the loading dependence of the

corresponding unary diffusivity values. Put another way, the M-S diffusivity $Đ_i$ can be estimated from experimental data on *unary* diffusion in the porous material.

The M-S diffusivity $Đ_{ij}$ has the units m^2 s^{-1} and the physical significance of an *inverse* drag coefficient. The magnitudes of the M-S diffusivities $Đ_{ij}$ do not depend on the choice of the mixture reference velocity because equation (S-30) is set up in terms of velocity differences. At the molecular level, the $Đ_{ij}$ reflect how the facility for transport of species *i correlates* with that of species *j*; they are also termed *exchange coefficients*.

For *meso*porous materials with pores in the 20 Å to 100 Å size range the values of the exchange coefficient $Đ_{12}$ are the nearly the same as the binary *fluid phase* M-S diffusivity, $Đ_{12,fl}$, over the entire range of pore concentrations.[16, 17, 21-23] For micro-porous materials, the exchange coefficient $Đ_{12}$ cannot be directly identified with the corresponding fluid phase diffusivity $Đ_{12,fl}$ because the molecule-molecule interactions are also significantly influenced by molecule-wall interactions.

The Maxwell-Stefan diffusion formulation (S-30) is consistent with the theory of irreversible thermodynamics. The Onsager Reciprocal Relations imply that the M-S pair diffusivities are symmetric

$$Đ_{ij} = Đ_{ji} \tag{S-31}$$

We define N_i as the number of moles of species *i* transported per m^2 of crystalline material per second

$$N_i \equiv \rho q_i u_i \tag{S-32}$$

where ρ is the framework density with units of kg m^{-3}. Multiplying both sides of equation (S-30) by ρq_i, the M-S equations for *n*-component diffusion in zeolites, MOFs, and ZIFs take the form [22, 24, 25]

$$-\rho \frac{q_i}{RT}\frac{\partial \mu_i}{\partial r} = \sum_{\substack{j=1 \\ j\neq i}}^{n} \frac{x_j N_i - x_i N_j}{Đ_{ij}} + \frac{N_i}{Đ_i}; \qquad i = 1, 2, ..n \tag{S-33}$$

The fluxes N_i in equations (S-33) are defined in terms of the moles transported per m^2 of the *total surface of crystalline material*.

4.2 Thermodynamic correction factors

At thermodynamic equilibrium, the chemical potential of component *i* in the bulk fluid mixture equals the chemical potential of that component in the adsorbed phase. For the bulk fluid phase mixture we have

$$\frac{1}{RT}\frac{\partial \mu_i}{\partial r} = \frac{\partial \ln f_i}{\partial r} = \frac{1}{f_i}\frac{\partial f_i}{\partial r}; \qquad i = 1, 2, ..n \tag{S-34}$$

The chemical potential gradients $\partial \mu_i / \partial r$ can be related to the gradients of the molar loadings, q_i, by defining thermodynamic correction factors Γ_{ij}

$$\frac{q_i}{RT}\frac{\partial \mu_i}{\partial r} = \sum_{j=1}^{n} \Gamma_{ij}\frac{\partial q_j}{\partial r}; \quad \Gamma_{ij} = \frac{q_i}{f_i}\frac{\partial f_i}{\partial q_j}; \qquad i, j = 1, ...n \tag{S-35}$$

The thermodynamic correction factors Γ_{ij} can be calculated by differentiation of the model describing mixture adsorption equilibrium. Generally speaking, the Ideal Adsorbed Solution Theory (IAST) of Myers and Prausnitz[11] is the preferred method for estimation of mixture adsorption equilibrium. In some special case, the mixed-gas Langmuir model

$$\frac{q_i}{q_{i,sat}} = \theta_i = \frac{b_i f_i}{1 + \sum_{i=1}^{n} b_i f_i}; \quad i = 1, 2, ...n \tag{S-36}$$

may be of adequate accuracy. Analytic differentiation of equation (S-36) yields

$$\Gamma_{ij} = \delta_{ij} + \left(\frac{q_{i,sat}}{q_{j,sat}}\right)\left(\frac{\theta_i}{\theta_V}\right); \quad i, j = 1, 2 \ldots n \tag{S-37}$$

where the fractional vacancy θ_V is defined as

$$\theta_V = 1 - \theta_t = 1 - \sum_{i=1}^{n} \theta_i \tag{S-38}$$

The elements of the matrix of thermodynamic factors Γ_{ij} can be calculated explicitly from information on the component loadings q_i in the adsorbed phase; this is the persuasive advantage of the use of the

mixed-gas Langmuir model. By contrast, the IAST does not allow the calculation of Γ_{ij} explicitly from knowledge on the component loadings q_i in the adsorbed phase; a numerical procedure is required.

4.3 Explicit expression for the fluxes as function of loading gradients

By defining an n-dimensional square matrix $[B]$ with elements

$$B_{ii} = \frac{1}{Đ_i} + \sum_{\substack{j=1 \\ j\neq i}}^{n} \frac{x_j}{Đ_{ij}}; \qquad B_{ij} = -\frac{x_i}{Đ_{ij}}; \quad i, j = 1,2....n \tag{S-39}$$

we can recast equation (S-33) into the following form

$$-\rho \frac{q_i}{RT}\frac{\partial \mu_i}{\partial r} = \sum_{j=1}^{n} B_{ij} N_j; \qquad i = 1,2,..n \tag{S-40}$$

Equation (S-40) can be re-written in n-dimensional matrix notation as

$$(N) = -\rho \left[B\right]^{-1} \left[\Gamma\right] \frac{\partial (q)}{\partial r} = -\rho \left[\Lambda\right]\left[\Gamma\right] \frac{\partial (q)}{\partial r} \tag{S-41}$$

We denote the inverse of $[B]$ as $\left[\Lambda\right]$:

$$[B]^{-1} \equiv \left[\Lambda\right] \tag{S-42}$$

Compliance with the Onsager Reciprocal Relations demands

$$n_j \Lambda_{ij} = n_i \Lambda_{ji}; \quad i, j = 1,2,....n \tag{S-43}$$

If the correlation effects are considered to be of negligible importance, the first term on the right of equations (S-33) may be ignored; this results in a simplified set of equations

$$N_i = -\rho Đ_i \sum_{j=1}^{n} \Gamma_{ij} \frac{\partial q_j}{\partial r}; \qquad i = 1,2..n \tag{S-44}$$

Furthermore, if the thermodynamic coupling effects are also ignored, Equation (S-44) degenerates to a set of uncoupled flux relations

$$N_i = -\rho Đ_i \frac{\partial q_i}{\partial r}; \qquad i = 1,2..n \tag{S-45}$$

4.4 M-S formulation for binary mixture diffusion

For binary mixture diffusion inside microporous crystalline materials the Maxwell-Stefan equations (S-33) are written

$$\begin{aligned} -\rho\frac{q_1}{RT}\frac{\partial\mu_1}{\partial r} &= \frac{x_2N_1 - x_1N_2}{Đ_{12}} + \frac{N_1}{Đ_1} \\ -\rho\frac{q_2}{RT}\frac{\partial\mu_2}{\partial r} &= \frac{x_1N_2 - x_2N_1}{Đ_{12}} + \frac{N_2}{Đ_2} \end{aligned} \tag{S-46}$$

The first members on the right hand side of Equation (S-46) are required to quantify slowing-down effects that characterize binary mixture diffusion.[16, 17, 26] There is no experimental technique for direct determination of the exchange coefficients $Đ_{12}$, that quantify molecule-molecule interactions.

In two-dimensional matrix notation, equation (S-35) take the form

$$-\begin{pmatrix} \frac{q_1}{RT}\frac{\partial\mu_1}{\partial r} \\ \frac{q_2}{RT}\frac{\partial\mu_2}{\partial r} \end{pmatrix} = [\Gamma]\begin{pmatrix} \frac{\partial q_1}{\partial r} \\ \frac{\partial q_2}{\partial r} \end{pmatrix} \tag{S-47}$$

For the mixed-gas Langmuir model, equation (S-36), we can derive simple analytic expressions for the four elements of the matrix of thermodynamic factors:[27]

$$\begin{bmatrix} \Gamma_{11} & \Gamma_{12} \\ \Gamma_{21} & \Gamma_{22} \end{bmatrix} = \frac{1}{1-\theta_1-\theta_2}\begin{bmatrix} 1-\theta_2 & \frac{q_{1,sat}}{q_{2,sat}}\theta_1 \\ \frac{q_{2,sat}}{q_{1,sat}}\theta_2 & 1-\theta_1 \end{bmatrix} \tag{S-48}$$

where the fractional occupancies, θ_i, are defined by equation (S-36).

Let us define the square matrix [B]

$$[B] = \begin{bmatrix} \frac{1}{Đ_1}+\frac{x_2}{Đ_{12}} & -\frac{x_1}{Đ_{12}} \\ -\frac{x_2}{Đ_{12}} & \frac{1}{Đ_2}+\frac{x_1}{Đ_{12}} \end{bmatrix}; \quad [B]^{-1} = \frac{1}{1+\frac{x_1Đ_2}{Đ_{12}}+\frac{x_2Đ_1}{Đ_{12}}}\begin{bmatrix} Đ_1\left(1+\frac{x_1Đ_2}{Đ_{12}}\right) & \frac{x_1Đ_1Đ_2}{Đ_{12}} \\ \frac{x_2Đ_1Đ_2}{Đ_{12}} & Đ_2\left(1+\frac{x_2Đ_1}{Đ_{12}}\right) \end{bmatrix} \tag{S-49}$$

In proceeding further, it is convenient to define a 2×2 dimensional square matrix $[\Lambda]$:

$$[\Lambda]=\begin{bmatrix} \frac{1}{Đ_1}+\frac{x_2}{Đ_{12}} & -\frac{x_1}{Đ_{12}} \\ -\frac{x_2}{Đ_{12}} & \frac{1}{Đ_2}+\frac{x_1}{Đ_{12}} \end{bmatrix}^{-1}=\frac{1}{1+\frac{x_1Đ_2}{Đ_{12}}+\frac{x_2Đ_1}{Đ_{12}}}\begin{bmatrix} Đ_1\left(1+\frac{x_1Đ_2}{Đ_{12}}\right) & \frac{x_1Đ_1Đ_2}{Đ_{12}} \\ \frac{x_2Đ_1Đ_2}{Đ_{12}} & Đ_2\left(1+\frac{x_2Đ_1}{Đ_{12}}\right) \end{bmatrix} \tag{S-50}$$

Equation (S-46) can be re-cast into 2-dimensional matrix notation

$$(N)=-\rho[\Lambda][\Gamma]\frac{\partial(q)}{\partial r};$$

$$\begin{pmatrix} N_1 \\ N_2 \end{pmatrix}=-\frac{\rho}{1+\frac{x_1Đ_2}{Đ_{12}}+\frac{x_2Đ_1}{Đ_{12}}}\begin{bmatrix} Đ_1\left(1+\frac{x_1Đ_2}{Đ_{12}}\right) & \frac{x_1Đ_1Đ_2}{Đ_{12}} \\ \frac{x_2Đ_1Đ_2}{Đ_{12}} & Đ_2\left(1+\frac{x_2Đ_1}{Đ_{12}}\right) \end{bmatrix}\begin{bmatrix} \Gamma_{11} & \Gamma_{12} \\ \Gamma_{21} & \Gamma_{22} \end{bmatrix}\begin{pmatrix} \frac{\partial q_1}{\partial r} \\ \frac{\partial q_2}{\partial r} \end{pmatrix} \tag{S-51}$$

The elements of $[B]$ can be obtained by inverting the matrix $[\Lambda]$:

$$\begin{bmatrix} B_{11} & B_{12} \\ B_{21} & B_{22} \end{bmatrix}=\begin{bmatrix} \frac{1}{Đ_1}+\frac{x_2}{Đ_{12}} & -\frac{x_1}{Đ_{12}} \\ -\frac{x_2}{Đ_{12}} & \frac{1}{Đ_2}+\frac{x_1}{Đ_{12}} \end{bmatrix}=[\Lambda]^{-1} \tag{S-52}$$

A 2×2 dimensional Fick diffusivity matrix $[D]$ is defined as the product of $[\Lambda]$ and the matrix of thermodynamic correction factors $[\Gamma]$:

$$[D]=[B]^{-1}[\Gamma]=\frac{1}{1+\frac{x_1Đ_2}{Đ_{12}}+\frac{x_2Đ_1}{Đ_{12}}}\begin{bmatrix} Đ_1\left(1+\frac{x_1Đ_2}{Đ_{12}}\right) & \frac{x_1Đ_1Đ_2}{Đ_{12}} \\ \frac{x_2Đ_1Đ_2}{Đ_{12}} & Đ_2\left(1+\frac{x_2Đ_1}{Đ_{12}}\right) \end{bmatrix}\begin{bmatrix} \Gamma_{11} & \Gamma_{12} \\ \Gamma_{21} & \Gamma_{22} \end{bmatrix} \tag{S-53}$$

$$(N)=-\rho[D]\frac{\partial(q)}{\partial r};$$

4.5 Degree of correlations

In order to appreciate the relative importance of correlations on the calculations of the fluxes for binary mixture diffusion, we define the *degrees of correlation*, $Đ_1/Đ_{12}$, and $Đ_2/Đ_{12}$; the values can be determined from those backed-out from mixture MD simulations for earlier publications.[17, 18, 21, 22, 28-35]

The magnitude of $Đ_1$, relative to that of $Đ_{12}$, determines the extent to which the flux of species 1 is influenced by the chemical potential gradient of species 2. The larger the degree of correlation, $Đ_1/Đ_{12}$, the stronger is the influence of coupling. Generally speaking, the more-strongly-adsorbed-tardier partner species will have the effect of slowing down the less-strongly-adsorbed-more-mobile partner in the mixture.

Figure S-16 shows MD simulation data for the degree of correlations, $Đ_1/Đ_{12}$, for diffusion of equimolar ($q_1 = q_2$) binary mixtures (a) CO_2/CH_4, (b) H_2/CO_2, (c) N_2/CO_2, (d) Ne/CO_2, (e) CH_4/Ar (f) H_2/CH_4, (g) Ne/Ar, (h) CH_4/C_2H_6, and (i) CH_4/C_3H_8 at 300 K in a variety of host materials. For any guest/host combination, $Đ_1/Đ_{12}$ is seen to increase as the pore concentration increases; this implies that correlation effects are expected to be stronger for high pore occupancies.

The degree of correlations is weakest in cage-type structures such as CHA, DDR and LTA; the reason is that the molecules jump one-at-a-time across the narrow windows separating adjacent cages; CO_2 molecules jump length-wise across the windows. At the other end of the spectrum, correlations are strongest in one-dimensional (1D) channel structures (e.g. BTP-COF, MgMOF-74, NiMOF-74), intersecting channels (e.g. MFI), and "open" structures (e.g. IRMOF-1, FAU, NaY, NaX) consisting of large cages separated by wide windows.

4.6 Negligible correlations scenario for M-S diffusivities

For values of $Đ_1/Đ_{12} \to 0$, and $Đ_2/Đ_{12} \to 0$, the contribution of the first right member of M-S Equation (S-46) can be ignored and correlations can be considered to be of negligible importance; we derive

$$\frac{Đ_1}{Đ_{12}} \to 0; \quad \frac{Đ_2}{Đ_{12}} \to 0; \quad \begin{bmatrix} \Lambda_{11} & \Lambda_{12} \\ \Lambda_{21} & \Lambda_{22} \end{bmatrix} \to \begin{bmatrix} Đ_1 & 0 \\ 0 & Đ_2 \end{bmatrix}$$

$$\begin{pmatrix} N_1 \\ N_2 \end{pmatrix} = -\rho \begin{bmatrix} Đ_1 & 0 \\ 0 & Đ_2 \end{bmatrix} \begin{bmatrix} \Gamma_{11} & \Gamma_{12} \\ \Gamma_{21} & \Gamma_{22} \end{bmatrix} \begin{pmatrix} \frac{\partial q_1}{\partial r} \\ \frac{\partial q_2}{\partial r} \end{pmatrix} \tag{S-54}$$

Equation (S-54) is valid, as a first approximation, for diffusion in cage-type zeolites with 8-ring windows (CHA, LTA, DDR, ERI) and ZIF-8; see earlier publications.[18, 22, 29, 31, 36-39]

When correlation effects are negligible, the diffusional coupling effects are solely traceable to mixture adsorption thermodynamics, embodied in the matrix $[\Gamma]$.

If the mixed-gas Langmuir model is used to describe mixture adsorption equilibrium, the matrix of thermodynamic correction factors is given by Equation (S-48). Combining equations (S-48)., and (S-54) we obtain the flux expression

$$\begin{pmatrix} N_1 \\ N_2 \end{pmatrix} = -\rho \begin{bmatrix} Đ_1 & 0 \\ 0 & Đ_2 \end{bmatrix} \frac{1}{1-\theta_1-\theta_2} \begin{bmatrix} 1-\theta_2 & \frac{q_{1,sat}}{q_{2,sat}}\theta_1 \\ \frac{q_{2,sat}}{q_{1,sat}}\theta_2 & 1-\theta_1 \end{bmatrix} \begin{pmatrix} \frac{\partial q_1}{\partial r} \\ \frac{\partial q_2}{\partial r} \end{pmatrix} \tag{S-55}$$

Equation (S-55) is essentially equivalent to the flux relation used by Habgood[40] to model transient overshoots in the loading of N_2 during transient uptake of N_2/CH_4 in LTA-4A zeolite. These flux relations (S-55) are also incorporated into the models for describing the transient breakthroughs in fixed bed adsorbers by Ruthven, Farooq, Knaebel, and co-workers.[5, 41-43]

4.7 Ignoring thermodynamic coupling effects

In the Henry regime of adsorption, i.e. at low component loading, thermodynamic correction factors may be adequately described by $\Gamma_{ij} = \delta_{ij}$, the Kronecker delta.

$$\begin{bmatrix} \Gamma_{11} & \Gamma_{12} \\ \Gamma_{21} & \Gamma_{22} \end{bmatrix} = \begin{bmatrix} 1 & 0 \\ 0 & 1 \end{bmatrix}; \quad \begin{pmatrix} N_1 \\ N_2 \end{pmatrix} = -\rho \begin{bmatrix} Đ_1 & 0 \\ 0 & Đ_2 \end{bmatrix} \begin{pmatrix} \frac{\partial q_1}{\partial r} \\ \frac{\partial q_2}{\partial r} \end{pmatrix} \tag{S-56}$$

Indeed, the major objective of this article is to demonstrate the inadequacy of Equation (S-56) to model transient mixture uptake in microporous crystals, and transient breakthroughs in fixed bed adsorbers.

4.8 List of Figures for Diffusion in Microporous Crystalline Materials

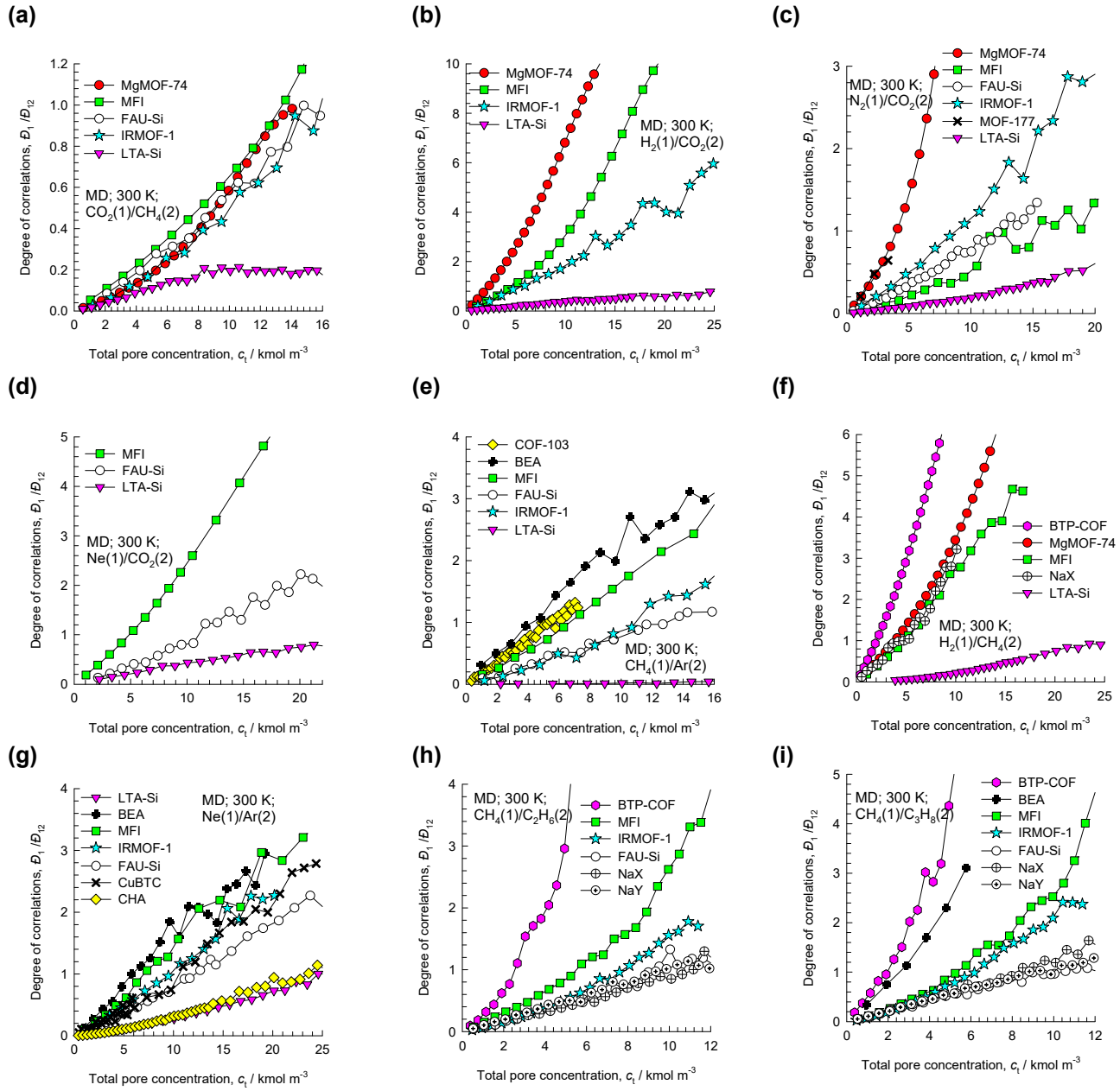

Figure S-16. MD simulation data for the degree of correlations, $Đ_1/Đ_{12}$, for diffusion of equimolar ($q_1 = q_2$) binary mixtures (a) CO_2/CH_4, (b) H_2/CO_2, (c) N_2/CO_2, (d) Ne/CO_2, (e) CH_4/Ar (f) H_2/CH_4, (g) Ne/Ar, (h) CH_4/C_2H_6, and (i) CH_4/C_3H_8 at 300 K in a variety of host materials. The x- axes represent the pore concentration, c_i, based on accessible pore volume.

5 Transient breakthroughs in fixed bed adsorbers

We first analyze the transient uptake of mixtures within a spherical micro-porous crystalline particle.

5.1 Transient uptake inside microporous crystals

The radial distribution of molar loadings, q_i, within a spherical crystallite, of radius r_c, is obtained from a solution of a set of differential equations describing the uptake

$$\rho \frac{\partial q_i(r,t)}{\partial t} = -\frac{1}{r^2}\frac{\partial}{\partial r}\left(r^2 N_i\right) \tag{S-57}$$

The intra-crystalline fluxes N_i, in turn, are related to the radial gradients in the molar loadings by Equation (S-51), or the simplified Equation (S-54) for the negligible correlations scenario. At time $t = 0$, i.e. the initial conditions, the molar loadings $q_i(r,0)$ at all locations r within the crystal are uniform (zero loadings). For all times $t \geq 0$, the exterior of the crystal is brought into contact with a bulk gas mixture at partial pressures p_{i0} that is maintained constant till the crystal reaches thermodynamic equilibrium with the surrounding gas mixture. At any time t, the component loadings at the surface of the particle $q_i(r_c,t) = q_i^*$ is in equilibrium with the bulk phase gas mixture with partial pressures p_{i0}. In the general case, the component loadings are calculated using the Ideal Adsorbed Solution Theory (IAST) of Myers and Prausnitz.[11] Alternatively, in some cases, the mixed-gas Langmuir equation (S-36) may be of sufficient accuracy. An important advantage of the use of the mixed-gas Langmuir model is that the matrix of the thermodynamic correction factors can be determined explicitly using Equation (S-48).

At any time t, during the transient approach to thermodynamic equilibrium, the spatial-averaged component loading within the crystallites of radius r_c is calculated using

$$\bar{q}_i(t) = \frac{3}{r_c^3}\int_0^{r_c} q_i(r,t) r^2 dr \tag{S-58}$$

Summing equation (S-58) over all *n* species in the mixture allows calculation of the *total average* molar loading of the mixture within the crystallite

$$\bar{q}_t(t,z) = \sum_{i=1}^{n} \bar{q}_i(t,z) \tag{S-59}$$

The spatial-averaged $\bar{q}_i(t)$ and $\bar{q}_t(t,z)$ can be compared directly with experimental transient uptake data.

For transient uptake of binary 1-2 mixtures, with partial pressures in the bulk gas phase, p_{10}, p_{20} the selectivity during transient uptake may be defined as

$$\frac{\bar{q}_1(t)/\bar{q}_2(t)}{p_{10}/p_{20}} \tag{S-60}$$

As $t \to \infty$, the uptake selectivity will approach the value of the adsorption selectivity

$$\frac{q_1^*/q_2^*}{p_{10}/p_{20}} \tag{S-61}$$

An exact analytic solution is obtainable for transient uptake of unary guest molecules, for which the flux relation can be described by the Fickian flux relation with constant, i.e. loading independent, Fick diffusivity *D*:

$$N = -\rho D \frac{\partial q}{\partial r} \tag{S-62}$$

The analytic solution, derived first by Geddes[44] to describe diffusion inside spherical vapor bubbles on distillation trays, is expressed as

$$\frac{\left(q^* - \bar{q}(t)\right)}{\left(q^* - q(r_c,0)\right)} = \frac{6}{\pi^2} \sum_{m=1}^{\infty} \frac{\exp(-m^2\pi^2 \frac{D}{r_c^2} t)}{m^2} \tag{S-63}$$

Equation (S-63) hold when (a) the initial locations at all locations *r* within the crystal are uniform, i.e. $q(r,0) = q(r_c,0)$, and (b) for all times $t \geq 0$, the exterior of the crystal is brought into contact with a

bulk fluid mixture at a bulk pressure $p(r_c,t)$, and molar loading , q^* that is maintained constant till the crystal reaches thermodynamic equilibrium with the surrounding fluid mixture.

For the more general case of binary mixture uptakes, described by the Maxwell-Stefan flux relations (S-51), there is no generally applicable analytical solution to describe transient diffusion of binary mixtures and the set of equations (S-51), (S-57), and (S-58), and (S-59) need to be solved numerically using robust computational techniques. However, see Krishna[45] for simplified approaches to describe transient mixture uptake using the matrix generalization of the Geddes[44] and Glueckauf[46] models.

Equations (S-57) are first subjected to finite volume discretization. One of two strategies can be adopted: (a) equi-volume discretization, or (b) equi-distant discretization; see Figure S-17. The choice of the discretization scheme used is crucially important in obtaining accurate, converged results. The choice of equi-volume slices is needed when the gradients of the loadings are particularly steep nearer to $r = r_c$. For either strategy, about 20 – 150 slices were employed in the simulations presented in this work, depending on the guest/host combination. Combination of the discretized partial differential equations (S-57) along with algebraic equations describing mixture adsorption equilibrium (IAST or mixed-gas Langmuir model), results in a set of differential-algebraic equations (DAEs), which are solved using BESIRK.[47] BESIRK is a sparse matrix solver, based on the semi-implicit Runge-Kutta method originally developed by Michelsen,[48] and extended with the Bulirsch-Stoer extrapolation method.[49] Use of BESIRK improves the numerical solution efficiency in solving the set of DAEs. The evaluation of the sparse Jacobian required in the numerical algorithm is largely based on analytic expressions.[27] Further details of the numerical procedures used in this work, are provided by Krishna and co-workers;[9, 27, 33, 50] interested readers are referred to our website that contains the numerical details.[50]

5.2 Modelling transient breakthroughs in fixed bed

We describe below the simulation methodology used to perform transient breakthrough calculations for fixed bed adsorbers (see schematics in Figure S-17, and Figure S-18). The simulation methodology

is the same as used in our earlier publications.[24, 25, 51, 52] For an *n*-component gas mixture flowing through a fixed bed maintained under isothermal, isobaric, conditions, the molar concentrations in the gas phase at any position and instant of time are obtained by solving the following set of partial differential equations for each of the species *i* in the gas mixture[5, 24, 27, 50]

$$-D_{ax}\frac{\partial^2 c_i(t,z)}{\partial z^2}+\frac{\partial c_i(t,z)}{\partial t}+\frac{\partial\left(v(t,z)c_i(t,z)\right)}{\partial z}+\frac{(1-\varepsilon)}{\varepsilon}\rho\frac{\partial \bar{q}_i(t,z)}{\partial t}=0;\quad i=1,2,...n \tag{S-64}$$

In equation (S-64), t is the time, z is the distance along the adsorber, ρ is the framework density, ε is the bed voidage, D_{ax} is the axial dispersion coefficient, v is the interstitial gas velocity, and $\bar{q}_i(t,z)$ is the *spatially averaged* molar loading within the crystallites of radius r_c, monitored at position z, and at time t. The time $t = 0$, corresponds to the time at which the feed mixture is injected at the inlet to the fixed bed. Prior to injection of the feed, it is assumed that an inert, non-adsorbing, gas flows through the fixed bed. In this model described by equation (S-64), the effects of all mechanisms that contribute to axial mixing are lumped into a single effect axial dispersion coefficient D_{ax}. Ruthven et al.[5] state that more detailed models that include radial dispersion are generally not necessary. They also make the following remark "when mass transfer resistance is significantly greater than axial dispersion, one may neglect the axial dispersion term and assume plug flow". This is the situation that manifests for kinetically controlled separations, the focus of the present article.Consequently, all of the analysis and breakthrough simulations were carried out using the plug flow assumption.

The term $\frac{\partial \bar{q}_i(t,z)}{\partial t}$ in equation (S-64) is determined by solving the set of equations (S-57), and (S-58), and (S-59). At any time t, and position z, the component loadings at the outer surface of the particle $q_i(r_c,t,z)$ is in equilibrium with the bulk phase gas mixture with partial pressures $p_i(t,z)$ in the bulk gas mixture. In the general case, the component loadings $q_i(r_c,t,z)$ are calculated using the Ideal Adsorbed Solution Theory (IAST) of Myers and Prausnitz.[11] Alternatively, in some cases, the mixed-gas Langmuir equation (S-36) may be of sufficient accuracy.

The *interstitial* gas velocity is related to the *superficial* gas velocity by

$$v = \frac{u}{\varepsilon} \tag{S-65}$$

In all of the simulations reported in this article, the entire bed of crystalline particles is considered to be devoid of adsorbates at time $t = 0$, i.e. we have the initial condition

$$t = 0; \quad q_i(0,z) = 0 \tag{S-66}$$

Equation (S-66) is relevant to the operation of the transient breakthrough experiments on a laboratory scale, but are not truly reflective of industrial operations.

At time, $t = 0$, the inlet to the adsorber, $z = 0$, is subjected to a step input of the n-component gas mixture and this step input is maintained till the end of the adsorption cycle when steady-state conditions are reached.

$$t \geq 0; \quad p_i(0,t) = p_{i0}; \quad u(0,t) = u_0 \tag{S-67}$$

where $u_0 = v_0\varepsilon$ is the superficial gas velocity at the inlet to the adsorber.

Typically, the adsorber length is divided into 100 slices, and each spherical crystallite was discretized into 20 - 150 equi-volume slices. The results thus obtained were confirmed to be of adequate accuracy. Combination of the discretized partial differential equations (PDEs) along with the algebraic equations describing mixture adsorption equilibrium (IAST, or mixed-gas Langmuir model, as appropriate), results in a set of differential-algebraic equations (DAEs), which are solved using BESIRK.[47] BESIRK is a sparse matrix solver, based on the semi-implicit Runge-Kutta method originally developed by Michelsen,[48] and extended with the Bulirsch-Stoer extrapolation method.[49] Use of BESIRK improves the numerical solution efficiency in solving the set of DAEs. The evaluation of the sparse Jacobian required in the numerical algorithm is largely based on analytic expressions.[27] Further details of the numerical procedures used in this work, are provided by Krishna and co-workers;[9, 27, 33, 50] interested readers are referred to our website that contains the numerical details.[50]

Transient breakthroughs in fixed bed adsorbers

For presenting the breakthrough simulation results, we use the dimensionless time, $\tau = \frac{tv}{L}$, obtained by dividing the actual time, t, by the characteristic time, $\frac{L}{v}$, where L is the length of adsorber, v is the interstitial gas velocity.[53]

For all the simulations reported in this article we choose the following: adsorber length, L = 0.3 m; cross-sectional area, A = 1 m^2; superficial gas velocity in the bed, u_0 = 0.04 m s^{-1}; voidage of the packed bed, ε = 0.4. Also, the total pressures is assumed to be constant along the length of the fixed bed. Please note that since the superficial gas velocity is specified, the specification of the cross-sectional area of the tube, A, is not relevant in the simulation results presented. The total volume of the bed is $V_{bed} = LA$. The volume of zeolite or MOF used in the simulations is $V_{ads} = LA(1-\varepsilon)$ = 0.18 m^3. If ρ is the framework density, the mass of the adsorbent in the bed is $m_{ads} = \rho LA(1-\varepsilon)$ kg. It is important to note that the volume of adsorbent, V_{ads}, includes the pore volume of the adsorbent material. In these breakthrough simulations we use the same volume of adsorbent in the breakthrough apparatus, i.e. (1 - ε) A L = 0.18 m^3 = 180 L.

5.3 List of Figures for Transient breakthroughs in fixed bed adsorbers

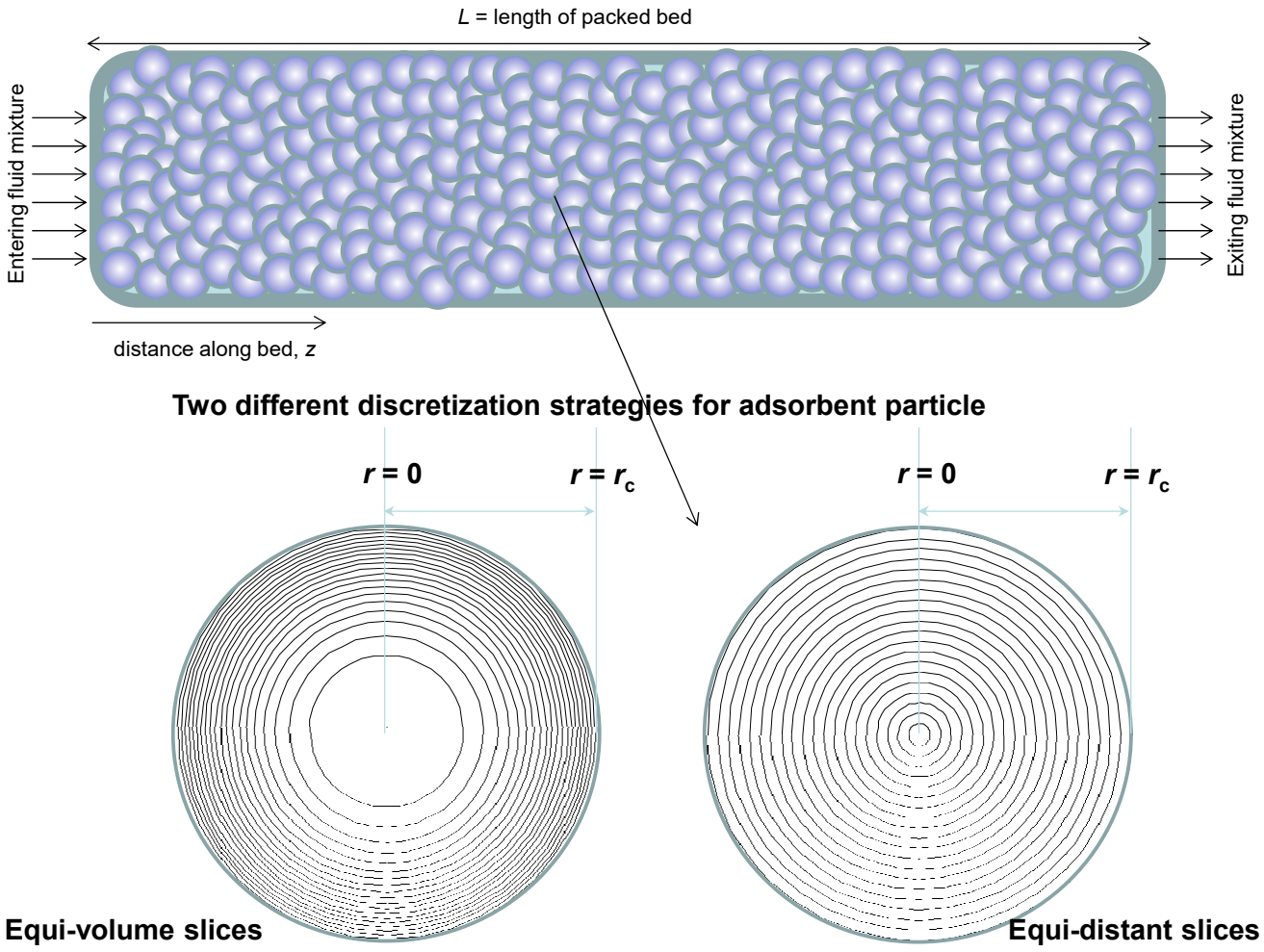

Figure S-17. Two different discretization schemes for a single spherical crystallite.

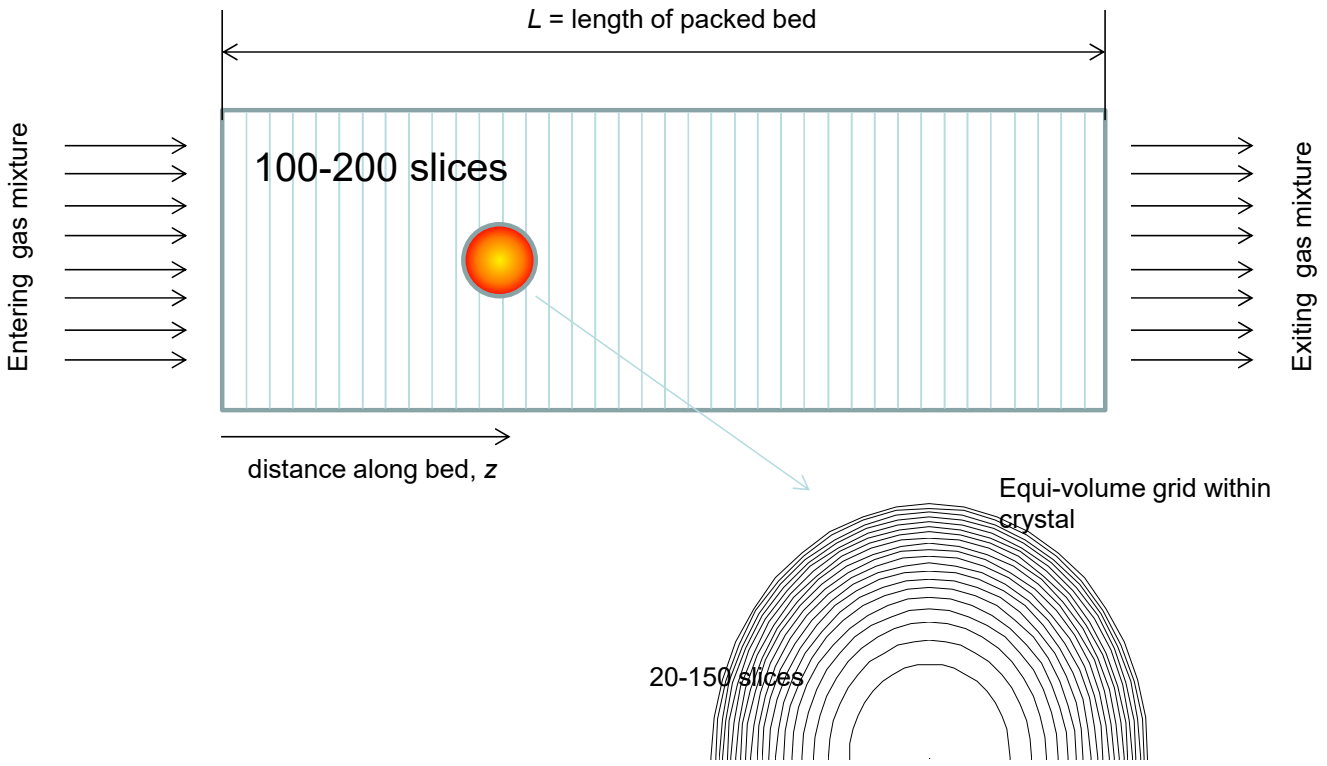

Figure S-18. Discretization scheme for fixed bed adsorber.

6 Separation of N_2/CH_4 mixtures

Many natural gas reserves contain nitrogen in concentrations ranging to about 20%.[54] To meet pipeline specifications, the nitrogen level must be reduced to below 4%.[55] A large majority of nitrogen removal facilities use cryogenic distillation, but such units are economical only for large capacity wells. For smaller reserves pressure swing adsorption technology has economic benefits, especially because the feed mixtures are available at high pressures.[54, 55] It is desirable to use adsorbents in pressure swing adsorption (PSA) units that are selective to N_2. For most known adsorbents, the adsorption selectivity for separation of N_2/CH_4 mixtures is in favor of CH_4 due to its higher polarizability. The notable exception is MIL-100(Cr), activated at 523 K, that shows adsorption selectivity in favor of N_2.[7]

One practical solution is to rely on diffusion selectivities by using microporous materials, such as LTA-4A zeolite, ETS-4 (ETS = Engelhard Titano Silicate; ETS-4 is also named as CTS-1 = Contracted Titano Silicate -1), and clinoptilolites, that have significantly higher diffusivities of N_2, compared to that of CH_4.[2, 40, 55-57]

6.1 Transient uptake of N_2/CH_4 mixtures in LTA-4A zeolite

The earliest study demonstrating the possibility of using LTA-4A zeolite, utilizing diffusion selectivities for separating $N_2(1)/CH_4(2)$ mixtures is contained in the classic paper of Habgood.[40] LTA-4A zeolite (also called 4A or NaA zeolite) contains extra-framework cations (containing 96Si, 96 Al, 96 Na^+ per unit cell; Si/Al=1). LTA-4A zeolite consists of cages of 743 $Å^3$ volume, separated by 4.11 Å × 4.47 Å 8-ring windows. The pore landscape and structural details of LTA-4A zeolite are provided in Figure S-19. The Na^+ cations partially block the window sites, leading to low magnitudes of guest diffusivities. The partial blocking of the windows enhances efficacy of kinetic separations, because it significantly enhances the ratio of the diffusivities of mobile and tardier species. Molecules jump one-at-a-time across the windows of LTA-4A. Extensive Molecular Dynamics (MD) simulations have confirmed that correlation effects are of negligible importance for mixture diffusion across cage-type

zeolites such as CHA, LTA, DDR, ERI that consist of cages separated by windows in the 3.4 Å – 4.2 Å size range.[16, 17, 26, 39] Consequently, the appropriate flux description is provided by Equation (S-54).

Habgood[40] performed experimental data on transient uptake of $N_2(1)/CH_4(2)$ mixtures in crystallites of LTA-4A; the data measured at 194 K with partial pressures (a) p_1 =50.9 kPa; p_2 = 49.1 kPa, and (b) p_1 =10 kPa; p_2 = 90 kPa are shown in Figure S-20(a,b). Nitrogen is a "pencil-like" molecule (4.4 Å × 3.3 Å) that can hop length-wise across the narrow windows; the "spherical" CH_4 (3.7 Å) is much more severely constrained and has a diffusivity that is 21.7 times lower than that of N_2. The adsorption strength of CH_4, as reflected in the Langmuir "*b*" parameter, is higher than that of N_2 by a factor 2.2; see unary isotherm data fits in Table S-1. The $N_2(1)/CH_4(2)$ mixture constitutes a combination of more-mobile-less-strongly-adsorbed-N_2 and tardier-more-strongly-adsorbed-CH_4. During the initial stages of the transient uptake, the pores of LTA-4A are predominantly richer in the more mobile N_2, but this is displaced by the more strongly adsorbed, tardier CH_4 molecules at longer times. This results in an overshoot in the N_2 uptake in both the experimental campaigns. The continuous solid lines in Figure S-20(a,b) are Maxwell-Stefan model simulations based on Equation (S-54); these simulations successfully capture the overshoot in the uptake of the more mobile N_2. The Maxwell-Stefan diffusivities used in the simulations are: $Đ_1/r_c^2 = 1.56\times10^{-5}$ s^{-1}; $Đ_2/r_c^2 = 7.2\times10^{-9}$ s^{-1}; these values based on the diffusivity data provided by Habgood.[40] The dashed lines are the simulations based on Equation (S-56), in which the thermodynamic correction factors are assumed to be described by $\Gamma_{ij} = \delta_{ij}$, i.e. $\begin{bmatrix}\Gamma_{11} & \Gamma_{12}\\ \Gamma_{21} & \Gamma_{21}\end{bmatrix} = \begin{bmatrix}1 & 0\\ 0 & 1\end{bmatrix}$; in this scenario, no N_2 overshoot is experienced. We conclude that the overshoots in the N_2 uptake, that signal the phenomenon of uphill diffusion,[12, 41] is engendered by thermodynamic coupling effects.

Based on his experimental results for transient uptake, Habgood filed a patent claiming that natural gas could be upgraded by removing the faster diffusing nitrogen using 4A zeolite and a kinetically controlled separation process at a low sub-ambient temperatures. We now investigate the consequence of thermodynamic coupling and uphill diffusion on $N_2(1)/CH_4(2)$ mixture separations in a fixed bed adsorber packed with LTA-4A adsorbent.

6.2 Separating N_2/CH_4 mixtures in fixed bed adsorbers packed with LTA-4A

We consider the separations of 20/80 $N_2(1)/CH_4(2)$ mixtures in a fixed bed adsorber using LTA-4A zeolite operating at a total pressure of 100 kPa, and T = 194 K. Figure S-21 show the transient breakthrough simulations for 20/80 $N_2(1)/CH_4(2)$ mixtures through fixed bed adsorber packed with LTA-4A crystals operating at 194 K, and total pressure p_t = 100 kPa. The y-axis is the % CH_4 at the adsorber outlet. The x-axis is the dimensionless time, $\tau = tv/L$, obtained by dividing the actual time, t, by the characteristic time, L/v. The continuous solid lines are simulations taking due account of intra-crystalline diffusion using Equation (S-54) with parameters: $Đ_1/r_c^2 = 1.56\times10^{-5}$ s^{-1}; $Đ_2/r_c^2 = 7.2\times10^{-9}$ s^{-1}. The dashed lines are the corresponding simulations based on Equation (S-56), in which the thermodynamic correction factors are assumed to be described by $\Gamma_{ij} = \delta_{ij}$, the Kronecker delta.

For the target purity of CH_4 is 96%, corresponding to prescribed pipeline specification, we can determine the moles of 96%+ pure CH_4 produced from a material balance on the adsorber. Expressed per kg of LTA-4A zeolite in the packed bed, the respective productivities are 0.09 and 0.002 mol kg^{-1}. Ignoring thermodynamic coupling effects severely underestimates the separation performance by a factor of about 50.

6.3 Transient uptake of N_2/CH_4 mixtures in Ba-ETS-4

By tuning the size of the microporous channels and using ETS-4 as adsorbent, CH_4 can be practically excluded from the pores favor the selective uptake of N_2 from $N_2(1)/CH_4(2)$ mixtures (see schematic in Figure S-22).[55, 56, 58] Nitrogen is a "pencil-like" molecule, of 4.4 Å × 3.3 Å size; CH_4 is a spherical molecule of 3.7 Å size. The pores of Ba-ETS-4 virtually exclude methane molecules.

The transient uptake data of Majumdar et al.[56] for Ba-ETS-4 are shown in Figure S-22(a,b) for (a) 10/90, and (b) 50/50 mixtures show overshoots in the uptake of the more mobile N_2.

Bhadra[55, 59] have developed a detailed mathematical model for a PSA scheme for purification of natural gas using Ba-ETS-4, using the steps shown in Figure S-23. In this scheme the inclusion of the

co-current blowdown step (suggested by Jayaraman et al.[57] for N_2/CH_4 mixture separations with clinoptilolites) increases the CH_4 recovery. At the end of the counter-current blowdown step, the bed contains both nitrogen (fast diffusing) and methane (slow diffusing). Thus if the bed is simply closed at one end and left for a period of time the nitrogen will diffuse out first followed by the methane so the system is, in effect, self-purging (fifth step in the sequence).

6.4 Separating N_2/CH_4 mixtures in fixed bed adsorbers with MIL-100(Cr)

Figure S-24 presents a comparison of transient breakthrough of 20/80 $N_2(1)/CH_4(2)$ mixture in fixed bed adsorber packed with MIL-100(Cr) operating at 283 K, and total pressure p_t = 1 MPa. In the simulations intra-crystalline diffusional influences are neglected. We note that a significant amount of CH_4 gets adsorbed. This implies that recovery of 96%+ pure CH_4 is likely to be unacceptably low.

6.5 List of Tables for Separation of N2/CH4 mixtures

Table S-1. 1-site Langmuir parameters for N_2 and CH_4 in LTA-4A zeolite at 194 K. These parameters have been fitted from the isotherm data scanned from the paper by Habgood[40]

	q_{sat} mol kg^{-1}	b Pa^{-1}
N_2	3.6	9.4×10^{-5}
CH_4	3.6	2.08×10^{-4}

6.6 List of Figures for Separation of N2/CH4 mixtures

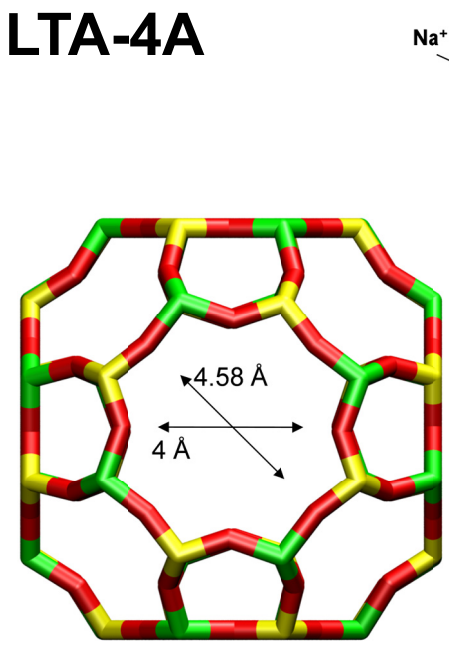

LTA-4A

The window dimension calculated using the van der Waals diameter of framework atoms = 2.7 Å is indicated above by the arrow.

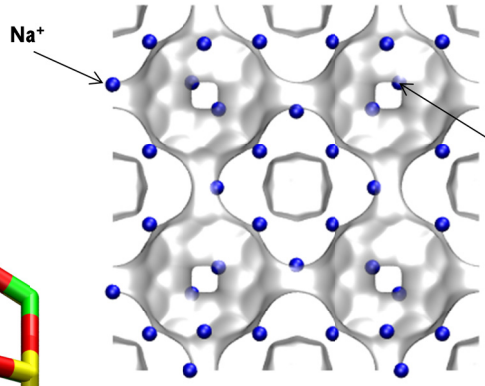

LTA-4A (96 Na+)

	LTA-4A
a /Å	24.555
b /Å	24.555
c /Å	24.555
Cell volume / Å^3	14805.39
conversion factor for [molec/uc] to [mol per kg Framework]	0.0733
conversion factor for [molec/uc] to [kmol/m^3]	0.2991
ρ [kg/m3] (with cations)	1529.55
MW unit cell [g/mol(framework+cations)]	13637.27
ϕ, fractional pore volume	0.375
open space / Å^3/uc	5552.0
Pore volume / cm^3/g	0.245
Surface area /m^2/g	
DeLaunay diameter /Å	4.00

Figure S-19. Structural details of LTA-4A zeolite.

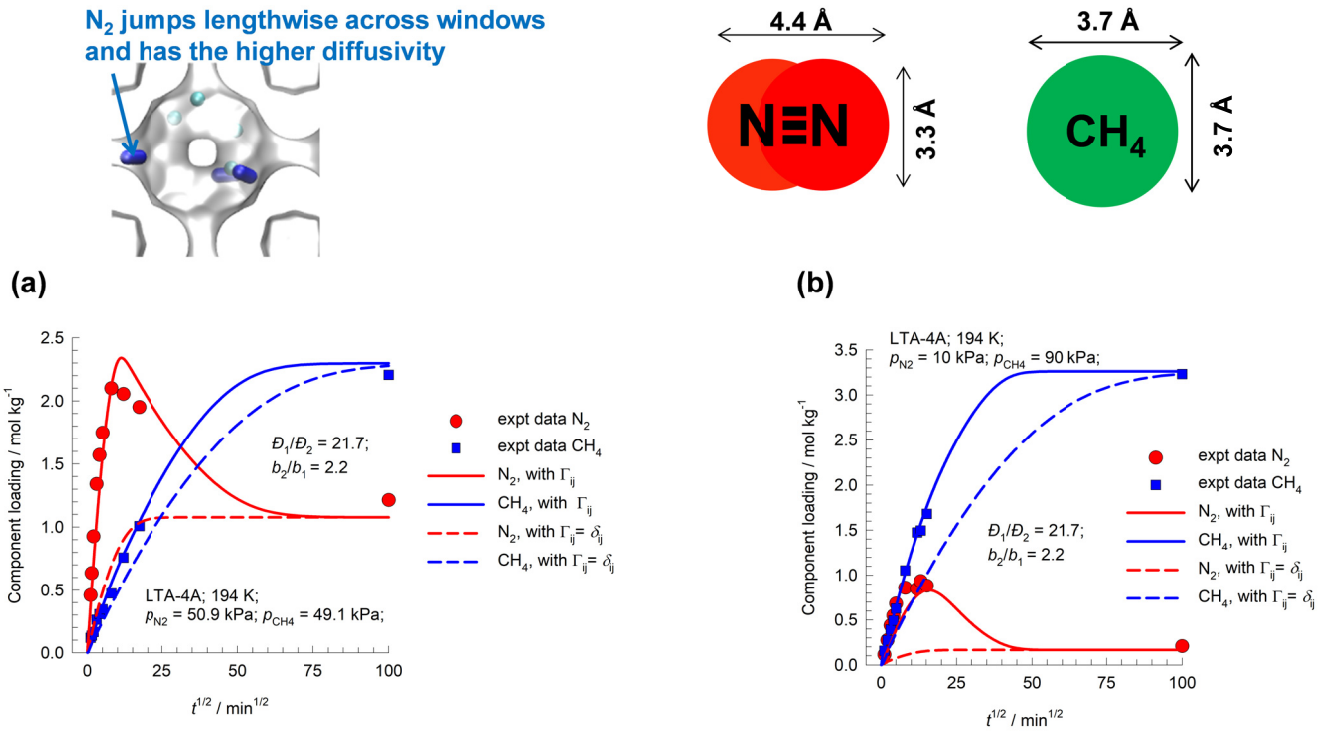

Figure S-20. (a, b) Experimental data of Habgood[40] on transient uptake of $N_2(1)/CH_4(2)$ mixture within LTA-4A crystals, exposed to binary gas mixtures at partial pressures (a) p_1 =50.9 kPa; p_2 = 49.1 kPa, and (b) p_1 =10 kPa; p_2 = 90 kPa at 194 K. The unary isotherms are provided in Table S-1. The continuous solid lines are Maxwell-Stefan model simulations based on Equation (S-54). The dashed lines are the simulations based on Equation (S-56), in which the thermodynamic correction factors are assumed to be described by $\Gamma_{ij} = \delta_{ij}$, the Kronecker delta. The Maxwell-Stefan diffusivities used in the simulations are: $Đ_1/r_c^2 = 1.56\times10^{-5}$ s^{-1}; $Đ_2/r_c^2 = 7.2\times10^{-9}$ s^{-1}.

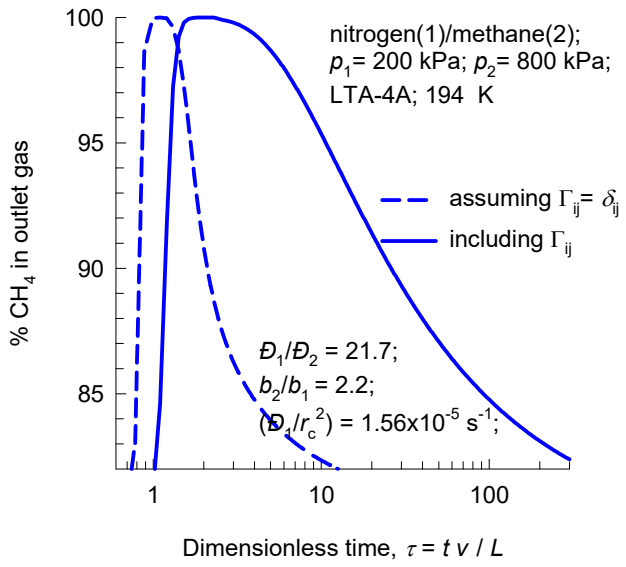

Figure S-21. Transient breakthrough of 20/80 $N_2(1)/CH_4(2)$ mixture in fixed bed adsorber packed with LTA-4A crystals operating at 194 K, and total pressure p_t = 100 kPa. The continuous solid lines are Maxwell-Stefan model simulations based on Equation (S-54). The dashed lines are the simulations based on Equation (S-56), in which the thermodynamic correction factors are assumed to be described by $\Gamma_{ij} = \delta_{ij}$, the Kronecker delta. The Maxwell-Stefan diffusivities used in the simulations are: $Đ_1/r_c^2$ = 1.56×10^{-5} s^{-1}; $Đ_2/r_c^2$ = 7.2×10^{-9} s^{-1}.

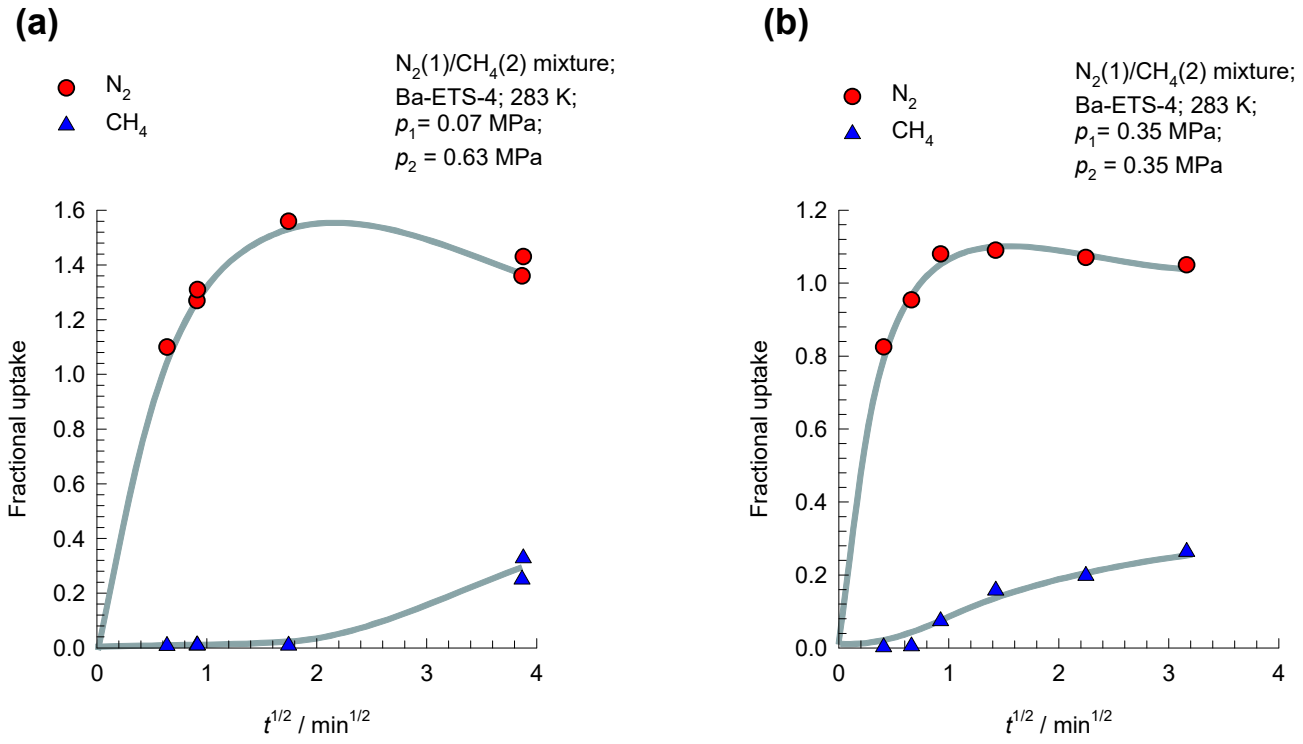

Figure S-22. (a, b) The transient uptake data of Majumdar et al.[56] for Ba-ETS-4 for (a) 10/90, and (b) 50/50 mixtures in Ba-ETS-4 at 283 K and 0.7 MPa. Note that the *y*-axes are plotted in terms of fractional uptake.

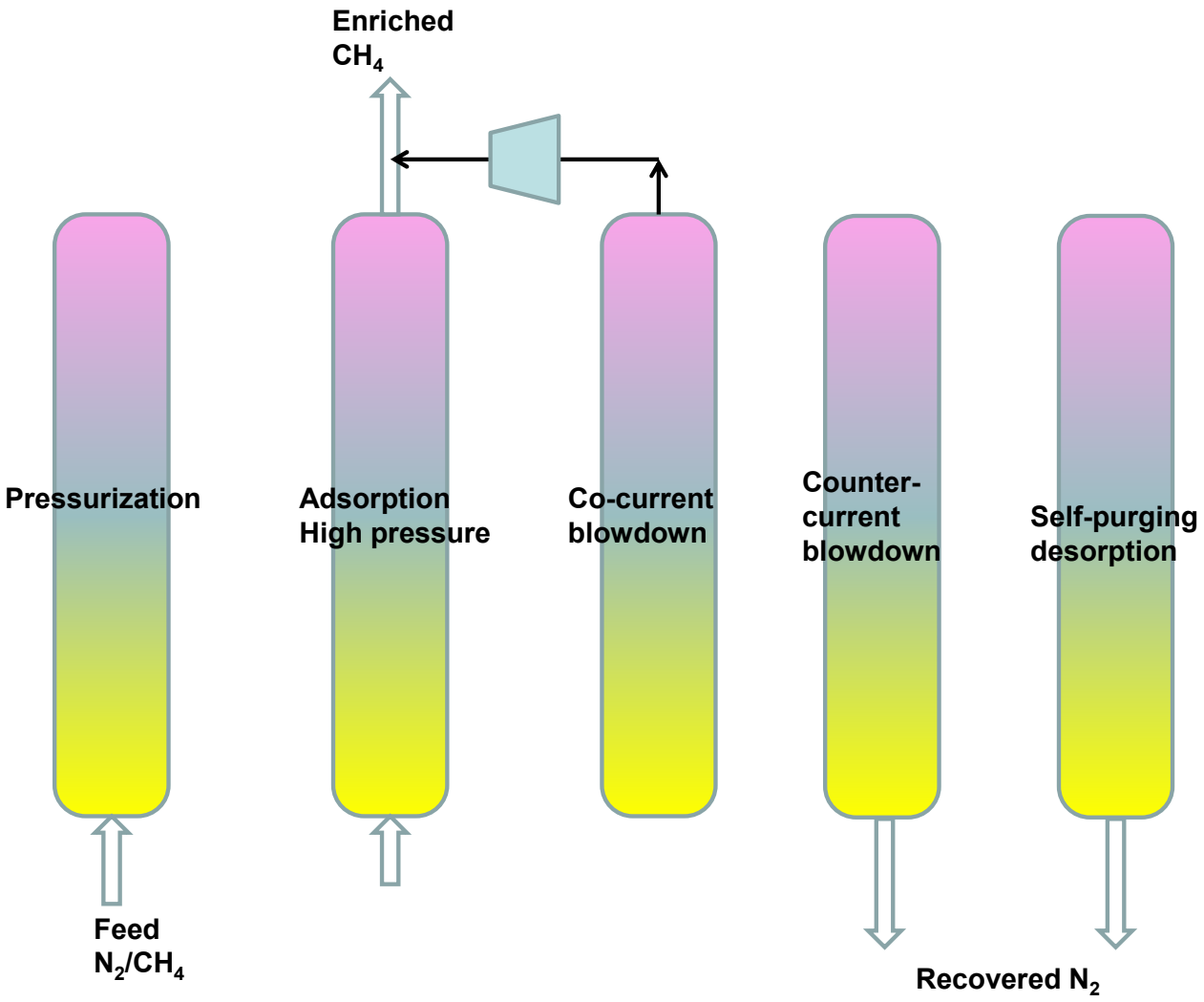

Figure S-23. Different steps in the production of purified CH_4 using an adsorbent such as LTA-4A zeolite, Ba-ETS-4, and clinoptilolite, that rely on kinetic selectivity. The scheme shows the sequence of processing of a single bed in a multi-bed PSA scheme. Adapted from Jayaraman et al.[57]

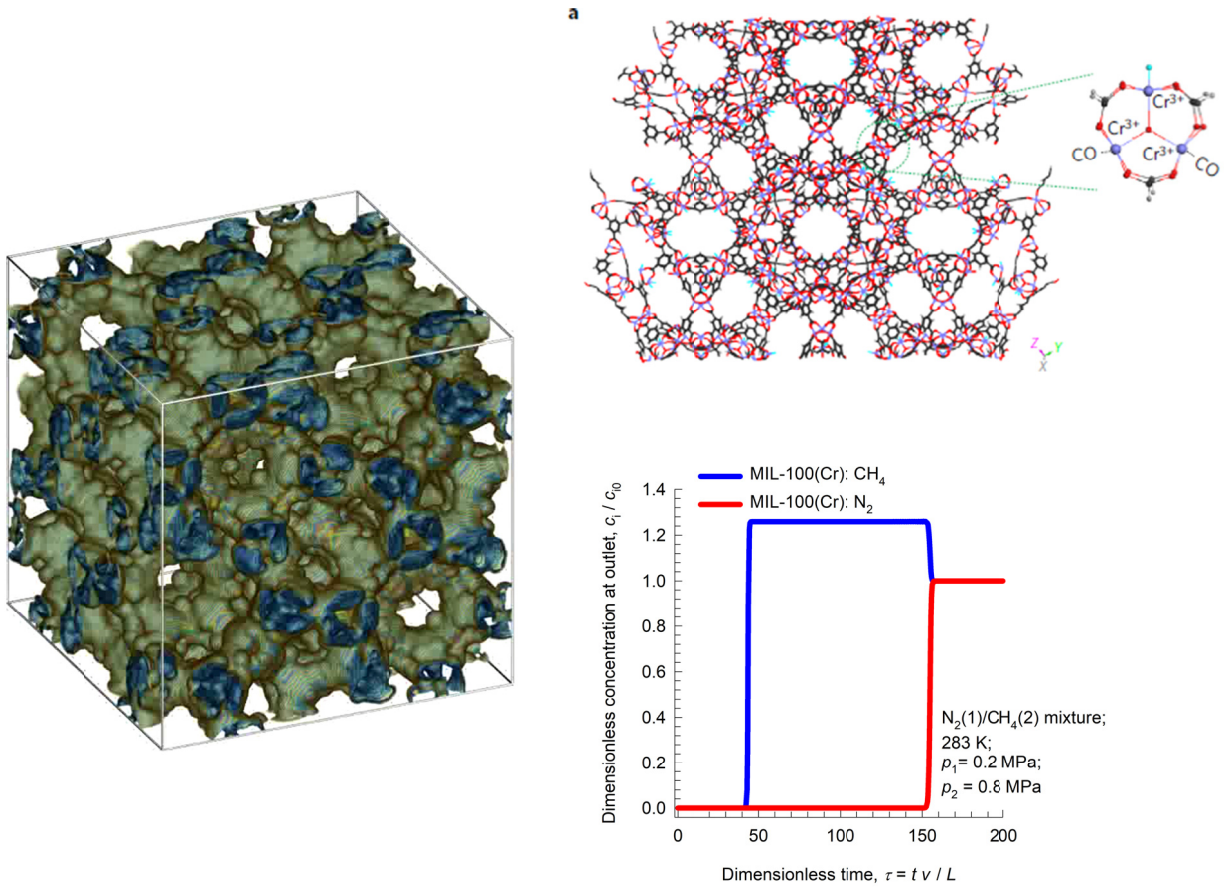

Figure S-24. Structure of MIL-100 (Cr). Transient breakthrough of 20/80 N_2(1)/CH_4(2) mixture in fixed bed adsorber packed with MIL-100(Cr) operating at 283 K, and total pressure p_t = 1 MPa. The unary isotherms are those reported by Yoon et al.[7]

7 Separation of CO_2/C_2H_6 mixtures with DDR zeolite

DDR consists of cages of 277.8 $Å^3$ volume, separated by 3.65 Å × 4.37 Å 8-ring windows; the pore landscapes and structural details are provided in Figure S-25, and Figure S-26. The guest molecules jump one-at-a-time across the narrow 8-ring windows. Consequently, correlation effects are of negligible importance; the intra-crystalline fluxes N_i, in turn, are related to the radial gradients in the molar loadings by Equation (S-54).

Binder et al.[60] and Lauerer et al.[61] report a set of three mixture uptake experiments with 1:1, 2:1, and 3:1 partial pressure ratios for CO_2 and C_2H_6 in the gas phase.

Experiment 1: 1:1 $CO_2(1)/C_2H_6(2)$ bulk gas mixture at 298 K, p_1 = 20 kPa, p_2 = 20 kPa.

Experiment 2: 2:1 $CO_2(1)/C_2H_6(2)$ bulk gas mixture at 298 K, p_1 = 40 kPa, p_2 = 20 kPa.

Experiment 3: 3:1 $CO_2(1)/C_2H_6(2)$ bulk gas mixture at 298 K, p_1 = 60 kPa, p_2 = 20 kPa.

The data on the unary isotherms of CO_2 and C_2H_6 at 298 K are provided in Figure 36, Chapter 4 of the PhD dissertation of Binder.[62] The unary isotherms for both CO_2, and C_2H_6 can be described adequately by a single-site Langmuir isotherm

$$q_i = \frac{q_{i,sat} b_i p_i}{1 + b_i p_i} \tag{S-68}$$

The single-site Langmuir parameters are provided in Table S-2. On the basis of comparisons with IAST calculations, Krishna[25] has established that the mixed-gas Langmuir model predicts the mixture adsorption equilibrium with good accuracy.

Both of the guest molecules CO_2, and C_2H_6 jump length-wise across the 8-ring windows of DDR zeolite. The cross-sectional dimension of CO_2 is smaller than that of C_2H_6 (see Figure S-27), and therefore the intra-crystalline M-S diffusivity of CO2 is significantly higher than that of C_2H_6. The diffusivity input values of $Đ_1/r_c^2$, and $Đ_2/r_c^2$ are taken from earlier work[25]:

Experiment 1: $Đ_1/r_c^2$ = 0.125 s^{-1}; $Đ_1/Đ_2$ = 1333.

Experiment 2: $Đ_1/r_c^2 = 9.375\times10^{-3}$ s^{-1}; $Đ_1/Đ_2 = 100$.

Experiment 3: $Đ_1/r_c^2 = 6.25\times10^{-3}$ s^{-1}; $Đ_1/Đ_2 = 50$.

For the uptake simulations, the crystallite radius was taken to be 40 μm.

Figure S-28(a,b,c) show the experimental data of Binder et al.[60] and Lauerer et al.[61] (indicated by symbols) for spatial-averaged transient uptake of (a) 1:1 (b) 2:1, and (c) 3:1 $CO_2(1)/C_2H_6(2)$ gas mixtures within crystals of DDR zeolite at 298 K. The continuous solid lines are simulations of the transient uptake using the flux relations (S-54). The Maxwell-Stefan model captures the overshoots in CO_2 loadings with good accuracy for all three cases. The overshoots in the CO_2 uptake signal the phenomenon of uphill diffusion, engendered by thermodynamic coupling.[25, 63] In order to confirm that thermodynamic coupling effects are responsible for the overshoots, we also performed transient uptake in which the thermodynamic correction factors are assumed to be described by $\Gamma_{ij} = \delta_{ij}$, the Kronecker delta. The dashed lines in Figure S-28(a,b,c) represent the simulation results based on Equation (S-56); with this simplified model, no overshoots in the CO_2 uptake are experienced. An important consequence of thermodynamic coupling effects is that supra-equilibrium loadings of CO_2 are realized during the early transience. We now investigate the consequence of thermodynamic coupling and uphill diffusion on CO_2/C_2H_6 mixture separations in a fixed bed adsorber packed with DDR adsorbent.

7.1 Separating CO_2/C_2H_6 mixtures in fixed bed adsorber packed with DDR zeolite

The separation of CO_2/C_2H_6 is relevant in the context of natural gas processing. Current technologies for CO_2/C_2H_6 separations use extractive distillation because of CO_2/C_2H_6 azeotrope formation.[64] Another alternative is to combine distillation technology with membrane separations; for this purpose cross-linked polyethylene oxide (XLPEO) membranes have demonstrated to have good separation potential.[23, 65, 66] The Binder/Lauerer uptake experiments suggest the possibility of diffusion-selective purification of ethane by selective removal of CO_2 present as impurities in mixtures with ethane.

To demonstrate the concept of diffusion-selective separations, we carried out transient breakthrough simulations in a fixed bed adsorber packed with crystallites of DDR.

Separation of CO2/C2H6 mixtures with DDR zeolite

Figure S-29(a,b) show the transient breakthrough simulations for 1:1 CO_2/C_2H_6 mixtures through fixed bed adsorber packed with DDR crystals operating at 298 K, and total pressure p_t = 40 kPa. The *y*-axis is the % component at the adsorber outlet. The *x*-axis is the dimensionless time, $\tau = tv/L$, obtained by dividing the actual time, *t*, by the characteristic time, L/v. The continuous solid lines are simulations taking due account of intra-crystalline diffusion using Equation (S-54) with parameters: $Đ_1/r_c^2$ = 0.00125 s^{-1}; $Đ_1/Đ_2$ = 1333.

We note that C_2H_6 breaks through earlier and can be recovered in purified form during the early stages of the transient operations, prior to the breakthrough of CO_2. The dashed lines in Figure S-29(a,b) are the simulations in which thermodynamic coupling effects are ignored and Equation (S-56) is used to describe the transfer fluxes. In this scenario, the breakthrough of CO_2 occurs earlier and therefore the productivity of purified C_2H_6 is lower. If we assume that the target purity of C_2H_6 is 90%, we can determine the moles of 90%+ pure C_2H_6 produced from a material balance on the adsorber. Expressed per kg of DDR zeolite in the packed bed, the respective productivities are 0.18 and 0.054 mol kg^{-1}, respectively. Ignoring thermodynamic coupling effects severely underestimates the separation performance.

The breakthrough simulations indicated by the dotted lines in Figure S-29(c) correspond to the scenario in which intra-crystalline diffusion limitations are considered to be of negligible importance, i.e. $Đ_1/r_c^2 \to \infty$; $Đ_2/r_c^2 \to \infty$. In this "equilibrium" scenario, CO_2 breaks through earlier and purified C_2H_6 cannot be produced during the adsorption phase of fixed bed operations.

7.2 List of Tables for Separation of CO2/C2H6 mixtures with DDR zeolite

Table S-2. 1-site Langmuir parameters for CO_2 and C_2H_6 in DDR zeolite at 298 K. These parameters have been fitted from the data scanned from Figure 36, Chapter 4 of the PhD dissertation of Binder.[62]

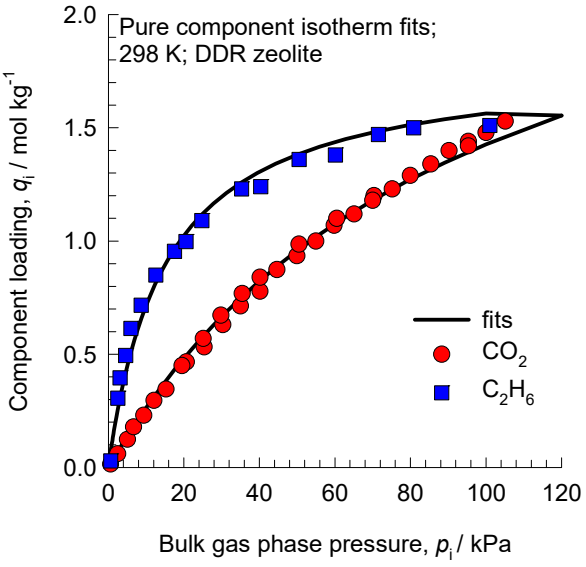

	q_{sat} mol kg^{-1}	b Pa^{-1}
CO_2	2.8	1.04×10^{-5}
C_2H_6	1.8	6.6×10^{-5}

7.3 List of Figures for Separation of CO2/C2H6 mixtures with DDR zeolite

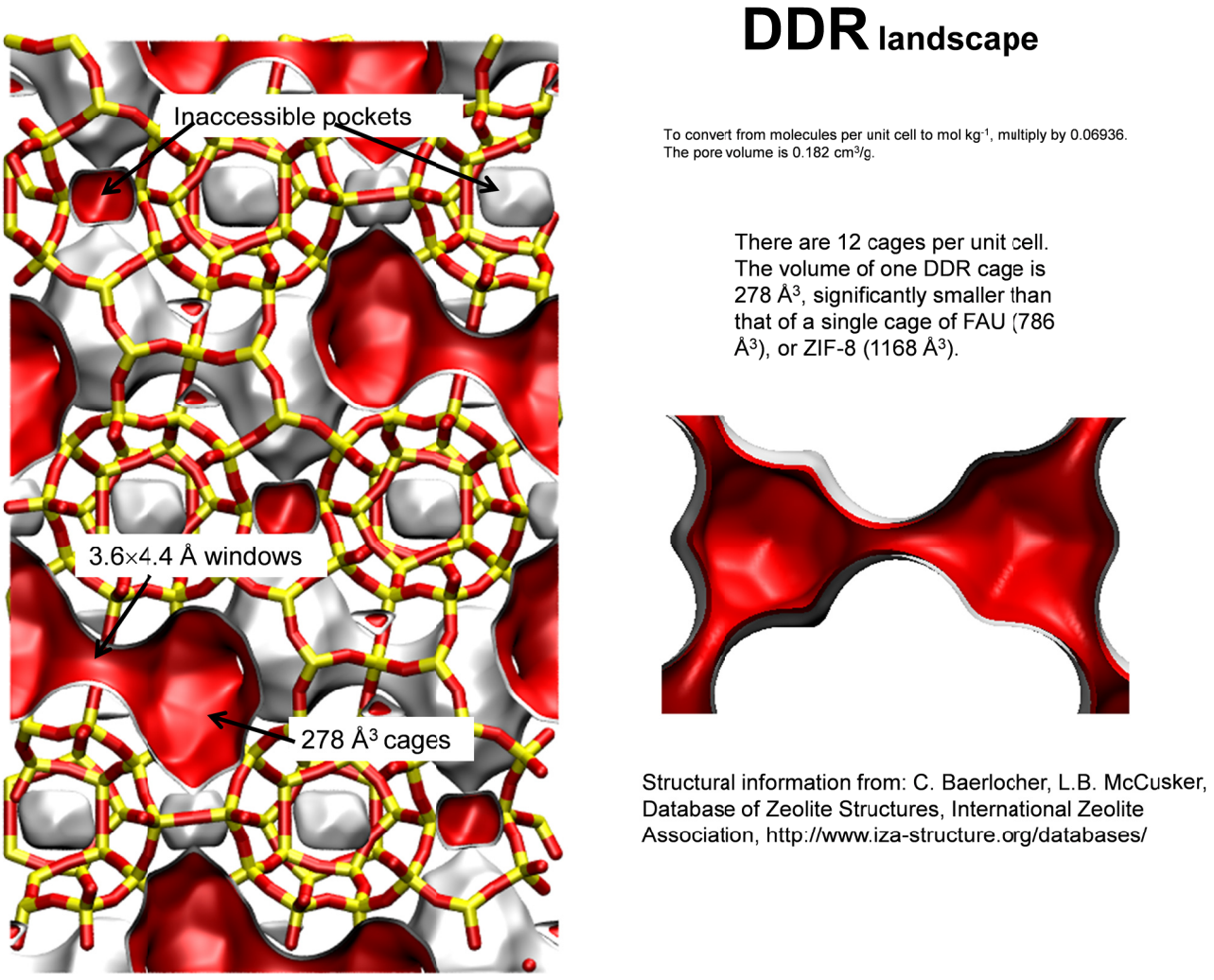

Figure S-25. Pore landscape of all-silica DDR zeolite.

DDR window and pore dimensions

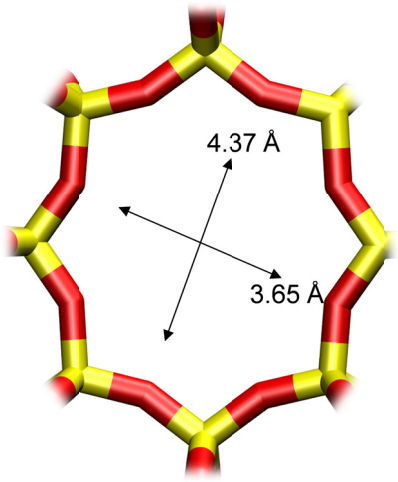

DDR

The window dimensions calculated using the van der Waals diameter of framework atoms = 2.7 Å are indicated above by the arrows.

	DDR
a /Å	24.006
b /Å	13.86
c /Å	40.892
Cell volume / Å^3	13605.72
conversion factor for [molec/uc] to [mol per kg Framework]	0.0693
conversion factor for [molec/uc] to [kmol/m^3]	0.4981
ρ [kg/m3]	1759.991
MW unit cell [g/mol(framework)]	14420.35
ϕ, fractional pore volume	0.245
open space / Å^3/uc	3333.5
Pore volume / cm^3/g	0.139
Surface area /m^2/g	350.0
DeLaunay diameter /Å	3.65

Figure S-26. Structural details of all-silica DDR zeolite.

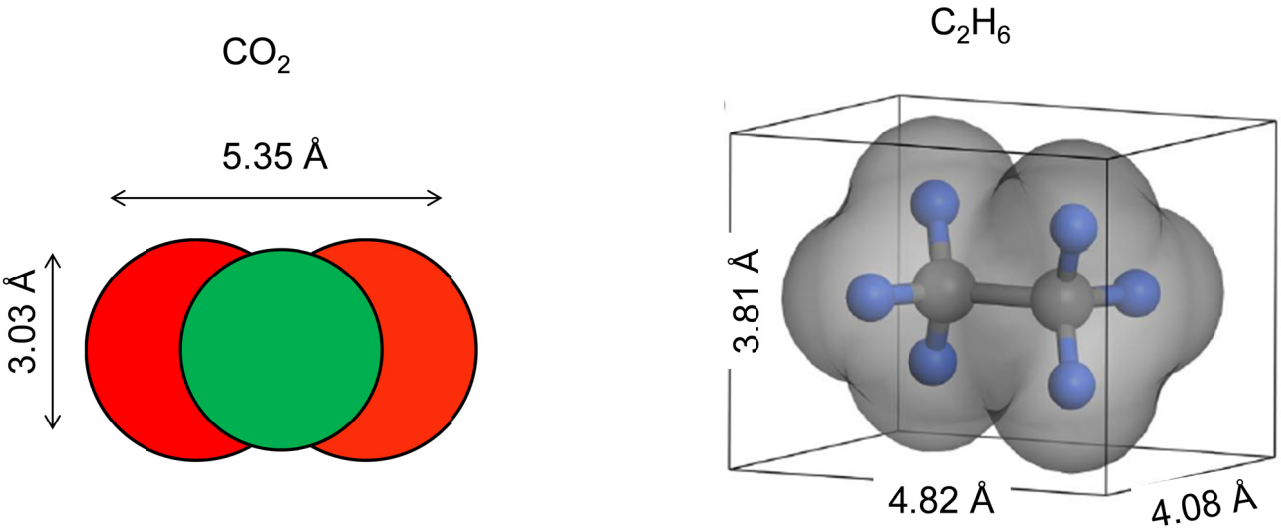

Figure S-27. Molecular dimensions of CO_2 and C_2H_6. The molecular dimensions of C_2H_6 are taken from Lin et al.[67]

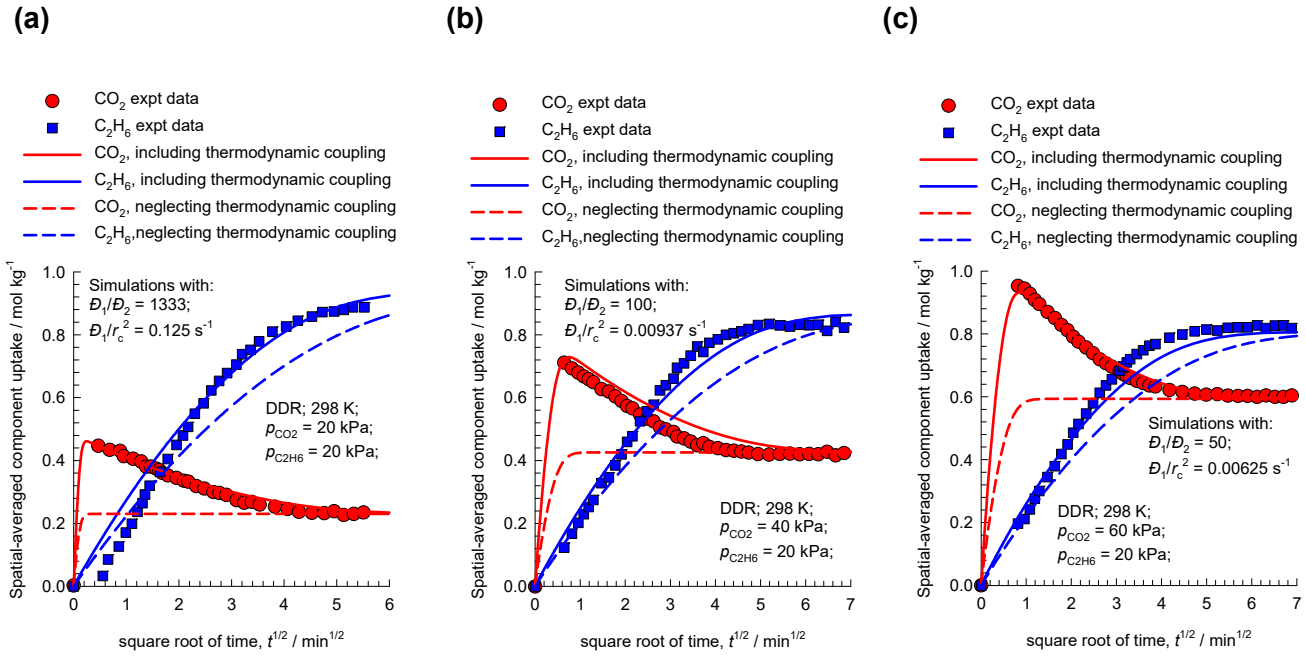

Figure S-28. (a, b, c) Experimental data of Binder et al.[60] and Lauerer et al.[61] (indicated by symbols) for spatial-averaged transient uptake of (a) 1:1 (b) 2:1, and (c) 3:1 $CO_2(1)/C_2H_6(2)$ gas mixtures within crystals of DDR zeolite at 298 K. The continuous solid lines are Maxwell-Stefan model simulations based on Equation (S-54). The dashed lines are the simulations based on Equation (S-56), in which the thermodynamic correction factors are assumed to be described by $\Gamma_{ij} = \delta_{ij}$, the Kronecker delta.

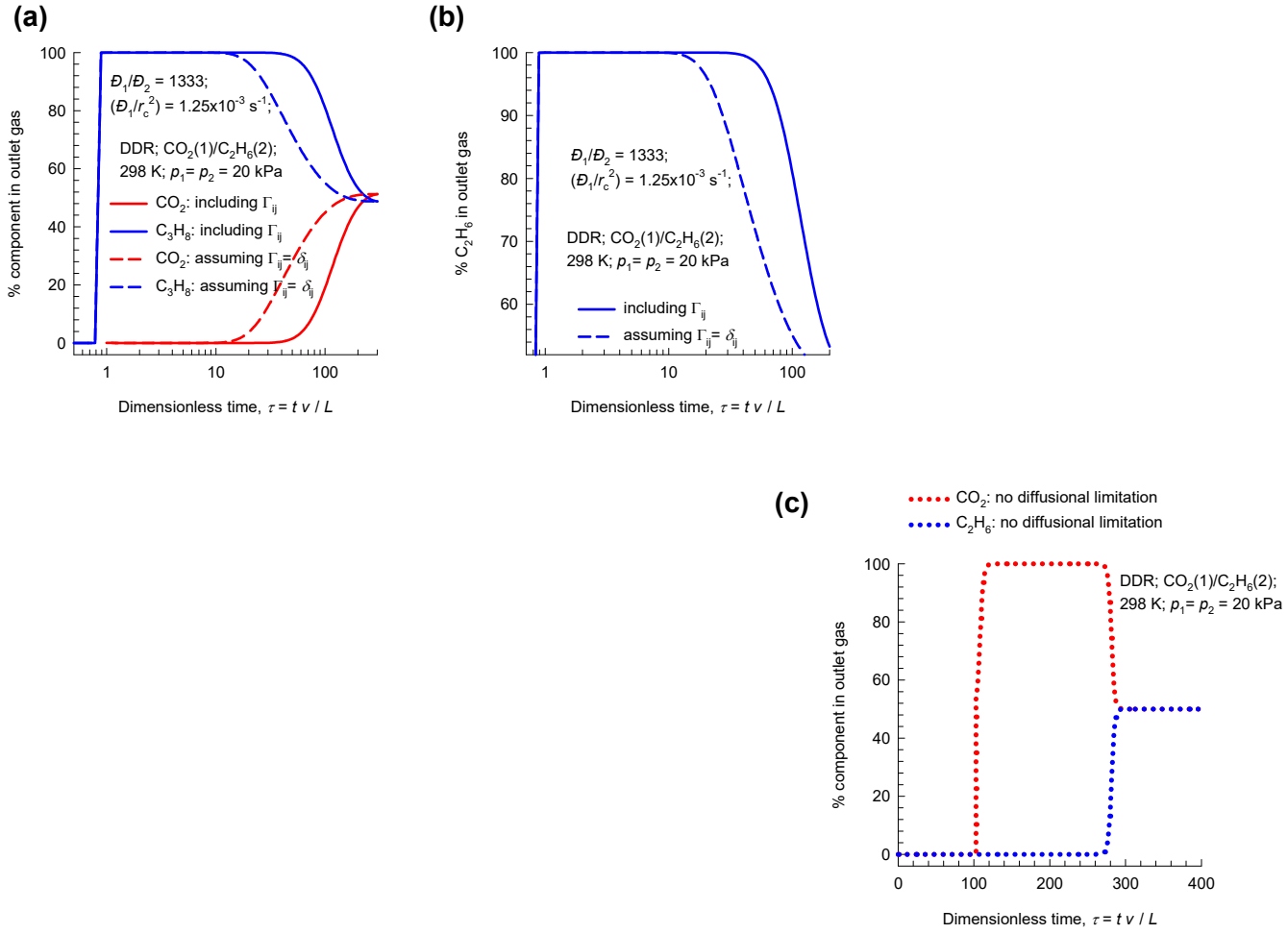

Figure S-29. (a, b, c) Transient breakthrough of 1:1 CO_2/C_2H_6 mixtures through fixed bed adsorber packed with DDR crystals operating at 298 K, and total pressure p_t = 40 kPa. The continuous solid lines are simulations based on Equation (S-54) for the transfer fluxes, with parameters: $Đ_1/r_c^2$ = 0.00125 s^{-1}; $Đ_1/Đ_2$ = 1333. The dashed lines are the simulations based on Equation (S-56), in which the thermodynamic correction factors are assumed to be described by $\Gamma_{ij} = \delta_{ij}$, the Kronecker delta. The dotted lines in (c) are simulations in which intra-crystalline diffusion limitations are considered to be of negligible importance, i.e. $Đ_1/r_c^2 \to \infty$; $Đ_2/r_c^2 \to \infty$.

8 Separation of O_2/N_2 mixtures

The separation of air to produce N_2 and O_2 of high purities is one of the most important industrial processes that uses pressure swing adsorption technology.[5, 68] The process technologies are geared to either production of purified O_2 or purified N_2. Cryogenic distillation has been the common technologies for this separation, but adsorptive separations offer energy efficient alternatives. Purified O_2 is required for a wide variety of applications that include portable adsorption units for medical applications and in space vehicles. Nitrogen is required in applications where it is desired or necessary to exclude oxygen. Typical industrial applications include preservation of fruit and produce during trucking, the blanketing of fuel tanks of fighter aircraft, the inerting of reactors in a number of pharmaceutical processes, laser cutting. N_2 is required for use in laboratory analytical equipment such as GC, LC, LCMS, FTIR, ICP, and in glove boxes.

For production of purified O_2, cation-exchanged zeolites LTA-5A (also called 5A or NaCaA zeolite containing 96 Si, 96 Al, 32 Na^+, 32 Ca^{++} per unit cell; Si/Al=1), NaX (also called 13 X zeolite, containing 106 Si, 86 Al, 86 Na^+ per unit cell; Si/Al=1.23), CaX, LiX, and LiLSX (= low silica LiX zeolite) and can be used as selective adsorbents.[4, 68-71] The larger permanent quadrupole of N_2 compared to that of O_2 is responsible for the stronger adsorption strength of N_2 on these zeolites.[4] Both O_2, and N_2 have similar polarizabilities and magnetic susceptibilies. However, the quadrupole moment of N_2 is about 4 times that of O_2. The Skarstrom cycle can be used, with modifications such as the introduction of a pressure equalization step, for production of enriched O_2 using say LiLSX zeolite. The different steps (stages) in the operation of a single bed for producing oxygen in small-scale units are shown in Figure S-30, that has been adapted from Ruthven and Farooq.[6] Desorption of the preferentially adsorbed nitrogen is achieved by pressure reduction followed by purging with a fraction of the oxygen product to remove the nitrogen from the interstices of the bed. Further details are available in the excellent texts of Ruthven et al.[5], and Yang.[2, 72]

For production of purified N_2 from air, a different strategy is often employed that rely on diffusion selectivity.[42, 73] Diffusion-selective separation are achieved with Carbon Molecular Sieve (CMS), and LTA-4A zeolite. Diffusion limitations manifest in LTA-4A because the window regions are partially blocked by the cations; see pore landscape in Figure S-31. The same basic Skarstrom cycle can be used, with the kinetically selective 4A zeolite or carbon molecular sieve adsorbent, in a nitrogen production process. However, in such a system purging with nitrogen to remove the faster diffusing oxygen from the bed is undesirable since, as well as wasting product, a certain fraction of the slowly diffusing nitrogen will be adsorbed, thus reducing the capacity for oxygen during the next adsorption step. At the end of the counter-current blowdown step (see Figure S-32), the adsorbent contains both oxygen (fast diffusing) and nitrogen (slow diffusing). Thus if the bed is simply closed at one end and left for a period of time the oxygen will diffuse out first followed by the nitrogen so the system is, in effect, self purging.[5, 6]

8.1 Transient uptake of O_2/N_2 mixtures in LTA-4A

Figure S-33 presents the simulations of transient uptake of $O_2(1)/N_2(2)$ mixture in LTA-4A zeolite at 298 K and total pressure of 600 kPa. The partial pressures of the components in the bulk gas phase are p_1 = 126 kPa, p_2 = 474 kPa. The continuous solid lines are Maxwell-Stefan model simulations based on Equation (S-54), that accounts for thermodynamic coupling. The O_2 overshoot signals uphill diffusion.[12,41] The dashed lines are the simulations based on Equation (S-56), in which the thermodynamic correction factors are assumed to be described by $\Gamma_{ij} = \delta_{ij}$, the Kronecker delta; in this scenario there is no O_2 overshoot. The conclusion to be drawn is that the O_2 overshoot is engendered by thermodynamic coupling effects.

8.2 O_2/N_2 mixture separations in fixed bed adsorber packed with LTA-4A

Diffusion-selective separations may be exploited for production of pure N_2 relying on the significantly lower diffusivity of N_2 as compared to O_2, and uphill diffusion. To demonstrate the feasibility of this concept, Figure S-34 presents transient breakthrough simulations for a fixed bed operating at 298 K and

total pressure of 600 kPa. The continuous solid lines are Maxwell-Stefan model simulations based on Equation (S-54), that accounts for thermodynamic coupling.[42, 73] Neglecting thermodynamic coupling effects leads to lower productivity of purified N_2, during the initial transience.

For an assumed target purity of 95%+ N_2, we can determine the moles of 95%+ pure N_2 produced from a material balance on the adsorber. Expressed per kg of LTA-4A zeolite in the packed bed, the respective productivities are 0.066 and 0.036 mol kg^{-1}. Ignoring thermodynamic coupling effects underestimates the separation performance by about 40%.

8.3 List of Tables for Separation of O2/N2 mixtures

Table S-3. 1-site Langmuir parameters for O_2 and N_2 in LTA-4A zeolite at 298 K. These isotherm data are taken from Farooq et al.[42, 73] These data are for RS-10, a modified version of LTA-4A that affords higher diffusion selectivity in favor of O_2.

	q_{sat} mol kg^{-1}	b Pa^{-1}
O_2	1.91	5.65×10^{-7}
N_2	1.91	1.13×10^{-6}

On the basis of the information provided in Table 3 of Farooq et al.[42]

The crystal framework density $\rho = 1100$ kg m^{-3};

The Maxwell-Stefan diffusivities are

$Đ_1/r_c^2 = 2.75\times10^{-2}$ s^{-1}; $Đ_2/r_c^2 = 7.5\times10^{-4}$ s^{-1}; $Đ_1/Đ_2 = 36.7$.

8.4 List of Figures for Separation of O2/N2 mixtures

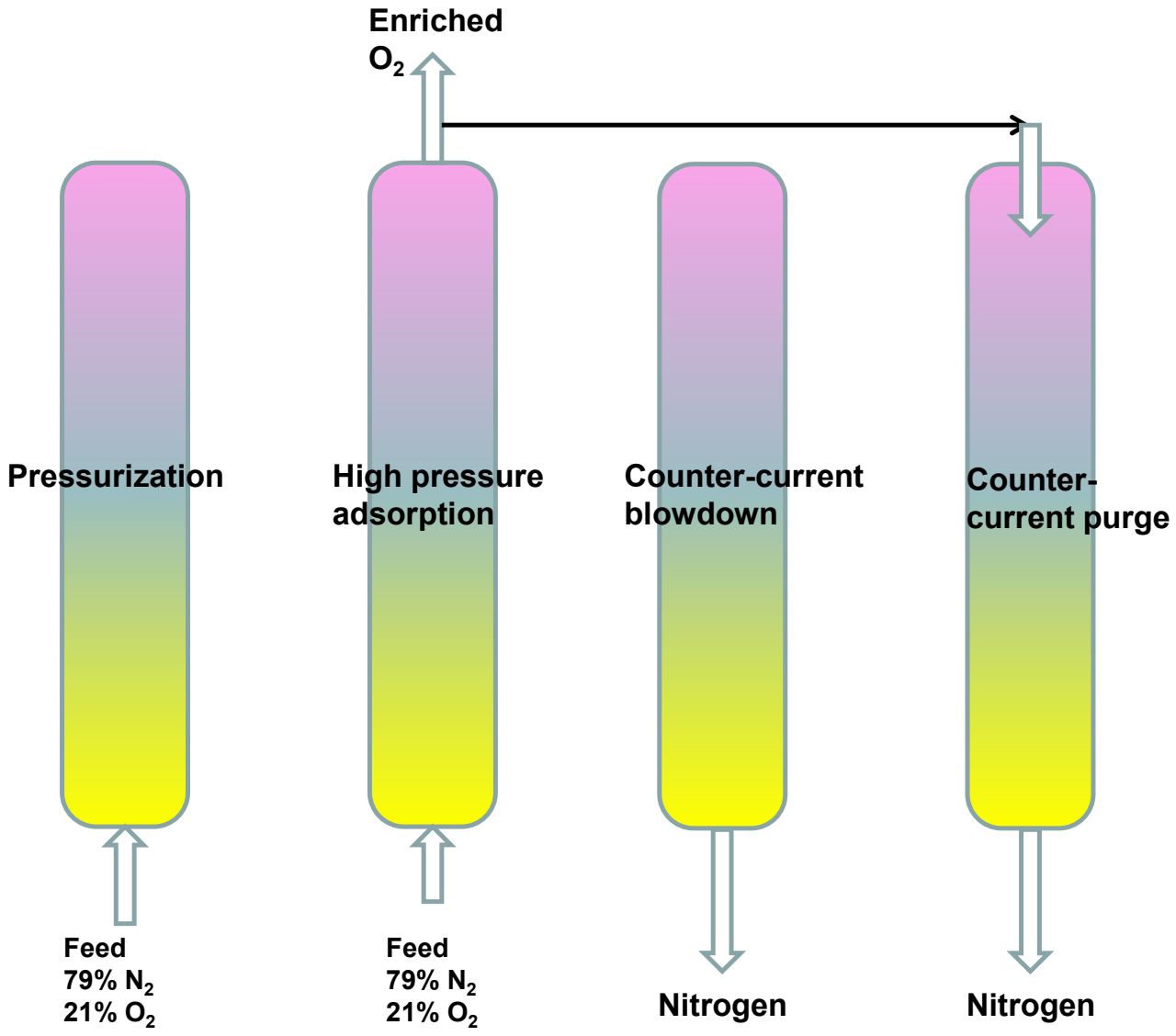

Figure S-30. Different steps in the production of purified O_2 using an adsorbent such as LiLSX. The scheme shows the sequence of processing of a single bed in a multi-bed PSA scheme. Adapted from Ruthven and Farooq.[6]

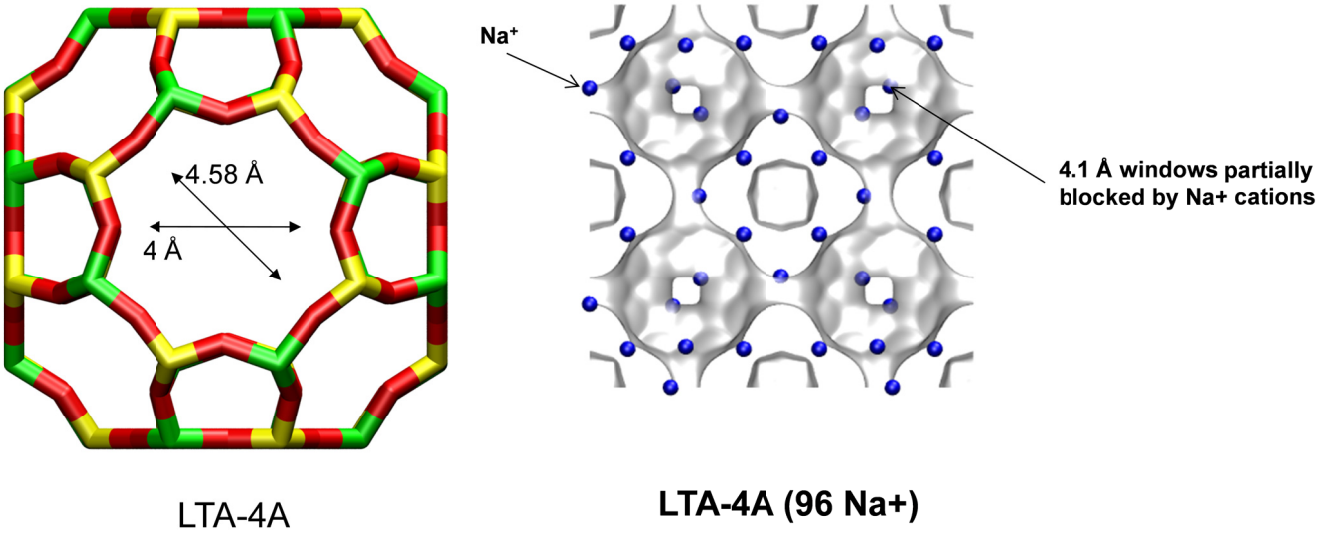

Figure S-31. Partial blocking of the windows of LTA-4A zeolite.

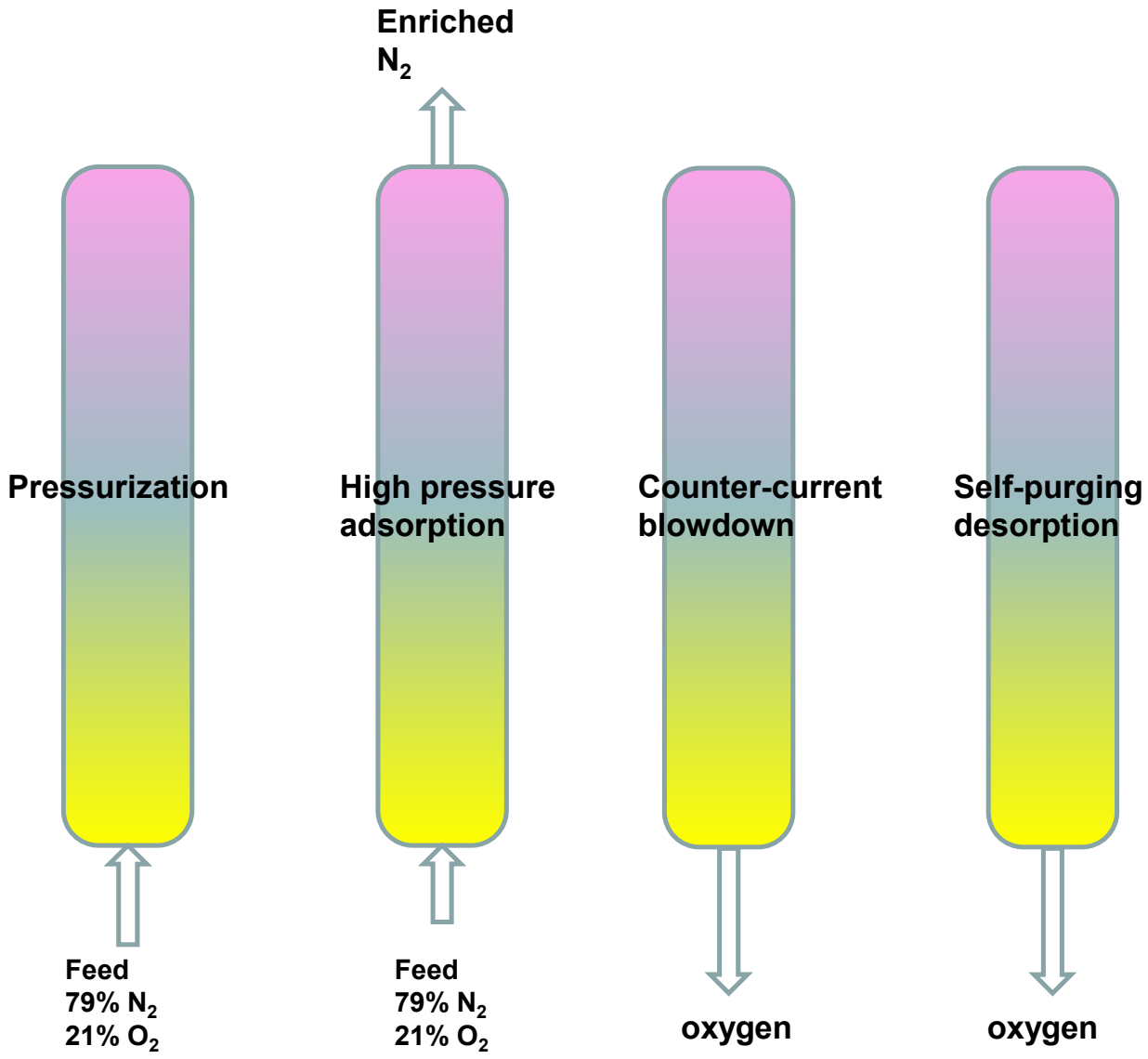

Figure S-32. Different steps in the production of purified N_2 using an adsorbent such as LTA-4A, that relies on kinetic selectivity. The scheme shows the sequence of processing of a single bed in a multi-bed PSA scheme. Adapted from Ruthven and Farooq.[6]

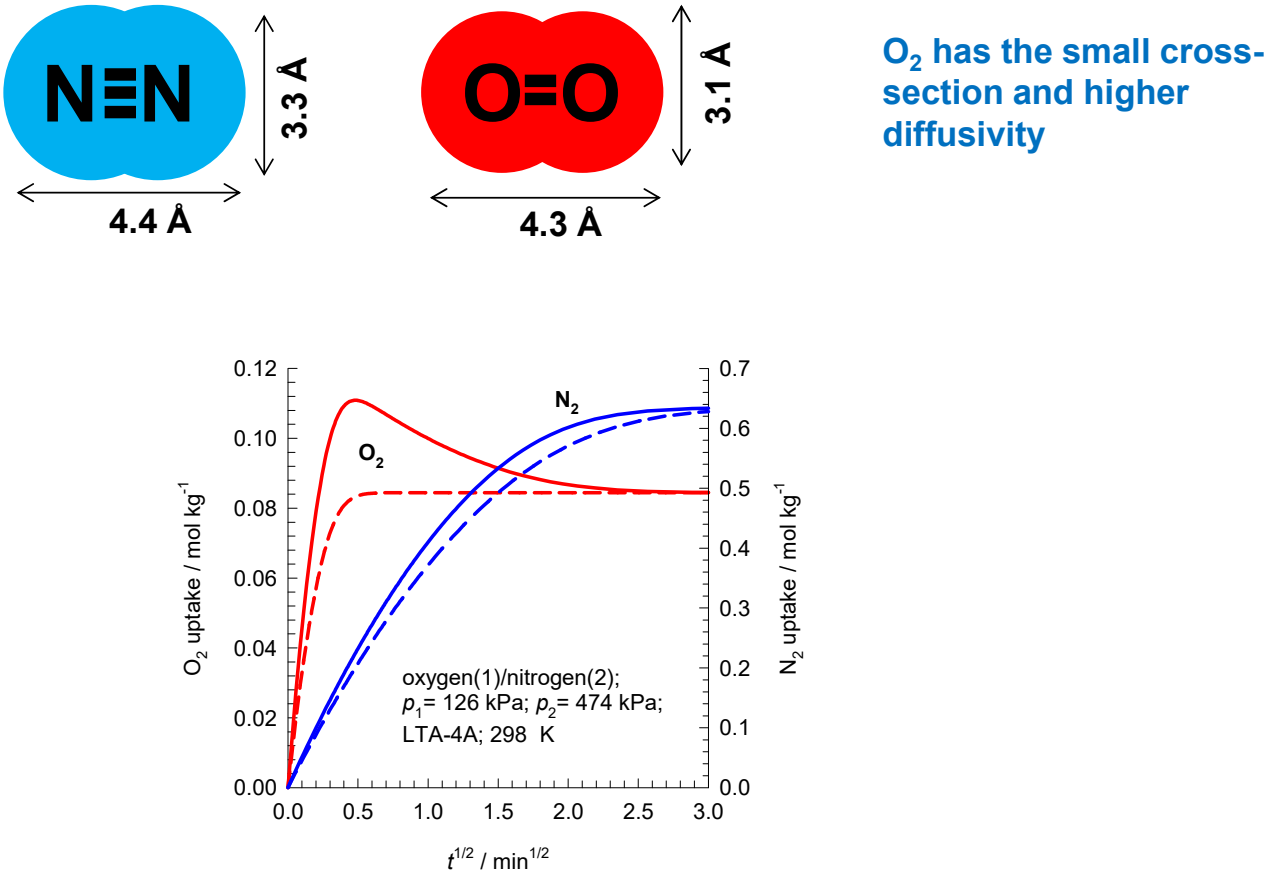

Figure S-33. Transient uptake of O_2(1)/N_2(2) mixture in LTA-4A zeolite at 298 K and total pressure of 600 kPa. The partial pressures of the components in the bulk gas phase are p_1 = 126 kPa, p_2 = 474 kPa. The unary isotherms are provided in Table S-3. The continuous solid lines are Maxwell-Stefan model simulations based on Equation (S-54). The dashed lines are the simulations based on Equation (S-56), in which the thermodynamic correction factors are assumed to be described by $\Gamma_{ij} = \delta_{ij}$, the Kronecker delta. The Maxwell-Stefan diffusivities used in the simulations are: $Đ_1/r_c^2 = 2.75\times10^{-2}$ s^{-1}; $Đ_2/r_c^2 = 7.5\times10^{-4}$ s^{-1}; $Đ_1/Đ_2 = 36.7$.

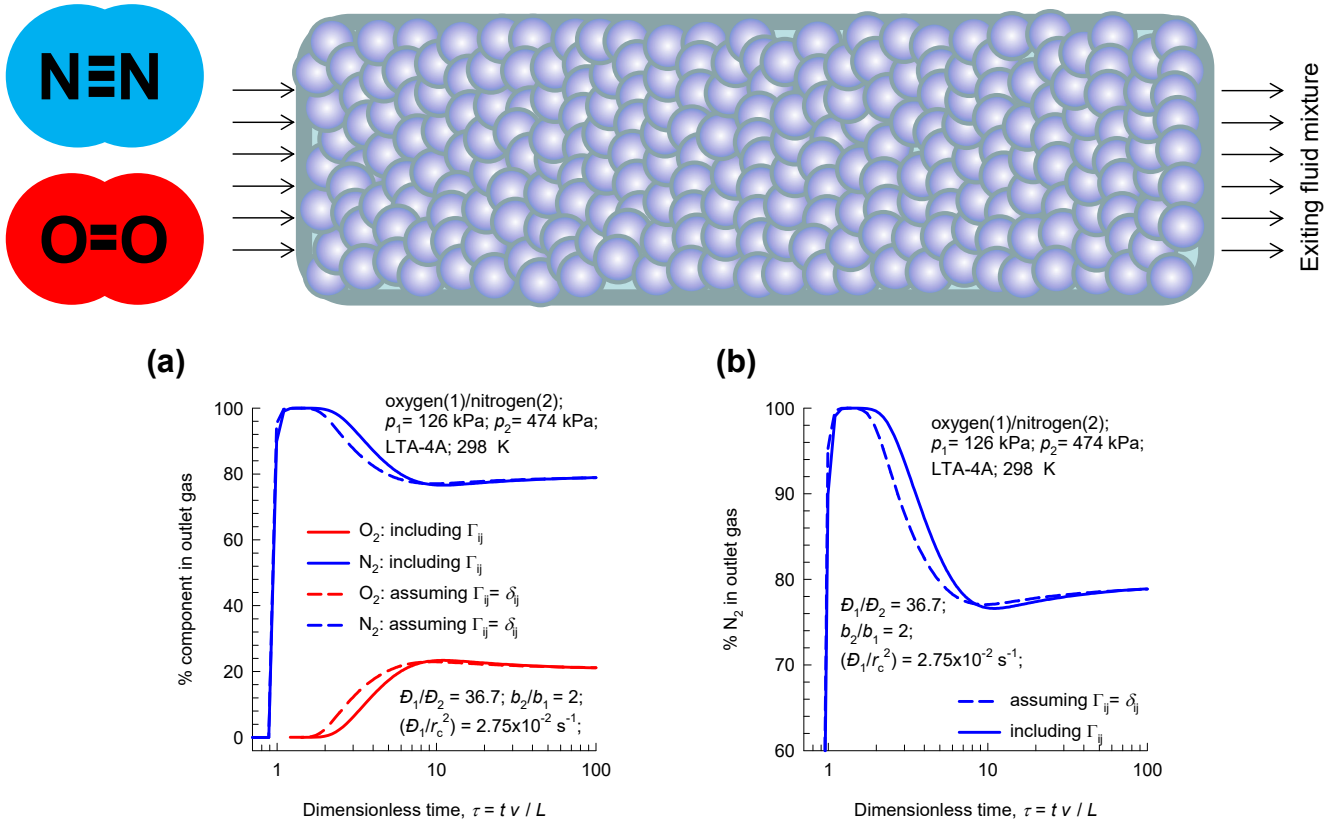

Figure S-34. (a,b) Influence of diffusional limitations on the breakthrough characteristics of $O_2(1)/N_2(2)$ mixture in a fixed bed adsorber packed with LTA-4A operating at a total pressure of 600 kPa and 298 K. The partial pressures of the components in the bulk gas phase at the inlet are p_1 = 126 kPa, p_2 = 474 kPa. The continuous solid lines are breakthrough simulations based on Equation (S-54). The dashed lines are the simulations based on Equation (S-56), in which the thermodynamic correction factors are assumed to be described by $\Gamma_{ij} = \delta_{ij}$, the Kronecker delta. The unary isotherms are provided in Table S-3. The Maxwell-Stefan diffusivities used in the simulations are: $Đ_1/r_c^2 = 2.75\times10^{-2}$ s^{-1}; $Đ_2/r_c^2 = 7.5\times10^{-4}$ s^{-1}; $Đ_1/Đ_2 = 36.7$.

9 Separation of C_3H_6/C_3H_8 mixtures

Propene is an important feedstock in the petrochemical industry. Propene is mostly used to make polypropylene, which accounts for nearly two-thirds of global propylene consumption. Other outlets include acrylonitrile, propylene oxide, a number of alcohols, cumene and acrylic acid. Propene is a by-product from the steam cracking of liquid feedstocks such as naphtha and liquefied petroleum gas (LPG), as well as off-gases produced in fluid catalytic cracking (FCC) units in refineries. It is also made via on-purpose technologies such as propane dehydrogenation and metathesis.

Cryogenic distillation of C_3H_6/C_3H_8 mixtures is the currently used technology for making polymer grade propene (99.5% minimum purity). 90% pure propane is used for various purposes such as fuel for engines, oxy-gas torches, barbecues; this can be obtained as the bottoms product of the cryogenic distillation column.[43] The boiling points are close to each other: propene (226 K), and propane (231.3 K). Consequently the distillation columns are some of the largest and tallest distillation columns used in the petrochemical industries with about 150 - 200 trays, and operating at reflux ratios of about 15. In fact, the U.S. Department of Energy has established that propene/propane separation is the most energy-intensive single distillation process practiced commercially.[43]

A pressure swing adsorption (PSA) process can be an attractive alternative for propene/propane separation, because of its expected low energy demand. A variety of adsorbents have been investigated for this separation task.[43, 74-76] With great potential for alkene/alkane separations are MOFs with coordinatively unsaturated metal centers that may be created by evacuation of frameworks that have metal-bound solvent molecules. This strategy has been employed to expose M^{2+} cation sites in M_2(dobdc) [M = Mg, Mn, Co, Ni, Zn, Fe; $dobdc^{4-}$ = 2,5- dioxido-1,4-benzenedicarboxylate]; these MOFs are also referred to as M-MOF-74 and CPO-27-M. Unsaturated alkynes, and alkenes such as C_2H_2, C_2H_4, and C_3H_6 can bind with Fe^{2+} of FeMOF-74, with side-on attachment and π-coordination; [8,

[77] see Figure S-35. The capability of M-MOF-74 for the technologically important separations of C_2H_2/C_2H_4, C_2H_4/C_2H_6, and C_3H_6/C_3H_8 mixtures has been established in laboratory studies.[8, 77] Other adsorbents that are also based on adsorption selectivity in favor of the unsaturated propene include: CuBTC,[78] LTA-4A zeolite,[74, 75] and NaX (= 13X) zeolite.[74, 76]

An important disadvantage of the C_3H_6/C_3H_8 separations with the adsorbents listed above is that the desired alkene product, required for production of polymer grade feedstock, can only be recovered in the desorption phase. It becomes necessary to operate with multiple beds involving five different steps; the C_3H_6 product of the desired purity is recovered in the final step by counter-current vacuum blowdown;[75, 76, 79] see Figure S-36.

The recovery of high purity C_3H_6 product in the final vacuum blowdown step is expected to be enhanced if C_3H_8 is (almost) excluded during the high pressure adsorption cycle. Near-total exclusion of C_3H_8 is achievable by kinetically based separations using cage-type zeolites with 8-ring windows. Due to the small cross-section of the propene molecule (see Figure S-37), kinetic separations, selective to propene, are possible using all-silica CHA zeolite (all-silica CHA zeolite, also named SiCHA, consists of cages of volume 316 $Å^3$, separated by 3.8 Å × 4.2 Å 8-ring windows; the pore landscape and structural details are provided in Figure S-38, and Figure S-39).[43, 80-82]

Ruthven and Reyes[82] compare the ratio of diffusivities of propene to that of propene in CHA with the corresponding values in DDR; see Figure S-40. Their data show that CHA is the more effective sieve.

It is to be noted for LTA-4A zeolite,[74, 75] both mixture adsorption and diffusion favor propene, whereas with all-silica CHA zeolite, the adsorption equilibrium is in favor of propane, whereas diffusion favors propene.

9.1 Transient uptake of C_3H_6/C_3H_8 within crystals of all-silica CHA

Figure S-41(a,b) shows the simulations of transient uptake of 50/50 $C_3H_6(1)/C_3H_8(2)$ mixtures within crystals of all-silica CHA at 353 K. The bulk gas mixture is at a total pressure of 100 kPa. The continuous solid lines are Maxwell-Stefan model simulations based on Equation (S-54). The Maxwell-

Stefan diffusivities are $Đ_1/r_c^2 = 1.7\times10^{-4}$ s^{-1}; $Đ_2/r_c^2 = 3.4\times10^{-8}$ s^{-1}; $Đ_1/Đ_2 = 5000$. The more mobile C_3H_6 exhibits a pronounced overshoot in its approach to thermodynamic equilibrium. The attainment of supra-equilibrium loadings during the initial stages of transience signals the phenomenon of uphill diffusion, and enhanced separation. The dashed lines are the simulations based on Equation (S-56), in which the thermodynamic correction factors are assumed to be described by $\Gamma_{ij} = \delta_{ij}$, the Kronecker delta. In this scenario, no C_3H_6 overshoot is observed indicating that thermodynamic coupling effects are the root cause of uphill diffusion.

Figure S-41(b) is a plot of the transient uptake selectivity as a function of the Fourier number, $Đ_1 t/r_c^2$, defined by

$$\frac{\overline{q}_1(t)/\overline{q}_2(t)}{p_{10}/p_{20}} \tag{S-69}$$

As $t \to \infty$, the uptake selectivity will approach the value of the adsorption selectivity

$$\frac{q_1^*/q_2^*}{p_{10}/p_{20}} \tag{S-70}$$

From the unary Langmuir isotherm parameters Table S-4, we calculate the equilibrium adsorption selectivity $\frac{q_1^*/q_2^*}{p_{10}/p_{20}} = \frac{b_1}{b_2} = 0.375$. At short contact times, the transient uptake selectivity is strongly in favor of the more mobile propene.

In order to appreciate the significance of thermodynamic coupling, Figure S-42 presents the calculations of the thermodynamic correction factors Γ_{ij} using Equation (S-48). We note that at a total pressure of 100 kPa, the cross-coefficients are about 60-80% of the magnitudes of the diagonal elements, indicating that coupling effects cannot be ignored.

9.2 Transient breakthrough of C_3H_6/C_3H_8 mixtures in fixed bed with CHA

Figure S-43 show the simulations of transient breakthrough of 50/50 $C_3H_6(1)/C_3H_8(2)$ mixtures in a fixed bed adsorber packed with crystals of all-silica CHA at 353 K and operating at a total pressure of

100 kPa. The continuous solid lines are Maxwell-Stefan model simulations based on Equation (S-54). The simulations clearly show that 90%+ pure C_3H_8 can be collected during the earlier stages of transience. If thermodynamic coupling effects are ignored (these simulations are shown by the dashed lines), the time interval during which 90%+ pure C_3H_8 can be recovered is reduced by about an order of magnitude. Expressed per kg of CHA zeolite in the packed bed, the respective productivities of 90%+ pure C_3H_8 are 0.62 and 0.06 mol kg^{-1}. Ignoring thermodynamic coupling effects underestimates the separation performance by a factor of about 10.

9.3 Separation of C_3H_6/C_3H_8 mixtures in fixed bed with KAUST-7

Customized for C_3H_6/C_3H_8 separations, Cadiau et al.[83] report the synthesis of NbOFFIVE-1-Ni (= KAUST-7), that belongs to the same class of SIFSIX materials,[84] using pyrazine as the organic linker; see Figure S-44(a). The $(SiF_6)^{2-}$ pillars in the cage are replaced with somewhat bulkier $(NbOF_5)^{2-}$ pillars. This causes tilting of the pyrazine molecule on the linker, effectively reducing the aperture opening from 0.50 nm [with $(SiF_6)^{2-}$ pillars] to 0.30 nm. The small aperture permits ingress of the smaller C_3H_6 molecules, but practically excludes C_3H_8 on the basis of subtle differences in bond lengths, bond angles, molecular sizes and conformations (see Figure S-37).

Figure S-44(b) shows transient breakthrough simulations for the adsorption cycle for separation of 50/50 C_3H_6/C_3H_8 mixtures in fixed bed adsorbers packed with KAUST-7. The unary isotherms data and the M-S diffusivities used in the simulations, determined on the basis of the experimental data in Cadiau et al.[83] are provided in Table S-5. In the transient breakthrough simulations, the IAST was used to describe mixture adsorption equilibrium. Due to the near total exclusion of C_3H_8 from the pores of KAUST-7, the achievement of the 99.95% purity target during the final evacuation phase of the PSA cycle in Figure S-36.

Figure S-44(c) presents a comparison of the % C_3H_8 in outlet gas leaving fixed bed adsorbers packed with KAUST-7, and CHA zeolite. Both of these adsorbents appear to be equally effective in near-total exclusion of C_3H_8. It is to be noted, however, the comparison is not entirely fair because the CHA

breakthroughs are at 353 K, whereas the KAUST-7 breakthroughs are at 298 K. Further, detailed, investigation is required to determine whether KAUST-7 offers significant improvements over CHA zeolite. It is worth mentioning in Figure S12 of Cadiau et al.[83] breakthroughs of KAUST-7 are compared with data on LTA-4A, and LTA-5A zeolites, but not with all-silica CHA.

9.4 Transient breakthrough of C_3H_6/C_3H_8 mixtures in fixed bed with ZIF-67

Andres-Garcia et al.[85] report experimental data on transient breakthrough simulations for $C_3H_6(1)/C_3H_8(2)$ mixtures in fixed bed adsorber packed with crystals of ZIF-67 operating at 298 K. Their experimental data show that the saturated alkane C_3H_8 is preferentially adsorbed so that the unsaturated alkene C_3H_6 can be recovered in nearly pure form in the raffinate leaving the adsorption phase of a PSA cycle. Their experimental data show strong diffusion limitations, but the separation principle is not "kinetic", but based on mixture adsorption equilibrium. Figure S-45(a,b,c,d) show the simulations of the two sets of transient breakthrough experiments, as reported Figures 3a, and 3b of Andres-Garcia et al.[85] In these simulations, the mixture adsorption equilibrium was determined using the IAST, with the unary isotherm fits in Table S-6. The continuous solid lines are Maxwell-Stefan model simulations based on Equation (S-54). The dashed lines are the simulations based on Equation (S-56), in which the thermodynamic correction factors are assumed to be described by $\Gamma_{ij} = \delta_{ij}$, the Kronecker delta. The Maxwell-Stefan diffusivities are $Đ_1/r_c^2 = Đ_2/r_c^2 = 0.01$ s^{-1}; $Đ_1/Đ_2 = 1$. For both sets of simulations, the influence of the thermodynamic correction factors is negligible, because the M-S diffusivities of the guest molecules are equal to each other. For the set of simulations (a, b) with the partial pressures at the inlet: $p_1 = p_2 = 87.5$ kPa, it is possible to recover 99% pure C_3H_6 from the raffinate phase leaving the adsorber. However, for the set of simulations (c, d) with $p_1 = p_2 = 262.5$ kPa, the recovery of 99% pure C_3H_6 does not seem to be possible. At the operating temperature of 298 K and at high pressures, the pores are nearly saturated and the adsorption strengths of the guest molecules are close to each other.

9.5 List of Tables for Separation of C3H6/C3H8 mixtures

Table S-4. 1-site Langmuir parameters for C_3H_6/, and C_3H_8 in all-silica CHA zeolite at 353 K. These isotherm data are taken from Table 4 of Khalighi et al.[43]

	q_{sat} mol kg^{-1}	b Pa^{-1}
C_3H_6	2.9	3×10^{-5}
C_3H_8	2.9	8×10^{-5}

On the basis of the information provided in Table 4 of Khalighi et al.:[43]

The Maxwell-Stefan diffusivities are

$Đ_1/r_c^2 = 1.7\times10^{-4}$ s^{-1}; $Đ_2/r_c^2 = 3.4\times10^{-8}$ s^{-1}; $Đ_1/Đ_2 = 5000$.

Separation of C3H6/C3H8 mixtures

Table S-5. Dual-site Langmuir-Freundlich parameters for C_3H_6, and C_3H_8 in KAUST. These isotherm isotherm fit parameters were determined by scanning the experimental data at 298 K as reported in Figures 3b of Cadiau et al.[83] The unary isotherm data for C_3H_6, and C_3H_8 were fitted with the dual-site Langmuir-Freundlich isotherm model

$$q = q_{A,sat}\frac{b_A p^{\nu A}}{1+b_A p^{\nu A}} + q_{B,sat}\frac{b_B p^{\nu B}}{1+b_B p^{\nu B}}$$

The dual-site Langmuir-Freundlich parameters are

	Site A			Site B		
	$q_{A,sat}$ mol kg^{-1}	b_{A0} Pa$^{-\nu_A}$	ν_A dimensionless	$q_{B,sat}$ mol kg^{-1}	b_{B0} Pa$^{-\nu_B}$	ν_B dimensionless
C_3H_6	2	3.58-07	1.4	1	1E-07	1
C_3H_8	2.1	2.6E-05	1			

We note that the C_3H_8 is virtually excluded from the pores of KAUST-7, so its Langmuir isotherm fit is reflects virtual size exclusion, not physical adsorption.

By simulation of the experimental data on transient breakthroughs in Figures 3c of Cadiau et al.[83], in combination with the IAST description of mixture adsorption equilibrium, the Maxwell-Stefan diffusivities were fitted as follows

$Đ_1/r_c^2 = 2.5\times10^{-4}$ s^{-1}; $Đ_2/r_c^2 = 2.5\times10^{-4}$ s^{-1}; $Đ_1/Đ_2 = 1$.

The equal diffusivities of both guest molecules was chosen, because the C_3H_8 exclusion effect is already included in the isotherm fit. The choice of $Đ_1/r_c^2 = 2.5\times10^{-4}$ s^{-1} reflects the distended nature of the breakthroughs in Figures 3c of Cadiau et al.[83]

Separation of C3H6/C3H8 mixtures

Table S-6. Dual-site Langmuir-Freundlich parameters for C_3H_6/C_3H_8 in ZIF-67. These isotherm isotherm fit parameters were determined by scanning the experimental data at 273 K and 298 K as reported in Figures 2c of Andres-Garcia et al.[85]

The pure component isotherm data for C_3H_6, and C_3H_8 in ZIF-67, measured at 273 K, and 298 K by Andres-Garcia et al.[85] were fitted with the dual-site Langmuir-Freundlich isotherm model

$$q = q_{A,sat}\frac{b_A p^{\nu A}}{1+b_A p^{\nu A}} + q_{B,sat}\frac{b_B p^{\nu B}}{1+b_B p^{\nu B}}$$

with T-dependent parameters b_A, and b_B

$$b_A = b_{A0}\exp\left(\frac{E_A}{RT}\right); \quad b_B = b_{B0}\exp\left(\frac{E_B}{RT}\right)$$

The dual-site Langmuir-Freundlich parameters are

	Site A				Site B			
	$q_{A,sat}$ mol kg^{-1}	b_{A0} Pa$^{-\nu_A}$	E_A kJ mol^{-1}	ν_A dimensionless	$q_{B,sat}$ mol kg^{-1}	b_{B0} Pa$^{-\nu_B}$	E_B kJ mol^{-1}	ν_B dimensionless
C_3H_6	2.4	1.59E-09	20	1	3	1.17E-24	46	3.4
C_3H_8	2.6	7.64E-11	36	0.83	1.7	4.23E-20	52	2.5

9.6 List of Figures for Separation of C3H6/C3H8 mixtures

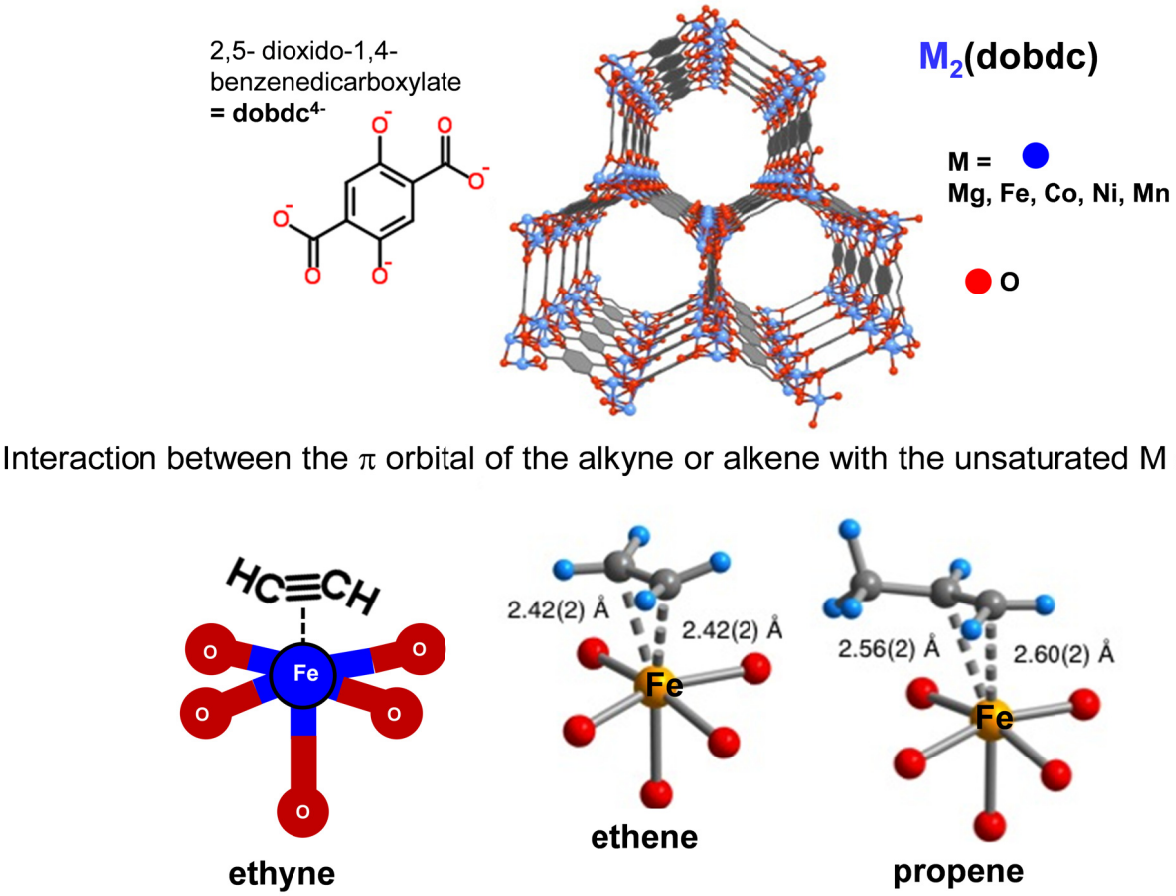

Figure S-35. Unsaturated alkynes, and alkenes such as C_2H_2, C_2H_4, and C_3H_6 can bind with M^{2+} of M-MOF-74, with side-on attachment and π-coordination; [8] Adapted from Bloch et al.[8]

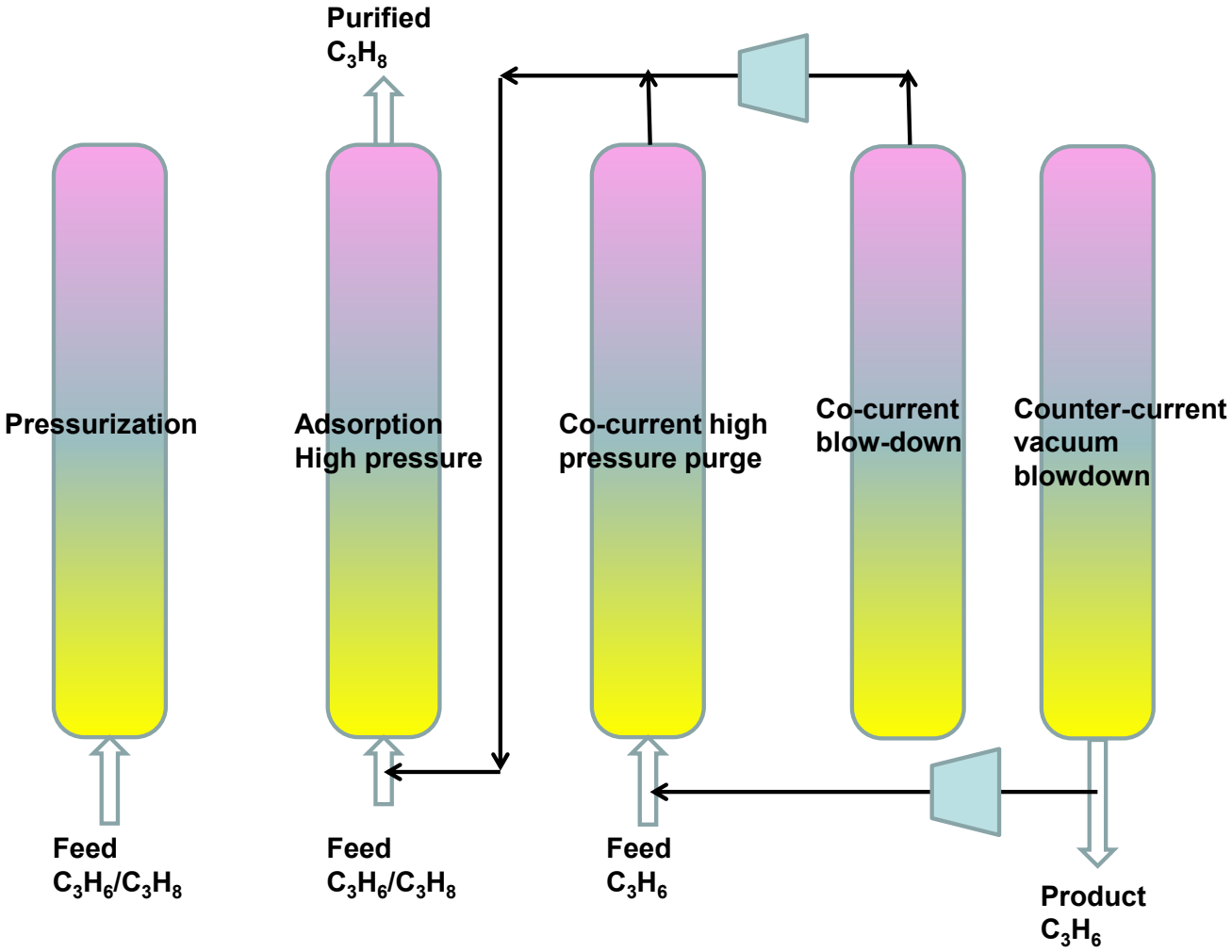

Figure S-36. Five-step P(V)SA process for separating C_3H_6/C_3H_8 mixtures.[75, 76, 79]

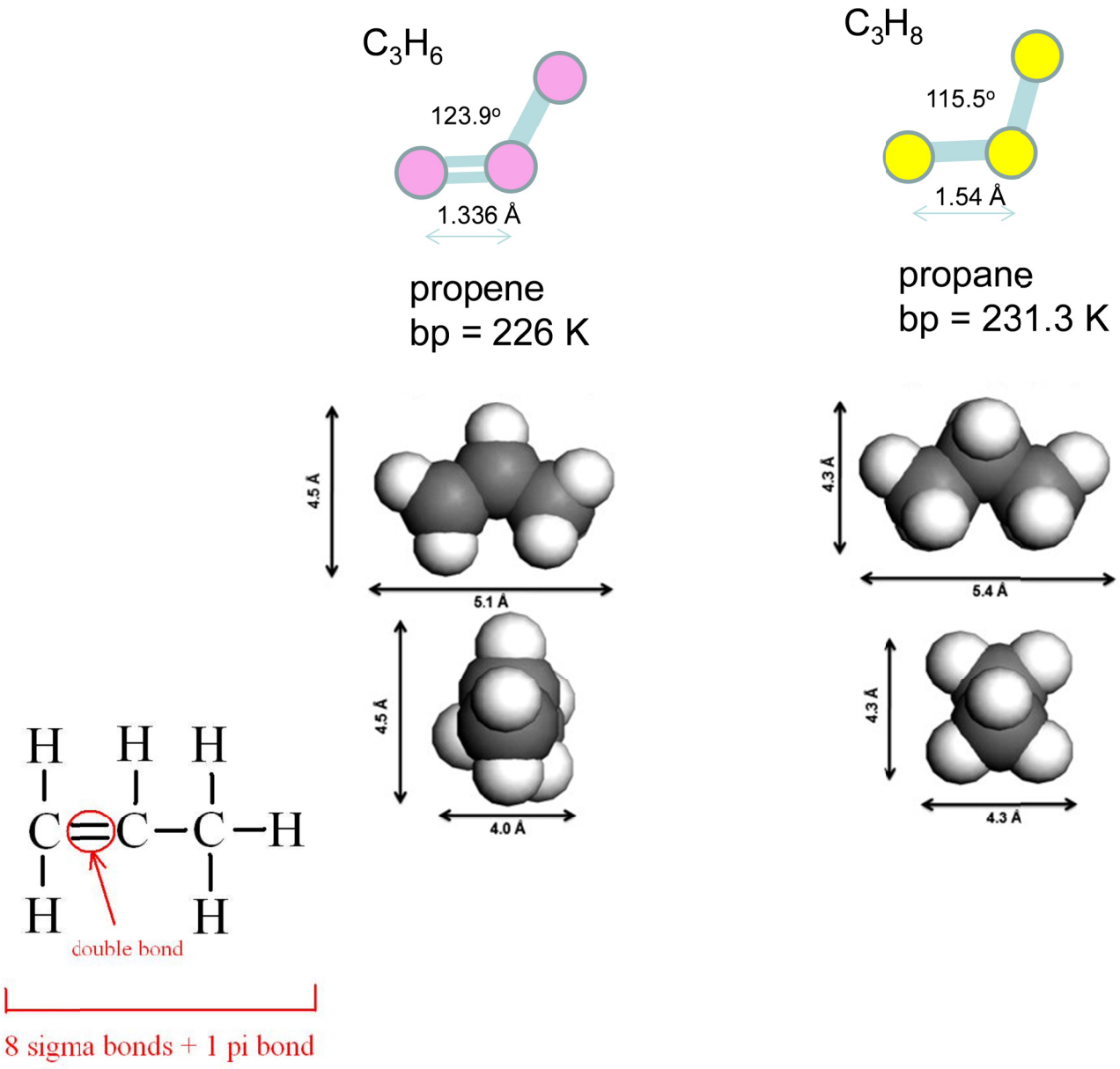

Figure S-37. Molecular dimensions of C_3H_6 and C_3H_8, culled from the literature.[86]

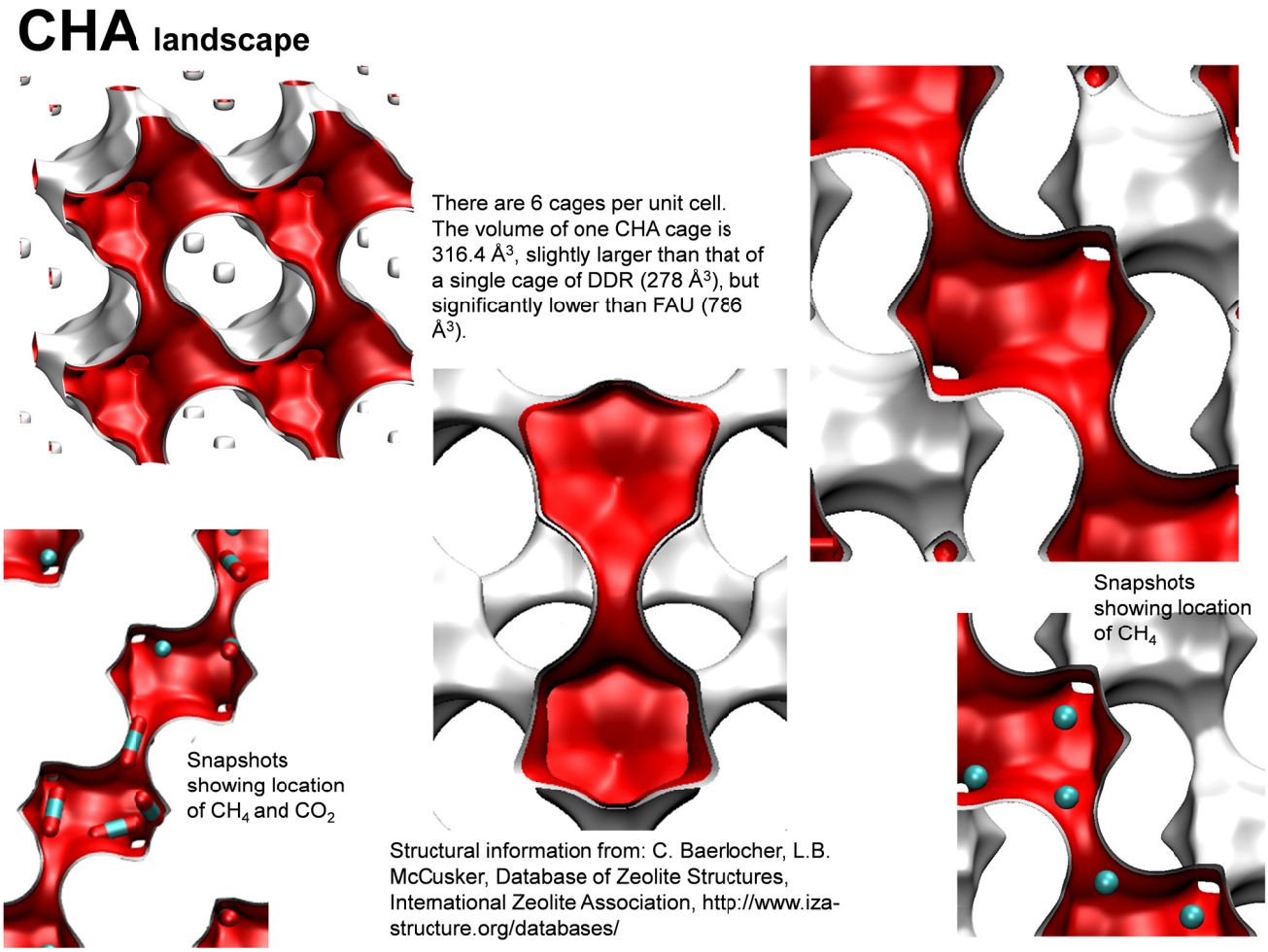

Figure S-38. Pore landscape and structural details of all-silica CHA zeolite, also called SiCHA.

CHA window and pore dimensions

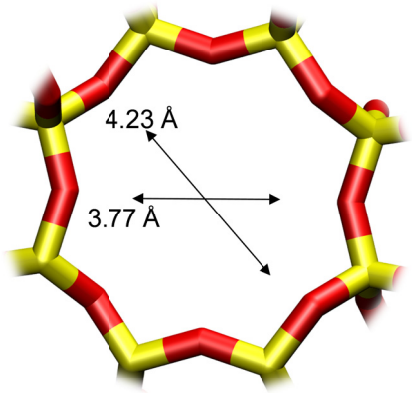

CHA

The window dimensions calculated using the van der Waals diameter of framework atoms = 2.7 Å are indicated above by the arrows.

	CHA
a /Å	15.075
b /Å	23.907
c /Å	13.803
Cell volume / Å^3	4974.574
conversion factor for [molec/uc] to [mol per kg Framework]	0.2312
conversion factor for [molec/uc] to [kmol/m^3]	0.8747
ρ [kg/m3]	1444.1
MW unit cell [g/mol(framework)]	4326.106
ψ, fractional pore volume	0.382
open space / Å^3/uc	1898.4
Pore volume / cm^3/g	0.264
Surface area /m^2/g	758.0
DeLaunay diameter /Å	3.77

Figure S-39. Pore landscape and structural details of all-silica CHA zeolite, also called SiCHA.

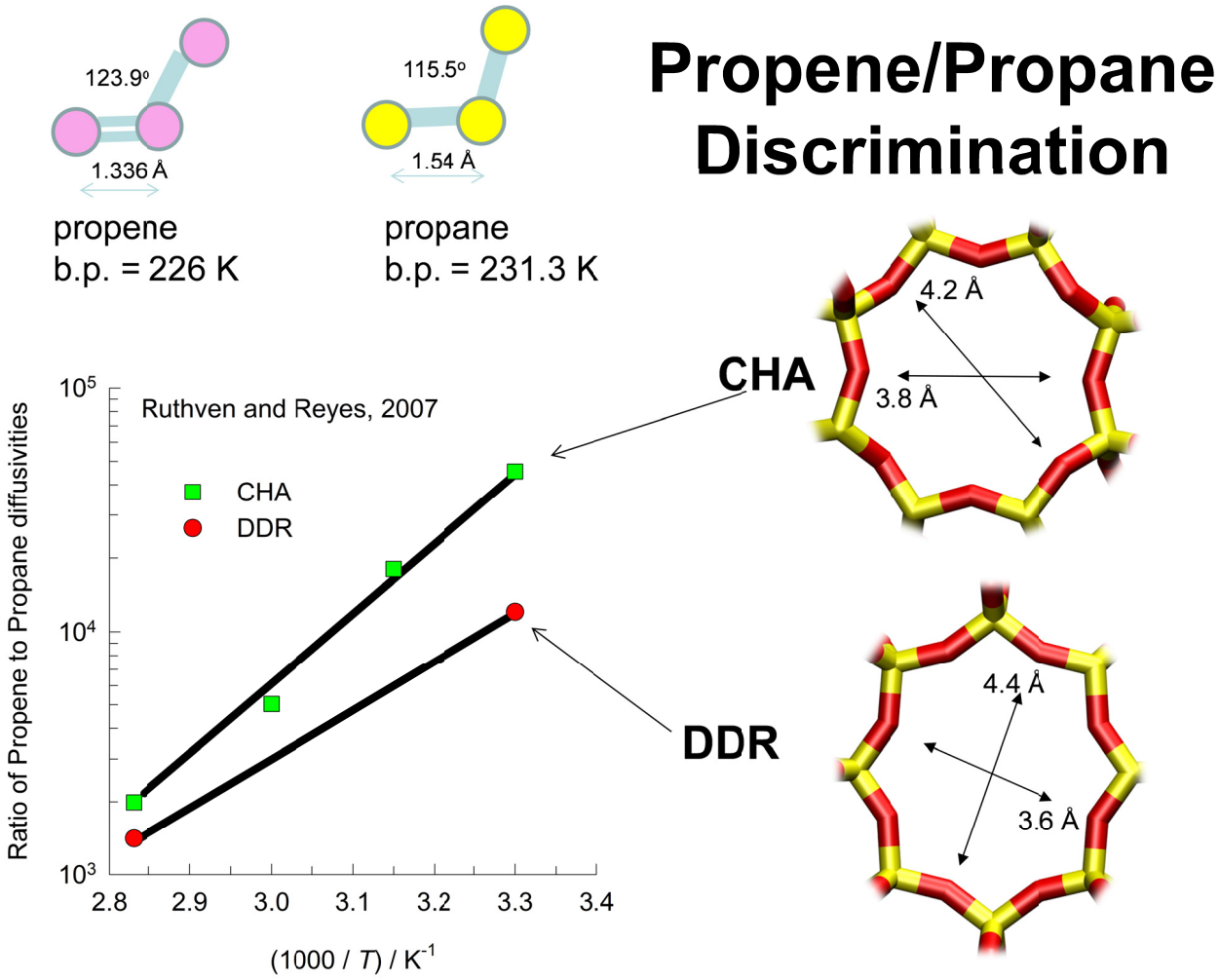

Figure S-40. Data of Ruthven and Reyes[82] for the ratio of diffusivities of propene to that of propane in all-silica CHA and DDR zeolites.

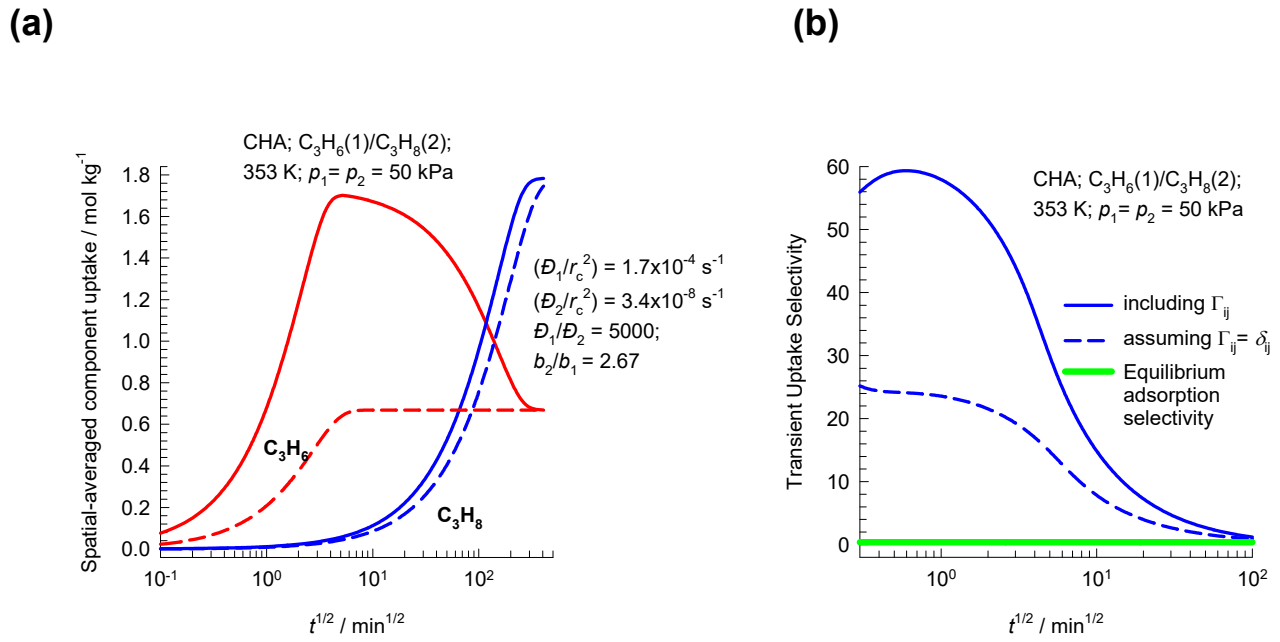

Figure S-41. (a, b) Simulations of transient uptake of 50/50 $C_3H_6(1)/C_3H_8(2)$ mixtures within crystals of all-silica CHA at 353 K. The bulk gas mixture is at a total pressure of 100 kPa. The unary isotherms are provided in Table S-4. The continuous solid lines are Maxwell-Stefan model simulations based on Equation (S-54). The dashed lines are the simulations based on Equation (S-56), in which the thermodynamic correction factors are assumed to be described by $\Gamma_{ij} = \delta_{ij}$, the Kronecker delta. The Maxwell-Stefan diffusivities are $Đ_1/r_c^2 = 1.7\times10^{-4}$ s^{-1}; $Đ_2/r_c^2 = 3.4\times10^{-8}$ s^{-1}; $Đ_1/Đ_2 = 5000$.

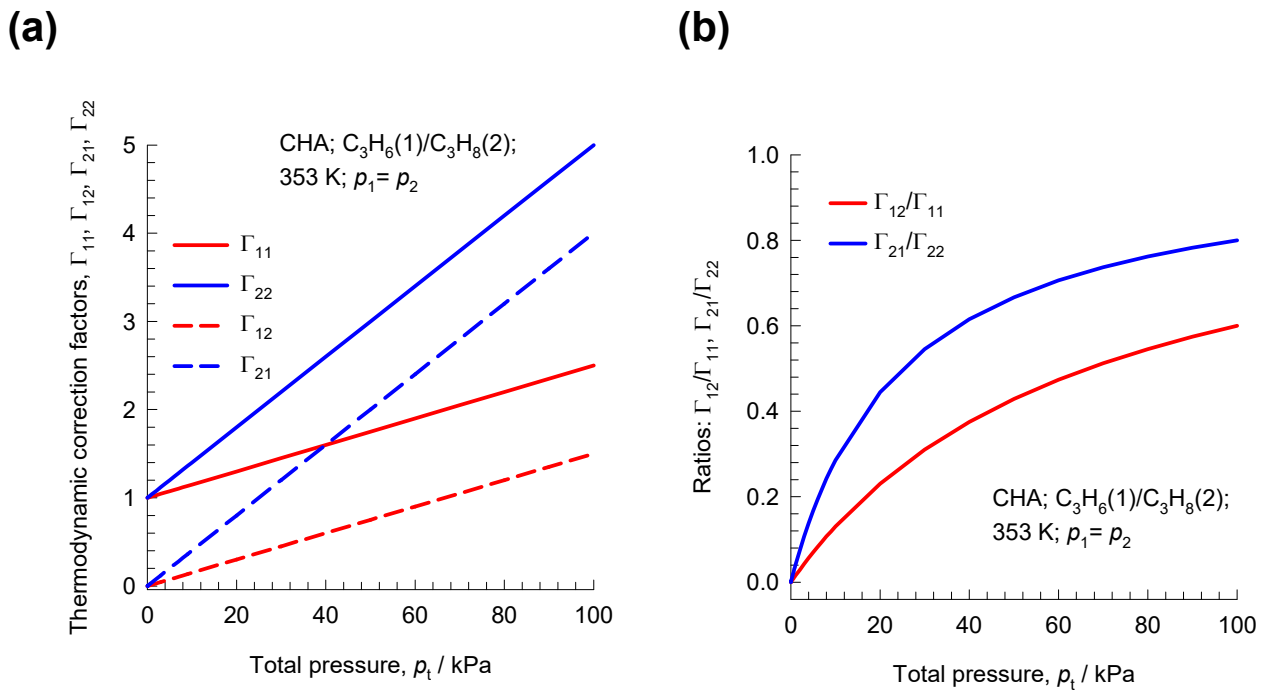

Figure S-42. (a) Calculations of the elements of the matrix of thermodynamic factors for 50/50 $C_3H_6(1)/C_3H_8(2)$ mixture adsorption within crystals of all-silica CHA at 353 K using Equation (S-48). (b) Ratios of the off-diagonal elements to the diagonal elements of the matrix of thermodynamic factors.

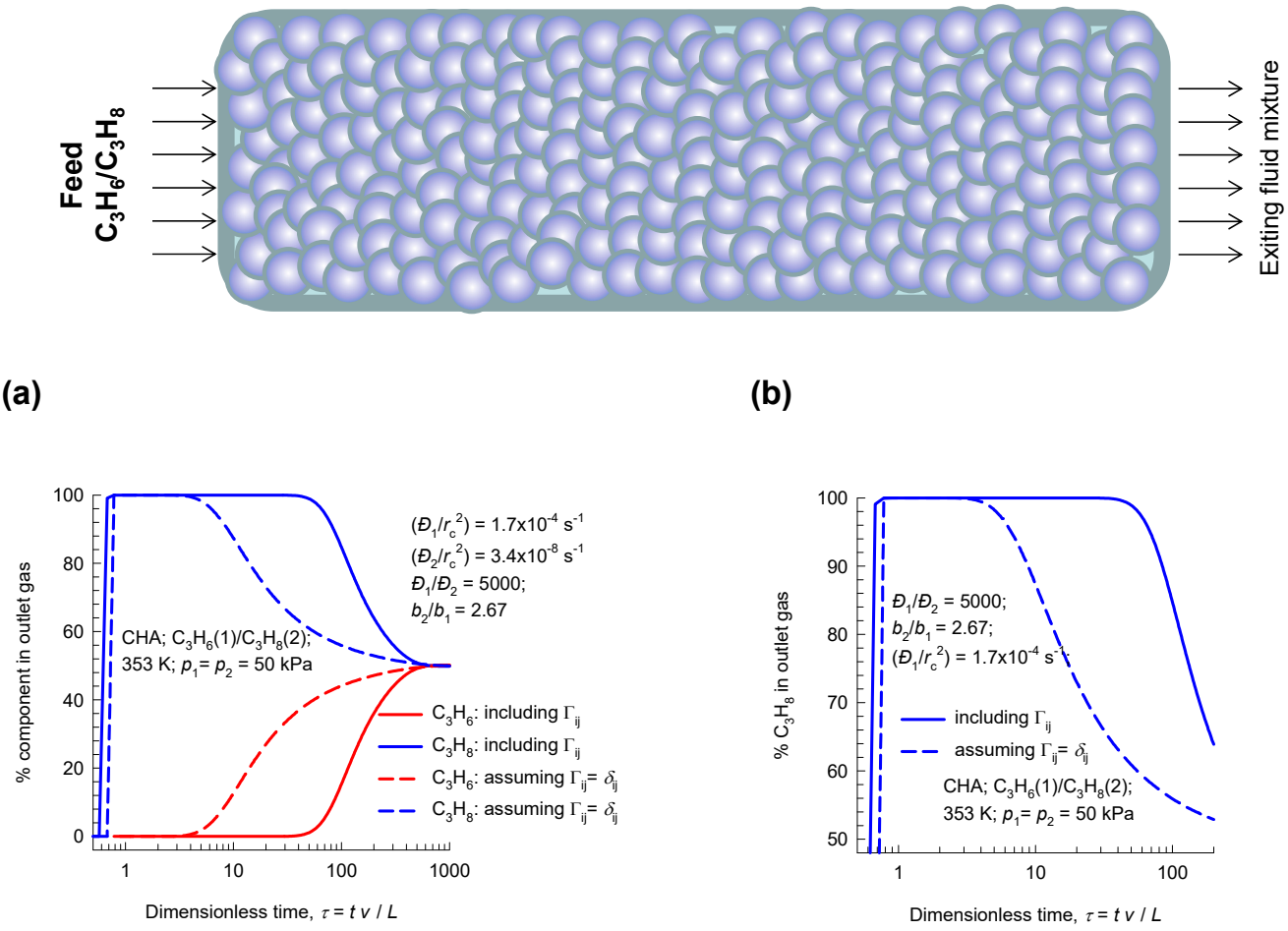

Figure S-43. (a,b) Simulations of transient breakthrough of 50/50 $C_3H_6(1)/C_3H_8(2)$ mixtures in a fixed bed adsorber packed with crystals of all-silica CHA at 353 K and operating at a total pressure of 100 kPa. The unary isotherms are provided in Table S-4. The continuous solid lines are Maxwell-Stefan model simulations based on Equation (S-54). The dashed lines are the simulations based on Equation (S-56), in which the thermodynamic correction factors are assumed to be described by $\Gamma_{ij} = \delta_{ij}$, the Kronecker delta. The Maxwell-Stefan diffusivities are $Đ_1/r_c^2 = 1.7\times10^{-4}$ s^{-1}; $Đ_2/r_c^2 = 3.4\times10^{-8}$ s^{-1}; $Đ_1/Đ_2 = 5000$.

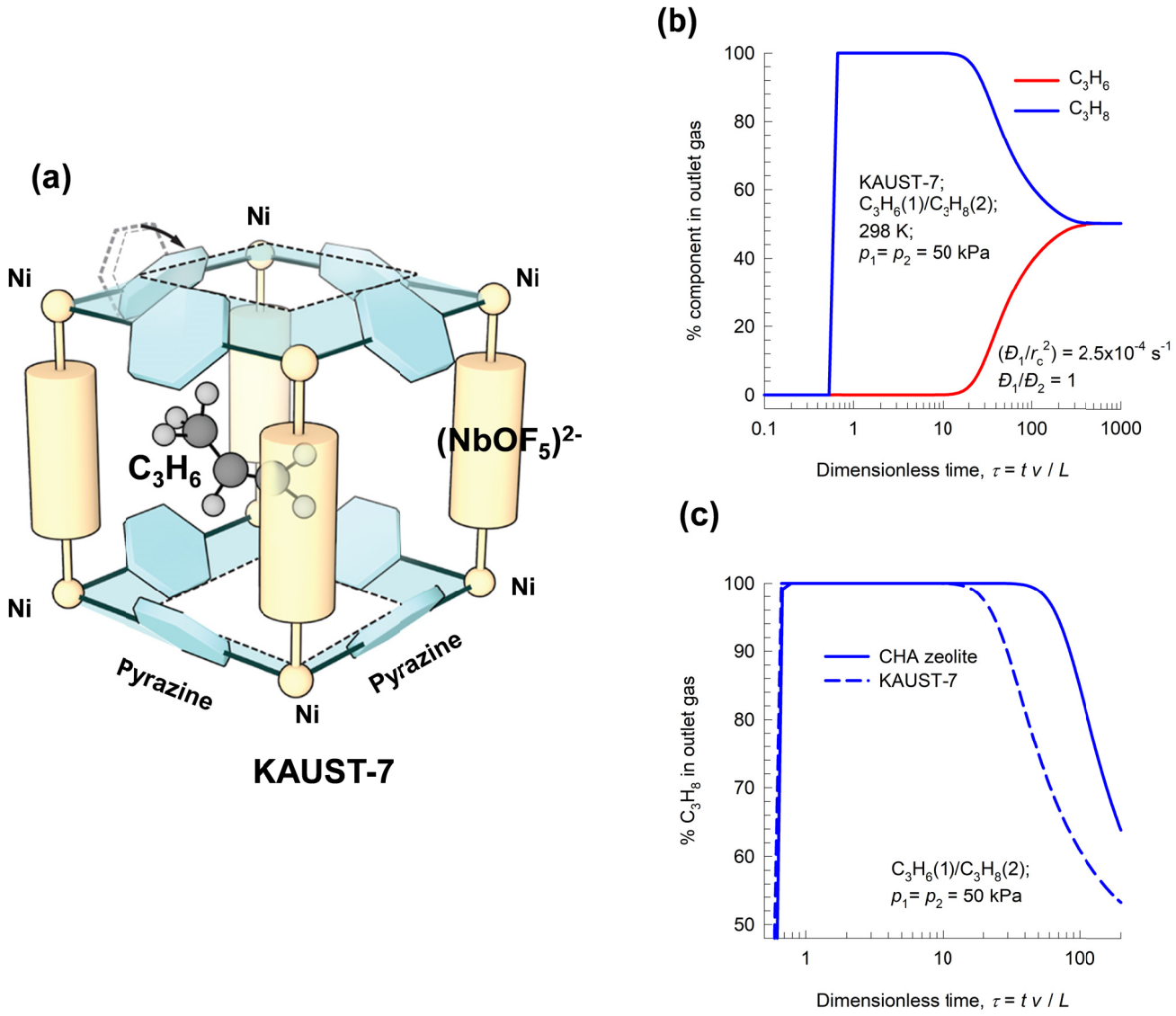

Figure S-44. (a) Structure of NbOFFIVE-1-Ni (= KAUST-7), highlighting the C_3H_6 binding with $(NbOF_5)^{2-}$ anions. Adapted from Lin.[87] (b) Transient breakthrough simulations for the adsorption cycle for separation of 50/50 C_3H_6/C_3H_8 mixtures in fixed bed adsorbers packed with KAUST-7, operating at 298 K and 100 kPa total pressure. The unary isotherms data and the M-S diffusivities used in the simulations are provided in Table S-5. In the transient breakthrough simulations, the IAST was used to describe mixture adsorption equilibrium. (c) Comparison of the % C_3H_8 in outlet gas leaving fixed bed adsorbers packed with KAUST-7, and CHA zeolite.

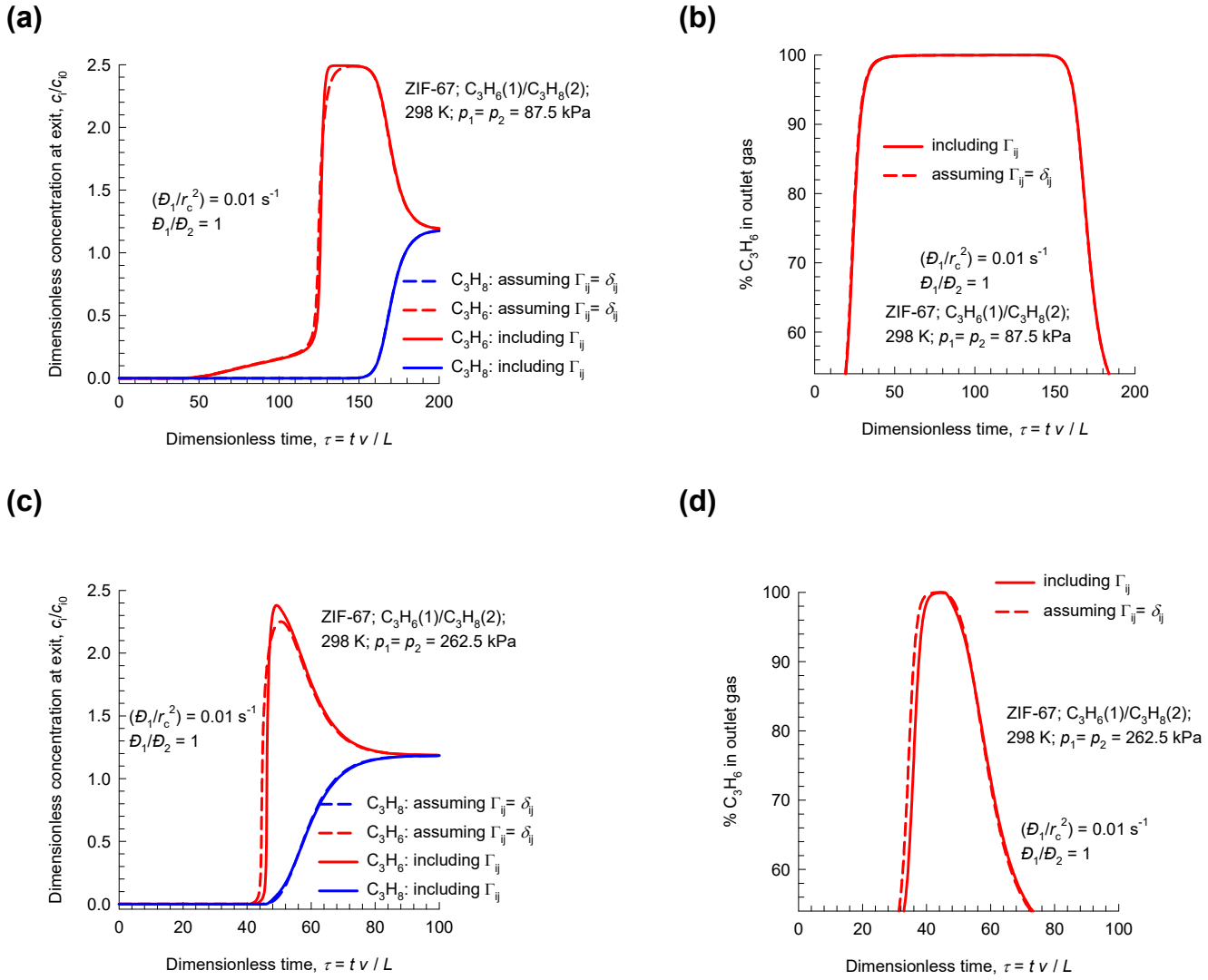

Figure S-45. (a, b, c, d) Simulations of transient breakthrough of 50/50 $C_3H_6(1)/C_3H_8(2)$ mixtures in a fixed bed adsorber packed with crystals of ZIF-67, operating at 298 K. The partial pressures at the inlet are: (a, b) $p_1 = p_2 = 87.5$ kPa, and (c, d) $p_1 = p_2 = 262.5$ kPa corresponding, respectively to the experimental conditions in Figures 3a, and 3b of Andres-Garcia et al.[85] The unary isotherms are provided in Table S-6. The continuous solid lines are Maxwell-Stefan model simulations based on Equation (S-54). The dashed lines are the simulations based on Equation (S-56), in which the thermodynamic correction factors are assumed to be described by $\Gamma_{ij} = \delta_{ij}$, the Kronecker delta. The Maxwell-Stefan diffusivities are $Đ_1/r_c^2 = Đ_2/r_c^2 = 0.01$ s^{-1}; $Đ_1/Đ_2 = 1$.

10 Separation of alkane isomers with MFI zeolite

10.1 Background on alkane isomers separation

The separation of hexane isomers, n-hexane (nC6), 2-methylpentane (2MP), 3-methylpentane (3MP), 2,2 dimethylbutane (22DMB), and 2,3 dimethylbutane (23DMB) is required for production of high-octane gasoline. The values of the Research Octane Number (RON) increases with the degree of branching; Table S-7 lists the Research Octane Numbers (RON) of C5, C6, and C7 alkanes.[88] The di-branched isomers (neo-P, 22DMB, 23DMB, 22DMP, 23DMP) have significantly higher RON values than that of the linear isomers (nC5, nC6, and nC7), and mono-branched isomers (2MB, 2MP, 3MP, 2MH, 3MH). For example, for hexane isomers, the RON values are: nC6 = 30, 2MP = 74.5, 3MP = 75.5, 22DMB = 94, 23DMB = 105. Therefore, di-branched isomers are preferred products for incorporation into the high-octane gasoline pool.[24, 89, 90] Table S-8 lists the boiling points of alkane isomers. Due to the small differences in boiling points, distillation is energy intensive.

Currently, the separation of hexane isomers is performed using LTA-5A zeolite that operates on the principle of molecular sieving; see Figure S-46. Linear nC6 can hop from one cage to the adjacent cage through the 4 Å windows of LTA-5A, but branched alkanes are largely excluded. An improved separation scheme, pictured in Figure S-47, would require an adsorbent that would separate the di-branched isomers 22DMB and 23DMB from the nC6, 2MP, and 3MP; this would allow the low-RON components to be recycled back to the isomerization reactor. The separation of 22DMB and 23DMB from the remaining isomers is a difficult task because it requires distinguishing molecules on the *degree* of branching; such a separation is not feasible with the currently used LTA-5A. Typically, in such a processing scheme the aim would be to produce a product stream from the separation step with RON value > 92. This requirement of 92+ RON implies that the product stream will contain predominantly the di-branched isomers 22DMB and 23DMB, while allowing a small proportion of 2MP and 3MP to be

incorporated into the product stream. Sharp separations between mono- and di- branched isomers is not a strict requirement.

According to a patent granted to Universal Oil Products (UOP) for separation of hexane isomers,[91-93] the desired separation of hexane isomers as portrayed in Figure S-47 is achievable with a variety of materials; see the pulse chromatographic separation data as presented in the UOP patents, and reproduced in Figure S-48. The UOP patent states:

"The adsorbent may be silicalite, ferrierite, zeolite Beta, MAPO-31, SAPO-31, SAPO-11, zeolite X ion exchanged with alkaline cations, alkaline earth cations, or a mixture thereof, and zeolite Y ion exchanged with alkaline cations…."

Even though a vast number of zeolites are named in the patent, a careful examination of the separation performance of all zeolites[24, 52, 94] reveals the pulse chromatographic separation data in Figure S-48 is obtained with MFI (silicalite) zeolite. MFI zeolite (also called silicalite-1) has a topology consisting of a set of intersecting straight channels, and zig-zag (or sinusoidal) channels of approximately 5.5 Å size. The pore landscapes and structural details are provided in Figure S-49, and Figure S-50. This chromatographic pulse data clearly shows the potential of MFI zeolite to separate a mixture of hexane isomers into three different fractions consisting of linear, mono-branched, and di-branched isomers. The separation relies essentially on configurational entropy effects. Linear alkanes can locate anywhere along the straight and zig-zag channels; see snapshots in Figure S-51. The linear isomers are not "configurationally challenged". Mono-branched and di-branched isomers prefer to locate at the intersections of MFI, because these are too bulky to locate within the channels; see computational snapshots in Figure S-52 and Figure S-53.[95] The branched isomers are subject to a configurational "penalty".

We highlight the importance of thermodynamic coupling effects on the separation of alkane isomers with MFI zeolite by first analyzing a set of experiments on transient uptake.

10.2 Transient nC6/2MP uptake in MFI

The transient uptake of nC6/2MP mixtures in microporous crystals of MFI zeolite, exposed to an equimolar gas phase mixture at constant total pressure (= 2.6 Pa) have been reported by Titze et al.;[96] see Figure S-54. The transient equilibration of nC6 displays a pronounced overshoot, achieving supra-equilibrium loadings during transient equilibration.

Titze et al.[96] have established the validity of the uncoupled M-S equations (S-54) to model intra-crystalline fluxes by detailed consideration of correlation effects. The mixture adsorption equilibrium is determined using the IAST; the unary isotherm data are provided in Table S-9. The essential features of the transient uptake on nC6/2MP uptake in MFI zeolite can be adequately captured by the flux equation (S-54) taking $Đ_{nC6}/r_c^2$ = 0.016 s^{-1}; $Đ_{2MP}/r_c^2$ = 1.6×10^{-4} s^{-1} $Đ_{nC6}/Đ_{2MP}$ = 100.[96] The lower diffusivity of the mono-branched isomer 2MP is due to the severe configurational constraints within 5.5 Å sized channels of MFI. The nC6 overshoot is caused by the off-diagonal elements of $[\Gamma]$. If we take $\Gamma_{ij} = \delta_{ij}$, and invoke Equation (S-56), the nC6 overshoot disappears.[96] The overshoot of nC6 signifies uphill diffusion within the crystals during transient equilibration; this phenomenon is advantageous in the PSA process for separation of hexane isomers, deployed in a process for octane enhancement of gasoline.[24]

The transient uptake simulations using the equation (S-54) are in good agreement with IRM experimental data for transient uptake of nC6/2MP mixtures in four different experimental campaigns, Runs 1, 2, 3, and 4, with different step changes in the bulk gas pressures; see Figure S-55(a).

In Figure S-55(b) the fitted values of the M-S diffusivities $Đ_{nC6}/r_c^2$ and $Đ_{2MP}/r_c^2$ in each individual campaign is plotted as a function of the loading of 2MP. The ratio of the M-S diffusivities of nC6 and 2MP is maintained at 100.

Each of the diffusivities is strongly dependent on the loading of 2MP, increasing by a factor of 10 as we progress from Run 1 to Run 4; the ratio $Đ_1/Đ_2$ has a constant value of 100. Also indicated at the top of Figure S-55(b) are the values of the total mixture loadings Θ_t for each of the four Runs. We note that as we proceed from Run 1 the total mixture loading increases from Θ_t = 4.5/uc in Run 1, to Θ_t = 7.54/uc

in Run 4, the 2MP loading decreases from 1.84/uc to 0.14/uc, emphasizing the significant configurational-entropy effects. Concomitantly, we note that the diffusivities of both species, nC6 and 2MP, increase by about an order of magnitude with increased total mixture loading, Θ_t. While there are many practical examples of increased adsorption leading to a lowering of diffusivities,[32, 97] The diffusion of nC6/2MP mixture in MFI has very special and unusual characteristics; nC6 is much more mobile, by about one order of magnitude. Furthermore, as a consequence of configurational entropy effects, the more strongly adsorbed species is also nC6. We therefore have a mixture of more-mobile-more-strongly-adsorbed-nC6 and tardier-less-strongly-adsorbed-2MP. Configurational entropy effects cause 2MP to be excluded from the adsorbed phase for operations at $\Theta_t > 4$; concomitant with this exclusion is an increase, by about an order of magnitude, in the diffusivities of both species. The nC6/2MP uptake data are unique because the diffusivity trends in Figure S-55(b) imply that there is synergy between mixture adsorption and mixture diffusion; this synergy aspect is discussed in detail by Titze et al.[96] In the Supporting Information accompanying the article by Titze et al.[96] detailed arguments are presented to show that correlation effects are of negligible importance in nC6/2MP diffusion in MFI zeolite.

10.3 Separation of nC6/2MP/3MP/22DMB/23DMB mixtures with MFI zeolite

We now examine the influence of thermodynamic coupling on the uptake of 5-component mixtures of hexane isomers nC6/2MP/3MP/22DMB/23DMB in MFI zeolite. Firstly, we get gather some insights in the relative magnitudes of the intra-crystalline diffusivities.

Schuring et al.[98] have reported experimental data on the self-diffusivities of both nC6 and 2MP in nC6/2MP mixtures. These measurements were made at a total loading that is kept nearly constant at 3.5 molecules per unit cell. Their data, that were measured at 433 K shows that *both* self-diffusivities are reduced with increasing loading of 2MP in the mixture; see Figure S-56(a). The preferential location of 2MP at the intersections causes blocking of molecular traffic in the intersecting channel system of MFI. MD simulations show that such intersection blocking effects also manifest in nC6/22DMB mixtures.[99]

We also note that the linear nC6 has a diffusivity that is about an order of magnitude higher than that of the branched 2MP. MD simulations show that the results such as that in Figure S-56(a) also hold for nC6/22DMB mixtures.[99]

For the transient uptake simulations, we assume value $Đ_{nC6}/Đ_{2MP}$ = 5.

We now try to get an estimate of the relative values of diffusivities of the branched isomers in MFI. On the basis of the experimental data on diffusivities of hexane isomers reported by Cavalcante and Ruthven[100] and Jolimaître et al,[101] we note that the hierarchy of diffusivities is 2MP ≈ 3MP > > 23DMB > 22DMB; see Arrhenius plots in Figure S-56(b,c).

The data in Figure S-56 implies that inclusion of diffusional considerations will result in sharper separations with MFI between 3MP and 23DMB than is possible on the basis of equilibrium considerations alone. For a conservative evaluation of the separations we assume the ratios of diffusivities as $Đ_{2MP}/Đ_{3MP}$ =1; $Đ_{2MP}/Đ_{22DMB}$ =5; $Đ_{22MB}/Đ_{23DMB}$ =1; these values are also in agreement with those used in the work of Herm et al.[88] By fixing the value of $Đ_{nC6}/r_c^2$, the diffusional characteristics are fully determined. Herm et al.[88] have taken the value of $Đ_{nC6}/r_c^2$ = 0.002 s^{-1} for MFI zeolite. This value of $Đ_{nC6}/r_c^2$ = 0.002 s^{-1} for nC6 is lower than the values of either 2MB and 2MP that are used to simulate the Jolimaître experiments. We therefore conclude that the value of $Đ_{nC6}/r_c^2$ = 0.002 s^{-1} is a conservative estimate.

Figure S-57(a,b) present simulations of transient uptake inside MFI crystal exposed to a gas phase 5-component nC6/2MP/3MP/22DMB/23DMB mixture at a total pressure of 100 kPa and 433 K. The partial pressures of the components in the bulk gas phase at the inlet are $p_1 = p_2 = p_3 = p_4 = p_5$ = 20 kPa. For the uptake simulations that include the influence of thermodynamic coupling, using Equation (S-44), we note that nC6 shows an overshoot in the uptake during the early stages of the transience. If thermodynamic coupling is ignored and Equation (S-45) is invoked for determining intra-crystalline fluxes, the nC6 overshoot disappears. The nC6 overshoot signifies uphill diffusion and attainment of

supra-equilibrium conversions for a brief time span; these phenomena are beneficial to the separation of alkane isomers.

Figure S-58(a,b) present simulations of transient breakthroughs in a fixed bed adsorber packed with MFI crystals. The feed mixture consists of gas phase 5-component nC6/2MP/3MP/22DMB/23DMB mixture at a total pressure of 100 kPa and 433 K. The partial pressures of the components in the bulk gas phase at the inlet are $p_1 = p_2 = p_3 = p_4 = p_5 = 20$ kPa. A detailed comparison of the simulations that include thermodynamic coupling (Figure S-58(a)), with the simulations that ignore thermodynamic coupling (Figure S-58(b)), shows that the breakthrough times are delayed due to thermodynamic coupling. The delay in the breakthrough of nC6 is the largest; this is beneficial to separations.

The objective of the separation of hexane isomers is to obtain a raffinate product that has a higher octane number. For two simulation scenarios in Figure S-58(a,b), the RON of the mixture exiting the fixed bed is calculated from the pure component RON values in Table S-7. The RON calculations are based a linear mixing rule using the mole fractions in the product gas exiting the adsorber; no non-linear mixing rules are applied. Figure S-58(c) compares the RON values of the product gas for the two breakthrough simulations, including thermodynamic coupling, or ignoring it. Let us assume a target RON value of the raffinate from the adsorber is 92 RON. From a material balance on the adsorber, we can determine the number of moles of 92 RON+ product that can be recovered. Expressed per kg of MFI zeolite packed in the adsorber, the 92+ RON productivity is 0.36 mol kg^{-1} for the scenario in which thermodynamic coupling is included. The 92+ RON productivity is lowered to a value of 0.28 mol kg^{-1} for the breakthrough simulations that ignore thermodynamic coupling.

10.4 Analysis of Jolimaître experiments on 2MB/2MP/22DMB separations with MFI zeolite

In this Section we analyse a set of seven experiments reported by Jolimaître et al.[102] for transient breakthrough of both binary and ternary mixtures containing 2-methylbutane (2MB), 2-methylpentane (2MP), and 2,2 dimethylbutane (22DMB) mixtures at 473 K in a fixed bed packed with MFI zeolite.

The branched isomers preferentially locate at the channel intersections, that provides extra "leg-room"; see computational snapshots in Figure S-52 and Figure S-53. Per unit cell of MFI zeolite, there are 4 channel intersection sites. The unary isotherms, determined experimentally by Jolimaître et al.[102] , are fitted very well with a 1-site Langmuir model with equal saturation capacities (= 4 molecules per unit cell) for 2MB, 2MP, and 22DMB; see Table S-11.

The hierarchy of adsorption strengths, quantified by the Langmuir binding constants, b, is 2MB < 2MP > 22DMB, i.e. 2MP is preferentially adsorbed. However, due to the differences in the molecular sizes the ratio of Maxwell-Stefan (M-S) diffusivities are: $Đ_{2MB}/Đ_{2MP}=1.5;\quad Đ_{2MP}/Đ_{22DMB}=80;\quad Đ_{2MB}/Đ_{22DMB}=120$.

For the ternary 2MB/2MP/22DMB mixtures with equal saturation capacities, the matrix of thermodynamic correction factors can be calculated explicitly from the mixed-gas Langmuir model (cf. Equation (S-37)):

$$\left[\Gamma\right]=\frac{1}{1-\theta_1-\theta_2-\theta_3}\begin{bmatrix}1-\theta_2-\theta_3 & \theta_2 & \theta_3\\ \theta_1 & 1-\theta_1-\theta_3 & \theta_3\\ \theta_1 & \theta_2 & 1-\theta_1-\theta_2\end{bmatrix} \tag{S-71}$$

For diffusion of pentane, and hexane isomers in MFI zeolite, we had presented detailed arguments and calculations in our earlier works[24, 96] to demonstrate that the correlation effects are of negligible importance. Therefore, the Maxwell-Stefan flux relations for intra-crystalline transport, Equation (S-41), reduces for ternary mixtures to

$$\begin{pmatrix}N_1\\N_2\\N_3\end{pmatrix}=-\rho\begin{bmatrix}Đ_1 & 0 & 0\\ 0 & Đ_2 & 0\\ 0 & 0 & Đ_3\end{bmatrix}\frac{1}{1-\theta_1-\theta_2-\theta_3}\begin{bmatrix}1-\theta_2-\theta_3 & \theta_2 & \theta_3\\ \theta_1 & 1-\theta_1-\theta_3 & \theta_3\\ \theta_1 & \theta_2 & 1-\theta_1-\theta_2\end{bmatrix}\begin{pmatrix}\frac{\partial q_1}{\partial r}\\ \frac{\partial q_2}{\partial r}\\ \frac{\partial q_3}{\partial r}\end{pmatrix} \tag{S-72}$$

Figure S-59(a,b,c) present the transient breakthrough experimental data (indicated by colored symbols) of Jolimaître et al.[102] for (a) 2MB/2MP, and (b, c) 2MP/22DMB binary mixtures at 473 K. The continuous solid black lines are Maxwell-Stefan model simulations based on Equation (S-54), that

include thermodynamic coupling. The agreement of the simulation results with the experiments is good in all three cases. The dashed black lines in (b), and (c) are the simulations based on Equation (S-56), in which the thermodynamic correction factors are assumed to be described by $\Gamma_{ij} = \delta_{ij}$, the Kronecker delta. If thermodynamic coupling effects are ignored, the agreement of the simulations with experimental data is significantly poorer.

Figure S-60(a,b,c,d) present the transient breakthrough experimental data (indicated by colored symbols) of Jolimaître et al.[102] for 2MB/2MP/22DMB ternary mixtures at 473 K, corresponding to Runs 19, 20, 21 and 22, respectively. The continuous solid black lines are the breakthrough simulations using M-S flux expression (S-72), including thermodynamic coupling. In all four Runs, the sequence of breakthroughs is 22DMB, 2MB, and 2MP reflecting the combined influences of adsorption and diffusion. The adsorption hierarchy is 2MP > 22DMB > 2MB, whereas the diffusion hierarchy is 2MB > 2MP > > 22DMB. The agreement of the simulation results, that including diffusional limitations along with thermodynamic coupling, with the experiments is good in all four cases. The important point to stress is that all seven breakthrough experimental runs for binary and ternary mixtures can be simulated reasonably quantitatively by using the same set of adsorption and diffusion parameters as specified in Table S-11.

Due to the strong diffusional limitation experienced by 22DMB, the di-branched isomer is the first one to breakthrough in the experiments, despite the fact that its binding strength is lower than that of 2MP. The earlier breakthrough of 22DMB is desirable from the point of view of producing a product with high RON number. In other words, diffusional limitations are key to the use of MFI zeolite for octane enhancement as it increases the RON productivity.

In order to underscore the strong influence of the thermodynamic coupling on the productivity of high-RON product, we examine Run 20 in more detail. In Figure S-61(a,b) the experimental data for Run 20 are compared with three types of simulations: ignoring diffusional influences (colored solid lines in Figure S-61(a)), (b) including diffusional influences along with Γ_{ij} (continuous black lines in

Figure S-61(b)), and including diffusional influences, but ignoring thermodynamic coupling, i.e. $\Gamma_{ij} = \delta_{ij}$ (dashed black lines in Figure S-61(b)). If diffusional influences are ignored, 2MB is the component that is expected to elute first; this is an undesirable scenario; see Figure S-61(a). Both of the simulations that include diffusional influences anticipate the correct sequence of breakthroughs, but good quantitative agreement with experiments is only obtained when thermodynamic coupling effects are included; see Figure S-61(b).

For each of the simulation scenarios, the RON of the mixture exiting the fixed bed is calculated from the pure component RON values in Table S-7. The RON calculations are based a linear mixing rule using the mole fractions in the product gas exiting the adsorber; no non-linear mixing rules are applied. Figure S-61(c) presents the calculations the temporal development of the RON of the gaseous effluent from the adsorber. For a target RON of say 92, we can determine the number of mole of product with 92+ RON in the outlet from a material balance. The RON productivities, expressed as moles produced per L of MFI zeolite are for the diffusion scenarios are:

(a) including diffusional influences along with Γ_{ij} (continuous black line in Figure S-61(c)) = 0.135 mol L^{-1}

(b) including diffusional influences, but ignoring thermodynamic coupling, i.e. $\Gamma_{ij} = \delta_{ij}$ (dashed black line in Figure S-61(c)) = 0.156 mol L^{-1}

Ignoring thermodynamic coupling effects overestimates the productivity of 92+ RON product from the adsorber.

10.5 List of Tables for Separation of alkane isomers with MFI zeolite

Table S-7. Research Octane Numbers (RON) of C4, C5, C6, and C7 alkanes. Information collected from a variety of web sources.

Alkane		Research Octane Number (RON)
Symbol	Chemical Name	
nC4	n-butane	94
iC4	iso-butane = 2-methyl propane	102
nC5	n-pentane	61.7
2MB	2-methyl butane	93.5
neoP	2,2 dimethyl propane	98
nC6	n-hexane	30
2MP	2-methyl pentane	74.5
3MP	3-methyl pentane	75.5
22DMB	2,2 dimethyl butane	94
23DMB	2,3 dimethyl butane	105
nC7	n-heptane	0
2MH	2-methyl hexane	42.4
3MH	3-methyl hexane	52
22DMP	2,2 dimethyl pentane	92.8
23DMP	2,3 dimethyl pentane	91.1

Table S-8. Boiling points of alkane isomers.

Alkane		Boiling point
Symbol	Chemical Name	K
nC4	n-butane	263.1
iC4	iso-butane = 2-methyl propane	261.5
nC5	n-pentane	309
2MB	2-methyl butane	301
neo-P	2,2 dimethyl propane	282.5
nC6	n-hexane	341.5
2MP	2-methyl pentane	333.1
3MP	3-methyl pentane	336.5
22DMB	2,2 dimethyl butane	323.15
23DMB	2,3 dimethyl butane	331.2
nC7	n-heptane	371.5
2MH	2-methyl hexane	363.15
3MH	3-methyl hexane	365
22DMP	2,2 dimethyl pentane	352.15
23DMP	2,3 dimethyl pentane	362

Table S-9. Dual-site Langmuir-Freundlich parameters for pure component isotherms for hexane isomers in MFI at 298 K. This data is from the Supporting Information of Titze et al.[96] The unary isotherm data are fitted with the dual-Langmuir-Freundlich model

$$\Theta_i = \Theta_{i,A,sat}\frac{b_{i,A}p_i^{\nu_A}}{1+b_{i,A_i}{}^{\nu_A}} + \Theta_{i,B,sat}\frac{b_{i,B}p_i^{\nu_B}}{1+b_{i,B}p_i^{\nu_B}}$$

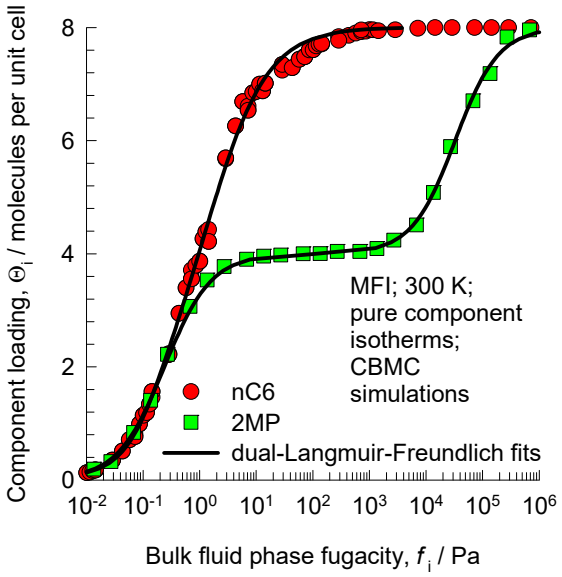

	Site A			Site B		
	$\Theta_{i,A,sat}$ molecules uc^{-1}	$b_{i,A}$ Pa$^{-\nu_i}$	$\nu_{i,A}$ dimensionless	$\Theta_{i,B,sat}$ molecules uc^{-1}	$b_{i,B}$ Pa$^{-\nu_i}$	$\nu_{i,B}$ dimensionless
nC6	6.6	0.7084	0.83	1.4	16.5765	1.5
2MP	4	4.51	1.05	4	7.92×10^{-6}	1.13

Table S-10. Dual-site Langmuir-Freundlich parameters for pure component pentane and hexane isomers at 433 K in MFI zeolite. $\Theta_i = \Theta_{i,A,sat} \frac{b_{i,A} p_i^{\nu_A}}{1 + b_{i,A_i}^{\nu_A}} + \Theta_{i,B,sat} \frac{b_{i,B} p_i^{\nu_B}}{1 + b_{i,B} p_i^{\nu_B}}$

The fits are based on CBMC simulation data of Krishna and van Baten.[95]

	Site A			Site B		
	$\Theta_{A,sat}$ molecules uc^{-1}	b_A $Pa^{-\nu_A}$	ν_A dimensionless	$\Theta_{B,sat}$ molecules uc^{-1}	b_B $Pa^{-\nu_B}$	ν_B dimensionless
nC6	3.2	2.21×10^{-8}	1.6	4.3	7.42×10^{-4}	1
2MP	4	7.85×10^{-4}	1.03			
3MP	4	4.22×10^{-4}	1.02	1	9.88×10^{-7}	1
22DMB	4	2.55×10^{-4}	1.02			
23DMB	4	4.59×10^{-4}	1.02			

The data on M-S diffusivities is taken from our earlier analysis:[24]

$Đ_{nC6}/r_c^2 = 0.002\ s^{-1}$; $Đ_{nC6}/Đ_{2MP} = 5$; $Đ_{2MP}/Đ_{3MP} = 1$; $Đ_{2MP}/Đ_{22DMB} = 5$; $Đ_{22MB}/Đ_{23DMB} = 1$

Table S-11. Single-site Langmuir parameters, and M-S diffusivities $Đ_i/r_c^2$, for pure component 2MB, 2MP, and 22DMB at 473 K in MFI zeolite. The parameters are based on the experimental data of Jolimaître et al.[101, 102] All simulations of the breakthrough experiments of Jolimaître et al.[102] were performed for extrudate 2; bed voidage, $\varepsilon = 0.4$; density of extrudate 2, $\rho = 620.8$ kg m^{-3}. The length of the adsorber bed is 0.795 m. The interstitial velocity v varied with each run and were taken from Table 6 of Jolimaître et al.[102] The partial pressures of each of the components 2MB, 2MP, and 22DMB at the inlet to the adsorber are specified using the data provided in Table 6 of Jolimaître et al.[102]

$\Theta_i = \frac{\Theta_{i,sat} b_i p}{1 + b_i p}$. The conversion factor to convert loading expressed in molecules per unit cell to mol per kg is 0.1734.

	$\Theta_{i,sat}$ molecules uc^{-1}	b_i Pa^{-1}	$Đ_i/r_c^2$ s^{-1}
2MB	4	4.12×10^{-5}	0.0075
2MP	4	1.27×10^{-4}	0.005
22DMB	4	7.12×10^{-5}	0.0000625

10.6 List of Figures for Separation of alkane isomers with MFI zeolite

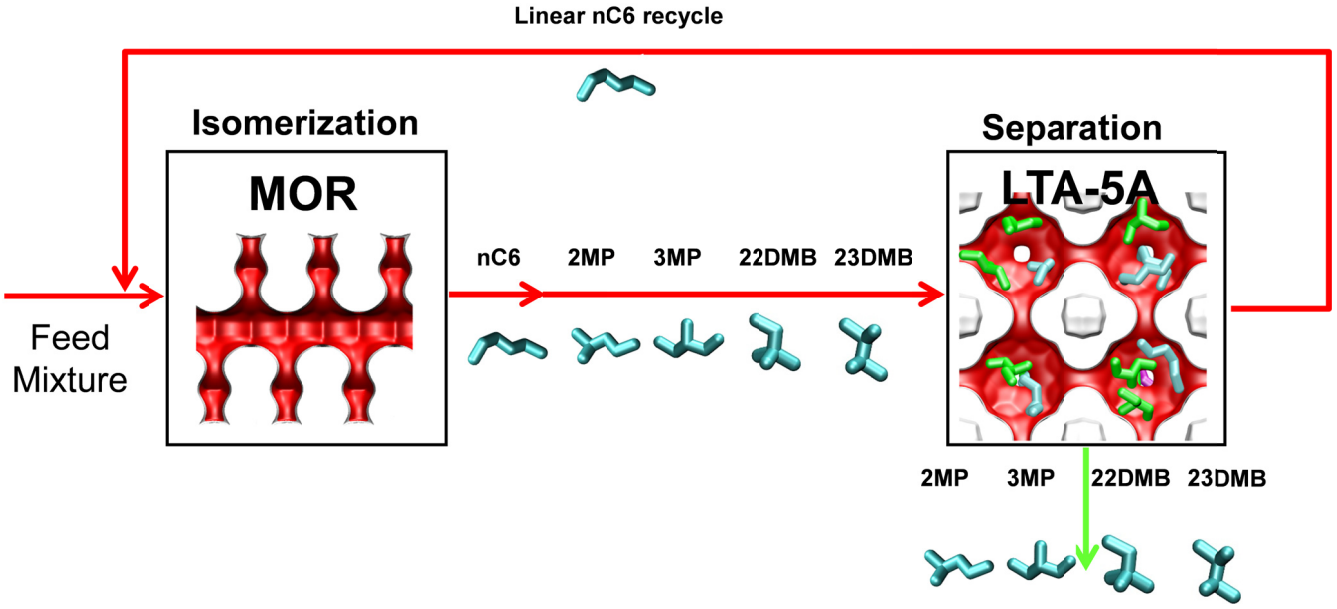

Figure S-46. Currently employed processing scheme for nC6 isomerization and subsequent separation step using LTA-5A zeolite.

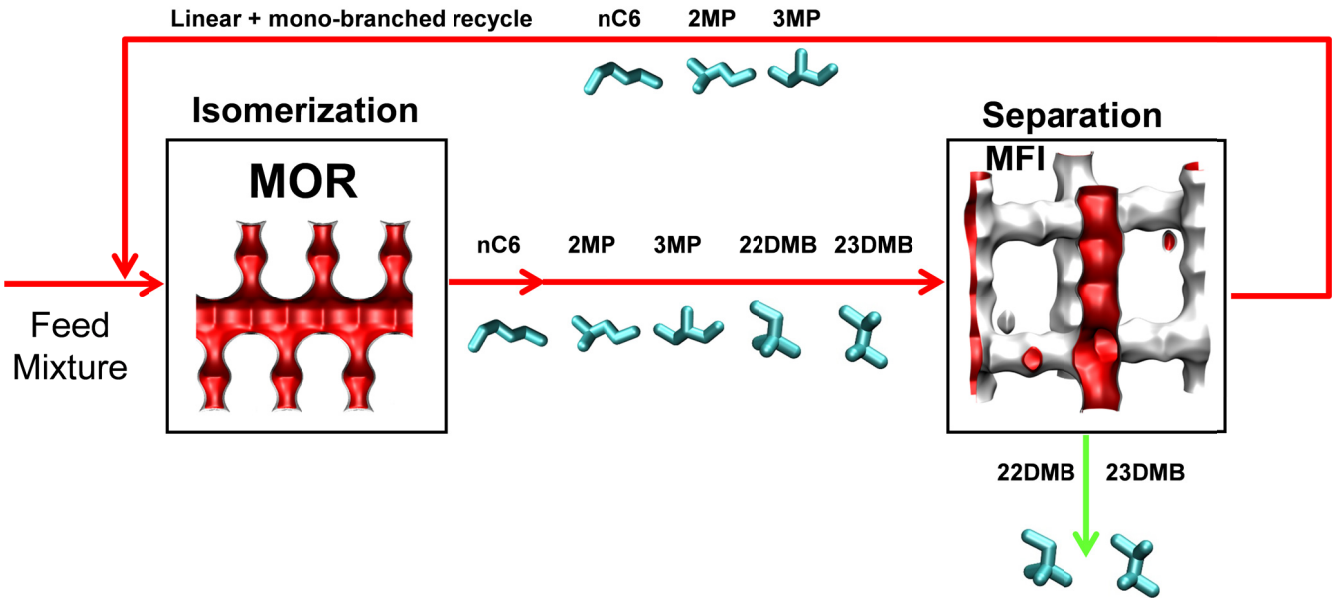

Figure S-47. Improved processing scheme for the nC6 isomerization process using MFI zeolite in the separation step.

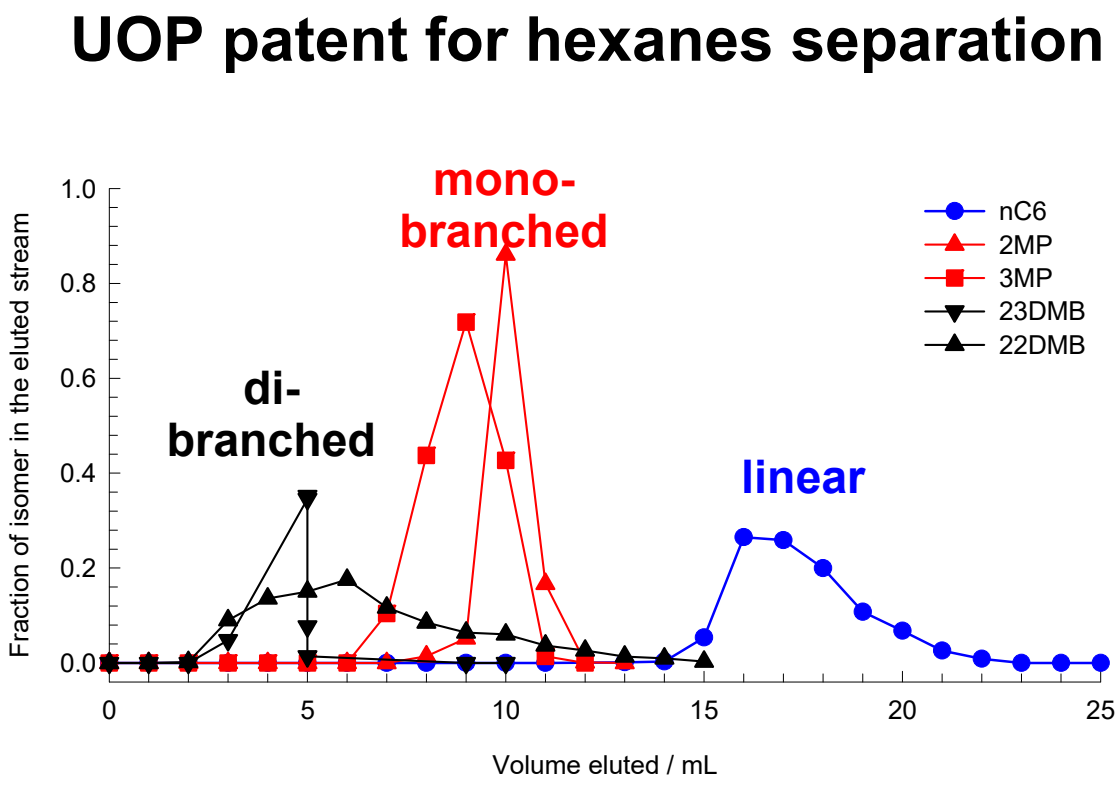

The adsorbent may be silicalite, ferrierite, zeolite Beta, MAPO-31, SAPO-31, SAPO-11, zeolite X ion exchanged with alkaline cations, alkaline earth cations, or a mixture thereof, and zeolite Y ion exchanged with alkaline cations..

Figure S-48 Pulsed chromatographic separation of hexane isomers as reported in the patents assigned to Universal Oil Products (UOP).[91-93]

MFI pore landscape

	MFI
a /Å	20.022
b /Å	19.899
c /Å	13.383
Cell volume / Å^3	5332.025
conversion factor for [molec/uc] to [mol per kg Framework]	0.1734
conversion factor for [molec/uc] to [kmol/m^3]	1.0477
ρ [kg/m3]	1796.386
MW unit cell [g/mol(framework)]	5768.141
ϕ, fractional pore volume	0.297
open space / Å^3/uc	1584.9
Pore volume / cm^3/g	0.165
Surface area /m^2/g	487.0
DeLaunay diameter /Å	5.16

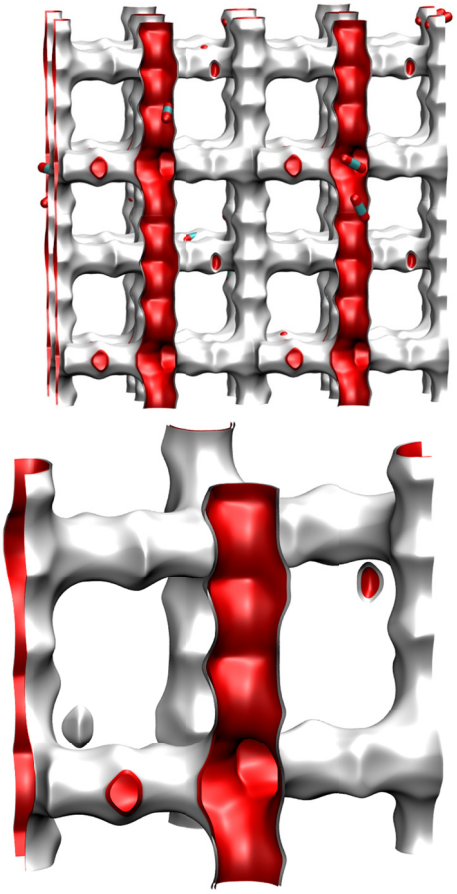

Figure S-49. Structural details and pore landscape for MFI zeolite.

10 ring channel of MFI viewed along [100]

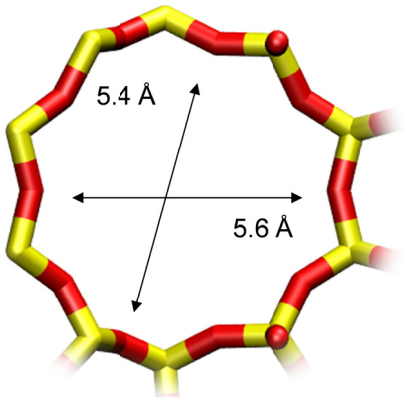

10 ring channel of MFI viewed along [010]

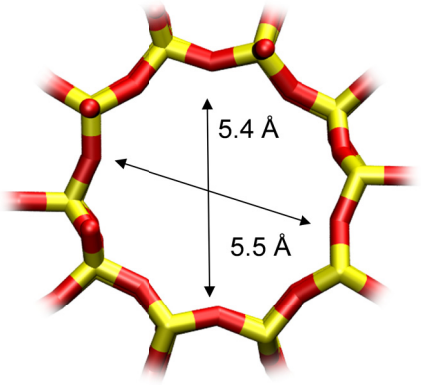

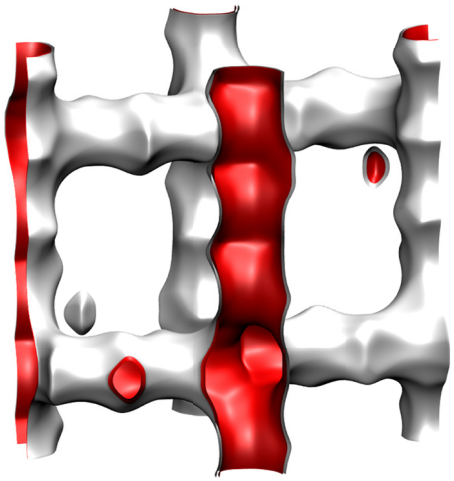

Figure S-50. Structural details and pore landscape for MFI zeolite.

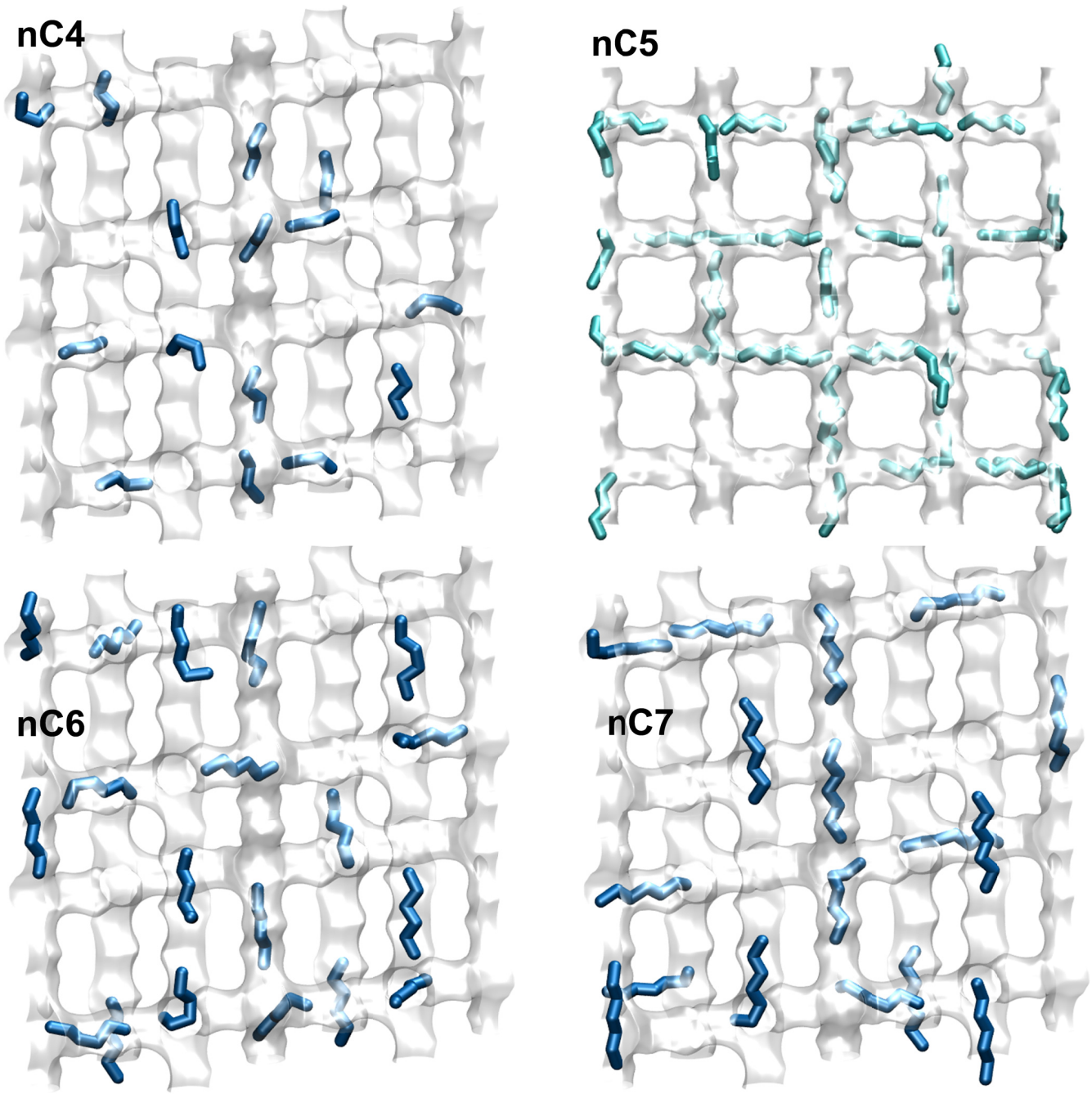

Figure S-51. Computational snapshots showing the location of linear alkanes (nC4, nC5, nC6, nC7) within the intersecting channel topology of MFI zeolite.

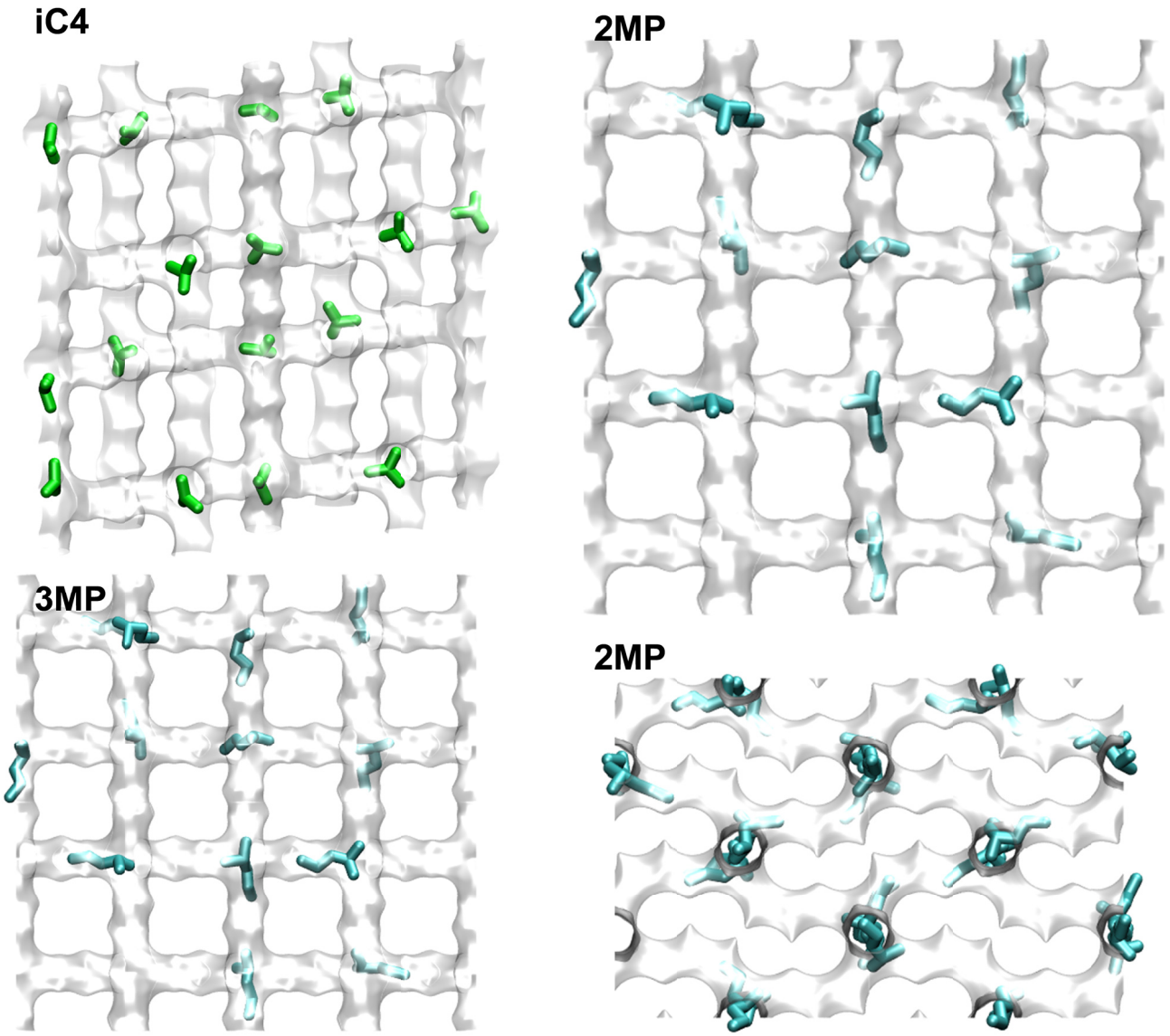

Figure S-52. Computational snapshots showing the location of mono-branched alkanes at the channel intersections of MFI zeolite.

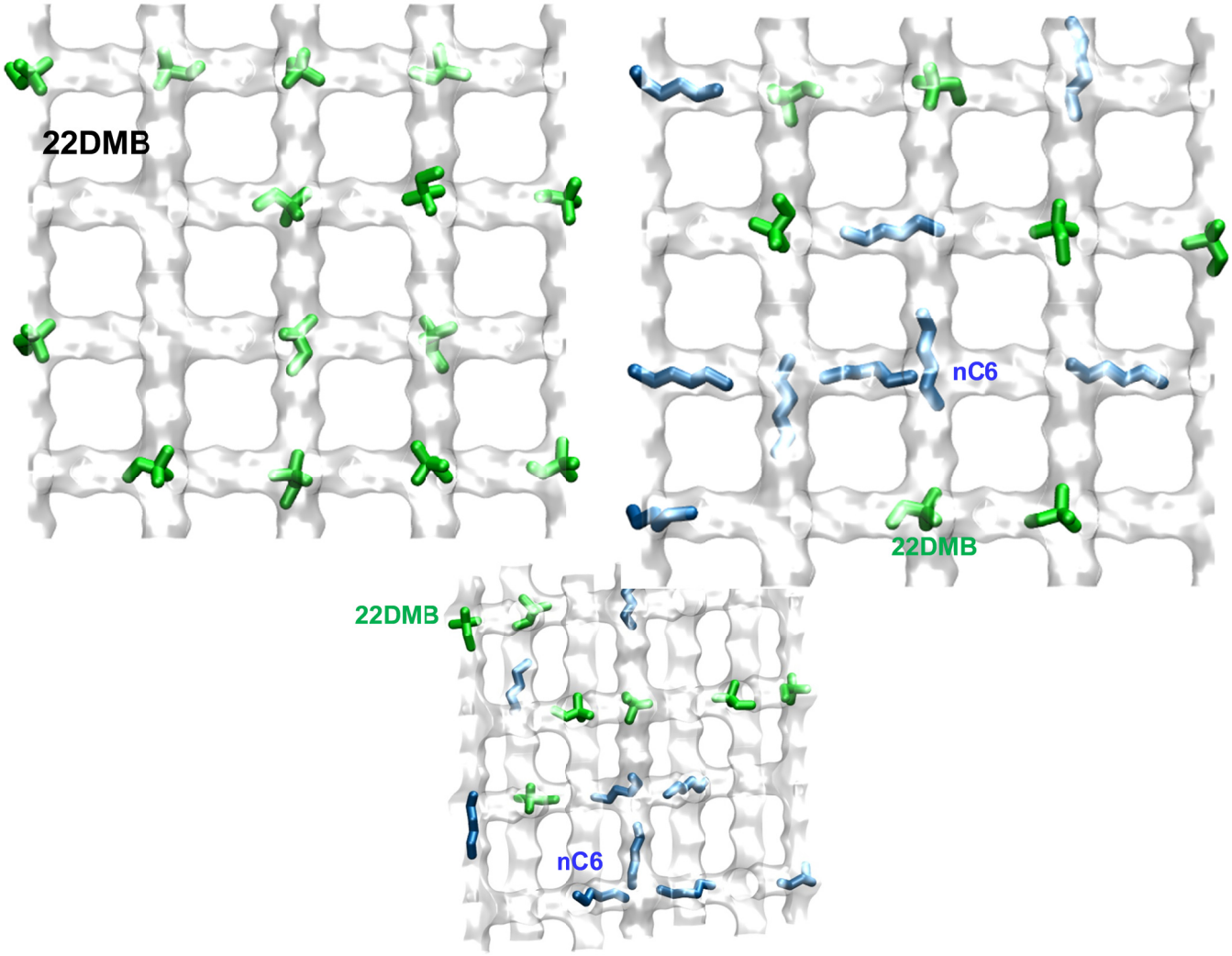

Figure S-53. Computational snapshots showing the location of di-branched 22DMB at the channel intersections of MFI zeolite.

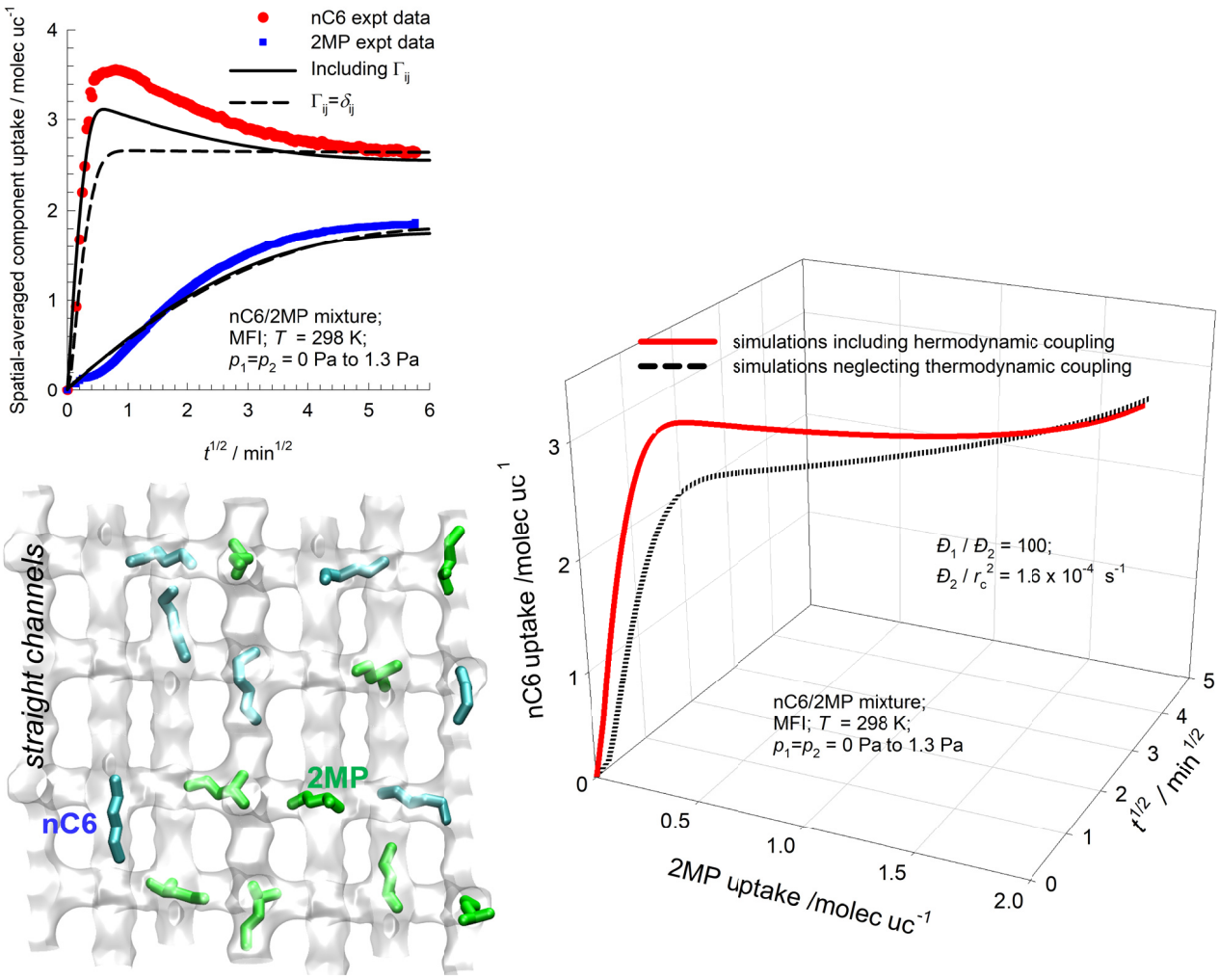

Figure S-54. Experimental data of Titze et al.[96] for Run 1 transient uptake of nC6/2MP mixtures in MFI zeolite. Input data simulation of Run 1: $Đ_1/r_c^2 = 0.016$ s^{-1}; $Đ_2/r_c^2 = 1.6\times10^{-4}$ s^{-1}; $t = 0$; $p_1(r_c,0) = p_2(r_c,0) = 0$ Pa; $t \geq 0$; $p_1(r_c,t) = p_2(r_c,t) = 1.3$ Pa. The isotherm data are provided in Table S-9. The mixture adsorption equilibrium is determined using the Real Adsorbed Solution Theory (RAST).

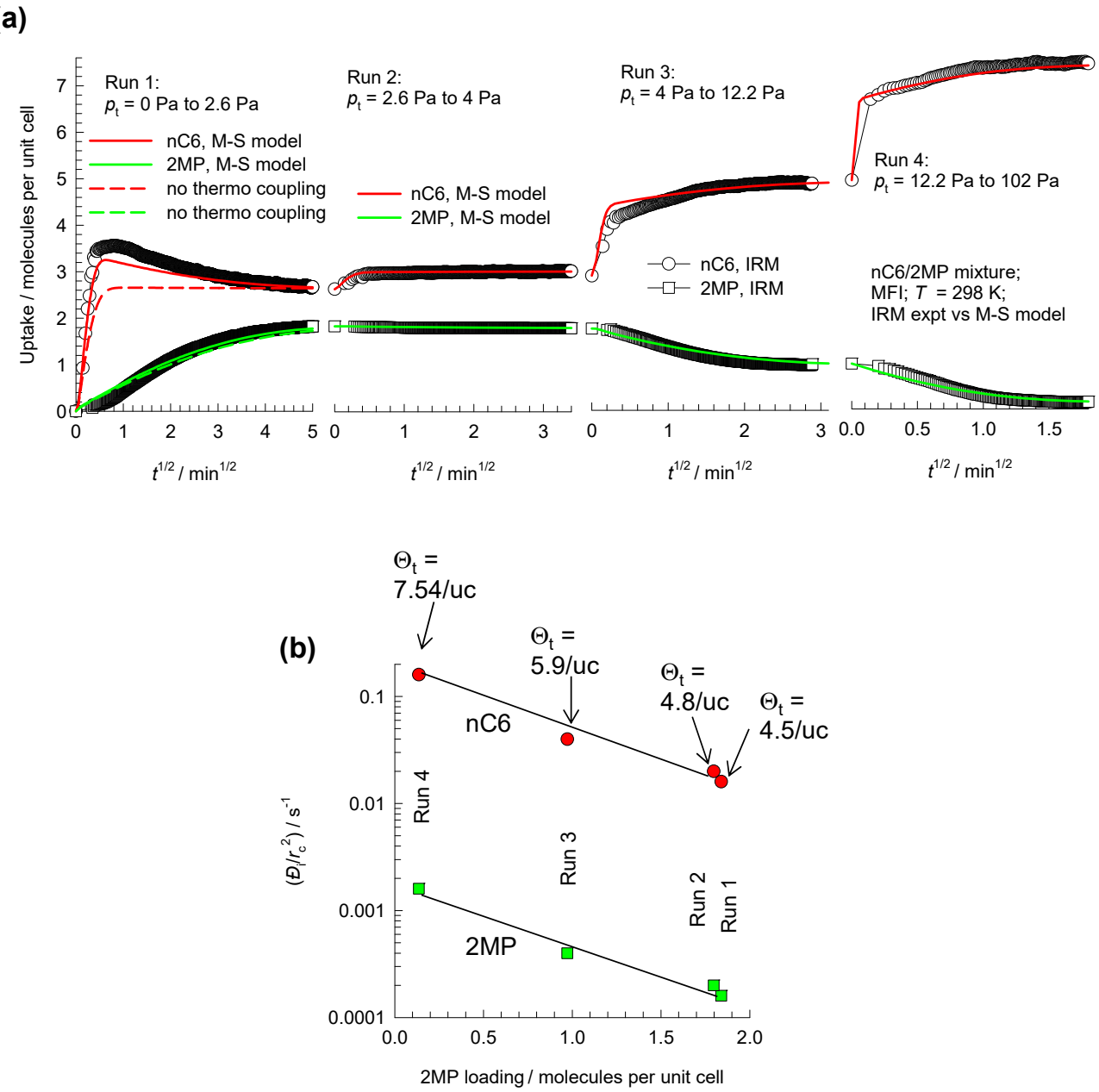

Figure S-55. (a) Experimental data of Titze et al.[96] for four different experimental campaigns (Runs 1, 2, 3, and 4) for transient uptake of nC6/2MP mixtures in MFI zeolite with different step changes in the bulk gas pressures. The continuous solid lines are transient uptake simulations using the equation (S-54) are in good agreement. The isotherm data are provided in Table S-9. (b) The fitted values of the M-S diffusivities $Đ_{nC6}/r_c^2$ and $Đ_{2MP}/r_c^2$ in each individual campaign is plotted as a function of the loading of 2MP. The ratio of the M-S diffusivities of nC6 and 2MP is maintained at 100.

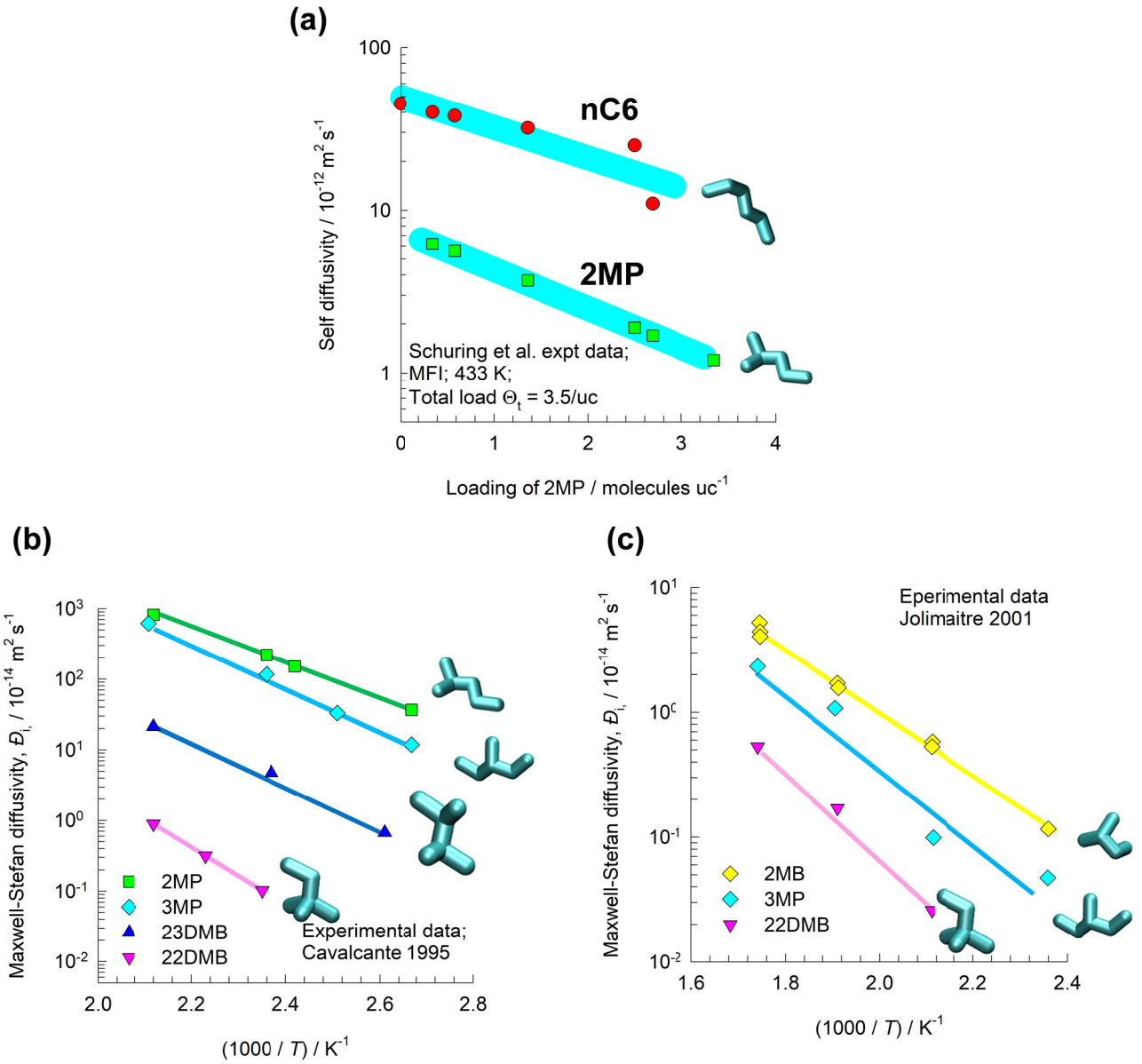

Figure S-56. (a) Experimental data[98] on self-diffusivities of nC6 and 2-methylpentane (2MP) as a function of the loading of 2MP, keeping the total loading Θ_t = 3.5/uc. (b, c) Arrhenius plot of diffusivities of 2MB, 2MP, 3MP, 22DMB, and 23DMB in MFI zeolite. The data are re-plotted from the experimental results of (b) Cavalcante and Ruthven,[100] and (c) Jolimaître et al.[101]

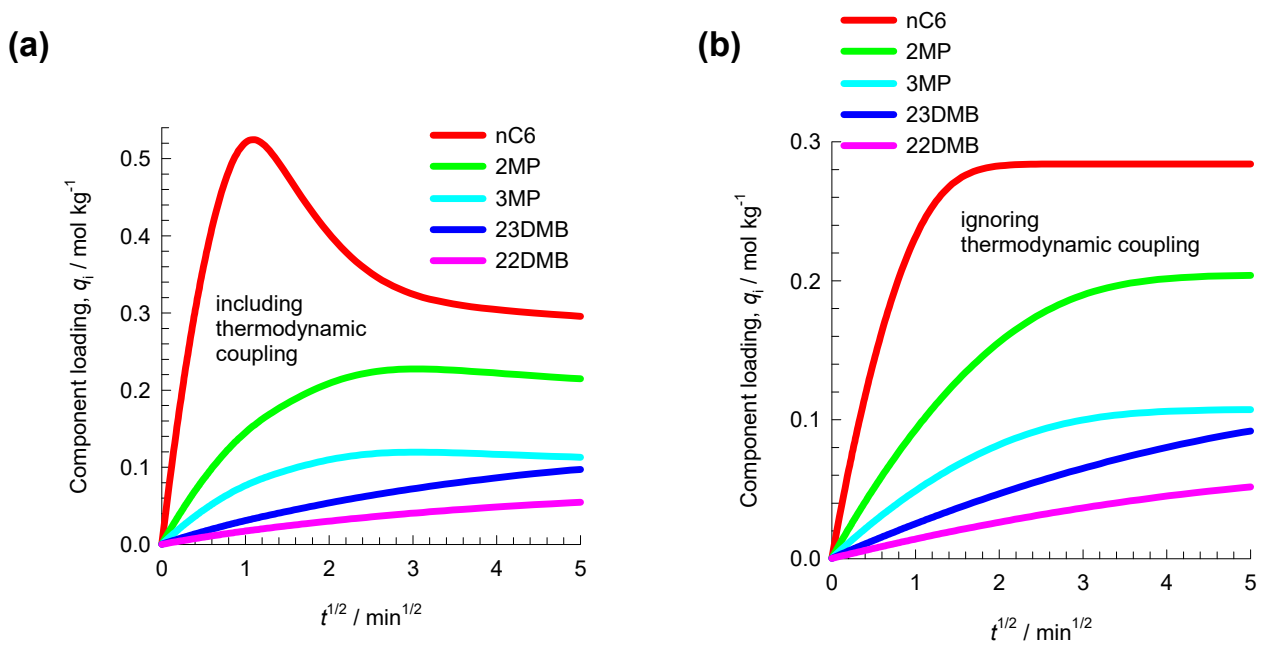

Figure S-57. (a, b) Transient uptake inside MFI crystal exposed to a gas phase 5-component nC6/2MP/3MP/22DMB/23DMB mixture at a total pressure of 100 kPa and 433 K. The partial pressures of the components in the bulk gas phase at the inlet are $p_1 = p_2 = p_3 = p_4 = p_5 = 20$ kPa. (a) These uptake simulations ignore thermodynamic coupling: Equation (S-44). (b) In these uptake simulations, thermodynamic coupling is ignored: Equation (S-45). The input data on unary isotherms and M-S diffusivities are provided in Table S-10.

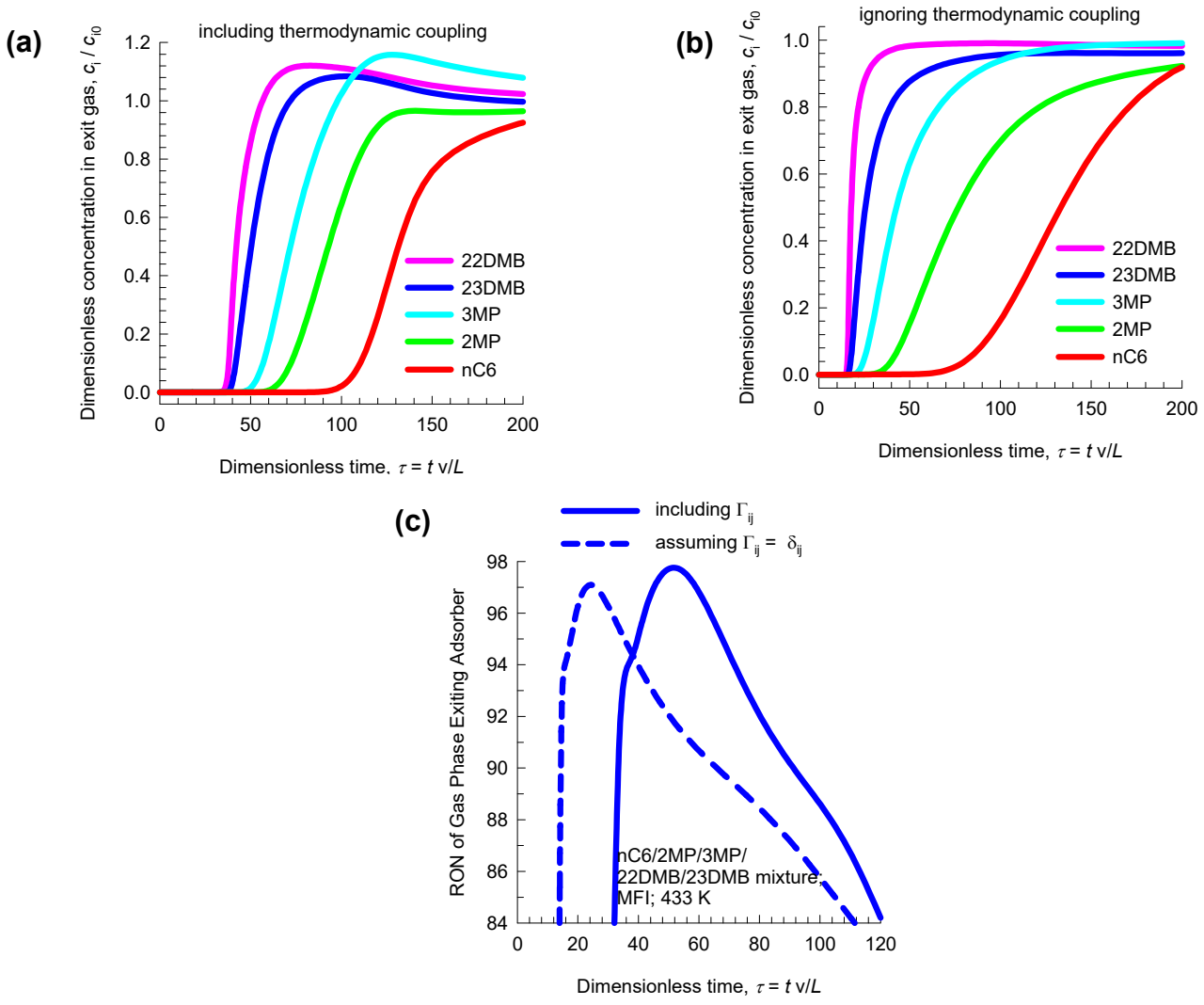

Figure S-58. (a, b) Influence of diffusional limitations on the breakthrough characteristics for 5-component nC6/2MP/3MP/22DMB/23DMB mixture in a fixed bed adsorber packed with MFI operating at a total pressure of 100 kPa and 433 K. The partial pressures of the components in the bulk gas phase at the inlet are $p_1 = p_2 = p_3 = p_4 = p_5 = 20$ kPa. (a) In these breakthrough simulations the flux equations include thermodynamic coupling: Equation (S-44). (b) In these breakthrough simulations, thermodynamic coupling is ignored: Equation (S-45). (c) Comparison of the RON of the product gas exiting the MFI adsorber. The input data on unary isotherms and M-S diffusivities are provided in Table S-10.

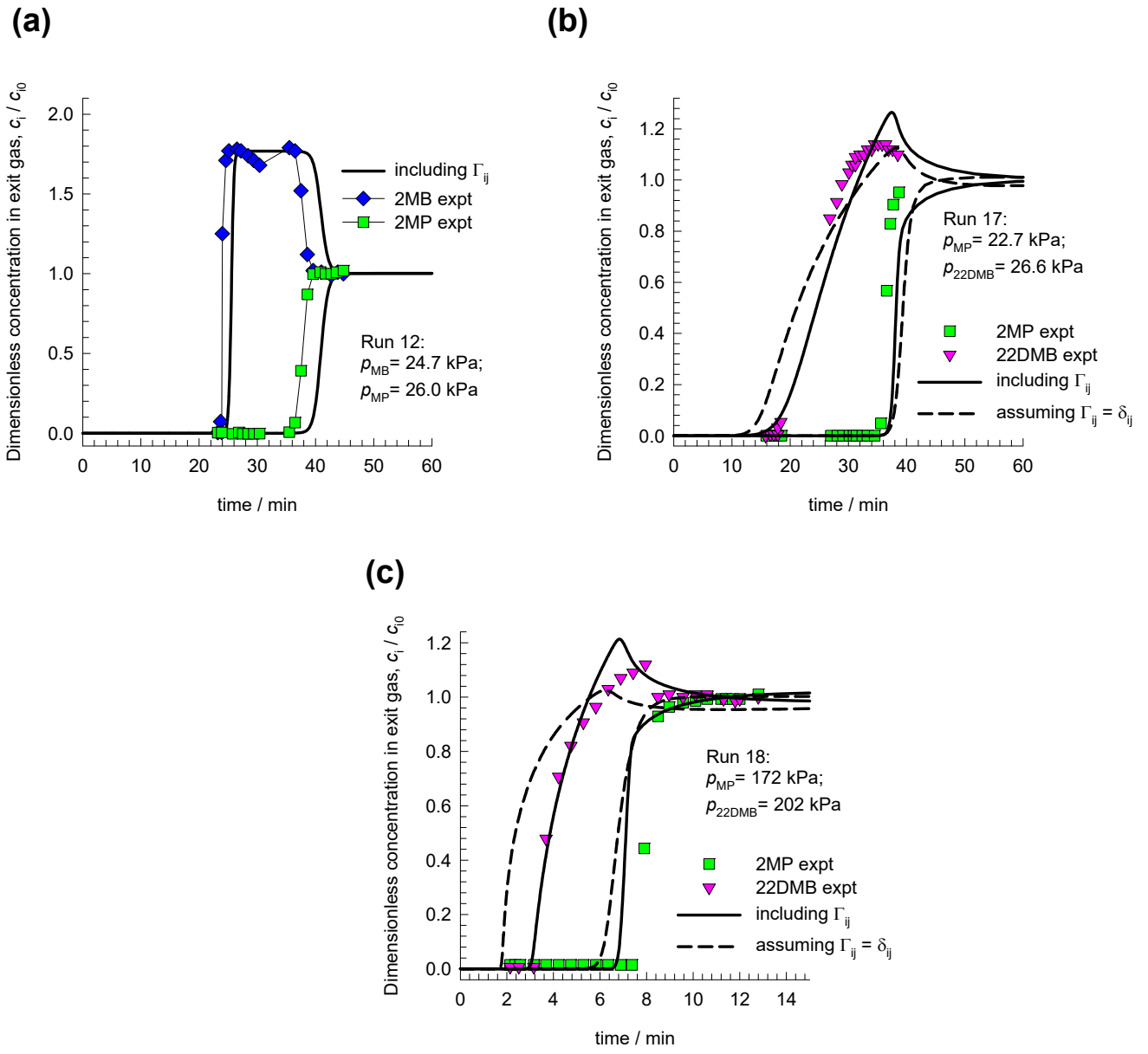

Figure S-59. (a, b, c) Transient breakthrough experiments of Jolimaître et al.[102] for (a) 2MB/2MP, and (b, c) 2MP/22DMB binary mixtures at 473 K. The experimental data correspond to (a) Run 12, (b) Run 17, and (c) Run 18. The continuous solid black lines are Maxwell-Stefan model simulations based on Equation (S-54). The dashed black lines in (b), and (c) are the simulations based on Equation (S-56), in which the thermodynamic correction factors are assumed to be described by $\Gamma_{ij} = \delta_{ij}$, the Kronecker delta. The input data on unary isotherms and M-S diffusivities are provided in Table S-11.

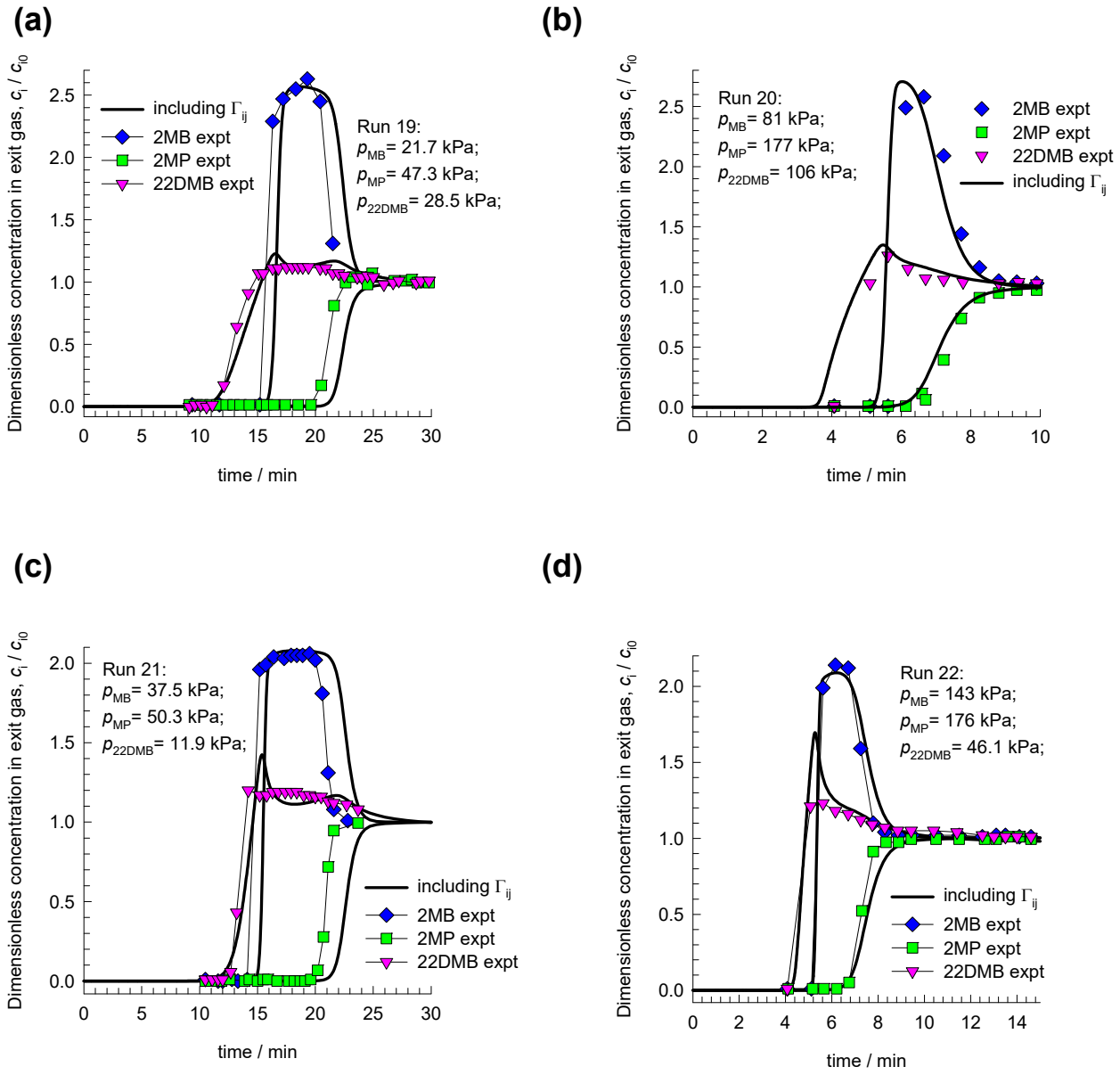

Figure S-60. (a, b, c, d) Transient breakthrough experiments of Jolimaître et al.[102] for 2MB/2MP/22DMB ternary mixtures at 473 K. The experimental data correspond to (a) Run 19, (b) Run 20, (c) Run 21, and (d) Run 22. The continuous solid black lines are the breakthrough simulations using flux expression (S-72). The input data on unary isotherms and M-S diffusivities are provided in Table S-11.

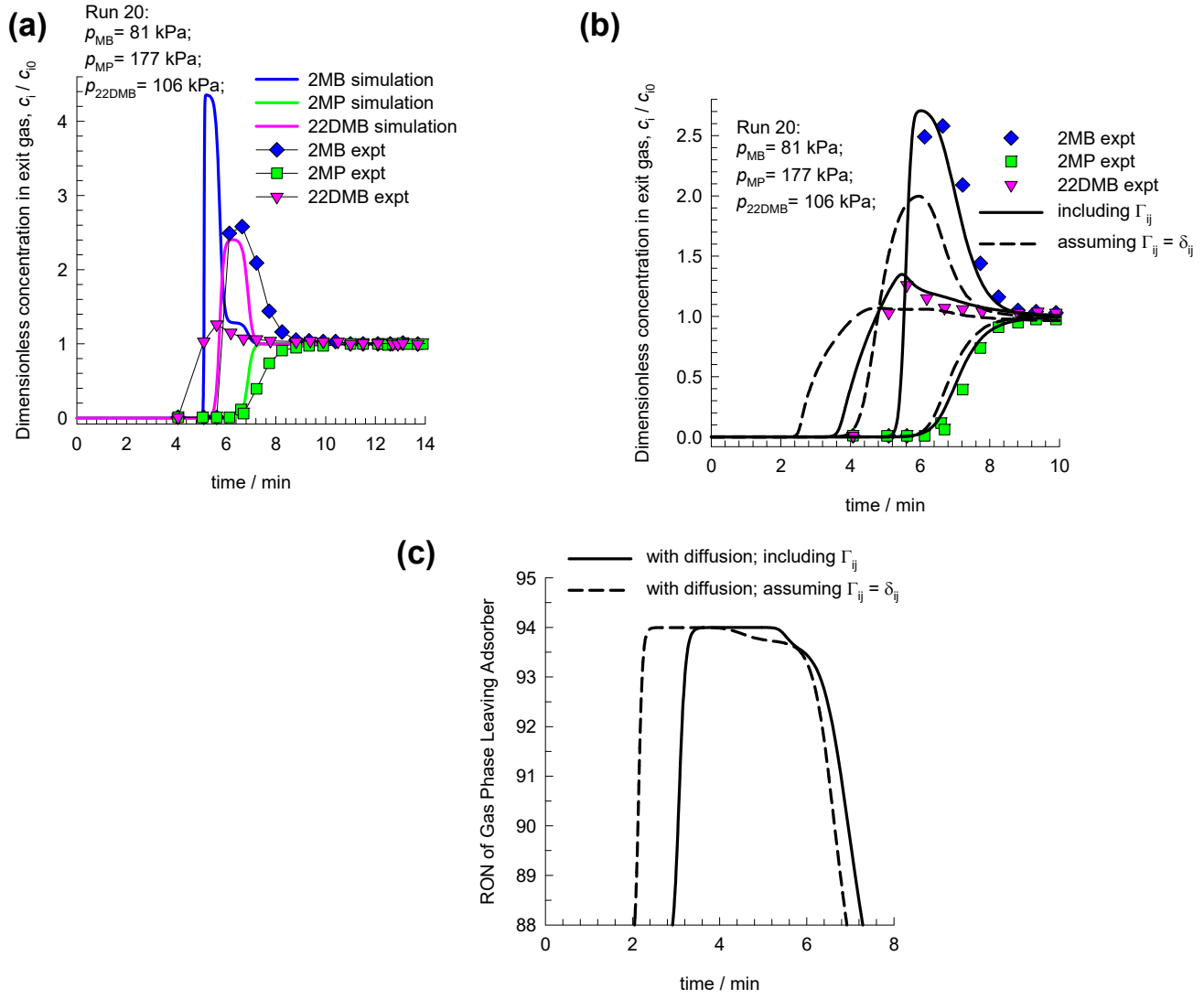

Figure S-61. (a, b) Transient breakthrough experiments of Run 20 of Jolimaître et al.[102] for 2MB/2MP/22DMB ternary mixtures at 473 K. The continuous colored solid lines in (a) are the simulations in which the diffusional influences are considered to be negligible. In (b) the continuous solid black lines are simulations using the M-S flux expression (S-72). The dashed black lines in (b), are simulations in which the thermodynamic correction factors are assumed to be described by $\Gamma_{ij} = \delta_{ij}$. (c) The RON calculations show the influence of the two types of simulations including diffusional influences. The input data on unary isotherms and M-S diffusivities are provided in Table S-11.

11 Nomenclature

Latin alphabet

b_i	Langmuir parameter, Pa^{-1}
$[B]$	matrix of inverse M-S coefficients, m^{-2} s
c_i	molar concentration of species *i*, mol m^{-3}
c_t	total molar concentration in mixture, mol m^{-3}
c_{i0}	molar concentration of species *i* in fluid mixture at inlet to adsorber, mol m^{-3}
$Đ_i$	Maxwell-Stefan diffusivity for molecule-wall interaction, m^2 s^{-1}
$Đ_{ij}$	M-S exchange coefficient for *n*-component mixture, m^2 s^{-1}
$Đ_{12}$	M-S exchange coefficient for binary mixture, m^2 s^{-1}
$[D]$	matrix of Fick diffusivities, m^2 s^{-1}
f_i	partial fugacity of species *i*, Pa
n	number of species in the mixture, dimensionless
L	length of packed bed adsorber, m
N_i	molar flux of species *i* with respect to framework, mol m^{-2} s^{-1}
p_i	partial pressure of species *i* in mixture, Pa
p_t	total system pressure, Pa
q_i	component molar loading of species *i*, mol kg^{-1}
$q_{i,sat}$	molar loading of species *i* at saturation, mol kg^{-1}
q_t	total molar loading in mixture, mol kg^{-1}
$\bar{q}_i(t)$	spatial-averaged component uptake of species *i*, mol kg^{-1}
r	radial direction coordinate, m
r_c	radius of crystallite, m
R	gas constant, 8.314 J mol^{-1} K^{-1}

Nomenclature

t	time, s
T	absolute temperature, K
u_i	velocity of motion of adsorbate species i with respect to the framework material, m s^{-1}
u	superficial gas velocity in packed bed, m s^{-1}
v	interstitial gas velocity in packed bed, m s^{-1}
x_i	mole fraction of species i in adsorbed phase, dimensionless
z	distance along the adsorber, m

Greek alphabet

Γ_{ij}	thermodynamic factors, dimensionless
$[\Gamma]$	matrix of thermodynamic factors, dimensionless
δ_{ij}	Kronecker delta, dimensionless
ε	voidage of packed bed, dimensionless
θ_i	fractional occupancy of component i, dimensionless
θ_t	fractional occupancy of adsorbed mixture, dimensionless
θ_V	fractional vacancy, dimensionless
$[\Lambda]$	matrix of Maxwell-Stefan diffusivities, m^2 s^{-1}
μ_i	molar chemical potential, J mol^{-1}
ρ	framework density, kg m^{-3}
τ	time, dimensionless

Subscripts

i	referring to component i
t	referring to total mixture

sat	referring to saturation conditions

12 References

(1) Materials for Separation Technologies: Energy and Emission Reduction Opportunities. U.S. Department of Energy, Energy Efficiency and Renewable Energy, 2005.

(2) Yang, R. T. *Adsorbents: Fundamentals and Applications*. John Wiley & Sons, Inc.: Hoboken, New Jersey, 2003.

(3) Ruthven, D. M. *Principles of Adsorption and Adsorption Processes*. John Wiley: New York, 1984.

(4) Sircar, S.; Myers, A. L. *Gas Separation by Zeolites, Chapter 22*. Handbook of Zeolite Science and Technology; Edited by S.M. Auerbach, K.A. Carrado and P.K. Dutta, Marcel Dekker: New York, 2003.

(5) Ruthven, D. M.; Farooq, S.; Knaebel, K. S. *Pressure swing adsorption*. VCH Publishers: New York, 1994.

(6) Ruthven, D. M.; Farooq, S. Air Separation by Pressure Swing Adsorption. *Gas Sep. Purif.* **1990**, *4*, 141-148.

(7) Yoon, J. W.; Chang, H.; Lee, S.-J.; Hwang, Y. K.; Hong, D.-Y.; Lee, S.-K.; Lee, J. S.; Jang, S.; Yoon, T.-U.; Kwac, K.; Jung, Y.; Pillai, R. S.; Faucher, F.; Vimont, A.; Daturi, M.; Férey, G.; Serre, C.; Maurin, G.; Bae, Y.-S.; Chang, J.-S. Selective Nitrogen Capture by Porous Hybrid Materials Containing Accessible Transition Metal Ion Sites. *Nature Materials* **2017**, *16*, 526-531.

(8) Bloch, E. D.; Queen, W. L.; Krishna, R.; Zadrozny, J. M.; Brown, C. M.; Long, J. R. Hydrocarbon Separations in a Metal-Organic Framework with Open Iron(II) Coordination Sites. *Science* **2012**, *335*, 1606-1610.

(9) He, Y.; Krishna, R.; Chen, B. Metal-Organic Frameworks with Potential for Energy-Efficient Adsorptive Separation of Light Hydrocarbons. *Energy Environ. Sci.* **2012**, *5*, 9107-9120.

(10) Ribeiro, A. M.; Grande, C. A.; Lopes, F. V. S.; Loureiro, J. M.; Rodrigues, A. E. A parametric study of layered bed PSA for hydrogen purification. *Chem. Eng. Sci.* **2008**, *63*, 5258-5273.

(11) Myers, A. L.; Prausnitz, J. M. Thermodynamics of Mixed Gas Adsorption. *A.I.Ch.E.J.* **1965**, *11*, 121-130.

(12) Siperstein, F. R.; Myers, A. L. Mixed-Gas Adsorption. *A.I.Ch.E.J.* **2001**, *47*, 1141-1159.

(13) Rao, M. B.; Sircar, S. Thermodynamic consistency for binary gas adsorption equilibria. *Langmuir* **1999**, *15*, 7258-7267.

(14) Skoulidas, A. I.; Sholl, D. S.; Krishna, R. Correlation effects in diffusion of CH_4/CF_4 mixtures in MFI zeolite. A study linking MD simulations with the Maxwell-Stefan formulation. *Langmuir* **2003**, *19*, 7977-7988.

(15) Chempath, S.; Krishna, R.; Snurr, R. Q. Nonequilibrium MD simulations of difusion of binary mixtures containing short n-alkanes in faujasite. *J. Phys. Chem. B* **2004**, *108*, 13481-13491.

(16) Krishna, R. Describing the Diffusion of Guest Molecules inside Porous Structures. *J. Phys. Chem. C* **2009**, *113*, 19756-19781.

(17) Krishna, R. Diffusion in Porous Crystalline Materials. *Chem. Soc. Rev.* **2012**, *41*, 3099-3118.

(18) Krishna, R.; van Baten, J. M. Onsager coefficients for binary mixture diffusion in nanopores. *Chem. Eng. Sci.* **2008**, *63*, 3120-3140.

(19) Hansen, N.; Keil, F. J. Multiscale modeling of reaction and diffusion in zeolites: from the molecular level to the reactor. *Soft Mater.* **2012**, *10*, 179-201.

(20) Krishna, R.; van Baten, J. M. An Investigation of the Characteristics of Maxwell-Stefan Diffusivities of Binary Mixtures in Silica Nanopores. *Chem. Eng. Sci.* **2009**, *64*, 870-882.

(21) Krishna, R.; van Baten, J. M. Unified Maxwell-Stefan Description of Binary Mixture Diffusion in Micro- and Meso- Porous Materials. *Chem. Eng. Sci.* **2009**, *64*, 3159-3178.

(22) Krishna, R.; van Baten, J. M. Maxwell-Stefan modeling of slowing-down effects in mixed gas permeation across porous membranes. *J. Membr. Sci.* **2011**, *383*, 289-300.

(23) Krishna, R. Using the Maxwell-Stefan formulation for Highlighting the Influence of Interspecies (1-2) Friction on Binary Mixture Permeation across Microporous and Polymeric Membranes. *J. Membr. Sci.* **2017**, *540*, 261-276.

(24) Krishna, R. The Maxwell-Stefan Description of Mixture Diffusion in Nanoporous Crystalline Materials. *Microporous Mesoporous Mater.* **2014**, *185*, 30-50.

(25) Krishna, R. Tracing the Origins of Transient Overshoots for Binary Mixture Diffusion in Microporous Crystalline Materials. *Phys. Chem. Chem. Phys.* **2016**, *18*, 15482-15495.

(26) Krishna, R.; van Baten, J. M. Investigating the Influence of Diffusional Coupling on Mixture Permeation across Porous Membranes *J. Membr. Sci.* **2013**, *430*, 113-128.

(27) Krishna, R.; Baur, R. Modelling Issues in Zeolite Based Separation Processes. *Sep. Purif. Technol.* **2003**, *33*, 213-254.

(28) Krishna, R. Adsorptive separation of $CO_2/CH_4/CO$ gas mixtures at high pressures. *Microporous Mesoporous Mater.* **2012**, *156*, 217-223.

(29) Krishna, R.; van Baten, J. M. Diffusion of alkane mixtures in zeolites. Validating the Maxwell-Stefan formulation using MD simulations. *J. Phys. Chem. B* **2005**, *109*, 6386-6396.

(30) Krishna, R.; van Baten, J. M. Diffusion of alkane mixtures in MFI zeolite. *Microporous Mesoporous Mater.* **2008**, *107*, 296-298.

(31) Krishna, R.; van Baten, J. M. Insights into diffusion of gases in zeolites gained from molecular dynamics simulations. *Microporous Mesoporous Mater.* **2008**, *109*, 91-108.

(32) Krishna, R.; van Baten, J. M. Investigating the Relative Influences of Molecular Dimensions and Binding Energies on Diffusivities of Guest Species Inside Nanoporous Crystalline Materials *J. Phys. Chem. C* **2012**, *116*, 23556-23568.

(33) Krishna, R.; van Baten, J. M. Investigating the potential of MgMOF-74 membranes for CO_2 capture. *J. Membr. Sci.* **2011**, *377*, 249-260.

(34) Krishna, R.; van Baten, J. M. Investigating the Validity of the Knudsen Prescription for Diffusivities in a Mesoporous Covalent Organic Framework. *Ind. Eng. Chem. Res.* **2011**, *50*, 7083-7087.

(35) Krishna, R.; van Baten, J. M. Investigating the Validity of the Bosanquet Formula for Estimation of Diffusivities in Mesopores. *Chem. Eng. Sci.* **2012**, *69*, 684-688.

(36) Krishna, R.; van Baten, J. M. Influence of segregated adsorption on mixture diffusion in DDR zeolite. *Chem. Phys. Lett.* **2007**, *446*, 344-349.

(37) Krishna, R.; van Baten, J. M. Segregation effects in adsorption of CO_2 containing mixtures and their consequences for separation selectivities in cage-type zeolites. *Sep. Purif. Technol.* **2008**, *61*, 414-423.

(38) Krishna, R.; van Baten, J. M. Describing Mixture Diffusion in Microporous Materials under Conditions of Pore Saturation. *J. Phys. Chem. C* **2010**, *114*, 11557-11563.

(39) Krishna, R.; van Baten, J. M. A molecular dynamics investigation of the diffusion characteristics of cavity-type zeolites with 8-ring windows. *Microporous Mesoporous Mater.* **2011**, *137*, 83-91.

(40) Habgood, H. W. The Kinetics of Molecular Sieve Action. Sorption of Nitrogen-Methane Mixtures by Linde Molecular Sieve 4A. *Canad. J. Chem.* **1958**, *36*, 1384-1397.

(41) Farooq, S.; Ruthven, D. M. Numerical-Simulation of a Kinetically Controlled Pressure Swing Adsorption Bulk Separation Process Based on a Diffusion-Model. *Chem. Eng. Sci.* **1991**, *46*, 2213-2224.

(42) Farooq, S.; Rathor, M. N.; Hidajat, K. A Predictive Model for a Kinetically Controlled Pressure Swing Adsorption Separation Process. *Chem. Eng. Sci.* **1993**, *48*, 4129-4141.

(43) Khalighi, M.; Chen, Y. F.; Farooq, S.; Karimi, I. A.; Jiang, J. W. Propylene/Propane Separation Using SiCHA. *Ind. Eng. Chem. Res.* **2013**, *52*, 3877-3892.

(44) Geddes, R. L. Local efficiencies of bubble-plate fractionators. *Trans. Am. Inst. Chem. Engrs.* **1946**, *42*, 79-105.

(45) Krishna, R. A Maxwell-Stefan-Glueckauf Description of Transient Mixture Uptake in Microporous Adsorbents. *Sep. Purif. Technol.* **2018**, *191*, 392-399. https://doi.org/10.1016/j.seppur.2017.09.057.

(46) Glueckauf, E. Theory of Chromatography. Part 10- Formulae for Diffusion into Spheres and their Application to Chromatography. *Trans. Faraday Soc.* **1955**, *51*, 1540-1551.

(47) Kooijman, H. A.; Taylor, R. A dynamic nonequilibrium model of tray distillation columns. *A.I.Ch.E.J.* **1995**, *41*, 1852-1863.

(48) Michelsen, M. An efficient general purpose method of integration of stiff ordinary differential equations. *A.I.Ch.E.J.* **1976**, *22*, 594-597.

(49) Bulirsch, R.; Stoer, J. Numerical treatment of ordinary differential equations by extrapolation methods. *Numer. Math.* **1966**, *8*, 1-14.

(50) Krishna, R.; Baur, R. Diffusion, Adsorption and Reaction in Zeolites: Modelling and Numerical Issues. http://krishna.amsterchem.com/zeolite/, University of Amsterdam, Amsterdam, 1 January 2015.

(51) Krishna, R. Screening Metal-Organic Frameworks for Mixture Separations in Fixed-Bed Adsorbers using a Combined Selectivity/Capacity Metric. *RSC Adv.* **2017**, *7*, 35724-35737. https://doi.org/10.1039/C7RA07363A.

(52) Krishna, R. Methodologies for Evaluation of Metal-Organic Frameworks in Separation Applications. *RSC Adv.* **2015**, *5*, 52269-52295.

(53) Krishna, R.; Long, J. R. Screening metal-organic frameworks by analysis of transient breakthrough of gas mixtures in a fixed bed adsorber. *J. Phys. Chem. C* **2011**, *115*, 12941-12950.

(54) Tagliabue, M.; Farrusseng, D.; Valencia, S.; Aguado, S.; Ravon, U.; Rizzo, C.; Corma, A.; Mirodatos, C. Natural gas treating by selective adsorption: Material science and chemical engineering interplay. *Chem. Eng. J.* **2009**, *155*, 553-566.

(55) Bhadra, S. J.; Farooq, S. Separation of MethaneNitrogen Mixture by Pressure Swing Adsorption for Natural Gas Upgrading. *Ind. Eng. Chem. Res.* **2011**, *50*, 14030-14045.

(56) Majumdar, B.; Bhadra, S. J.; Marathe, R. P.; Farooq, S. Adsorption and Diffusion of Methane and Nitrogen in Barium Exchanged ETS-4. *Ind. Eng. Chem. Res.* **2011**, *50*, 3021-3034.

(57) Jayaraman, A.; Hernandez-Maldonado, A. J.; Yang, R. T.; Chinn, D.; Munson, C. L.; Mohr, D. H. Clinoptilolites for Nitrogen/Methane Separation. *Chem. Eng. Sci.* **2004**, *59*, 2407-2417.

(58) Kuznicki, S. M.; Bell, V. A.; Nair, S.; Hillhouse, H. W.; Jacubinas, R. M.; Braunbarth, C. M.; Toby, B. H.; Tsapatsis, M. A titanosilicate molecular sieve with adjustable pores for size-selective adsorption of molecules. *Nature* **2001**, *412*, 720-724.

(59) Bhadra, S. J. *Methane-Nitrogen Separation by Pressure Swing Adsorption*. Ph.D. Dissertation, National University of Singapore, Singapore, 2007.

(60) Binder, T.; Lauerer, A.; Chmelik, C.; Haase, J.; Kärger, J.; Ruthven, D. M. Micro-imaging of transient intracrystalline concentration profiles during two-component uptake of light hydrocarbon - carbon dioxide mixtures by DDR-type zeolites. *Ind. Eng. Chem. Res.* **2015**, *54*, 8997-9004.

(61) Lauerer, A.; Binder, T.; Chmelik, C.; Miersemann, E.; Haase, J.; Ruthven, D. M.; Kärger, J. Uphill Diffusion and Overshooting in the Adsorption of Binary Mixtures in Nanoporous Solids. *Nat. Commun.* **2015**, *6*, 7697. http://dx.doi.org/doi:10.1038/ncomms8697.

(62) Binder, T. *Mass Transport in Nanoporous Materials: New Insights from Micro-Imaging by Interference Microscopy*. Ph.D. Dissertation, Universität Leipzig, Leipzig, 2013.

(63) Krishna, R. Diffusing Uphill with James Clerk Maxwell and Josef Stefan. *Chem. Eng. Sci.* **2018**, *XX*, XX-XX. https://doi.org/10.1016/j.ces.2018.10.032.

(64) Lastari, F.; Pareek, V.; Trebble, M.; Tade, M. O.; Chinn, D.; Tsai, N. C.; Chan, K. I. Extractive Distillation for CO_2–Ethane Azeotrope Separation. *Chem. Eng. Process.* **2012**, *52*, 155-161.

(65) Ribeiro, C. P.; Freeman, B. D.; Paul, D. R. Pure- and Mixed-Gas Carbon Dioxide/Ethane Permeability and Diffusivity in a Cross-linked Poly(ethylene oxide) Copolymer. *J. Membr. Sci.* **2011**, *377*, 110-123.

(66) Krishna, R. Describing Mixture Permeation across Polymeric Membranes by a Combination of Maxwell-Stefan and Flory-Huggins Models. *Polymer* **2016**, *103*, 124-131.

(67) Lin, R.-B.; Li, L.; Zhou, H.-L.; Wu, H.; He, C.; Li, S.; Krishna, R.; Li, J.; Zhou, W.; Chen, B. Molecular Sieving of Ethylene from Ethane using a Rigid Metal-Organic Framework. *Nature Materials* **2018**, *17*, 1128-1133. http://dx.doi.org/10.1038/s41563-018-0206-2.

(68) Farooq, S.; Ruthven, D. M.; Boniface, H. A. Numerical-Simulation of a Pressure Swing Adsorption Oxygen Unit. *Chem. Eng. Sci.* **1989**, *44*, 2809-2816.

(69) Rama Rao, V.; Farooq, S.; Krantz, W. B. Design of a Two-Step Pulsed Pressure-Swing Adsorption-Based Oxygen Concentrator. *A.I.Ch.E.J.* **2010**, *56*, 354-370.

(70) Rama Rao, V. *Adsorption based portable oxygen concentrator for personal medical applications*. Ph.D. Dissertation, National University of Singapore, Singapore, 2011.

(71) Ritter, J. A. Development of Pressure Swing Adsorption Technology for Spaceflight Oxygen Concentrators. http://www.dsls.usra.edu/meetings/hrp2010/pdf/Friday/Ritter.pdf, NASA Human Research Program, Houston, 2010.

(72) Yang, R. T. *Gas separation by adsorption processes*. Butterworth: Boston, 1987.

(73) Farooq, S. Sorption and Diffusion of Oxygen and Nitrogen in Molecular- Sieve RS-10. *Gas Sep. Purif.* **1995**, *9*, 205-212.

(74) Da Silva, F. A.; Rodrigues, A. E. Vacuum swing adsorption for propylene/propane separation with 4A zeolite. *Ind. Eng. Chem. Res.* **2001**, *40*, 5758-5774.

(75) Grande, C. A.; Poplow, F.; Rodrigues, A. E. Vacuum pressure swing adsorption to produce polymer-grade polypropylene. *Separ. Sci. Technol.* **2010**, *45*, 1252-1259.

(76) Da Silva, F. A.; Rodrigues, A. E. PropylenePropane Separation by Vacuum Swing Adsorption Using 13X Zeolite. *A.I.Ch.E.J.* **2001**, *47*, 341-357.

(77) Geier, S. J.; Mason, J. A.; Bloch, E. D.; Queen, W. L.; Hudson, M. R.; Brown, C. M.; Long, J. R. Selective adsorption of ethylene over ethane and propylene over propane in the metal–organic frameworks M_2(dobdc) (M = Mg, Mn, Fe, Co, Ni, Zn). *Chem. Sci.* **2013**, *4*, 2054-2061.

(78) Yoon, J. W.; Jang, I. T.; Lee, K.-Y.; Hwang, Y. K.; Chang, J.-S. Adsorptive Separation of Propylene and Propane on a Porous Metal-Organic Framework, Copper Trimesate. *Bull. Korean Chem. Soc.* **2010**, *31*, 220-223.

(79) Khalighi, M.; Karimi, I. A.; Farooq, S. Comparing SiCHA and 4A Zeolite for Propylene/Propane Separation using a Surrogate-Based Simulation/Optimization Approach. *Ind. Eng. Chem. Res.* **2014**, *53*, 16973-16983.

(80) Olson, D. H.; Camblor, M. A.; Vallaescusa, L. A.; Kuehl, G. H. Light hydrocarbon sorption properties of pure silica Si-CHA and ITQ-3 and high silica ZSM-58. *Microporous Mesoporous Mater.* **2004**, *67*, 27-33.

(81) Hedin, N.; DeMartin, G. J.; Roth, W. J.; Strohmaier, K. G.; Reyes, S. C. PFG NMR self-diffusion of small hydrocarbons in high silica DDR, CHA and LTA structures. *Microporous Mesoporous Mater.* **2008**, *109*, 327-334.

(82) Ruthven, D. M.; Reyes, S. C. Adsorptive separation of light olefins from paraffins. *Microporous Mesoporous Mater.* **2007**, *104*, 59-66.

(83) Cadiau, A.; Adil, K.; Bhatt, P. M.; Belmabkhout, Y.; Eddaoudi, M. A Metal-Organic Framework–Based Splitter for Separating Propylene from Propane. *Science* **2016**, *353*, 137-140.

(84) Cui, X.; Chen, K.; Xing, H.; Yang, Q.; Krishna, R.; Bao, Z.; Wu, H.; Zhou, W.; Dong, X.; Han, Y.; Li, B.; Ren, Q.; Zaworotko, M. J.; Chen, B. Pore Chemistry and Size Control in Hybrid Porous Materials for Acetylene Capture from Ethylene. *Science* **2016**, *353*, 141-144.

(85) Andres-Garcia, E.; Oar-Arteta, L.; Gascon, J.; Kapteijn, F. ZIF-67 as Silver-Bullet in Adsorptive Propane/Propylene Separation. *Chem. Eng. J.* **2018**, *XXX*, XXX-XXX. http://dx.doi.org/10.1016/j.cej.2018.11.118.

(86) Chng, M. L.; Xiao, Y.; Chung, T.-S.; Toriida, M.; Tamai, S. Enhanced propylene/propane separation by carbonaceous membrane derived from poly (aryl ether ketone)/2,6-bis(4-azidobenzylidene)-4-methyl-cyclohexanone interpenetrating network. *Carbon* **2009**, *47*, 1857-1866.

(87) Lin, Y. S. Molecular Sieves for Gas Separation. *Science* **2016**, *353*, 121-122.

(88) Herm, Z. R.; Wiers, B. M.; Van Baten, J. M.; Hudson, M. R.; Zajdel, P.; Brown, C. M.; Maschiocchi, N.; Krishna, R.; Long, J. R. Separation of Hexane Isomers in a Metal-Organic Framework with Triangular Channels *Science* **2013**, *340*, 960-964.

(89) Krishna, R.; van Baten, J. M. Screening of zeolite adsorbents for separation of hexane isomers: A molecular simulation study. *Sep. Purif. Technol.* **2007**, *55*, 246-255.

(90) Dubbeldam, D.; Krishna, R.; Calero, S.; Yazaydın, A. Ö. Computer-Assisted Screening of Ordered Crystalline Nanoporous Adsorbents for Separation of Alkane Isomers. *Angew. Chem. Int. Ed.* **2012**, *51*, 11867-11871.

(91) Dandekar, H. W.; Funk, G. A.; Gillespie, R. D.; Zinnen, H. A.; McGonegal, C. P.; Kojima, M.; Hobbs, S. H., Process for alkane isomerization using reactive chromatography. UOP, Des Plaines, Illinois, USA., *U.S. Pat.*, US 5763730, 1999.

(92) Dandekar, H. W.; Funk, G. A.; Zinnen, H. A., Process for separating and recovering multimethyl-branched alkanes. UOP LLC, Des Plaines, Illinois, USA., *U.S. Pat.*, US 6069289, 2000.

(93) Carr, R. W.; Dandekar, H. W. *Adsorption with reaction*. Reactive Separation Processes; 2nd, Edited by S. Kulprathipanja, Taylor & Francis: New York, USA, 2001.

(94) Krishna, R.; Smit, B.; Calero, S. Entropy effects during sorption of alkanes in zeolites. *Chem. Soc. Rev.* **2002**, *31*, 185-194.

(95) Krishna, R.; van Baten, J. M. In silico screening of metal-organic frameworks in separation applications. *Phys. Chem. Chem. Phys.* **2011**, *13*, 10593-10616.

(96) Titze, T.; Chmelik, C.; Kärger, J.; van Baten, J. M.; Krishna, R. Uncommon Synergy Between Adsorption and Diffusion of Hexane Isomer Mixtures in MFI Zeolite Induced by Configurational Entropy Effects *J. Phys. Chem. C* **2014**, *118*, 2660-2665.

(97) Krishna, R.; van Baten, J. M. Influence of Adsorption Thermodynamics on Guest Diffusivities in Nanoporous Crystalline Materials. *Phys. Chem. Chem. Phys.* **2013**, *15*, 7994-8016.

(98) Schuring, D.; Jansen, A. P. J.; van Santen, R. A. Concentration and chainlength dependence of the diffusivity of alkanes in zeolites studied with MD simulations. *J. Phys. Chem. B* **2000**, *104*, 941-948.

(99) Krishna, R.; van Baten, J. M. Diffusion of Hydrocarbon Mixtures in MFI Zeolite: Influence of Intersection Blocking. *Chem. Eng. J.* **2008**, *140*, 614-620.

(100) Cavalcante, C. L.; Ruthven, D. M. Adsorption of Branched and Cyclic Paraffins in Silicalite .2. Kinetics. *Ind. Eng. Chem. Res.* **1995**, *34*, 185-191.

(101) Jolimaître, E.; Tayakout-Fayolle, M.; Jallut, C.; Ragil, K. Determination of mass transfer and thermodynamic properties of branched paraffins in silicalite by inverse chromatography technique. *Ind. Eng. Chem. Res.* **2001**, *40*, 914-926.

(102) Jolimaître, E.; Ragil, K.; Tayakout-Fayolle, M.; Jallut, C. Separation of Mono- and Dibranched Hydrocarbons on Silicalite. *A.I.Ch.E.J.* **2002**, *48*, 1927-1937.